© Copyright 2008

Theresa Vivian Bullard

Luminescence Labeling and Dynamics of Growth Active Crystal Surface Structures

Theresa Vivian Bullard

A dissertation submitted in partial fulfillment of the
requirements for the degree of:

Doctor of Philosophy

University of Washington

2008

Program Authorized to Offer Degree: Department of Physics

UMI Number: 3303273

INFORMATION TO USERS

The quality of this reproduction is dependent upon the quality of the copy submitted. Broken or indistinct print, colored or poor quality illustrations and photographs, print bleed-through, substandard margins, and improper alignment can adversely affect reproduction.

In the unlikely event that the author did not send a complete manuscript and there are missing pages, these will be noted. Also, if unauthorized copyright material had to be removed, a note will indicate the deletion.

UMI®

UMI Microform 3303273

Copyright 2008 by ProQuest LLC.

All rights reserved. This microform edition is protected against unauthorized copying under Title 17, United States Code.

ProQuest LLC
789 E. Eisenhower Parkway
PO Box 1346
Ann Arbor, MI 48106-1346

University of Washington
Graduate School

This is to certify that I have examined this copy of a doctoral dissertation by

Theresa Vivian Bullard

and have found that it is complete and satisfactory in all respects,
and that any and all revisions required by the final
examining committee have been made.

Chair of The Supervisory Committee:

Marjorie Olmstead

Reading Committee:

Bart Kahr

Marjorie Olmstead

Gerald Seidler

Date: 10 March 2008

In presenting this dissertation in partial fulfillment of the requirements for the doctoral degree at the University of Washington, I agree that the Library shall make its copies freely available for inspection. I further agree that extensive copying of the dissertation is allowable only for scholarly purposes, consistent with "fair use" as prescribed in the U.S. Copyright Law. Requests for copying or reproduction of this dissertation may be referred to Proquest Information and Learning, 300 North Zeeb Road, Ann Arbor, MI 48106-1346, 1-800-521-0600 to whom the author has granted "the right to reproduce and sell (a) copies of the manuscript in microform and/or (b) printed copies of the manuscript made from microform."

Signature Theresa Bullard

Date 10 March, 2008

University of Washington

Abstract

Luminescence Labeling and Dynamics of Growth Active Crystal Surface Structures

Theresa Vivian Bullard

Chairperson of the Supervisory Committee:
Marjorie Olmstead
Department of Physics

One aspect of the multifaceted proposal by A. G. Cairns-Smith (CS), that imperfect crystals have the capacity to act as primitive genes by transferring the disposition of their imperfections from one crystal to another, is investigated. An experiment was designed in a model crystalline system unrelated to the composition of the pre-biotic earth but suited to a well-defined test. Plates of potassium hydrogen phthalate were studied in order to ascertain whether, according to CS, parallel screw dislocations could serve as an information store with cores akin to punches in an old computer card. Evidence of screw dislocations was obtained from their associated growth hillocks through differential interference contrast microscopy, atomic force microscopy, and luminescence labeling of hillocks in conjunction with confocal laser scanning microscopy. Inheritance was evaluated by the corresponding patterns of luminescence developed in 'daughter' crystals grown from seed in the presence of fluorophores. The dispositions and evolution of growth active hillock patterns were quantified by fractal correlation analysis and statistical analysis. Along the way, we came to realize that transferring information encoded in the disposition of screw dislocations is complicated by several factors that lead to 'mutations' in the information stored in the pattern of defects. These observations forced us to confront the fundamental mechanisms that give rise to screw dislocations. It

became clear that inter-hillock correlations play a significant role in the appearance of new dislocations through growth, and cause the overall pattern of hillocks to be non-random. Tendencies for clustering and correlations along various crystallographic directions were observed. Investigations into the dye-crystal surface chemistries and interactions with hillock steps also ensued through a combination of experimental techniques and force-field calculations. It was established that certain dye molecules not only recognize some propagating steps as opposed to others, but preferentially choose between kinks propagating in opposing directions on the same step. Beyond providing the first experimental test of the CS proposal, this work is aimed at understanding the nucleation, evolution, and impurity interactions of growth-induced screw dislocations, a necessary ingredient for the growth of crystals at low supersaturation.

TABLE OF CONTENTS

Page

List of Figures.....iv

List of Tables.....ix

List of Abbreviations.....x

Prologue.....1

Chapter 1 - INTRODUCTION.....3
1.1 Cairns-Smith Hypothesis - 'Crystals-as-Genes'.....3
1.2 Defects in Crystals.....7
1.2.1 Dislocations.....9
1.2.2 Screw Dislocations and Crystal Growth.....13
1.2.2.1 Burton-Cabrera-Frank Model.....22
1.2.2.2 Sources of Growth Induced Screw Dislocations.....28
1.2.2.3 Factors Affecting Spiral Growth.....31
1.3 Summary.....44
Notes and References to Chapter 1.....46

Chapter 2 - EXPERIMENTAL BACKGROUND.....50
2.1 Detecting Screw Dislocations.....50
2.2 Dyeing Crystals.....51
2.2.1 Intersectoral Zoning - Dyeing Growth Sectors.....53
2.2.2 Intrasectoral Zoning - Dyeing Hillocks.....55
2.3 Potassium Hydrogen Phthalate (KAP).....58
2.3.1 KAP Crystal Structure and Habit.....58
2.3.2 Experimental Conditions for KAP Growth.....61
2.3.3 Properties of KAP.....63
2.3.4 KAP Defects.....69
2.4 Dyes Used to Label KAP Hillocks.....78
2.4.1 Triphenylmethane Dyes.....81
2.4.2 2′,7′-Dichlorofluorescein.....88
2.5 Methods for Identifying Dye-Crystal Interactions.....97
2.5.1 Spectroscopy.....97
2.5.1.1 Beer's Law.....97
2.5.1.2 Dipole Transition Moment.....99
2.5.1.3 Luminescence Spectra.....101
2.5.2 Force-Field Calculations.....102
2.5.3 Observing Dyed Hillocks.....108

2.6 Confocal Microscopy.....109
2.6.1 Introduction.....109
2.6.2 Instrument Description and Settings Used.....113
2.7 Quantifying Information Content and 'Genetic Inheritance'.....117
2.7.1 Fractal Analysis.....119
2.7.2 Controlled Growth Experiments.....127
2.8 Summary of Experimental Methods.....131
Notes and References to Chapter 2.....133

Chapter 3 - ROLE OF KINKS IN DYEING CRYSTALS: DICHLOROFLUORESCEIN IN KAP.....140
3.1 Concentration Dependent Linear Dichroism.....140
3.1.1 Ensemble-Averaged DCF Orientations.....142
3.1.2 Single Molecule Studies of DCF Orientations in KAP.....143
3.2 Dye Impact on Hillock Morphology.....146
3.3 Experiments with Trivalent Cationic Impurities.....151
3.3.1 Fe^{3+} Additive.....153
3.3.2 Ce^{3+} Additive.....155
3.4 Force-Field Calculations.....159
3.4.1 Terrace Docking.....161
3.4.2 Step-Edge Docking.....164
3.4.3 Step-Vacancy Docking.....167
3.4.4 Kink Site Docking.....170
3.4.5 [100] Step Docking.....173
3.5 Summary.....177
Notes and References to Chapter 3.....182

Chapter 4 - INFORMATION CONTENT AND TRANSFER THROUGH CRYSTAL GROWTH.185
4.1 Information Transfer Through Crystal Growth.....185
4.1.1 Daughter Growth From Cleaved Surfaces.....185
4.1.2 Daughter Growth From Unadulterated Surfaces.....192
4.1.2.1 Solution Flow and Controlled Growth.....193
4.1.2.2 Particulate Inclusion.....195
4.1.2.3 X-ray Topography Of Dyed KAP.....197
4.2 Identifying Screw Dislocation Patterns and Evolution.....205
4.2.1 Locating Screw Dislocations.....207
4.2.2 Data Analysis Results.....210
4.2.3 Discussion.....249
4.3 Summary.....255
Notes and References to Chapter 4.....258

Chapter 5 - CONCLUSIONS.....264
Notes and References to Chapter 5.....270

Glossary.....272

Bibliography.....277

Appendix A - Code for Fractal Analysis and Monte Carlo Simulation.....287

Appendix B - Computer Vision Hillock Detection.....319

Appendix C – Sample Reference List.....329

LIST OF FIGURES

Figure Number Page

1.1 Generic 'genetic crystal' model of Cairns-Smith..... 4
1.2 Genetic 'punched-card' crystal..... 9
1.3 Burgers circuits.....10
1.4 Edge and screw dislocations..... 11
1.5 Diagram of dislocation branching at a node.....12
1.6 Idealized crystal surface model.....15
1.7 Terrace-ledge-kink model.....15
1.8 Qualitative schematic of the nucleation barrier.....20
1.9 Growth rate versus supersaturation schematic.....21
1.10 Spiral morphology..... 26
1.11 Idealized model of a hillock created by a screw dislocation..... 27
1.12 Polygonized growth spiral..... 28
1.13 Dislocation pairs.....36
2.1 Intersectoral zoning..... 54
2.2 Intrasectoral zoning and KAP hillocks..... 57
2.3 KAP chemical formula and ball-and-stick model..... 59
2.4 KAP crystal structure..... 60
2.5 Transmission spectra of KAP..... 68
2.6 KAP solubility curve..... 69
2.7 KAP defects.....71
2.8 KAP hillock morphology.....73
2.9 Trivalent cations in KAP hillocks..... 77
2.10 KAP crystal and hillocks dyed with LGSFY (**1**) at 10^{-5} M concentration....82
2.11 Absorbance spectra for **1**..... 83
2.12 Normalized fluorescence spectra for **1** in KAP crystals..... 83

2.13 Linear dichroism of **1** in KAP hillock fast slope at varying concentration. 84

2.14 Average dipole transition moment orientation of **1** in KAP at varying dye concentration.....84

2.15 KAP crystal and hillocks dyed with erioglaucine (**2**) at 10^{-5} M concentration..... 86

2.16 Absorbance spectra for **2**..... 86

2.17 Normalized fluorescence spectra for **2** in KAP crystals.....87

2.18 Linear dichroism of **2** in KAP hillock fast slope at varying concentration. 87

2.19 Average dipole transition moment orientation of **2** in KAP at varying dye concentration.....88

2.20 KAP crystal and hillocks dyed with DCF (**3**) at 5×10^{-5} M concentration....90

2.21 Normalized absorbance spectra for **3**.....90

2.22 Fluorescence spectra for **3** in KAP crystals..... 91

2.23 Linear dichroism of **3** in KAP hillock fast slope at varying concentration. 91

2.24 Average dipole transition moment orientation of **3** in KAP at varying dye concentration.....92

2.25 Equilibria of **3**.....93

2.26 Absorption spectra for **3** at different pH values (~10^{-5} M).....96

2.27 Beer's law plot of **3** in aqueous KAP solution.....98

2.28 Estimate DCF dipole transition moment orientation.....103

2.29 Example docking locations for DCF into KAP (010) steps.....105

2.30 Schematic of Airy diffraction pattern.....111

2.31 Confocal microscopy diagram..... 113

2.32 Confocal beam path for multi-spectral imaging.....115

2.33 Confocal slices of KAP with **3**.....117

2.34 Density correlation function analysis 123

2.35 Pair correlation plot for one optical *z*-section of hillock data.....124

2.36 Angular correlation analysis..... 126

2.37 Crystal growth flow system..... 129

3.1 Absorption dichroism of DCF (2.5×10^{-5}M) in the fast slopes of KAP hillocks.....141

3.2 Single molecule distribution of DCF in KAP.....145

3.3 AFM image of KAP/DCF hillock..... 149

3.4 Angle spanned by the boundary between the fast and slow steps of KAP hillocks..... 151

3.5 Selective kink adsorption of impurities into KAP hillock fast steps..... 152

3.6 Average DCF orientation as a function of Fe^{3+} dopant..... 154

3.7 Average DCF orientation as a function of Ce^{3+} dopant..... 156

3.8 Normalized emission intensity as a function of Ce^{3+} concentration for KAP/DCF/Ce^{3+} (10^{-6} M).....157

3.9 KAP/DCF/Ce^{3+} images at different Ce^{3+} concentrations.....158

3.10 Stable (010) surface terminations..... 161

3.11 Arrangement of K^+ ions on the partial-K^+ terminated (010) KAP surface.....163

3.12 Step edge docking of DCFH..... 166

3.13 Docking sites for DCF in KAP.....172

3.14 <100> step inclusion of DCF in KAP at high dye concentrations.....174

3.15 DCF^- docking into KAP [$\bar{1}$00] step..... 176

4.1 Information transfer through crystal growth.....186

4.2 Cleaved KAP/**3**..... 187

4.3 Information transfer from complimentary surfaces.....189

4.4 Complementary surfaces from imperfect cleavage.....190

4.5 DIC image of KAP re-growth after cleavage..... 191

4.6 Inheritance without cleavage..... 193

4.7 Confocal images of crystal grown with 1 μm red fluorescent polystyrene beads..... 196

4.8 Spontaneously nucleated pure KAP. Photo (a) and X-ray topograph of 400 reflection (b).....199

4.9 Spontaneously nucleated KAP/DCF (10^{-5} M). Photo (a) and X-ray topograph of 400 reflection (b)..... 200

4.10 Seed-grown KAP with 1 μm polystyrene beads included. Photo (a) and X-ray topograph (b)..... 201

4.11 Seed-grown KAP with 1 μm polystyrene beads included. Photo (a) and X-ray topograph (b)..... 202

4.12 Photo of tails or channels of bubbles typically resulting from capture of small solid particles during growth of crystal..... 203

4.13 Confocal slices of KAP with **3**..... 206

4.14 Confocal slices of KAP with **1**..... 207

4.15 Confocal imaging frame of KAP with **3**..... 208

4.16 Pair correlation plots for hillock pattern (a) and random pattern (b) relating to crystal #1..... 213

4.17 Nearest neighbor distributions for crystal #1..... 214

4.18 Angular correlations for crystal #1..... 217

4.19 Growth statistics for crystal #2..... 218

4.20 Fractal dimensions for all optical sections of crystal #2..... 220

4.21 Nearest neighbor distribution for hillock (a) and Monte Carlo (b) data of crystal #2..... 222

4.22 Angular correlations comparison for crystal #2 and simulated data..... 224

4.23 Growth statistics for crystal #3..... 226

4.24 Fractal dimensions for all optical sections of crystal #3..... 228

4.25 Nearest neighbor distribution for hillock (a) and Monte Carlo (b) data of crystal #3..... 230

4.26 Angular correlations comparison for crystal #3 and simulated data..... 231

4.27 Growth statistics for crystal #4..... 234

4.28 Fractal dimensions for all optical sections of crystal #4..... 236

4.29 Nearest neighbor distribution for hillock (a) and Monte Carlo (b) data of crystal #4..... 237

4.30 Angular correlations comparison for crystal #4 (a) and simulated data (b)..... 240

4.31 Growth statistics for crystal #5..... 242

4.32 Fractal dimensions for all optical sections of crystal #5..... 244

4.33 Nearest neighbor distribution for hillock (a) and Monte Carlo (b) data of crystal #5..... 245

4.34 Angular correlations comparison for crystal #5 (a) and simulated data (b)..... 248

B.1 Intensity line profiles of dyed hillocks..... 320

B.2 Laplacian and threshold operators applied to hillock image..... 321

B.3 Circular gradient and threshold operations applied to hillock image.....322
B.4 Edge template matching operations applied to hillocks.....323
B.5 Corner template matching operation applied to hillocks.....324
B.6 Harris detector eigenvalue contour map for feature selection.....326

LIST OF TABLES

Table Number Page

1.1 Types of crystal defects..... 7

2.1 Types of impurity adsorption sites in KAP.....76

2.2 Dye characteristics.....80

2.3 2′,7′-Dichlorofluorescein (**3**) species pK_a values, populations in KAP solution, and absorption peaks.....95

2.4 Wavelength-dependent indices of refraction and birefringence corrections for KAP..... 100

2.5 Calculated energies for DCF^- and DCFH docking simulations into KAP (010) steps.....107

2.6 Confocal settings.....116

3.1 Ensemble-averaged orientations of DCF in KAP.....143

3.2 Hillock morphology measurements from AFM and DIC images..... 150

3.3 Docking of DCFH at step edges.....167

3.4 Docking of DCF^- and DCFH into an "A" site vacancy in the upper half of straight KAP (010) fast steps.....170

3.5 Docking of DCF^- and DCFH into a kink in the $[\bar{1}1\bar{1}]$ fast step on the C-H terminated (010) KAP surface.....171

3.6 Docking for DCF^- and DCFH into the $[\bar{1}00]$ intermediate step on the (010) C-H terminated KAP surface.....175

4.1 Summary of data analysis results.....250

LIST OF ABBREVIATIONS

1 – Light Green SF Yellowish

2 – Erioglaucine

3 – 2′,7′-Dichlorofluorescein

AFM – Atomic Force Microscopy

AU – Airy Unit

BCF – Burton-Cabrera-Frank

CL – Cathodal Luminescence

CLSM – Confocal Laser Scanning Microscopy

CS – A. G. Cairns-Smith

DCF – 2′,7′-Dichlorofluorescein (equilibrium mixture)

DCF^- - Mono-anionic Form of DCF

DCF^{2-} - Di-anionic Form of DCF

DCFH – Neutral Form of DCF

DIC – Differential Interference Contrast (microscopy)

EDTA – Ethylenediamine Tetraacetic Acid

EGME - Ethylene Glycol Monomethyl Ether

Erio – Erioglaucine

FWHM – Full Width Half Max

GFP – Green Fluorescent Protein

GT – Genetic Takeover

HP^- - Hydrogen Phthalate

KAP – Potassium Hydrogen Phthalate (or potassium acid phthalate)

LD – Linear Dichroism

LGSFY – Light Green SF Yellowish

PBC – Periodic Bond Chain

PEG – Polyethylene Glycol

RNA – Ribonucleic Acid

STM – Scanning Tunneling Microscopy

TEM – Transmission Electron Microscopy

ACKNOWLEDGEMENTS

Thank you to my committee: Dr. Marjorie Olmstead, Dr. Bart Kahr, Dr. Gerald Seidler, Dr. Michael Schick, Dr. Samuel Fain, Dr. Stephen Ellis, and Dr. Woodruff Sullivan.

Thank you to my advisor, Dr. Bart Kahr, for your patience, your creativity, your friendship, your good heart, and for providing a model of a scientist who holds true to his core values and the pursuit of knowledge as a noble path.

Thank you Dr. Marjorie Olmstead for your guidance and support over the years and for serving as the co-chair of my committee.

Thank you Dr. Jerry Seidler for your assistance with the computer vision work, and for your cheerful disposition and laid-back mentorship.

Thank you to Dr. Andrew Rohl for your assistance with the molecular modeling and force field calculations of dye-crystal interactions.

Thank you Dr. Alexey Voloshin for your selfless assistance with the X-ray topography studies of our crystals.

Thank you to the now *Dr.* Jason Benedict for your ever-so-entertaining presence in our lab, your candid self, and for always being willing to lend a helping hand and share your wisdom.

Thank you to the now *Dr.* Kristin Wustholz for your exemplary approach to scientific research and your driven pursuit of a job well done, all the while keeping a social and fun-loving vibe around the lab. It was a delight to collaborate with you on projects.

Thank you to Dr. Ryan Sours for all your assistance during your time in our lab. The contribution you made was immense and you never ceased to amaze me with your broad skill-base as a scientist.

Thank you to John Freudenthal for your collaboration with the Cairns-Smith experimental studies and for the AFM imaging you did on KAP/DCF.

Thank you to Miranda Robertson, Joyce Chen, and Serine Avagyan for your assistance in the lab and all your hard work. I'm sure each of you will go on to become great scientists, doctors, teachers, or whatever you decide to pursue.

Thank you to my fellow members of the Kahr Labs: Dr. Yonghong Bing, Eric Bott, Charles Branham, Dr. Jason Benedict, Dr. Kacey Claborn, Miki Kurimoto, Dawn Cohen, John Freudenthal, Erica Gunn, Eva Hollis, Christine Isborne, Dr. Sei-Hum Jang, Laura Snyder, Dr. Ryan Sours, Dr. Kristin Wustholz, Dr. Werner Kaminsky, and of course Dr. Bart Kahr.

Thank you to my former research group of the SNO Collaboration, the skills, knowledge, and experience I gained working with you proved valuable and essential in my ability to complete much of the work herein.

Thank you to my parents, Jay and Barbara Bullard, for your support in all capacities, especially the financial support you have given me so that I could continue pursuing this Ph.D. until completion, as well as for your love, encouragement, and guidance over the years. I couldn't have asked for better parents. Beyond being great parents, you have also evolved into my closest, most cherished friends, and for that I am ever the more grateful.

Thank you to my siblings, Christina, Stephen, and John: I treasure the relationships we have been able to develop as we've grown. It is an honor to witness each of you chose your own paths, learn from your own challenges, and grow into the amazing and good individuals you are.

Thank you to my community of friends, who by now are all around the world. Your friendship and presence in my life has brought a greater sense of meaning, fulfillment, and purpose. To me you are much more than friends, you are my family of the heart and spirit.

And last, but certainly not least, I give special thanks to Gudni, Verla, Donna, and John E. for your ongoing support, encouragement, friendship, and guidance, and for helping hold the field for me over the last 7 years.

DEDICATION

I dedicate this work to my parents, Jay and Barbara Bullard, to whom I owe great gratitude for their continuous and unconditional support, and for providing me with the opportunity to pursue and complete this degree.

The completion of this work is also in honor of the memory of Julian Laserna, whose passionate pursuit of all life had to offer and whose full-throttle approach to achieving objectives have profoundly impacted my perspectives, attitudes, and approach to life, love, and the work at hand.

PROLOGUE

"Schrödinger's book [What is Life?] was seminal because he knew how to ask the right questions...He did not answer these questions, but by asking them he set biology moving along the path that led to the epoch-making discoveries of the subsequent forty years ...Schrödinger showed wisdom not only in the questions that he asked but also in the questions that he did not ask... He understood that the time was ripe in 1943 for a fundamental understanding of the physical basis of life. He also understood that the time was not then ripe for any fundamental understanding of life's origin... Now, half a century later, the time is ripe to ask the questions Schrödinger avoided... The questions of origin are now becoming experimentally accessible just as the questions of structure were becoming experimentally accessible in the 1940's."

~Freeman Dyson[1]

"The mystery of life's origin has puzzled philosophers, theologians, and scientists for over two and a half millennia. During the next decade, we have a golden opportunity to make some major advances in this field. That scientists are currently stumped makes this opportunity all the more exciting and compelling."

~Paul Davies[2]

Why are distinguished physicists such as Erwin Schrödinger, Freeman Dyson, Paul Davies, and many others interested in exploring the nature and origins of

life? Perhaps it is because physicists and astronomers are often attracted to unanswered problems of great import. And perhaps, as Schrödinger put it, "we have inherited from our forefathers the keen longing for unified, all-embracing knowledge," calling scientists to "embark on a synthesis of facts and theories", even if it takes them outside of their area of expertise.[3] Origin of life research today is truly an interdisciplinary field attracting the ideas and investigations of chemists, biologists, astronomers, astrobiologists, physicists, mathematicians, and philosophers. Solving this age-old riddle "remains one of the greatest scientific challenges of our age," according to Davies. And so it is that I, too, have ventured into this interdisciplinary frontier, with the intention of bringing an experimental foundation to one of the prominent untested ideas for how chemistry and the organization of information might have been turned into life. Namely, the hypothesis put forth by A. G. Cairns-Smith in Genetic Takeover and the Mineral Origins of Life.[4]

CHAPTER 1 - INTRODUCTION

1.1 Cairns-Smith Hypothesis - 'Crystals-as-Genes'

In *Genetic Takeover and the Mineral Origins of Life* (GT),[4,5] Cairns-Smith (CS) proposed that non-nucleic acid genetic systems were an essential part of the early stages of life's evolution. Convinced that the first organisms must have been constructed from entities that, unlike RNA, were abundant on the pre-biotic earth, CS argued that imperfect clay crystals played an integral part in the composition and construction of the first living organisms. He proposed that these crystals provided materials for the first genes, internal catalysts, membranes, and/or other higher order structures. In short, CS suggested, crystals "were among the central control materials of the first evolving systems".[5]

There is no universal agreement on the definition of life, although generally speaking *biological* life exhibits qualities such as homeostasis, complex organization, metabolism, growth, response to stimuli, reproduction, and through natural selection, adaptation and evolution of succeeding generations.[6] According to CS, a form of inheritable information must have been a *prerequisite* to life, because only *information* can endure and evolve.[4] This in turn requires a means of reproduction whereby specific information can be passed from one generation to the next. Also necessary is the potential for mutation, such that natural selection can occur. CS envisioned a pre-biotic genetics based on crystal growth, with information stored in patterns of crystal defects. The mutual disposition of the imperfections was presumed to be replicated, or transferred from one crystal to another, via fragmentation and epitaxy.[5,7] Such a process is

shown schematically in Figure 1.1. Much of GT is devoted toward the chemical illustration of the black squares pictured in Figure 1.1.

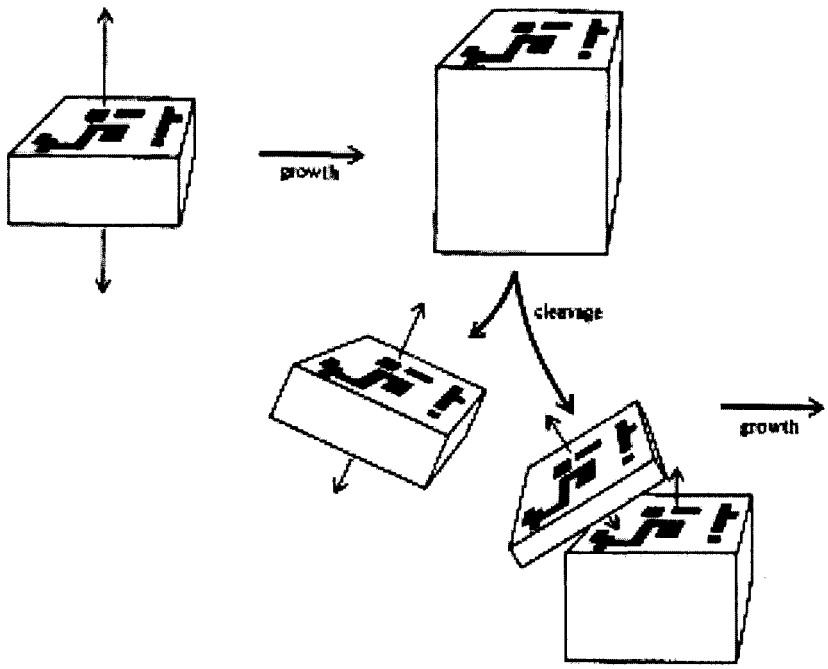

Figure 1.1 *Generic 'genetic crystal' model of Cairns-Smith.* Genetic information is stored in patterns of crystal defects, which are then replicated and transferred via fragmentation and epitaxy. Image reproduced from A. G. Cairns-Smith.[4]

The GT hypothesis requires genetic material capable of replicating in an open and unsheltered environment. These early genes presumably evolved to control their immediate environment by making increasingly elaborate 'phenotypes'. The phenotypes offered by the mutability of disordered clay crystals reproduced faster than others giving rise to natural selection. Additionally the crystals provided more habitable environments for the primitive genes allowing reproduction to be more efficient. Ultimately, a nucleic acid-like genetic material

must have taken over from the primary clay genes that were then discarded as mere scaffolds.[4]

CS's ideas have captured a place in the origin of life community and are widely cited, but acknowledgments of their virtues are almost always accompanied by the caveat that they lack verification by experiment. Below are typical commentaries on GT (phrases emboldened and underlined by author):

> *Although* ***there is no clear evidence*** *in support of a genetic takeover, several investigators have provided convincing evidence that clay minerals can, indeed, act as catalysts, particularly in driving significant polymerization reactions related to nucleotide chemistry.* (Dreamer and Fleischaker, 1994)[8]

> *Cairns-Smith's postulate of an inorganic life form* ***has failed to gather any experimental support****. The idea lives on in the limbo of uninvestigated hypotheses.* (Orgel, 1998)[9]

> *There is* ***no experimental evidence*** *to support the statement that clay can act either as a catalyst or as a replicator with enough specificity to serve as a basis for life. Cairns-Smith asserts that the chemical specificity of clay is adequate for these purposes. The experiments to prove him right or wrong have not been done.* (Dyson, 1999)[1]

> *It has to be said that there is* ***very little experimental evidence*** *to support Cairns-Smith's clay theory. Still, whatever the plausibility of clay as the primal life stuff, the basic principle of genetic takeover is sound.* (Davies, 1999)[2]

> ***As yet, there are no experimental indications to support Cairns-Smiths' model****... Most critics of Cairns-Smith's scenario focus on the fact that his presumed ancient scaffolding did not leave any mark that can be detected in present organisms.* (Fry, 2000)[10]

> *Cairns-Smith's ideas have been taken very seriously by the origin-of-life community, and his almost four decades of provocative publications are among the most widely cited in the field...By exploring the life-like properties of hypothetical evolving clays and* ***by proposing detailed (if as yet technically impossible) experiments****, he is squarely in the mainstream of the scientific enterprise.* (Hazen, 2005)[11]

In the excerpts, we confront an idea so attractive that it is invariably credited in reviews on the science of the origin of life, despite the fact that no one has been able to generate an experiment to test it for decades. Described herein is a long overdue experimental investigation of the CS 'crystals-as-genes' hypothesis. This research endeavors to evaluate one proposed mechanism whereby crystals act as a primitive source of transferable information through the arrangement of screw dislocations in a crystal (see Section 1.2). It includes:

- The introduction of a method for the identification of screw dislocations in crystals based on luminescence labeling.[12]
- The mapping of growth hillocks in a model crystal system and the evaluation of the associated information content.
- The testing of key factors that are purported to influence the appearance and behavior of screw dislocations throughout a crystal's growth history.
- The 'reproduction' of crystals to demonstrate the transfer of information between successive generations.

- The evaluation of the frequency of mutations generated during crystal growth.

1.2 Defects In Crystals

A crystal defect is any disturbance in the periodic arrangement of atoms in a lattice. All real crystals have defects. Many important characteristics, such as luminescence, diffusion of atoms, color, mechanical and plastic properties, and even crystal growth are often controlled more by the nature of the defects than by the actual host crystal. Given their far-reaching importance in the field of solid-state science, defects in crystals have been widely studied using a variety of techniques. However, there are still many unanswered questions regarding how various defects form, propagate, and influence crystal growth. Table 1.1 lists the four main classes of crystal defects.* Each one of these classes encompasses an entire volume of research in solid-state science.

Table 1.1. *Types of crystal defects.*[13,14,15]

Defect Class	Examples*
Point	*Lattice Vacancies; Chemical Impurities; Substitutional Atoms; Interstitial Atoms; Organic Dyes*
Line	*Edge Dislocations; Screw Dislocations; Steps*
Planar	*Stacking Faults; Grain Boundaries; Twin Boundaries*
Volume	*Fluid Inclusions; Voids; Precipitates*

So what exactly were CS's proposed clay genes composed of? Any combination of defects forming a pattern that reproducibly appears throughout a

---

* See Appendix A for a Glossary of terms (words in the body of the text that are *italicized and underlined* are also defined in the Glossary).

crystal could potentially qualify as 'genetic' information carriers. CS explored a number of ideas and emphasized the information stored in the relative disposition of *polytype twins* in clays within and between layers, as well as the distribution of cations (point defects) common in disordered silicate minerals. CS also considered the possibility of screw dislocations as carriers of information as follows:

> *A screw dislocation is an example of a defect that is often replicated through crystal growth. This kind of defect is faithfully copied, while other kinds, arising from initial misplacement of adding units, etc. can be put right by local reversals. A crystal containing many parallel screw dislocation lines might conceivably replicate information in the form of a particular disposition of these lines. This would be an example of a two-dimensional information store, like a stack of identical punched cards with their lines of superimposed holes analogous to the dislocation lines* (Figure 1.2).[4]

The latter proposition relating to screw dislocations motivated this dissertation, and it is the premise herein. In order to test this hypothesis it is first important to understand the basic mechanisms and interactions of screw dislocations and crystal growth.

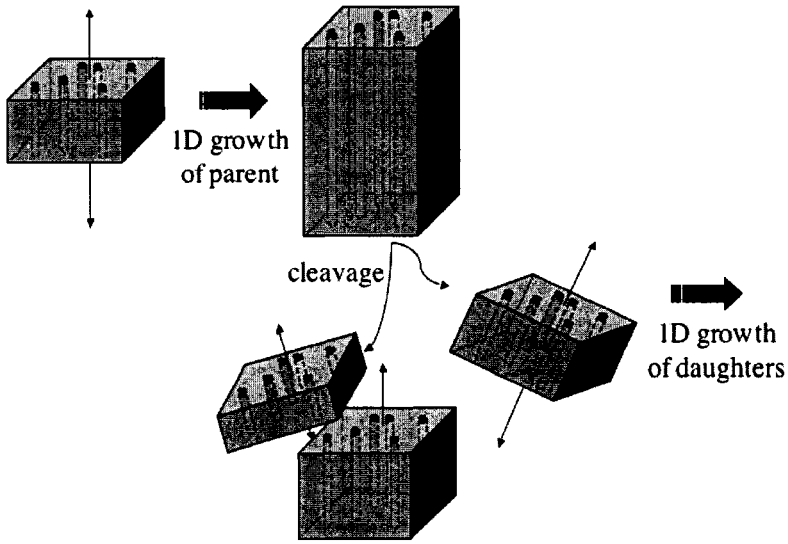

Figure 1.2 *Genetic 'punched-card' crystal.* Same as Figure 1.1, redrawn to emphasize that information is stored as a pattern of parallel dislocations, akin to an old punched computer card, that can be replicated through cleavage and subsequent crystal growth.

1.2.1 Dislocations

There are three basic types of dislocations in crystals: edge dislocations, screw dislocations, and mixed dislocations. These are best differentiated in terms of the Burgers circuit, which is any closed-loop path through a crystal lattice (atom-to-atom) that contains one or more dislocations (Figure 1.3). The same circuit path in a dislocation-free lattice will not close, and the extra vector needed to close the circuit is called the *Burgers vector*. The direction of the Burgers vector in relation to the dislocation line identifies whether a dislocation is of edge (Figure 1.4a), screw (Figure 1.4b), or mixed type:[14]

- An *edge dislocation* has a Burgers vector that is perpendicular to the dislocation line.

- A *screw dislocation* has a Burgers vector that is parallel to the dislocation line.
- A *mixed dislocation* has a Burgers vector comprised of both screw and edge components.

The Burgers vector, ***b***, is conventionally described in terms of the Miller indices for that crystal. A Burgers vector that matches a single lattice translation results in a *perfect dislocation*. Dislocations present in real crystalline solids are typically mixed types, although in some crystals pure edge or pure screw dislocations may be found.

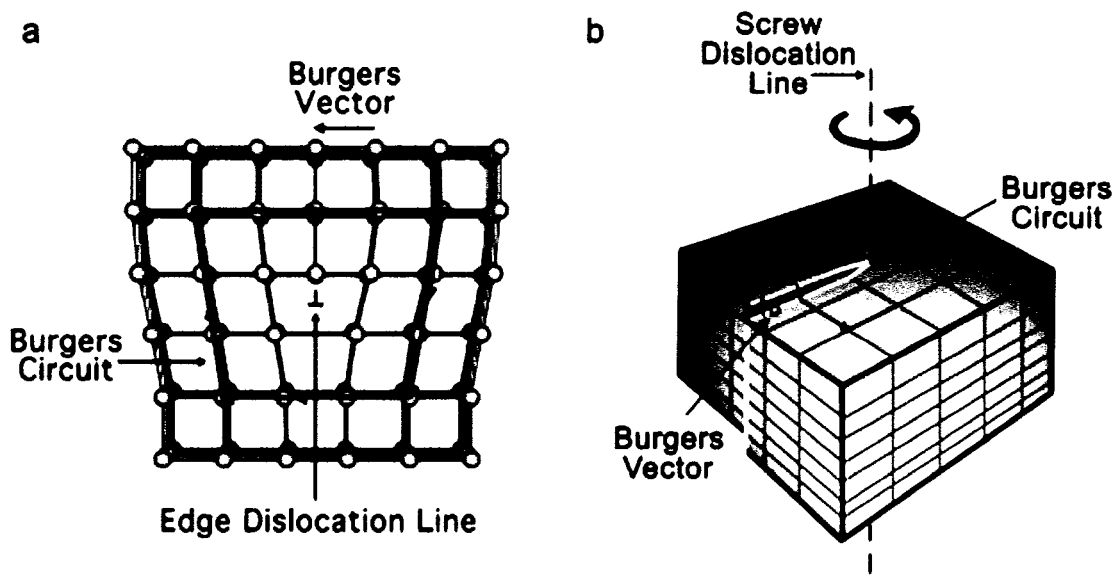

Figure 1.3 *Burgers circuits.* (a) An edge dislocation can be visualized as an extra half plane of atoms inserted in the lattice. (b) A screw dislocation creates a ramped step on the surface, as the atoms form a helicoid around the dislocation axis, like a spiral staircase. In both cases the Burgers vector is the displacement vector needed to close the equivalent Burgers circuits in a perfect lattice.

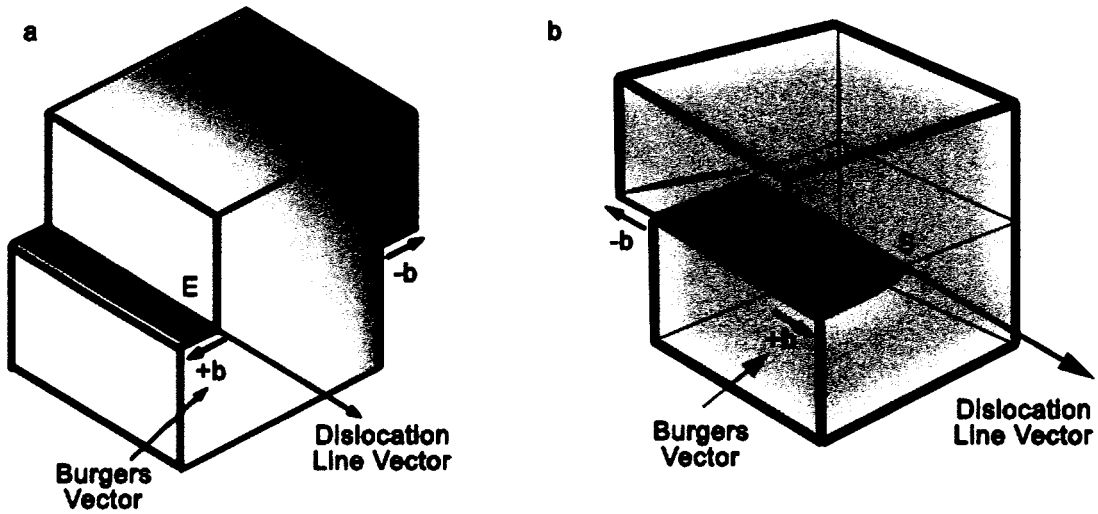

Figure 1.4 *Edge and screw dislocations.* (a) An edge dislocation has a Burgers vector that is perpendicular to the dislocation line. (b) A screw dislocation has a Burgers vector parallel to the dislocation line.

In the theory of crystal dislocations[15,16] a dislocation line cannot end inside a crystal, it can only end on the surface or at a grain boundary. When dislocations terminate inside the crystal bulk it is either because two dislocations of opposite sense have formed a closed loop and annihilated each other, the dislocation has met an obstacle such as a grain boundary or bulk inclusion, or a single dislocation has branched into other dislocations. The Burgers vectors must add to zero at any point where three or more dislocations meet inside the crystal bulk (see Equation (1.1) and Figure 1.5):

$$\sum_{i=1}^{n} \vec{b}_i = 0 \tag{1.1}$$

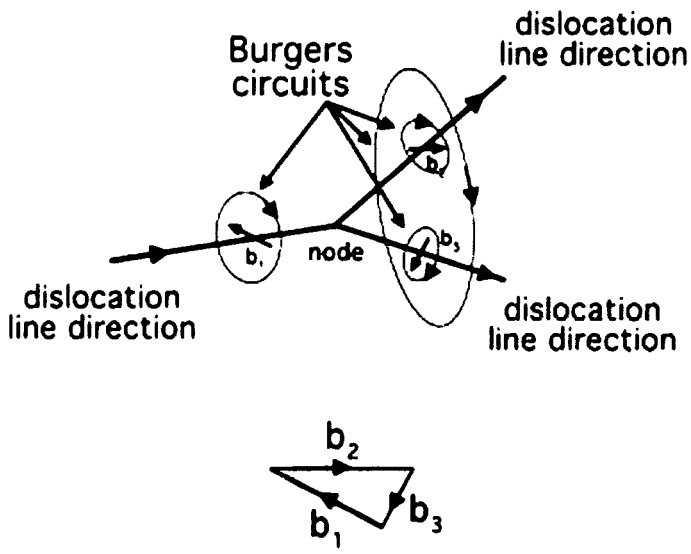

Figure 1.5 *Diagram of dislocation branching at a node.* Dislocation with arbitrary Burgers vector $\mathbf{b}_1$ splits into two dislocations with Burgers vectors $\mathbf{b}_2$ and $\mathbf{b}_3$, such that $\mathbf{b}_2+\mathbf{b}_3 = \mathbf{b}_1$.

The density of dislocations, ρ, is given by the total length, l, of dislocation lines within a volume, V, of the crystal:

(1.2) $$\rho = l/V$$

where the units for density are usually given as m^{-2} or cm^{-2}. A more commonly used definition is to identify the number, n, of dislocations that intersect a cross-sectional unit of area, A:

(1.3) $$\rho = n/A$$

For an array of parallel dislocations these two definitions for the density give the same value. However for a randomly mixed pattern of dislocations, the volume density is larger than the surface density by a factor of two.[14]

Understanding many of the physical and mechanical properties of solids rests upon a firm grasp and knowledge of dislocations. Much of the research on dislocations has predominantly focused on their formation and movement in metals and other crystals grown from melt. However, they equally play an important role in crystal growth at low supersaturations (see Section 1.2.2.1).

1.2.2 Screw Dislocations and Crystal Growth

> *"Among the numerous processes which are influenced by crystallographic defects, there can be few situations where the interconnections are as close as in the case of crystal growth. Crystallization both influences, and is influenced by the defect structure of a crystal." – Halfpenny, et. al.* [17]

Crystal growth occurs as a step-by-step self-assembly process where new ions, atoms, or molecules ("*adatoms*") adsorb onto and bond with the periodic arrangement of units in a crystal lattice. This process takes place in two stages: *nucleation* and *growth*. In the first stage, a pre-nucleation aggregate forms either in the mother liquor or upon a surface. This nucleation process is relatively slow because an activation barrier must be overcome, requiring the initial crystal components that are randomly diffusing around to bump into each other in the correct orientation and placement that allows them to adhere and form a stable "critical" nucleus. The size of the critical nucleus depends on temperature and the amount of adatom diffusion. Once a critical nucleus is formed the second stage of macroscopic crystal growth can commence.

Imagine an idealized model of a perfect, close-packed cubic crystal lattice composed of spherical units. Growth occurs by the deposition of new units onto the surface that diffuse around until they either find favorable sites to occupy or get desorbed back into solution. Elementary diffusion theory says the average distance, l_s, traveled by an adatom across the surface before being incorporated or desorbed is determined by a limited lifetime, τ, of the adsorbate and its surface diffusion coefficient, D:[18]

$$l_s \approx \sqrt{D\tau} \tag{1.4}$$

The determining factor of whether a site is favorable for adding new units is if there is a minimal change in surface energy upon occupancy. The specific surface energy is governed by the number of unsaturated dangling bonds or contact points on the surface. In this idealized model of a close-packed metal, a unit embedded in the bulk of the lattice has six neighbors and no unsaturated bonds remaining. A unit that is still free in the solution or vapor has all of its contact points open. At the growth interface, an adatom diffusing on the surface can attach to one of five potential sites: (1) on top of a flat surface or terrace, (2) at a step edge, (3) in a kink site, (4) in a step, (5) in a terrace site (see Figure 1.6). With the exception of position 3, adsorption or desorption from these sites will change the remaining number of unsaturated dangling bonds, thus changing the surface energy. While growth and dissolution can occur at all these sites, addition or removal of a unit from a kink site (3 neighbors) is most energetically favorable because it has an equal number of saturated and unsaturated bonds, thus preserving the surface energy (see Figure 1.7). The more available kink sites there are on a growing surface, the faster the growth rate at a given supersaturation will be. This is called the terrace-ledge-kink model or the Kossel-Stranski model of crystal growth.[19,20]

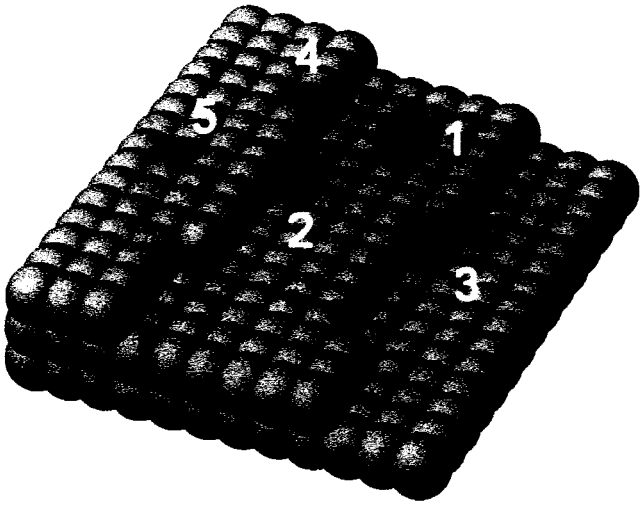

Figure 1.6 *Idealized crystal surface model.* Indicates five possible sites occupied by a unit during growth, numbered according to the number of points of attachment to the surface. The sites include adsorption and incorporation (1) on a terrace, (2) on a step edge, (3) at a kink site, (4) in a step front, (5) in a terrace vacancy. Image created by R. Sours and reproduced with permission.[21]

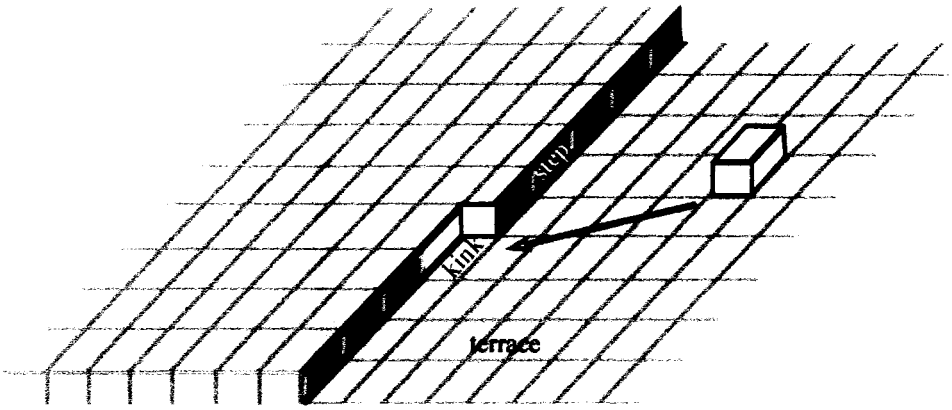

Figure 1.7 *Terrace-ledge-kink model.* Solute molecules (white block) adsorb onto terraces (grey) and diffuse along the surface towards step edges (blue), and then attach at kink sites (white) during crystal growth. This is known as the terrace-ledge-kink model.

The density of kink sites, and hence the growth rate, for a given crystal face depends on its crystallographic orientation as well as the substrate temperature. The growing faces of a crystal can be classified into one of three categories: flat (F), stepped (S), and kinked (K).[22,23] F-faces are those that contain more than one *periodic bond chain*[24] (PBC) of building units (atoms or molecules) per layer, resulting in the greatest number of saturated, short, strong chemical bonds, and therefore minimal specific free energy on the surface. S-faces are typically parallel to only one PBC of building units, creating more unsaturated bonds than on a flat face, and they contain kinks running along the step edges. K-faces are those that have no PBC's and thus possess the highest number of unsaturated bonds. The K-faces grow fastest as they contain the greatest density of kink sites, and therefore they disappear first and will likely not be visible in the final crystal habit. Vicinal or S-faces will fill in the second fastest, leaving the crystal habit to be enclosed predominantly by the slow growing F-faces.[25] Thus the growth of a crystal face is explicitly dictated by its structure. While S and K surfaces contain sufficient density of kinks for comparatively rapid growth, smooth F-faces require overcoming an energy barrier for growth to occur.

A number of external factors can influence the crystal growth process and any energy barriers that must be overcome. Such variables include supersaturation, temperature, impurity type and concentration, solvent, and pH to name a few. At thermal equilibrium the F-face of a crystal should contain no steps or roughness. However, in most practical applications it is impossible to attain a perfectly smooth surface above absolute zero temperature. As temperature (T) rises, the total length of steps and binding sites found on the surface greatly increases. Even if the potential energy of unsaturated bonds at the step, U_{st}, undergoes minimal change with temperature, the laws of

thermodynamics dictate that the entropy, S, of the system increases as temperature rises above absolute zero. Thus the Gibbs free energy of the step decreases as entropy and temperature rise ($G = U_{st} - kTS$), where k is Boltzman's constant. When step free energy is positive ($G > 0$), it takes work to create a new step on the surface. On the other hand if the total step free energy becomes negative ($G < 0$) it is the removal of a step that requires work. Thus at some temperature, T_r, when the step free energy vanishes and thermal fluctuations increase, even an F-surface will possess a certain roughness.[18,26] This roughness results from the creation of kinks and steps. Experimental evidence has shown, however, that in most crystals the F-faces remain faceted all the way up to the melting point.[25] Thus, for the majority of crystals grown from vapor and aqueous solution other mechanisms whereby vicinal features may be introduced to the surface for continued growth are required.

For a perfectly smooth crystal face (ie, free of defects), growth is determined by the rate of formation of new steps on the surface. Below the thermodynamic critical temperature, this can occur by kinetic roughening via the formation of two-dimensional nuclei or "islands" that exceed the critical size needed for growth. Supersaturation is the main driving force of this process. When the chemical potential of a solute molecule in the mother liquor or vapor, μ, is greater than that of a crystal surface at equilibrium, μ_{eq}, then growth occurs. The fractional supersaturation (σ) is proportional to the difference between the chemical potential of the crystal and of the solution ($\Delta\mu = \mu - \mu_{eq}$):

$$\sigma = \frac{\Delta\mu}{kT} = \ln\left(\frac{c}{c_e}\right) \tag{1.5}$$

where the expression on the right is the experimental formula for determining the supersaturation in solution, with c being the concentration of the growth solution and c_e the equilibrium concentration. As the supersaturation increases so does the crystal growth rate.

The formation of a nucleus requires work, as the system's energy must rise above a nucleation barrier in order to activate new growth (Figure 1.8). Consider the homogeneous nucleation of a rounded 2D island with monatomic height a, radius r, and isotropic specific edge energy χ (energy per unit length). The thermodynamic potential for the system's pre-nucleation state, G_1, at constant temperature and pressure is given by:

(1.6) $$G_1 = n_s\mu_s$$

where n_s is the number of moles in a given volume of the solution or vapor phase with chemical potential μ_s. The nucleating crystal with chemical potential μ_c requires n_c moles taken from the solution phase, resulting in a thermodynamic potential for the nucleating system of:

(1.7) $$G_2 = (n_s - n_c)\mu_s + n_c\mu_c + 2\pi r\chi$$

The change in free energy upon nucleation, $\Delta G = G_2 - G_1$, then is:

(1.8) $$\Delta G = -n_c\Delta\mu + 2\pi r\chi$$

where n_c is given by the area of the island divided by the molecular area for one building unit of the crystal phase (in this case $n_c = \pi r^2/a^2$). This results in a free energy of:

(1.9) $$\Delta G = \frac{-\pi r^2}{a^2}\Delta\mu + 2\pi r\chi$$

The free energy is zero at $r = 0$ (ie, no island), reaches a maximum at r_c, where the height of this maximum gives the work of formation of the critical nucleus size. The free energy then crosses zero again at $2r_c$, and the goes negative for large r, where r_c is given by the following formula:

(1.10) $$r_c = \frac{\chi a^2}{\Delta\mu}$$

This is known as the Thomson-Gibbs equation for the critical size of a 2D island nucleus that is in equilibrium with the surrounding phase.[25,27] This is a delicate equilibrium, however, given that it rests at a maximum (hill) rather than a minimum (valley) on the free energy curve (Figure 1.8). Even a small variation in the size of the island will lower the thermodynamic potential, leading to either growth (increasing r) or decay (decreasing r). The corresponding critical free energy or work needed for nucleation to occur is:

(1.11) $$\Delta G(r_c) = \frac{\pi a^2 \chi^2}{\Delta\mu}$$

In order to readily form large terraces, the nucleation barrier of $\Delta G(r_c)$ must be less than the thermal energy kT. The supersaturation for which this condition is satisfied marks the transition between a smooth surface and one with nucleated steps that allow for growth:[28]

(1.12) $$\Delta\mu_c = \frac{\pi a^2 \chi^2}{kT}$$

Thus for $\Delta\mu > \Delta\mu_c$ the growth is dominated by 2D island nucleation and the surface becomes increasingly rougher as supersaturation increases, due to multiple islands growing simultaneously. The growing fronts combine to fill in each layer, but often vacancies are found, and the higher the supersaturation the more likely it is to have islands growing on top of other islands.

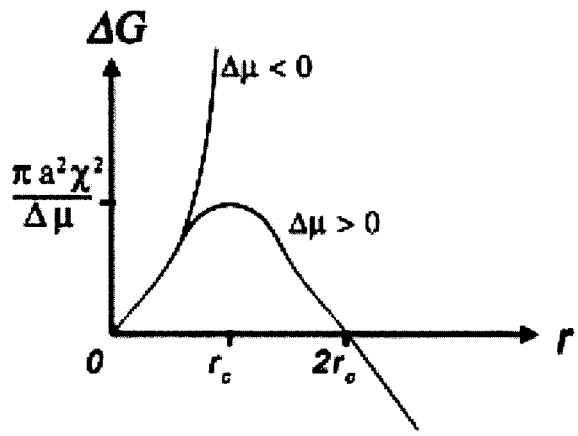

Figure 1.8 *Qualitative schematic of the nucleation barrier* (Gibbs free energy versus 2D radius). For $\Delta\mu<0$ no growth can occur because the ambient phase is under-saturated. For $\Delta\mu>0$, once an aggregate overcomes the free energy barrier and attains a critical size, r_c, two-dimensional island growth commences. For $0<\Delta\mu<\Delta\mu_c$ growth can only occur by filling into kink sites on pre-existing steps.

As the supersaturation is lowered, the two-dimensional growth slows down, becoming more controlled and creating a smoother growth interface for $0 < \Delta\mu < \Delta\mu_c$ (see Figure 1.9). Eventually, the supersaturation reaches such a low degree that no new nucleation can occur and as the kinks and steps fill in, this results in the formation of more perfectly smooth faces. Further growth requires a source of new steps, which is a much more difficult process to form when the supersaturation is lower than that needed for two-dimensional island nucleation. Thus at low supersaturation crystal growth is no longer just a two-step process of nucleation and growth, but a three-step process that involves the formation of an alternative step source.

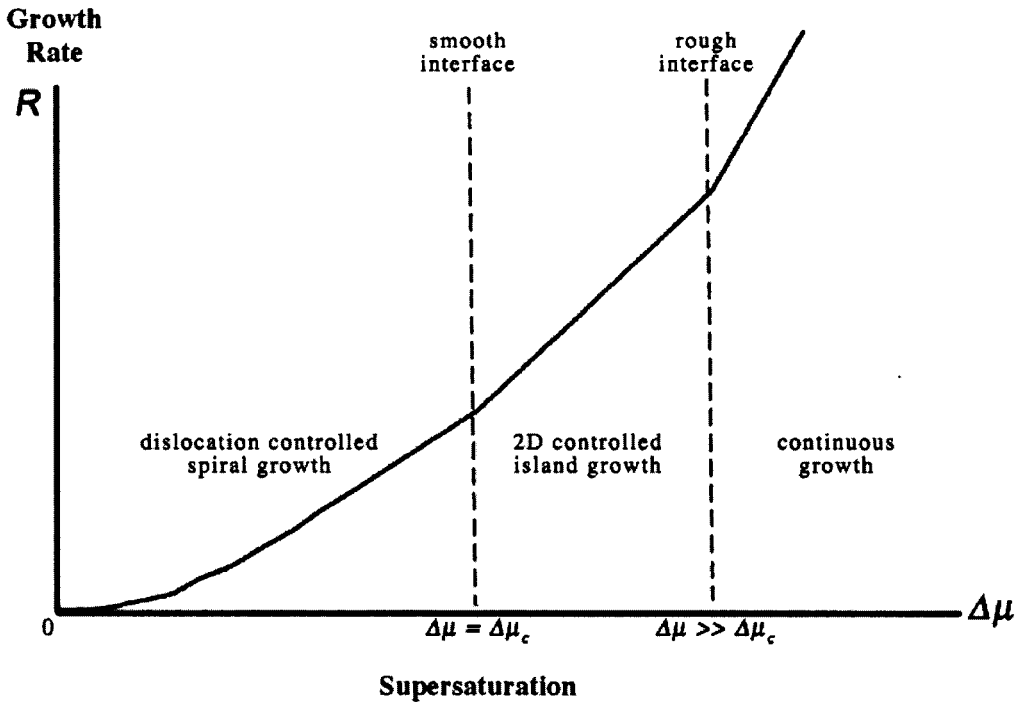

Figure 1.9 *Growth rate versus supersaturation schematic.* Supersaturation or chemical potential is the main driving force of crystal growth. The growth rate can be approximately divided into three regions with different dominating growth mechanisms (see Section 1.2.2.3 pages 38-39). Continuous growth at high supersaturation; Controlled 2D growth at mid-range supersaturation; Dislocation controlled growth at low supersaturation (below $\Delta\mu_c$).

The theory of perfect crystal growth by two-dimensional nucleation predicts that in order for growth to occur at the observed rates, the degree of supersaturation would need to be approximately 50%. This theory was shown to be clearly lacking when experimental observations of crystals grown from vapor or aqueous solution established that growth occurs at supersaturations as low as 0.01%. The reconciliation between theory and experiment came in 1951 when Burton, Cabrera, and Frank published an alternative model of crystal growth that relied upon the presence of screw dislocations as perpetual step edges, bypassing the need to overcome the nucleation barrier.[29] This model was based on an

earlier proposal by Frank in the famous 1949 Discussions of the Faraday Society, where he pointed out: [30]

> *"One ought not to expect that any visible crystal will exhibit a completed perfect face needing fresh two-dimensional nucleation in order to grow...It is clear that when dislocations of this [screw] type are present, the crystal face always has exposed molecular terraces on which growth can continue, and the need for fresh two-dimensional nucleation never arises. If just one dislocation of this type emerges at the centre of the face, that crystal face can grow perpetually 'up a spiral staircase'... "*

This new phenomenological model of crystal growth allowed for growth rates at low supersaturation that more closely matched those observed experimentally. It thus became clear that the presence of dislocations, and in particular screw dislocations, was a critical component of crystal growth. Since that time, the study of dislocations has expanded far beyond investigating their impact on the physical and mechanical properties of solids. Over the last 59 years, research into the nature of *growth-induced* defects and dislocations has begun to make significant contributions to the fields of crystal growth and solid-state science.[31]

1.2.2.1 Burton-Cabrera-Frank Model

Frank's statement was formalized in a landmark paper on the theory of crystal growth that has come to be known as the Burton-Cabrera-Frank Model (BCF Model). This model ventured away from using the idea of "perfect crystals" and for the first time proposed that screw dislocations play a critical role in the growth of crystals at low supersaturation. The implications of this model are far reaching. They asserted that defects are not just inconvenient, externally-generated imperfections, but that they are inherently connected to the birth and growth of "real crystals".

According to the definition given in Section 1.2.1 a screw dislocation begins with a kinked step resembling a ramp upon a crystal surface, where the displacement vector has a component perpendicular to the crystal face. Examination of the atomic arrangement of atoms about a screw dislocation resembles a spiral staircase. If one looks down the dislocation direction and the staircase follows clockwise twist it is referred to as a right-handed screw dislocation, whereas if it follows a counter-clockwise twist then it is a left-handed screw.[32] Frank proposed that such dislocations would create a perpetual step source. As a crystal grows, a step created in this way winds itself in a spiral around the dislocation core, sending out successive steps. This results in topographical features known as *hillocks*, shallow hills or pyramids with persistent step edges, long recognized as a trait of slow crystal growth. A single hillock may have one or multiple dislocations at the apex.[29,33]

For both island growth and hillock growth, the step directions larger than the critical nucleus size are determined by the dependence of the step velocity on different crystallographic orientations. BCF showed that the normal rate of step advancement at low supersaturation for a segment of spiral with radius of curvature r, is approximately:

(1.13) $$v(r) \approx v_\infty(1-r_c/r)$$

where v_∞ is the maximum velocity of a straight step of any orientation, which is a linear function of the supersaturation, and r_c is the critical nucleus size from equation (1.10) derived earlier.[29] The rate of growth, R, of a crystal face with a single isolated screw dislocation, is first governed by the distance between successive turns of the spiral, λ_0. To determine this value, we follow the

approach of BCF whereby the shape of the rotating spiral, $\rho(\theta)$, is obtained in terms of polar coordinates (ρ,θ). According to BCF, the radius of curvature, r, at point ρ of a spiral is given as:[25,29]

$$r(\rho,\theta) = \frac{\left(\rho^2 + \rho'^2\right)^{\frac{3}{2}}}{\rho^2 + 2\rho'^2 - \rho\rho''} \tag{1.14}$$

where ρ' and ρ'' are the first and second derivatives of $\rho(\theta)$. Taking the origin to be at the dislocation core, then the step advancement rate in the radial direction, $v(\rho)$, is given by:

$$v(\rho) = \frac{d\rho}{dt} = \frac{d\rho}{d\theta}\frac{d\theta}{dt} = \omega\rho' \tag{1.15}$$

where ω is the angular velocity of the entire rotating spiral. The step advancement rate in the normal direction is then given by the following relation:

$$v(r) = v(\rho)\cos\gamma = v(\rho)\frac{\rho}{\sqrt{\rho^2 + \rho'^2}} = \frac{\omega\rho\rho'}{\sqrt{\rho^2 + \rho'^2}} \tag{1.16}$$

where γ is the angle between the radial direction and the step advancement direction. Substituting (1.16), (1.15), and (1.14) into equation (1.13) gives:

$$v_\infty\left(1 - r_c\frac{\rho^2 + 2\rho'^2 - \rho\rho''}{\left(\rho^2 + \rho'^2\right)^{3/2}}\right) = \frac{\omega\rho\rho'}{\sqrt{\rho^2 + \rho'^2}} \tag{1.17}$$

Solving this differential equation gives the shape of the spiral, $\rho(\theta)$, which can be plugged into equation (1.14) to determine the radius of curvature.

Given the complexity of equation (1.17), it is typical to solve it for the limiting cases of large and small ρ, such that higher order terms can be dropped and a good approximation for the spiral shape is obtained. In the simple case of small

ρ, near the center of the spiral, and/or a step advancement rate that is independent of orientation, the resulting differential equation reduces to $\rho' = 2r_c$. Upon integration, this gives the shape for the hillock as an Archimedean spiral or low cone (see Figure 1.10a):

(1.18) $$\rho = 2r_c\theta > 0$$

In this case the distance between successive turns of a spiral (i.e. terrace widths) will be $\lambda_0 = \rho(\theta + 2\pi) - \rho(\theta) = 4\pi r_c$. Recalling that r_c is inversely proportional to supersaturation, this leads to the relationship that the slope of the hillock spiral $s = a/\lambda_0$ gets steeper as supersaturation is increased. Using equation (1.18) to solve for (1.14) it is found that the radius of curvature for an Archimedean spiral is:

(1.19) $$r = r_c \frac{\left(1+x^2\right)^{3/2}}{1+\frac{x^2}{2}}$$

where $x = \rho/2r_c$. Thus at $x = 0$, we obtain $r = r_c$, indicating that the center of the growth spiral is the same shape and size as a critical 2D nucleus. At the other extreme, as $x \rightarrow \infty$, the radius of curvature for an isotropic hillock flattens out to a constant and the steps far from the center of the spiral become straight. Furthermore, by plugging this into the equation (1.13) one can see that the rate of step advance varies from zero near the center to v_∞ far from the center. Thus, the step kinetics are much faster the further out from the dislocation core one gets. In 1956, Cabrera and Levine published a more detailed analysis using a better approximation for $\rho(\theta)$ to give a step spacing of:[34]

(1.20) $$\lambda_0 = 19r_c = \frac{19\chi a^2}{kT\sigma}$$

This expression will be used later for the step spacing of a single isotropic hillock.

Figure 1.10 *Spiral morphology.* The shape of a hillock is dictated by the dependence of the step velocity on orientation. (a) For isotropic step velocities the spiral forms a low cone like an Archimedes spiral. (b) When orientation influences step advancement rate, the growth hillock takes on a pyramidal shape.

Now consider the case when step orientation is important. Under this condition, the spiral becomes polygonized, taking on more of a stepped pyramid shape as shown in Figure 1.10b for example. In the simplest case, begin by assuming straight steps with equal step velocities, v_∞, moving along each of the crystallographic directions. The hillock will start out as a single straight step emerging from the dislocation core. As adatoms attach to the kink sites along this step, the growth front will move in the direction normal to the step edge, creating a second step edge that now leads back to the dislocation core (Figure 1.11a). This second step edge must surpass a critical length, l_c, before it can start to grow. This critical length is the same as the edge size for a critical 2D nucleus, $2r_c$, since a 2D cluster smaller than this value is thermodynamically unstable.[35] Thus, the step will behave the same whether it is originating from a 2D island or a dislocation spiral:[35]

$$l_c = 2r_c = 2\frac{\chi a^2}{kT\sigma} \tag{1.21}$$

where χ is again the edge energy per unit length, a, and σ is the supersaturation. Once the step exceeds the critical length it will grow at the same rate as the first

step, and as it does another step appears normal to it, and so on (Figure 1.11b). The amount of space between the steps λ_0, called the terrace width, is dependent on the rate of rotation of the growth spiral, which also relates to the critical length, l_c. For this idealized model, the terrace width turns out to be four times the size of the critical length.[25] Furthermore, this model demonstrates another general fact that the length of the innermost step emerging from the dislocation point will always be equal to the critical length, $l_c = 2r_c$.[25]

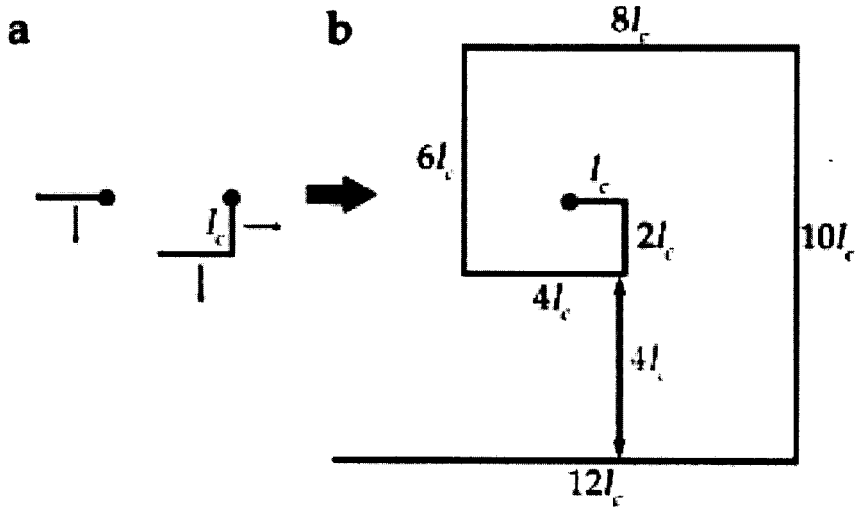

Figure 1.11 *Idealized model of a hillock created by a screw dislocation.* (a) The hillock begins as just a ramped step emerging from the dislocation core, and new adatoms attach to its kink sites to advance the step edge. Each new step front created must reach a critical length, l_c, before it can grow. (b) All steps created continue to grow and spread at their respective step advancement rates dictated by orientational dependence. The terrace width for this simple model where the step velocity is the same for all crystallographic directions is $4l_c$.

A hillock can be further polygonized if the step advancement rate is different for opposing orientations along a particular crystallographic axis, or along different directions in the same plane. This is seen for example in potassium

hydrogen phthalate (conventionally abbreviated KAP for potassium acid phthalate, $C_6H_4{\cdot}COOH{\cdot}COO^-K^+$, space group $Pca2_1$, see Section 2.3).[36,37] The *c*-direction is polar in KAP, therefore the steps that propagate in the +*c* and -*c* directions are different in structure.[38] The steps moving with a +*c* velocity component are slower than those moving with a -*c* component, leading the screw dislocations emerging on the (010) surface of KAP to produce growth spirals similar to that shown in Figure 1.12. This polygonization of the hillock steps is an important aspect of my research that will be discussed further in Chapter 2.

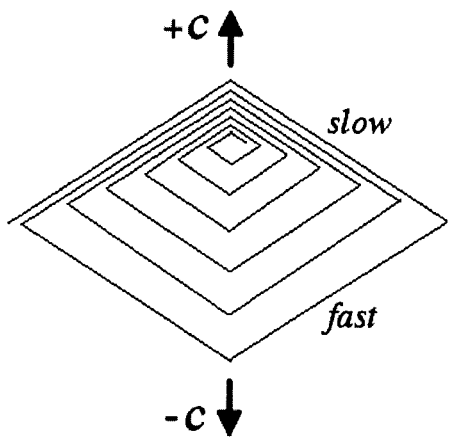

Figure 1.12 *Polygonized growth spiral.* The *c*-axis is polar in KAP, causing steps that propagate in the +*c* direction to be slower than those moving in the -*c* direction. This directional dependence of step kinetics alters the pyramidal morphology of the hillocks emerging on the (010) KAP surface.

1.2.2.2 *Sources of Growth Induced Screw Dislocations*

"The theory of crystal growth shows that dislocations present in the nucleus from which a crystal grows will propagate into the growing

crystal whether the material of the nucleus is the same as that of the growing crystal or different. Moreover, there is a natural selection of dislocated crystals, which in some circumstances grow much faster than perfect crystals. These arguments fail to explain the origin of the dislocations in the nuclei." - Nabarro[16]

Despite their ubiquity in crystals, the presence and nucleation of screw dislocations remains very much a mystery. With a large enthalpy of formation required to shift the crystal lattice and little increase in the entropy of the system, dislocations are not thermodynamically spontaneous.[15] Yet nearly all real crystals contain such defects. Why? How do they get there? And what factors influence their formation and propagation most strongly? The answers to such questions are vital to our ability to test the Cairns-Smith proposal of crystal 'genes', as well as to engineer more perfect materials.

While much is known regarding sources of dislocations induced by external stress, especially in crystals grown from melt, very little is definitively understood about the primary mechanisms for growth induced nucleation of screw dislocations. Many possibilities have been proposed, several of which are deduced from experimental observations with specific conditions and materials, often making it challenging to apply these to the generalized case.[15] Broadly, the proposed mechanisms can be grouped into two categories: *seed* nucleation and *accidental* nucleation. Seed nucleations are those dislocations or other defects present on the surface of the seed crystal or pre-growth nucleus that are transferred through subsequent growth – precisely the mechanism whereby the aspect at hand of the Cairns-Smith hypothesis finds its foundation. Under the class of accidental nucleations fall several sub-categories including: *heterogeneous*

nucleation due to internal stresses, impingement of different parts on the growing surface, and collapse of vacancy platelets from rapid cooling.[39] However, when it comes to *spontaneously nucleated single crystals grown at constant temperature from solution or vapor*, the latter two sub-categories are irrelevant, leaving internal stresses the most likely causes of dislocations.

Heterogeneous nucleation of dislocations can result from a number of different internal stresses (as opposed to applied stresses) including:[15,39]

- *Mechanical stress* - due to bulk inclusions and capture of impurity particles.
- *Stacking Error* - probability accidents from the encounter of two nuclei or advancing step fronts.
- *Constitutional stress or Heterometry-induced stress*[40]- due to a change in composition resulting in differential contraction and expansion of neighboring regions.
- *Random stress* - due to isolated vibrations from the laboratory environment.
- *Adhesive stress* - due to the growing crystal sticking to the sides of the growth container.

Of these, a few potential sources can be eliminated by controlled growth conditions. For example, constitutional stress is usually due to thermal gradients, a change in composition, or a change in lattice structure (such as in alloys). At constant temperature no significant thermal gradients will exist, and for a solution that has a pure grade single compound and a single solvent there will be no change in lattice structure or composition during growth of a single crystal. Thus, constitutional stress can be eliminated in the growth of pure crystals at

constant temperature. If however there is a change in pH during growth, or a significant influence of impurity segregation in the crystal, this stress cannot be ruled out all together. Adhesive stress can be ruled out when growing from seed, as the face of interest is positioned to grow vertically into solution from the seed surface. This leaves mechanical stress, stacking errors, heterometry due to impurities, and random stress as possible sources for any growth-induced dislocations that are not transferred from the seed crystal. Possible experiments to test some of these dislocation sources for their relative degree of influence on the nucleation and propagation of dislocations in a growing crystal will be further described in Chapter 2.

1.2.2.3 Factors Affecting Spiral Growth

The importance of supersaturation, temperature, dislocation source, and step velocity dependence on orientation have already been introduced and will continue to reappear throughout this thesis. Additional experimental parameters that influence spiral growth are the growth rate, the selection of solvents used, the level of solution flow or stirring that influences the diffusion layer at the growth interface, and the concentration, type, and size of impurity inclusions. The degree of influence and the level to which these factors can be controlled play important roles in attempting to preserve information content during the transfer of a particular pattern of defects from a crystal seed to its daughter.

<u>Growth Rate</u>

The rate of growth, R, normal to a terrace surface is given by:[25]

(1.22) $$R = pv$$

Where p is the step density and v is the lateral step advancement rate. The step density can also be understood in terms of the slope of the vicinal pyramid or hillock, $p = h/\lambda_0$, where h is the height of the dislocation or step ($h = a$ for a unit cell step height), and λ_0 is again the terrace width. This slope is directly proportional to the supersaturation as shown in Section 1.2.2.1 thus the more supersaturation is increased or decreased, the steeper or flatter a hillock becomes, respectively. Likewise, when supersaturation increases the terrace width, λ_0, decreases, leading to a greater density of steps along a given length of the surface.

The step advancement rates, v, of a growing spiral depend on several factors including the *height, structure, density, and mutual interactions of steps, the diffusion rates of adatoms on the surface, and the influence of various impurities and other defects*.[25] The higher a step is, the slower it moves, due to a greater flux of atoms being needed for the step front to grow. Steps of polyatomic height can appear due to a dislocation source with magnitude greater than one unit cell length, or they may result from the merger of several monatomic steps due to changes in the local supersaturation, impurity concentrations, or impediments posed by lattice imperfections.[25] When polyatomic steps are present, faster moving monatomic steps on the same face will likely catch up with them and merge to eventually form macrosteps. Even though these macrosteps are generally present on the growing surface their contribution to the overall growth rate is not appreciable due to their slower movement. Thus, in calculating the overall growth rate of a crystal face we can restrict our attention to steps of monatomic height, a.

For a detailed theoretical derivation of step advancement rates on a growing crystal, the reader is referred to the excellent book by Markov.[25] Here I take the liberty of summarizing what is comprehensively described in his book. As was explained early in Section 1.2.2 through the terrace-ledge-kink model, crystal growth, and hence the growth rate, is dependent on a few distinct elementary processes. First there is the population of adatoms on the terraces, second is the diffusion of these adatoms towards the steps, and third is the incorporation of adatoms into the kink sites. The evaporation of a step includes the same processes in reverse order. The step advancement rate then is a function of the flux of adatoms entering and leaving kink sites, as well as the density of kinks along a step. The in-flux and the out-flux are dependent on the energy barriers that must be overcome for incorporation and desorption respectively. This leads to an expression for the advancement rate of a straight step as:

$$v_{\infty} = 2a^2\beta_{st}(n_{st} - n_{se}) \tag{1.23}$$

where n_{st} is the adatom concentration in the vicinity of the step, n_{se} is the equilibrium adatom concentration, a^2 is the kink site area, the factor of 2 is due to adatoms arriving from both the upper and lower terraces, and the parameter β_{st} is known as the kinetic coefficient of the step, which is given by:

$$\beta_{st} = a\upsilon\frac{a}{\delta_0}\exp\left(-\frac{\Delta U}{kT}\right) \tag{1.24}$$

In this formula υ is the vibrational frequency of the adatoms, δ_0 is the kink spacing along the step, and ΔU is the energy barrier for incorporation of an atom into a kink site from the ambient phase. The kinetic coefficient is often used in comparison with the rate of diffusion from equation (1.4) to delineate between distinct growth regimes. When the kinetic coefficient is much greater than the rate of diffusion, then surface diffusion limits the growth:

(1.25) $$\beta_{st} \gg \frac{l_s}{\tau} = \frac{D}{l_s} \quad \rightarrow \quad \textit{diffusion regime}$$

Alternatively, when the kinetic coefficient is much less than the rate of diffusion it is the incorporation of adatoms into kink sites that controls the growth rate:

(1.26) $$\beta_{st} \ll \frac{D}{l_s} \quad \rightarrow \quad \textit{kinetic regime}$$

In either regime, the rate of advance of a straight step, v_∞, turns out to be linearly proportional to the supersaturation, σ. The complete derivation to arrive at a specific expression for v_∞ involves solving a second order differential equation subject to various initial conditions and boundary conditions, and is based on different crystal symmetries and physical scenarios. Again, the reader is directed to either Markov's book[25] or the BCF paper[29] of 1951 for a full treatment of these derivations.

In the case of a succession of parallel equidistant steps separated by y_0, and assuming the adatom concentration is high enough such that there is no competition between the steps for building units, the resulting equations for the step advancement rate under conditions (1.25) and (1.26) respectively are:

(1.27) $$v_\infty = 2\sigma \upsilon l_s \exp\left(-\frac{\varphi_{kink}}{kT}\right)\tanh\left(\frac{y_0}{2l_s}\right) \quad \rightarrow \quad \textit{diffusion regime}$$

and

(1.28) $$v_\infty = 2\sigma a^2 \beta_{st} n_{se} \quad \rightarrow \quad \textit{kinetic regime}$$

where φ_{kink} is the work of separation from a kink site. The hyperbolic tangent term in (1.27) starts out linear and then asymptotically approaches unity as its

argument gets large. Thus, for relatively large inter-step spacing (i.e. when $y_0 >> l_s$), the step advancement rate is equivalent to that of a single isolated step.

In real crystals it is common to find multiple dislocations or even groups of dislocations existing on a surface at once. Neighboring dislocations can sometimes work together, becoming more growth active and having a stronger influence on the overall growth of that face. We can distinguish four general scenarios for the interaction between a pair of neighboring dislocations of the same height as follows: i) two dislocations of opposite sign (ie, one right-handed, the other left-handed) spaced less than the critical length $l_c = 2r_c$, ii) two dislocations of opposite sign spaced greater than l_c, iii) two dislocations of the same sign spaced less than l_c, and iv) two dislocations of the same sign spaced greater than l_c. In scenario i) no spiral growth occurs. Scenario ii) results in the merger of spiral arms from the two dislocations, sending out successive closed loops of steps with the same step spacing as a single dislocation spiral, and therefore having the same activity as a single dislocation (Figure 1.13a).[29,30] Scenarios iii) and iv) are a little more complex. Let d be the spacing between the neighboring dislocation cores. If $d >> l_c$ (iv) then the step separation ends up being equal to d, and is independent of the supersaturation (Figure 1.13b).[25] If $d << l_c$ (iii) then the step separation is reduced to half that of a single dislocation spiral, which is also inversely proportional to the supersaturation (Figure 1.13c).[25,29]

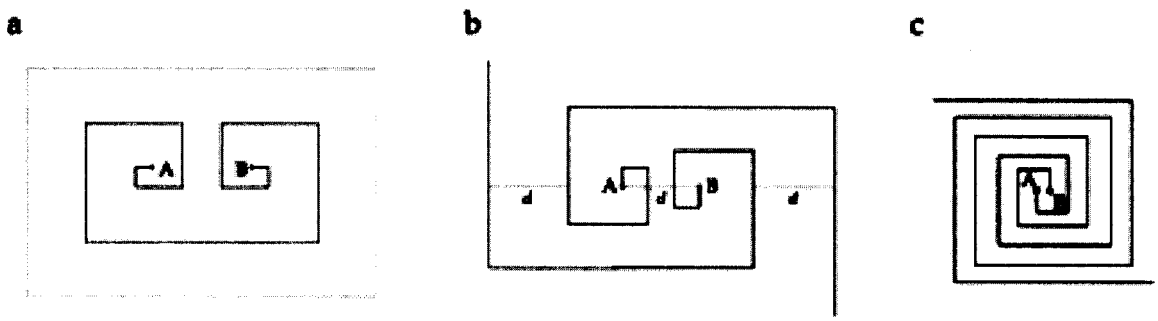

Figure 1.13 *Dislocation pairs.* (a) Closed-loop hillocks are formed from two dislocations of opposite signs with separation AB greater than l_c. (b) Spiral formed by two dislocations of same sign with separation d = AB >> l_c, leads to terrace widths equal to d and independent of supersaturation. (c) Spiral formed by two dislocations of same sign with separation AB << l_c, leads to terrace width half the size of a single dislocation.

We can extend this to a group of n dislocations equally spaced along a straight line spanning a total length of L, such that the inter-dislocation spacing is $d = L/n$. In this case, the condition $d >> l_c$ is the same as requiring $L >> \lambda_0$, where λ_0 is the step spacing or terrace width of a *single* dislocation. This results in a the multi-dislocation spiral having a step spacing of $y_0 = d = L/n$. Likewise $d << l_c$ is the same as $L << \lambda_0$, resulting in $y_0 = \lambda_0/n$. A general formula can be written to account for both these scenarios as follows:[25,29]

$$y_0 = \frac{\lambda_0}{\eta} \qquad \text{where} \qquad \eta = \frac{n}{(1 + L/\lambda_0)} \tag{1.29}$$

The above formula for η defines the so-called "strength" or "activity" of a spiral growth source. Referring back to Equation (1.22) for the growth rate perpendicular to a terrace, if the step spacing is y_0, we can write $R = av_\infty/y_0$, showing that *the smaller the inter-step spacing the more "growth-active" a dislocation source is*. Thus when many step sources are present on a crystal surface there is a

constant competition between them for dominance over the growth of that face. If the amount of nutrient available (or the local supersaturation) is the same among the growing step fronts, then the hierarchy of step sources that most contribute to the growth will be 1) groups of dislocations of same sign under the condition $L << \lambda_0$ as the greatest contributors, ranked according to the number of dislocations in the group; 2) groups of dislocations of the same sign under the conditions $L >> \lambda_0$ and $d < \lambda_0$; 3) single dislocation spirals or pairs of dislocations with opposite signs under the condition $d >> l_c$, resulting in an inter-step spacing equal to λ_0; 4) groups of dislocations of the same sign whose separation $d > \lambda_0$ and $L >> \lambda_0$; 5) monatomic steps from other sources; 6) polyatomic steps and macrosteps according to their height; 7) finally, pairs of dislocations with opposite signs under the condition $d << l_c$ are inactive and do not contribute to the overall growth rate, save for imposing a small delay on the passage of steps that originate elsewhere (although to first approximation this may be ignored). Furthermore, if there is a single dislocation that lies in the path of the more closely spaced advancing steps from a stronger group of dislocations, then it will not contribute to the growth rate because it will not have a chance to form its own growth spiral.[16] Thus the more active group is said to *dominate* the growth.

The theory of crystal dislocations[16] (Section 1.2.1) asserts, on the basis of geometrical arguments that a dislocation line cannot end inside a crystal, it can only end on the surface or at a grain boundary. However, the BCF theory of crystal growth clearly shows that while the dislocations may be present on a surface, they are not all growth-active, and that the growth rate of a particular face is dominated by the strongest groups of dislocations that work together. Both theory and experiment also show that the growth active hillocks can change by tuning experimental parameters such as supersaturation, solution flow, temperature, and so on.

We can substitute equations (1.20), (1.27), and (1.29) into (1.22) to solve for the rate of growth of a dislocation spiral in the diffusion regime (condition (1.25)) far from the dislocation core to obtain:

(1.30) $$R = C\frac{\sigma^2}{\sigma_c}\tanh\left(\frac{\sigma_c}{\sigma}\right)$$

where σ_c is a characteristic supersaturation given by:

(1.31) $$\sigma_c = \frac{19\chi a^2}{2nkTl_s}$$

and C is a rate constant:

(1.32) $$C = av\exp\left(-\frac{\varphi_{kink}}{kT}\right)$$

From equation (1.30) we can identify two extreme cases. At low supersaturations, where $\sigma << \sigma_c$, the hyperbolic tangent approaches unity, reducing R to the well-known parabolic growth rate law of BCF:[29]

(1.33) $$R = C\frac{\sigma^2}{\sigma_c}$$

At the other extreme, for $\sigma >> \sigma_c$, the hyperbolic tangent reduces to its argument ($\tanh(x) \rightarrow x$ for small x), resulting in a linear dependence of R on the supersaturation.

(1.34) $$R=C\sigma$$

Physically, this means that the kink density is so high that every adatom on the surface readily attaches to the crystal before desorption occurs.

A second linear dependence is also obtained when considering growth spirals whose terrace widths and slopes are independent of supersaturation (under the

condition $L >> \lambda_0$, for groups of dislocations with the same sign). In this case $R=C'\sigma$, where C' is given by:

(1.35) $$C' = C\frac{2l_s}{d}\tanh\left(\frac{d}{2l_s}\right)$$

again, there are two extreme cases: (1) for $d << 2l_s$, C' reduces to C, setting it equal to the first linear relation (1.34) and (2) $d >> 2l_s$ gives $C' = 2l_sC/d << C$.

The growth rate in the kinetic regime (condition (1.26)) can be determined by substituting equations (1.29) and (1.20) into (1.22) to obtain a second parabolic law:

(1.36) $$R = C''\sigma^2$$

where

(1.37) $$C'' = \frac{2nkTa}{19\chi}n_{se}\beta_{st}$$

It turns out that $C'' << C/\sigma_c$, thus this second parabolic dependence will intersect the linear portion of the diffusion regime growth rate curve at a second characteristic supersaturation given by:

(1.38) $$\sigma_c'' \cong \sigma_c \exp\left(-\frac{\varphi_{des} + \varphi_{sd} - 2\Delta U - 2w}{2kT}\right)$$

where φ_{des} is the activation energy for an adatom to be desorbed from the crystal surface, φ_{sd} is the activation energy for surface diffusion, ΔU is again the energy barrier for incorporation of an atom into a kink site from the ambient phase, and w is the work needed to create a kink on the step. This second characteristic supersaturation, σ_c', is much greater than σ_c.

To summarize, spiral growth from screw dislocations results in both linear as well as a parabolic dependences of the growth rate on supersaturation. The R versus σ graph will show three distinct regions with parabolic behavior in the diffusion regime at $\sigma << \sigma_c$, gradually transitioning into linear behavior in the diffusion regime where $\sigma >> \sigma_c$, and turning parabolic again in the kinetic regime for $\sigma \geq \sigma_c' >> \sigma_c$. This is depicted schematically in Figure 1.9, where the change in chemical potential is used in place of supersaturation as the x-axis ($\Delta\mu = kT\sigma$).

Growth from Solution

Much of what has been described thus far applies to simplified theoretical scenarios of crystal growth under ideal conditions from vapor deposition. It is stated in the famous 1949 Faraday Discussions[41] on crystal growth, from which these theories are based, as well as the recent 2007 Discussions[42] also devoted to crystal growth, that there is a large gap between theory and experiment. This gap, while getting smaller, is still too large to create a comprehensive model of crystal growth for realistic systems. Even less is understood about the atomic processes of nucleation. When it comes to experimental parameters that can add several degrees of complexity into the equations, growth from solution is one that is often preferred by experimentalists, but seen as a complication to theorists. There are three main factors that make crystal growth from solution a favorable method: 1) high concentrations can be obtained in solution, 2) the mobilities of those compounds in solution is often high, and 3) it is easy to grow from solution on a benchtop without a lot of fancy or expensive equipment.[43]

In the experimental world, the level of control over the growth environment plays a much more prominent role in determining the rate and perfection of crystals grown, than does a comprehensive understanding of growth mechanisms from first principles. Thus when it comes to the growth of the more complex crystal systems encountered in the lab it is important to have knowledge of factors such as solubility relations, solvent properties, flow dynamics, temperature and supersaturation control, and so forth. For example, the solvent chosen will influence the step and kink free energies, which will in turn determine their densities and hence the growth rate.[44] A complete description of growth from solution is indeed a formidable task but many are striving towards such a model.

The true driving force of crystal growth is not the bulk supersaturation but the surface supersaturation. A diffusion boundary layer exists at the solution-solid interface, leading to a surface supersaturation that is less than that of the bulk. A few experiments have been performed using Mach-Zehnder interferometry,[45,46] holography,[47,48] and Michelson interferometry[49] to directly measure the relation between the surface and bulk supersaturations and their influence on growth kinetics and hillock activity. Some of the important conclusions drawn from these experiments were that in addition to there being a significant difference between surface and bulk supersaturation, there is also a supersaturation gradient across the surface; the surface supersaturation is especially larger at the edges and corners of the crystal face than in the center. However, when the solution has a set flow rate these gradients are reduced until they asymptotically reach a negligible level. The solution flow rate that is required to ensure a consistent local supersaturation is directly proportional to the supersaturation level. Thus, in order to control the growth of crystals in solution it is imperative

to attain a high enough *laminar* solution flow that will overcome any diffusion layer gradients at the surface.

Inclusions

The faster a crystal grows in solution, the more common it is for some of the solvent to get trapped within the crystal bulk, resulting in fluid inclusions. These are especially common when growth occurs from static solution rather than one that is flowing or stirred. It has been verified by X-ray topography that many dislocations can originate off of such fluid inclusions, as has been seen for example in KAP by Halfpenny *et al.*,[17] as well as by our collaborator Alexey Voloshin in Russia (see Chapter 4).[50]

Beyond fluid inclusions, there are many other impurities that can affect both the nucleation of dislocations and their growth morphology. The impurity type, shape, and concentration are all important factors when considering the influence of these inclusions on spiral growth. Ionic impurities and point defects are unlikely to nucleate dislocations, however they have often been seen to alter hillock morphology. For example, Hottenhuis *et al.* have seen drastic alterations of KAP hillock morphology due to the presence of various trivalent cations during growth from solution.[51] Molecular impurities can also influence the morphology of a growth spiral, depending on the type of molecule and its specific interactions with the host crystal. As yet there is no evidence, to the best of our knowledge, for dislocations being generated from the presence of molecular impurities (this will be discussed further in Chapter 2). There are four main mechanisms whereby hillock morphology and/or step kinetics may be altered by ionic or molecular impurities. These include step pinning, impurity incorporation, kink blocking, and step edge adsorption. In each of these cases the impurities influence the growing steps either kinetically by impeding the step

advancement rate, or thermodynamically by changing the edge free energy. The mechanisms relevant for a given impurity can be determined by identifying how the step kinetics vary with supersaturation and impurity concentration.[52] For a more detailed description of this, the reader is referenced to the review by De Yoreo and Vekilov, where each of these mechanisms are nicely summarized.[53]

Larger particulate inclusions have often been sited as sources for the nucleation of dislocations due to the local mechanical stress they introduce into the lattice.[32,39] One of the earliest known demonstrations of the formation of screw dislocations from the presence of solid particles introduced during crystal growth was reported by Kozlovskii in 1958.[54] β-methyl-naphthalene grown from ethyl alcohol stationary solution in the presence of fine graphite particles, observed in situ via polarized light, displayed three behaviors: 1) some particles were repelled by the growing crystal front, 2) some particles were captured without any dislocation to the lattice, 3) other particles were captured with the formation of screw dislocations and subsequent spiral growth. The occurrence of capture and screw formation was low at slow growth rates and increased considerably with increasing growth rate. In other experiments of growth from melt in the presence of various insoluble impurities, it was verified that the capture or repulsion of a particle appears to be determined first by the ratio of surface energies at the paired interfaces in the crystal-melt-impurity system and only secondly by the crystal growth rate.[55] It has also been seen that the size and shape of a bulk inclusion or precipitate are directly related to the magnitude and complexity of the associated strain field. The larger, more asymmetric and complex a particle is, the more frequent and abundant the nucleation of dislocation arrays will be at that inclusion.[56]

Regardless of the type, size, and shape of an impurity inclusion, the concentration of those impurities in the crystal can also have a strong effect on hillock morphology as a result of step pinning. At very high concentrations of impurities, aggregation, segregation, or possible increase in the lattice parameter can become factors that may also alter the constitutional makeup of the crystal in significant ways, leading to the generation of new dislocations. For example, if a crystal is growing as layers of flat plates, a high impurity content can put the edges of the plates in a state of hoop tension. This tension may be relieved by a plastic buckling that produces several screw dislocations of the same sign near the center of the plate.[57,16]

1.3 Summary

This dissertation reports a long overdue investigation of the CS origin of life proposal whereby crystal growth might have acted as a means for pre-biotic genetics, with the information stored in aperiodic patterns of crystal defects. In particular, using a well-defined model crystal system, I investigate the reliability of crystals to act as a primitive source of transferable information through the arrangement of growth induced screw dislocations. In order to test this hypothesis it is important to understand the basic mechanisms and interactions of screw dislocations and crystal growth. Dislocations are found in crystals of all kinds. In fact, the very nature of crystal growth at low supersaturation is determined by the presence of screw dislocations in the crystal.

Despite their importance, the root cause of growth-induced screw dislocations is still not well understood. Understanding why and how these dislocations appear as well as the factors that influence spiral growth is most vital to our

ability to test the Cairns-Smith proposal of crystal 'genes'. Mutations can occur during growth due to the competition of growth-active hillocks as well as from accidental heterogeneous nucleations resulting from internal stresses such as inclusions, accidents, random lab vibrations, etc. In order to succeed at demonstrating 'genetic inheritance' through crystal growth, we must minimize the influence of mutations by controlling growth conditions. The primary experimental parameters to control include supersaturation, growth rate, solution flow, temperature, impurities, solvents used, and exposure to atmosphere. The nature of crystal growth via the screw dislocation mechanism is a complex process and because of this it is no wonder that the CS hypothesis has resisted experimental verification for over 37 years.

Beyond the complex nature of spiral growth in crystals, the ideas of GT have also proved challenging to test because they suggested that clay minerals were likely the first pre-biotic information carriers. Clays were undoubtedly abundant on the pre-biotic earth and could have served as suitable genes and scaffolding for the formation of early life by virtue of their imperfections and mutability. However, when it comes to experimental investigation of CS's proposal, researchers beginning with clays are at a disadvantage because, as crystals go, they are difficult to grow reproducibly, sizably, and with well-defined habits. CS's ideas must first be realized in chemically well-defined systems that are best suited to illustrations of his concept, irrespective of the likelihood that such crystals were part of the pre-biotic milieu. A key to the work reported herein is our ability to label crystal defects with organic luminophores in widely studied host crystals, a skill that is an outgrowth of our experience with dyeing crystals.[12]

NOTES AND REFERENCES TO CHAPTER 1

1. F. Dyson, *Origins of Life*, (Cambridge University Press: Cambridge, 1999).

2. P. Davies, *The 5th Miracle: The Search of the Origin and Meaning of Life*, (Touchstone: New York, 1999).

3. E. Schrodinger, *What is Life*? (Cambridge University Press: Cambridge, 1944).

4. a) A. G. Cairns-Smith, *Genetic Takeover and the Mineral Origins of Life*, (Cambridge University Press: Cambridge, 1982). These ideas were first articulated in the following: b) A. G. Cairns-Smith, *J. Theor. Biol*, **10** (1966), 53; c) A. G. Cairns-Smith, in *Towards a Theoretical Biology, I. Prolegomena* ed. C. H. Waddington, (Edinburgh University Press: Edinburgh, 1968); d) A. G. Cairns-Smith, *The Life Puzzle: On Crystals and Organisms and the Possibility of a Crystal as an Ancestor*, (Oliver and Boyd: Edinburgh, 1971); e) A. G. Cairns-Smith, *Proc. Roy. Soc. B*, **189** (1975), 249; f) A. G. Cairns-Smith, *Origins of Life*, **6** (1975), 2657.

5. A. G. Cairns-Smith, *Frontiers of Life, Vol. 1*, eds. D. Batlimore, R. Dulbecco, F. Jacob, and R. Levi-Montalcini, p. 169 (Academic Press: Sand Deigo, 2001).

6. a) S. Kauffman, *The Adjacent Possible: A Talk with Stuart Kauffman*, ed. J. Brockman (Content.com, Inc.: New York, 2003); b) G. Witzany, *Life: The Communicative Structure*. (Libri Books on Demand, 2000); c) L. Margulis and D. Sagan, *What Is Life?* (Simon and Schuster, New York, 1995).

7. A. G. Cairns-Smith, *Seven Clues to the Origin of Life*, (Cambridge University Press: Cambridge, 1985).

8. D. W. Deamer and G. R. Fleischaker, *Origins of Life: The Central Concepts*, (Jones and Bartlett Publishers: London, 1994).

9. L. E. Orgel, *Trends Biochem. Sci.*, **23** (1998), 491.

10. I. Fry, *The Emergence of Life on Earth: A Historical and Scientific Overview*, (Rutgers University Press: Piscataway, 2000).

11. R. M. Hazen, *Elements, vol. 1*, **3** (2005) 135.

12. B. Kahr and R. W. Gurney, *Chem. Rev.*, **101** (2001), 893.

13. C. Kittel, *Introduction to Solid State Physics*, (John Wiley and Sons, Inc.: New York, 1953).

14. D. Hull and D. J. Bacon, *Introduction to Dislocations, 4th Edition*, (Elsevier Butterworth-Heinemann: Oxford, 2001).

15. H. G. Van Bueren, *Imperfections in Crystals*, (North-Holland Publishing Company: Amsterdam, 1960).

16. F. R. N. Nabarro, *Theory of Crystal Dislocations*, (Oxford University Press: Oxford, 1967).

17. G. R. Ester, R. Price, and P. J. Halfpenny, *J. Phys. D: Appl. Phys.* **32** (1999), A128.

18. A. Pimpinelli and J. Villain, *Physics of Crystal Growth*, (Cambridge University Press: Cambridge, 1998).

19. W. Kossel, *Nachr. Ges. Wiss. Gottingen*, (1927), 135.

20. I. N. Stranski, *Z. phys. Chem.*, **136** (1928), 259.

21. R. Sours, *Uric Acid Crystal Growth*, (dissertation submitted to Georgetown University, 2004) Image adapted from thesis with permission.

22. W. K. Burton and N. Cabrera, *Disc. Faraday Soc.* **5** (1949), 33.

23. P. Hartman and W. G. Perdok, *Acta Cryst.*, **8** (1955) 49-52 (part I), 521-524 (part II), 525-529 (part III).

24. P. Hartman and W. G. Perdok, *Acta Cryst.*, **8** (1955) 49-52 (part I), 521-524 (part II), 525-529 (part III).

25. I. V. Markov, *Crystal Growth for Beginners*, (World Scientific: Singapore, 1995), see especially Chapter 3.

26. J. Frenkel, *J. Phys. U.S.S.R.* **9** (1945), 392.

27. J. W. Gibbs, *On the Equilibrium of Heterogeneous Substances, Collected Works*, (Green and Co: Longmans, 1928).

28. M. Elwenspoek and J. P. van der Eerden, *J. Phys. A*, **20** (1987), 669.

29. W. K. Burton, N. Cabrera, and F. C. Frank, *R. Soc. London Philos. Trans. A*, **243** (1951), 299.

30. F. C. Frank, *Disc. Faraday Soc.*, **5** (1949), 48.

31. See for example the conference proceedings "50 Years of Progress in Crystal Growth," *J. Cryst. Growth*, **264** (2004), xi.

32. D. Hull and D. J. Bacon, *Introduction to Dislocations*, (Butterworth-Heinemann, Oxford, 2001).

33. W. J. P. van Enckevort, *Prog. Cryst. Growth*, **9** (1984), 1.

34. N. Cabrera and M. M. Levine, *Philos. Mag.*, **1** (1956), 450.

35. G. H. Gilmer, R. Ghez, and N. Cabrera, *J. Cryst. Growth*, **8** (1971), 79.

36. Y. Okaya, *Acta Cryst.* **19** (1965), 879.

37. T. A. Eremina, N. G. Furmanova, L. F. Malakhova, T. M. Okhrimenko, and V. A. Kuznetsov, *Kristallografiya* **38** (1993), 236.

38. W. J. P. van Enckevort and L. A. M. J. Jetten, *J. Cryst. Growth*, **60** (1982), 275.

39. W. Tiller; in *The Art and Science of Growing Crystals*, p 302. ed. J. J. Gilman (John Wiley and Sons, Inc.: New York, 1963).

40. B. Kahr, A. Shtukenberg, and Y. O. Punin, *Optically Anomalous Crystals*, ed. B. Kahr, (Springer Verlag: New York, 2007).

41. Various authors, *Disc. Faraday Soc.*, **5** (Royal Society of Chemistry: London, 1949).

42. Various authors, *Disc. Faraday Soc.*, **136** (Royal Society of Chemistry: London, 2007).

43. Kohman; in *The Art and Science of Growing Crystals*, p 152. ed. J. J. Gilman (John Wiley and Sons, Inc.: New York, 1963).

44. E. Vlieg, M. Deij, D. Kaminski, H. Meekes, and W. van Enckevort, *Faraday Discuss.*, **136** (2007), 4.

45. K. Onuma, K. Tsukamoto, I. Sunagawa, *J. Crystal Growth*, **98** (1989), 377.

46. J. C. van Dam and F. H. Mischgofsky, *J. Crystal Growth*, **84** (1987), 539.

47. F. Bedarida, *J. Crystal Growth*, **79** (1986), 43.

48. F. Bedarida, L. Zefiro, P. Boccacci, D. Aquilano, M. Rubbo, G. Vaccari, G. Mantovani, and G. Sgualdino, *J. Crystal Growth*, **89** (1988), 395.

49. K. Maiwa, K. Tsukamoto, and I. Sunagawa, *J. Crystal Growth*, **102** (1990), 43.

50. Unpublished data - X-ray topography images taken by Alexey Voloshin (Russia) of KAP samples dyed with 10^{-5}M dichlorofluorescien grown by Theresa Bullard from spontaneous nucleation of 110 g/L KAP/H_2O solution in a 30°C water bath via slow evaporation. See Chapter 4. 2006.

51. a) M. H. J. Hottenhuis and C. B. Lucasius, *J. Cryst. Growth*, **78** (1986), 379; b) M. H. J. Hottenhuis, J. G. E. Gardeniers, L. A. M. J. Jeten, and P. Bennema, *J. Cryst. Growth*, **92** (1988), 171; c) M. H. J. Hottenhuis and A. Oudenampsen, *J. Cryst. Growth*, **92** (1988) 513.

52. P. M. Dove, K. J. Davis, J. J. De Yoreo, in *Solid-Fluid Interfaces to Nanostructural engineering, Vol. 2*, eds. X. Y. Liu and J. J. De Yoreo, (Kluewer/Plenum Academic Press: New York, 2004).

53. J. J. De Yoreo and P. G. Vekilov, in *Biomineralization*, eds. P. M. Dove, J. J. De Yoreo, and S. Weiner, (Mineral Soc. Am.: Washington, DC, 2003), p. 57.

54. M. I. Kozlovskii, *Soviet Phys. Cryst.*, **3** (1958), 206.

55. M. V. Pikunov and A. S. Petukhova, *Kristallografiya*, **22** (1977), 886.

56. J. C. M. Li, in *Dislocation Modeling of Physical Systems: Proceedings of the international conference*, ed. M. F. Ashby (Pergamon Press: New York, 1981).

57. A. R. Verma, *Phil. Mag.*, **43** (1952), 441.

CHAPTER 2 - EXPERIMENTAL BACKGROUND

2.1 Detecting Screw Dislocations

A wide variety of experimental techniques have been employed to study the distribution, arrangement, density, and properties of screw dislocations and their resulting growths spirals. In general, the detection methods used can be grouped into two broad categories: (1) Surface methods and (2) Bulk or sub-surface methods.

Surface Detection Methods

Etching and decoration procedures can reveal the presence of emergent dislocations on the surface of a crystal but they require alteration of that surface.[1] Reflected light differential interference contrast (DIC) microscopy is one of the most common techniques for detecting hillocks on highly reflective surfaces, but it is limited to observation of macro-features.[2] Scanning tunneling microscopy (STM)[3] and atomic force microscopy (AFM)[4] have been used to image hillocks and other surface defects at high resolution, but they are restricted in their field of view ($\leq 100 \times 100\ \mu m^2$). Real-time phase-shifting interferometry can reveal surface topography within a larger field ($2 \times 2\ mm^2$), but with poorer resolution[5]. These above techniques are limited to defects present on the surface during the analysis.

Bulk Detection Methods

There are relatively fewer methods used for detecting defects in the bulk of a crystal. X-ray topography[6] shows departures from the perfect crystal structure in

the crystal *volume*, but all defects are projected onto a common plane. This method is good for recording long-range distortion and/or strain fields associated with macroscopic crystal deformation, however it does not give dynamic information and it often requires highly collimated synchrotron radiation in crystals of the highest quality.[7] Transmission electron microscopy (TEM) has similar limitations and sample preparation can be laborious.[8] Cathodal luminescence (CL), visible light emitted from a sample during electron bombardment, has been used by Reeder *et al.* to qualitatively image hillocks in minerals with transition metal inclusions that have undergone chemical zoning on the vicinal faces of growth hillocks.[9] It requires material properties and guest ions such that incident electrons can excite an electron into the conduction band, resulting in a hole. Light is produced upon recombination of the hole with a free electron. CL is restricted to surface layers, has a resolution of about 1000 Å, and produces significant amounts of heat.

To better understand the macroscopic evolution of growth hillocks, it is necessary to observe *both* the bulk and surface defects throughout the entire crystal. Unfortunately, the traditional probes are all limited in one way or another towards this application, thus a new technique for observing hillocks is offered.

2.2 Dyeing Crystals

Colored gemstones and minerals have been highly prized by humans for millenia. Not only are they beautiful to the eye, but they often possess unique optical, chemical, and physical properties. Beyond colored crystals, humans have had a love affair with colored things of all kinds, inspired by, but not limited to,

the abundance of colors that nature provides us with. From dyeing fabrics to ceramics to a painter's canvas or a person's hair, entire crafts have been developed around the art of coloring materials for various purposes, some purely asthetic, while others more functional. Science, too, has found dyes useful in its industry. Pathologists and histologists dye tissues to study disease, biophysicists dye molecules to study cellular operations, optical engineers use colored lenses to filter light, and so on. Around the 1800's scientists also began dyeing crystals.

At first, one might think that large organic dyes could not possibly fit into the tight packed structure of a crystal lattice. Indeed, the Law of Isomorphism states that impurities must be similar in size, shape, and constitution to their crystal host if they are to be incorporated.[10] However, when grown in supersaturated solution (far from equilibrium), the adsorbtion and subsequent overgrowth of dyes and other large impurities on a growing crystal surface can occur readily. The driving force of supersaturation helps to overcome thermodynamic barriers upon which the Law of Isomorphism is based. Motivated by investigations into such phenomena as pleochroism, photophysics, habit modification of crystals, properties of oriented media, limitations to the Law of Isomorphism, and more, dyed crystals have intermittently appeared in the scientific literature.[11] It is only in more recent times, however, that the study of crystal dyeing has acheived a status of its own. With potential spectroscopic, photonic, and stereochemical applications of interest to today's scientists, dyed crystals have been launched into an independent field of investigation that holds much promise.

The Kahr labs have shown that simple molecular and ionic crystals can orient and overgrow a wide variety of dye molecules during growth from solution.[11]

For a more in-depth understanding of the science and history of dyeing crystals, including the wide variety of options and applications available through this technique, the reader is referred to the extensive review by Kahr and Gurney.[11] To date over a hundred crystal hosts, including sulfates, phosphates, and carboxylates, paired with hundreds of commercial dyes are known to produce dye inclusion crystals. These dyed crystals, typically containing about 1 dye molecule per 10^4 - 10^6 host molecules, display both *inter*sectoral and *intra*sectoral chemical zoning.

2.2.1 *Intersectoral Zoning – Dyeing Growth Sectors*

*Inter*sectoral chemical zoning occurs when adsorbed impurities express selective affinities for symmetry-distinct crystallographic faces, becoming overgrown and trapped within sub-volumes of the crystal called growth sectors. During growth from solution, this process is governed by the specificity of noncovalent interactions, which can include ionic forces, cation-π interactions, charge-transfer interactions, hydrogen bonding, and hydrophobic forces.[12] Any of these interactions can play a role in determining the segregation, orientation, and conformation of dyes within a host crystal, and thus the mechanisms whereby intersectoral zoning occurs are often complex.

One of the most remarkable crystals in its ability to orient and overgrow a wide variety of dye molecules is KAP (potassium acid phthalate, $C_6H_4{\cdot}COOH{\cdot}COO^-K^+$, space group $Pca2_1$ – see Section 2.3 for details).[13,14] KAP is easily grown from aqueous solution as large {010} plates with perfect (010) cleavage planes, and it readily incorporates well over a hundred dyes in various

growth sectors, a schematic of which is shown in Figure 2.1. Generally speaking, negatively charged dyes tend to become overgrown within the {111} sector, while positively charged ones more often recognize the $\{11\bar{1}\}$ sector.[15] This tendency confirms the effects that KAP's polar axis plays in the selectivity of impurity incorporation. Force-field calculations have been used to identify the energetically stable KAP surfaces, confirming the (111) surface termination to be primarily positive in charge, the $(11\bar{1})$ surface to be exclusively negative, while the (110) surface has a net charge that is slightly negative but is comprised of periodic pockets with alternating charges that are small compared to (111) and $(11\bar{1})$ (see Section 2.3.1 for further discussion of KAP structure).[15] While these tendencies for ionic dyes to recognize the respective growth faces of KAP via electronic forces helps us understand some of the selectivity, there have been several exceptions as well, making it difficult to reduce their behavior to concrete rules.

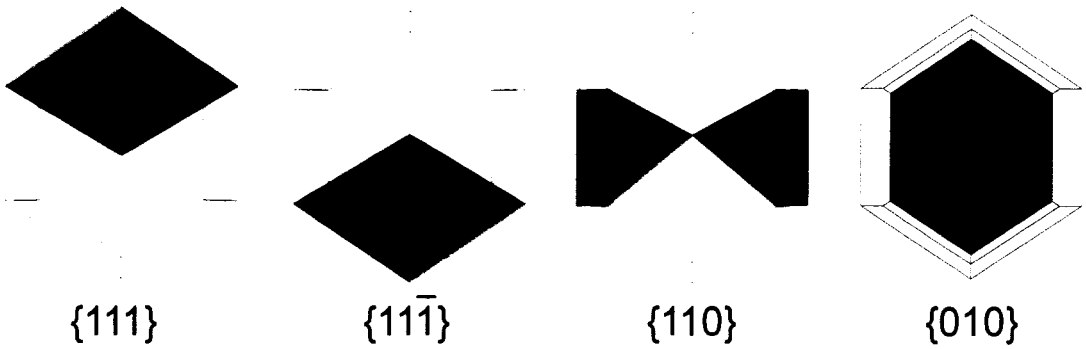

Figure 2.1. *Intersectoral zoning.* Schematic depicting how KAP displays intersectoral zoning by different dyes in each of its major growth sectors. Major symmetry-independent growth sectors are shaded.

Due to the chemical specificity of the dye-host interaction, a range of photophysical responses in different growth sectors can arise. For example, the dye molecules can become oriented within the crystal lattice leading to

differential absorption and/or emission of polarized light. If the electronic structures of the dyes are sufficiently understood, their transition dipole moments can be determined relative to the host lattice through measurements of *linear dichroism*. With this information we can identify the bulk ensemble orientation of the dye within the crystal lattice (see Section 2.5.1.2).

2.2.2 *Intrasectoral Zoning - Dyeing Hillocks*

Impurities may also inhomogeneously deposit *within* a single growth sector depending on the crystal's surface topography, a process known as *intra*sectoral zoning. If a crystal face grows through the spiral mechanism and the resulting hillocks are polygonized (see Section 1.2.2.1), this further partitions crystal faces into vicinal regions, each region having slightly different inclinations. Intrasectoral zoning may result from the selective interactions between the impurities and the distinct vicinal hillock slopes. Due to the active growth surfaces being more highly specified at the time of incorporation, this type of chemical zoning can provide more detail about the guest-host recognition mechanisms than intersectoral zoning.

Intrasectoral zoning with dyes was first observed on the {101} surfaces of KH_2PO_4 by Zaitseva and co-workers[16], using the anionic dyes, amaranth and Chicago sky blue, that Kahr *et al.* had previously shown to have an exclusive affinity for these faces.[17b] This original observation of intrasectoral zoning required the introduction of the dye during late growth, thereby coloring only a thin surface layer so that the patterns of color were not confounded by the superposition of many colored hillocks throughout the growth sector. Amaranth

was found to recognize two out of the three vicinal slopes, while Chicago sky blue preferred the remaining one. *Luminescence* labeling of hillocks with dyes was first seen in K_2SO_4 containing *o*-aminobenzenesulfonate.[17] This mixed crystal showed striking blue bands associated with the {021} faces when illuminated with ultraviolet light, due to recognition by the luminophore of the slowly advancing steps growing toward (001) but not the faster steps growing toward (010). Intrasectoral zoning was also observed in α-lactose monohydrate crystals grown in the presence of green fluorescent protein (GFP).[18] The (010) sector of α-lactose monohydrate grows unidirectionally toward +*b* through a spiral dislocation mechanism, resulting in polygonal hillocks that partition the face into four vicinal regions that are pair-wise related by 2-fold symmetry.[19] GFP only recognizes the lateral slopes with the greatest step advancement velocity. Adenosine monophosphate and adenosine triphosphate were also found to recognize the slopes of KH_2PO_4 avoided by amaranth.[20]

KAP also displays intrasectoral zoning in the (010) growth sectors (Figure 2.2d), due to its polar *c*-axis that causes the steps propagating in the +*c* and –*c* directions to be different in structure (Figure 2.2a,b).[21] The steps moving with a +*c* velocity component are slower than those moving with a –*c* component, leading the screw dislocations emerging on the (010) surface of KAP to produce polygonized growth spirals. To date more than 100 dyes have been shown to recognize KAP hillocks.[22] Luminescent labels that bind to the widely spaced "fast" steps in preference to the more closely spaced "slow" steps will reveal themselves in patterns of light bounded by the perimeters of the fast slopes; the vertices of the colored chevrons mark the core of the screw dislocations. The correspondence between hillocks and dye is evidenced by a comparison of images from reflected light differential interference contrast (DIC) microscopy and fluorescence microscopy (Figure 2.2c,d).

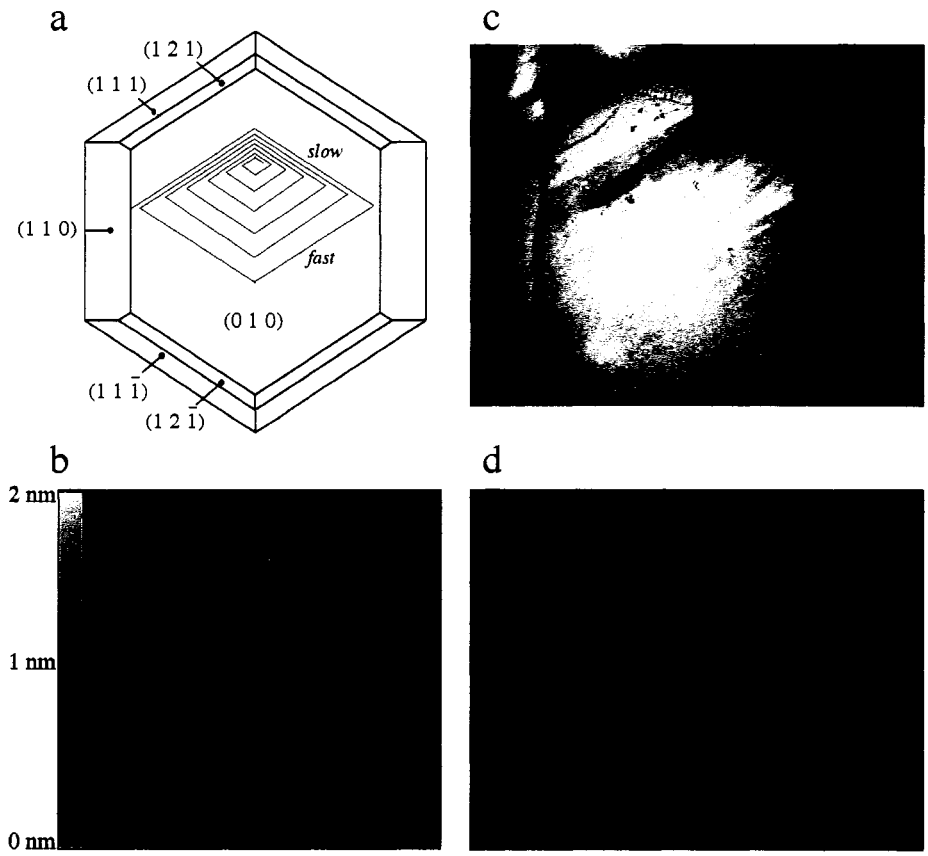

Figure 2.2. *Intrasectoral zoning and KAP hillocks.* (a) Idealized KAP crystal habit and absolute indices. The orientation of the fast (+*c* direction) and slow (-*c* direction) growing slopes of a hillock is shown on (010) in a comparison of images made by (b) *ex situ* AFM, (c) reflected light DIC microscopy, and (d) fluorescence microscopy of KAP dyed with **3** at 10^{-5} M. (c) and (d) represent the same areas.

As discussed in Section 1.2.2.3, there is a constant competition between hillocks for dominance over the growth of a face. Those hillocks that are growth active can begin and end at any point during the growth of real crystals, so they do not always persist all the way to the surface to be observable by DIC or other surface probes. The dyes, however, bind to the crystal throughout the growth process. Even after subsequent overgrowth, the luminophores create a 'fossil-record' of hillock evolution in patterns of light that can be revealed by successive

cleavage or with a confocal luminescence microscope (see Section 2.6). In such a way, the phenomenon of intrasectoral zoning of luminescent dye molecules within the polygonized hillocks of a crystal host can be used as a tool for investigating hillock dynamics and the transfer of "genetic" information through crystal growth. As a host crystal, KAP provides us with an excellent model system for just such an investigation due to its largest expressed face growing through the screw dislocation mechanism, its great affinity for intrasectoral zoning of luminophores, its perfect (010) cleavage planes, and its ease of growth from solution.

2.3 Potassium Hydrogen Phthalate (KAP)

2.3.1 KAP Crystal Structure and Habit

Potassium hydrogen phthalate (KAP), a compound belonging to a series of alkali acid phthalates, is an ideal material for crystal growth studies. This is due in part because of its well-developed step system on the largest expressed {010} faces, in addition to it being a well-characterized crystal. Figure 2.3 shows the molecular structure of KAP. Its crystals were described by Groth[23] in 1917, while the actual structure was originally determined by Okaya in 1965.[13] An exchange of axes was applied by Jetten in 1983 that will be used here as well.[24] Eremina *et al.* improved upon the crystal structure data in 1993, and determined the absolute direction of the polar *c*-axis, to which all (*hkl*) indices refer, by anomalous X-ray scattering.[14]

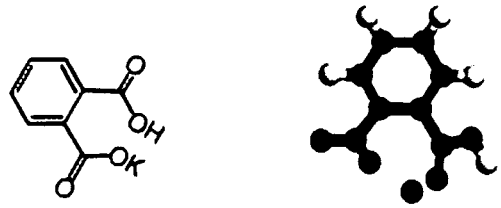

Figure 2.3. *KAP chemical formula and ball-and-stick model.* $K^+(C_6H_4{\cdot}COOH{\cdot}COO)^-$, an organic molecular salt of the alkali acid phthalate series. In the ball-and-stick representation, white balls are hydrogen atoms, grey balls are carbon atoms, red balls are oxygen atoms, and the purple one is the potassium cation. Ball-and-stick figure shows the geometry for a single KAP unit in the crystal, as determined by X-ray diffraction.[13]

As shown in Figure 2.4, KAP crystals are built of alternating bilayers of potassium cations (K^+) and hydrogen phtalate anions (HP^-) stacked along [010] (*b*-axis) in the orthorhombic space group $Pca2_1$. The unit cell consists of four chemical units of $K^+(C_6H_4{\cdot}COOH{\cdot}COO)^-$, with cell dimensions a = 9.614(4) Å, b = 13.330(1) Å, and c = 6.479(2) Å.[14] Three types of bonds exist between the K^+ and HP^- building units as follows:

- *Coulombic interactions*: ionic bonding between the K^+ and the ionized carboxyl group of the HP^-.
- *Hydrogen bonds*: a polar herringbone array of hydrogen bonded KAP molecules forms along [001] (*c*-axis) from the interaction between the ionized carboxyl group of one molecule and the non-ionized carboxyl group of a neighboring molecule.
- *Van der Waals bonds*: intermolecular bonding between aromatic rings. Perfect cleavage planes exist between the sheet-like layers perpendicular to the [010] (*b*-axis).

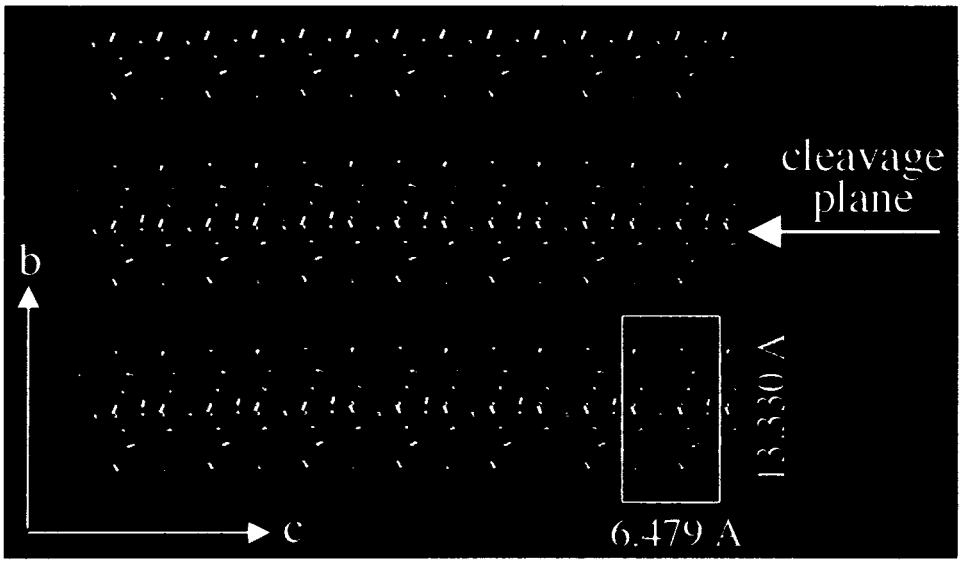

Figure 2.4. *KAP crystal structure.* Crystal packing schematic for KAP looking down [100] (*a*-axis). White box shows unit cell with dimensions a = 9.614(4) Å (not shown), b = 13.330(1) Å, and c = 6.479(2) Å. The *c*-axis is polar. Perfect cleavage planes exist between the aromatic rings stacked along the *b*-axis.[25]

When grown from pure aqueous solution, KAP crystals form as clear, colorless hexagonal plates with large {010} pinacoid faces bounded by the following additional forms in order of descending morphological importance: {110} prism faces, $\{11\bar{1}\}$ and {111} pyramid faces, and occasionally {121} pyramid faces (Figure 2.2a).[14] Due to the polar axis, the atomic configurations of the {111} and $\{11\bar{1}\}$ surfaces are distinctly different: the $\{11\bar{1}\}$ faces are predominantly terminated by the O^- atoms of the ionized carboxyl groups (acceptors of hydrogen bonds), while the {111} faces have OH terminations (donors of hydrogen bonds). This difference is in agreement with experimental growth rates and characteristics for these two growth sectors, namely that the $\{11\bar{1}\}$ sectors have been shown to grow at a rate 2.0-2.2 times faster than the {111} sectors in pure KAP solution, additionally they show a higher affinity for overgrowing di- and tri-valent cations.[14,26] Of the four K^+ ions in each unit cell, one is situated

within the anion layer while the other three are positioned between the layers. As a result of these structural features, there is a much greater density of K^+ ions on the {010} surface (1 cation per 15.6 Å^2) than there is on the $\{11\bar{1}\}$ and {111} surfaces (1 cation per 41.7 Å^2).[14] These surface terminations play a large role in determining growth kinetics of each face, as well as the degree of interaction with different impurities (see Section 2.2 and Section 2.3.4).

2.3.2 *Experimental Conditions for KAP Growth*

KAP crystals are typically grown by slow evaporation from aqueous solution at or near room temperature. Crystal sizes can range from micron length all the way up to several centimeters in their maximum dimension, however for this research crystals ranged from 0.4 - 1.2 cm along the *c*-axis. For the experiments reported herein, all chemicals were used as received by the manufacturers. Growth solutions were prepared from acidimetric grade KAP (Sigma-Aldrich, 99.95-100%) dissolved in purified deionized water (Barnstead NANOpure, 18.2 MΩ cm^{-1}) by heating to about 60-80°C and stirring with a Teflon coated magnetic stir-bar, then filtered and cooled to growth temperature. When growing by spontaneous nucleation through slow evaporation, starting solution concentrations were around 110 g/L of various volumes in glass crystallization dishes, which were placed in a water bath maintained at a growth temperature of 30.0 ± 0.1 °C. When the crystallization dishes were left uncovered, several single crystals (2-8 mm in size) would appear on the bottoms of the dishes after 2-6 days, depending on solution volume. Crystallization and growth rate could be slowed down by partly covering the dishes or by growing at lower temperatures.

When growing from seeds two different methods were used depending on the nature of the experiment. For the slow evaporation method, seeds were freshly harvested from a growth solution at 30°C (as described above) and immediately transferred to a new *slightly undersaturated* ($\sigma \approx -0.01\%$) solution in small 10 mL dishes at a slightly elevated temperature without exposing the surfaces to air. Dishes were then partly covered and placed under a plastic bin in a dry temperature controlled chamber maintained at 30°C and allowed to continue growth for 1-2 days. This method of growth however experiences varying supersaturation levels as water evaporates and solutions remain static. Thus a closed-loop flow system was also designed and assembled for more controlled growth conditions. The specifics of this flow system are described in Section 2.7.2 . In all experiments, grown crystals were harvested with tweezers and dried using a jet of nitrogen air through a 1 mm diameter nozzle to rapidly remove solution so as to preserve KAP surface features.[27]

KAP has no known polymorphs, however on rare occasions (~1% of growth experiments from spontaneous nucleation) we have observed a hydrated compound crystallize out of the same solution as KAP. This other form, potassium hydrogen diphthalate dihydrate, consists of a potassium cation coordinated to a proton-bound hydrogen phthalate dimer with two water molecules, with a habit consisting of heavily etched elongated prisms.[28] We were the first to analyze and report this new structure (see Reference 28 for this publication). Formation of this compound does not appear to depend on temperature, exposure to light, or rate of evaporation, and it has never appeared during growth of KAP from seeds. However there does seem to be more frequent appearance of this form when grown under ambient contions, such as on a lab bench or in a cabinet. The unpredictability of crystallizing this dihydrate form demonstrates the complexity of crystal nucleation processes. For the

experiments reported herein, however, any growth solutions that resulted in the crystallization of the dihydrate form were discarded.

2.3.3 *Properties of KAP*

Beyond being a good model system for investigating crystal growth and step kinetics, KAP is also widely used in X-ray monochromators and analyzers[29,30,31] due to its layer-like structure and small diffraction angle for long-wavelength X-rays. KAP is also known for its piezoelectric, pyroelectric, elastic, and nonlinear optical properties.[31,32,33] For a full listing of the values for various physical properties of KAP and the other acid phthalate salts, including thermal expansion, dielectric, elastic, pyroelectric, piezoelectric, optical, and decomposition properties the reader is referenced to a 1991 publication by Haussühl.[31] Recently, KAP has also been reported as a good substrate for the epitaxy of oriented organic crystal films that promise photonic applications.[33,34]

Birefringence

Being of the orthorhombic space group, KAP is a *biaxial crystal* that is optically *anisotropic*. This causes light traveling in any direction other than along an *optic axis* to be split into two eigenmodes having different velocities and perpendicular polarizations, a phenomenon known as *birefringence* or double refraction.[35,36] Birefringence is often expressed as the difference in refractive indicies, n_1 and n_2, that characterize the two eigenmodes:

(2.1) $$\Delta n = n_1 - n_2$$

In biaxial crystals there are two directions, or optic axes, along which light can travel without being doubly refracted or experiencing any change in its polarization state. These two directions together define the *optic or axial plane*, and the direction perpendicular to this plane is called the *optic normal*. The angle between the two optic axes is anywhere from 0° to 90°, depending on the crystal and the conditions to which it is subjected. There are two mutually perpendicular bisectors between these axes, called the acute and obtuse bisectrix. In the orthorhombic system, the acute bisectrix, obtuse bisectrix, and optic normal coincide with the crystallographic axes, and the indices of refraction along each of these directions define an ellipsoid known as the *optical indicatrix* such that:

$$\left(\frac{x_\alpha}{n_\alpha}\right)^2 + \left(\frac{x_\beta}{n_\beta}\right)^2 + \left(\frac{x_\gamma}{n_\gamma}\right)^2 = 1 \tag{2.2}$$

where x_i ($i = \alpha, \beta, \gamma$) are the coordinates that satisfy the equation of an ellipsoid. Traditionally the coordinate system is assigned such that $n_\alpha < n_\beta < n_\gamma$. Reported values for the indices of refraction at about 495 nm wavelength in KAP are n_c = 1.49 and n_a = 1.64, leading to a birefringence magnitude of $\Delta n = n_c - n_a$ = -0.15 for light directed along the *b*-axis (the most common view), which is very similar to that of calcite.[33,37] Earlier literature also gives an index of refraction along the *b*-axis to be n_b = 1.66.[38] Using these values that would make KAP an optically negative material along this view, with the optic normal parallel to the *a*-axis, the acute bisectrix parallel to the *c*-axis, and the obtuse bisectrix parallel to the *b*-axis. The angle between the two optic axes, $2V$, for which the slow direction bisects this angle, can be determined from the following equation:[36]

$$\tan^2 V = \frac{\dfrac{1}{n_\alpha^2} - \dfrac{1}{n_\beta^2}}{\dfrac{1}{n_\beta^2} - \dfrac{1}{n_\gamma^2}} \tag{2.3}$$

Given the above numbers for KAP indices of refraction in the visible range, this angle works out to $2V = 142.8°$, or each optic axis being oriented at 71.4° on either side of the *b*-axis in the *c*-*b* plane.

Anytime light is incident upon an interface between two media, such as air and a crystal, there is always a percentage of the electromagnetic wave that will be reflected at the surface, while the rest is transmitted. The amount of reflectance and transmittance can be described for linear, isotropic, homogenous media by the Fresnel equations. When the angle of incidence is normal to the interface (as is the common view for KAP), these equations reduce to the following forms:[39]

(2.4) $$R = \left(\frac{n_t - n_i}{n_t + n_i} \right)^2$$ *Reflectance*

and

(2.5) $$T = \frac{4 n_t n_i}{(n_t + n_i)^2}$$ *Transmittance*

where n_i is the index of refraction for the medium through which the incident light travels, n_t is that of the transmitting medium, and $R + T = 1$. However, for a birefringent material n_t is split into its two orthogonal eigenmodes, and as such the amount of reflected and transmitted light will vary for different polarization directions. This will result in a differential loss of signal when viewed under a polarized light microscope.

In our case, quantitative spectral measurements are taken with a transmission microscope, so we must correct for loss due to differential reflectance at the air-crystal interface for incident light polarized along the *a*-axis versus the *c*-axis.

Using the reported values for n_a and n_c in KAP as well as the index of refraction for air, we calculate the reflectance for *a*-polarization to be 0.059 and for *c*-polarization to be 0.039, resulting in a 2.0% greater reflectance for the *a*-polarization. Experimental values in the literature report a 3.3% difference in the absolute reflectance of KAP for incident light in the visible range polarized along the *a*-axis and *c*-axis.[33]

The birefringence has an additional subtle influence on optical behavior by anisotropically reducing the speed of light through the material, $c/n(\nu)$, where $n(\nu)$ is the frequency dependent index of refraction, and by creating an effective electric field, $\mathbf{E}_{eff}(\nu)$, experienced by the KAP molecules that is altered from the actual applied field, $\mathbf{E}(\nu)$, due to the effective polarizability of the medium, $\alpha(\nu)$:

(2.6) $$\mathbf{E}_{eff}(\nu) = \alpha(\nu)\, \mathbf{E}(\nu)$$

where $\alpha(\nu)$ is given approximately by $\alpha(\nu) = [n^2(\nu) + 2] / 3$.[38] For example, in linear dichroism measurements, where one can identify the orientation of a transition electric dipole moment through differential absorption of linearly polarized light, the measured absorbance intensity along the polar axis will be too large by:[38]

(2.7) $$|E_{\parallel}|^2 = \frac{\left[n_{\parallel}^2(\nu)+2\right]^2}{9n_{\parallel}(\nu)}|E|^2$$

and the measurement for perpendicularly polarized light will be too large by:

(2.8) $$|E_{\perp}|^2 = \frac{\left[n_{\perp}^2(\nu)+2\right]^2}{9n_{\perp}(\nu)}|E|^2$$

In these equations the extra factor of $n(\nu)$ in the denominator comes from the reduction to the speed of light through the material. For strongly birefringent

crystals like KAP, it is important to include these corrections when evaluating the dichroic ratio.

Linear Dichroism

If an anisotropic material absorbs light, the electronic response will vary along different directions according to its bonding structure. When polarized light is used to illuminate such a material, it will display different colors or intensities of transmitted light depending on the orientation of the polarization direction with respect to the optic axes, a phenomenon known as linear dichroism or pleochroism in biaxial crystals.[36] In addition to being orientation-dependent, the attenuation of light through an absorbing medium may also be frequency-dependent. This behavior may be included in a generalized form for the refractive index by expanding it into a complex quantity, where the imaginary part accounts for absorption:[35]

(2.9) $$\tilde{n}(\nu) = n(\nu) + ik(\nu)$$

$k(\nu)$ is the absorption coefficient that describes the attenuation of light as it passes through an absorbing medium: $I = I_0\, e^{-kL}$, where I_0 is the intensity of incident light, I is the intensity of transmitted light, and L is the thickness of the medium. Thus the difference in the refractive index between the two orthogonal eigenmodes of an anisotropic crystal becomes:[35]

(2.10) $$\Delta\tilde{n}_{linear} = (n_1 - n_2) + i(k_1 - k_2)$$

where the real component is the linear birefringence and the imaginary component is the linear dichroism. At visible wavelengths, KAP is optically transparent (very small k) and non-dichroic ($\Delta k = 0$). There is strong absorption of energy above 4 eV (ultraviolet region) and some strong dichroism of absorption peaks below 1 eV (infrared region), but for this research these regions

are irrelevant (Figure 2.5).[33] When organic dyes are sectorally zoned within the crystal, however, large dichroic signals may arise. This feature allows us to identify the bulk ensemble orientation of those dyes within the crystal (see Section 2.5.1.2).

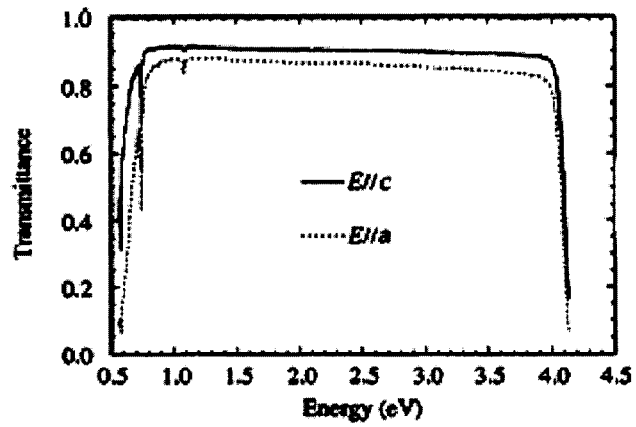

Figure 2.5. *Transmission spectra of KAP.* Solid line is for incident light polarized along the *c*-axis and dashed line is for light polarized along the *a*-axis. [Figure reproduced from Ref. 33].

KAP Solubility

One of the challenging aspects of working with KAP is that its supersaturation is particularly sensitive to small temperature fluctuations. This can be seen from the solubility relation for KAP (Figure 2.6):[40]

(2.11) $$C_{eq}(T) = 9.283 - 0.059T + 0.0058T^2$$

where $C_{eq}(T)$ is the equilibrium concentration of KAP, given in units of grams KAP per 100 grams water (100 g of water is about 100 mL in volume at room temperature). The supersaturation, $\sigma(T)$, is then determined by the following equation:

(2.12) $$\sigma(T) = \ln\left(\frac{C_{actual}}{C_{eq}(T)}\right) \times 100\%$$

where C_{actual} is the experimental concentration of KAP in solution. At 30 °C, for example, the equilibrium concentration of KAP is 12.7 g per 100 g of water, and it has a solubility/temperature gradient of 0.3 g/°C. As a result of this sensitivity to temperature, if supersaturation control is desired, it is necessary to grow KAP crystals in a closed environment with accurate temperature control, solution flow, and no evaporation.

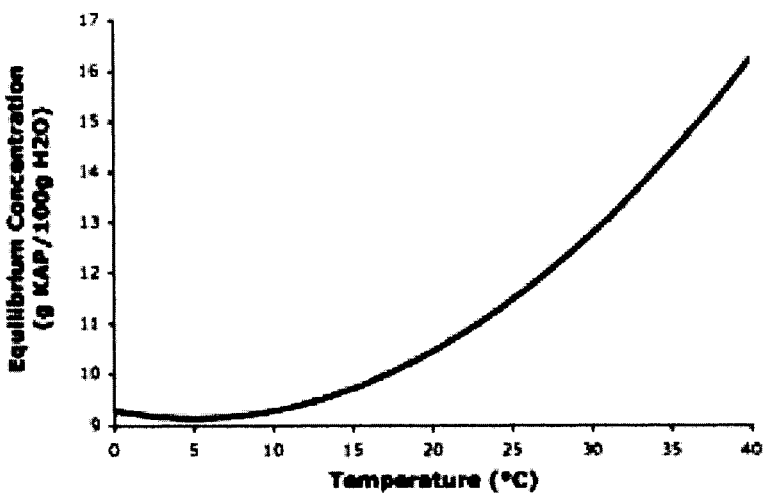

Figure 2.6. *KAP solubility curve.* The supersaturation, as determined by the concentration of KAP in solution, is very sensitive to small fluctuations in temperature.

2.3.4 *KAP Defects*

KAP, as grown from solution, has been shown by X-ray topography to have very low levels of strain and defect densities (5 - 15 cm^{-2}), with significant variation between growth sectors.[27,41] The main types of defects found in KAP are inclusions (I) and striations (S), found predominantly in the $\{11\bar{1}\}$ sectors and

likely due to solvent trapping, as well as growth-induced dislocations found in all growth sectors with the greatest densities in the $\{11\bar{1}\}$ and {111} sectors arising from solvent inclusions (I) and growth sector boundaries (B) (Figure 2.7a). The relatively low density of dislocations found in the (010) sector include pure edge-type dislocations with [001] Burgers vectors that bend into (010) from other growth sectors, and V-shape mixed dislocation pairs lying in the (001) plane with about 20° between arms and Burgers vectors [110] and $[\bar{1}10]$ (Figure 2.7b). These V-shaped pairs in (010) nucleate from sources that are invisible at X-ray topography resolutions. The dislocation pairs comprise a minority of the growth spirals on the (010) face, but they are still significant in number and can have strong influences on growth rate, as will be discussed below. Pure screw-type dislocations are also possible in the (010) sector, however they have proven challenging to detect in KAP via X-ray topography due to their short topographic projections and the difficulty in distinguishing them from the convolution of images from other growth sectors below (010).[27] Needless to say, there remains much that can be learned about dislocation nucleation and structure in KAP, especially in the (010) sector, which is indeed essential in using it to evaluate GT.

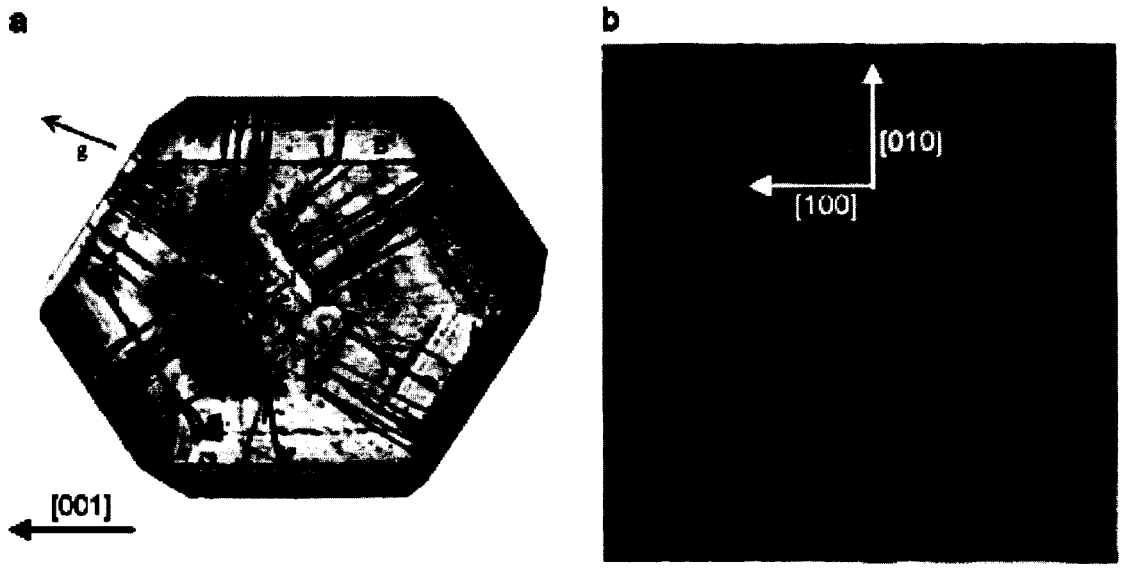

Figure 2.7. *KAP defects.* a) X-ray topograph (112 reflection) of whole as-grown KAP crystal (crystal size is about 7 mm × 9 mm). "B" indicates growth sector boundary where dislocations can be seen to bend upon crossing. "S" indicates striations. "I" indicates a fluid inclusion. "P" marks a pair of dislocations with opposite Burgers vectors that originate at the same source (invisible) in the $\{11\bar{1}\}$ sector. b) X-ray topograph (022 reflection) showing V-shaped dislocation pars of opposite Burgers vectors [110] and $[\bar{1}10]$ that originate from the same sources (invisible) in the (010) sector. (Images taken by Halfpenny, *et al.*, and reproduced from Ref. 27). Arrows indicating directions were added for ease of identifying approximate orientation of dislocations with respect to crystallographic axes.

In all cases of growth-induced dislocations in KAP, the dislocation lines are all straight and no post-growth movement or change of Burgers vectors were observed in the X-ray topographs taken by Halfpenny *et al.*[27] The V-shaped mixed dislocation pairs in (010) are of particular interest in relationship to variation of neighboring hillock proximity during growth. As discussed in Section 1.2.2.3, when multiple dislocations of the same sign are separated by less than one step spacing due to a single dislocation, λ_0, they will cooperate and

become more growth active than isolated spirals. In this case, because of the mixed nature of these dislocations, as the (010) face grows the spiral centers will become further separated and eventually no longer cooperate as step sources, thus changing the dominant growth behavior and rate. Utilizing Equation 1.20 we can theoretically determine approximately how close together these dislocation pairs must be in order to cooperate in KAP (010) growth. For small-molecule compounds that have good solubility, $\chi/kT \approx 1/2a$ (recall from Section 1.2.2 that χ is the isotropic specific edge energy, given as energy per unit length).[42] Taking the step height, a, to be 1.333 nm (KAP's b lattice constant), we arrive at a maximum spacing of $\lambda_0 \approx (12.635\ \text{nm})/\sigma$. At a low supersaturation, such as 1%, these dislocation pairs can be separated by as much as 1.26 μm and still cooperate to create more growth active spirals than isolated dislocations. Remember, however, that Equation 1.20 was arrived at assuming isotropic step spacing, which is not the case for KAP, so this value is likely much larger than what would be needed for enhanced spiral growth in a real KAP crystal.[43]

KAP Hillocks

As mentioned previously, KAP's polar c-axis causes the steps propagating in the $+c$ and $-c$ directions to be different in structure (Figure 2.2a,b).[21] This leads to different step kinetics that produce polygonized growth spirals on the (010) surface. Generally, a pure KAP hillock forms as a hexagonal stepped pyramid with three sets of steps (Figure 2.8):[44]

- *Fast Steps* – steps moving in the $<10\bar{1}>$ directions with large step spacing.
- *Slow Steps* – steps moving in the <101> directions with small step spacing.
- *Intermediate Steps* – steps moving with a medium velocity and step spacing in the <100> directions (these steps do not always appear).

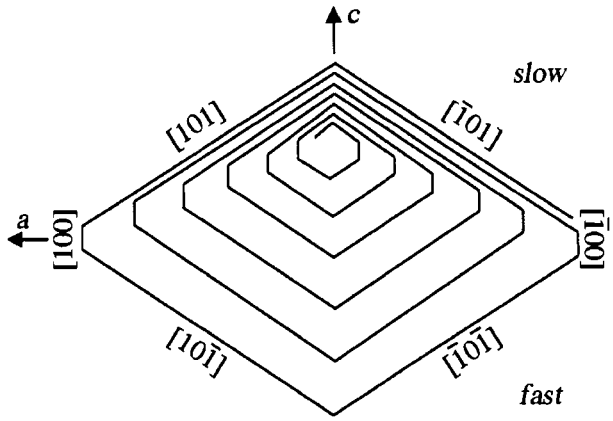

Figure 2.8. *KAP hillock morphology.* Pure KAP hillocks display hexagonal morphology with three types of steps: fast steps in the <10$\bar{1}$> directions, slow steps in the <101> directions, and intermediate steps in the <100> directions. Figure adapted after Hottenhuis *et al.*[44] Miller index labels indicate direction of step movement.

Kinetic differences between the step directions are attributed to two key factors: (i) the non-centrosymmetric crystal structure, and (ii) the dehydration of the K^+ ions from solution.[44] As mentioned before, the KAP molecules align in a herringbone array along the polar *c*-axis, creating a net dipole moment pointing in the +*c* direction. As partially hydrated K^+ ions adsorb onto the surface they preferentially bind to the fast steps where O^- atoms are sticking out from the ionized carboxyl groups, in contrast to the prominent OH terminations of the slow steps. Hottenhuis *et al.*[44] suggested that the dehydration of the K^+ ions is also favored at the fast steps due to the dipole moments of the water molecules aligning anti-parallel to the net *c*-axis dipole moment, whereas at the slow steps they align parallel. It has further been suggested by Jetten[24] and reiterated by Hottenhuis *et al.*[44,45] that the rate-limiting step for KAP growth is the dehydration of the K^+ ions, which is relatively slow compared to the dehydration of the HP^- building units. This is attributed to an internal stabilization of the HP^- units from a delocalized charge distribution over its multi-atom π-electron system.

Altogether, this results in the fast steps having a kinetic coefficient of $\beta \approx 75$ μm/s and the slow steps being about 10 times slower, while the intermediate steps (if present) behave somewhere between these two extremes.[44]

Impurity influences on KAP Hillocks

Using DIC imaging of macrosteps, Hottenhuis *et al.* observed drastic alterations of KAP step kinetics and hillock morphology due to the presence of various trivalent cationic impurities during growth from solution.[45] In all cases, these types of impurities act to slow down step movement through pinning and competition with K^+ building units for available binding sites. The specific action of the impurity on KAP hillock morphology and kinetics was attributed to site-specific adsorption of the ions. Four main categories of impurity adsorption were identified: on the terrace, at a step edge, and two non-equivalent kink sites within the fast steps. Table 2.1 and Figure 2.9 summarize their findings. Kink specific adsorption in KAP is anisotropic due to the crystal structure. Thus, there are two unique adsorption sties, one on the +*c* side of a step, where the kink site advances in the [101] direction upon addition of a new unit, the other is on the –*c* side of a step where the kink site advances in the $[10\bar{1}]$ direction. Early signs of kink-specific adsorption due to a low concentration of impurities (intentional or unintentional) can be seen through a rounding out of the hillock morphology at the junction between the $<10\bar{1}>$ fast steps and the <100> intermediate steps.[44,45] No kink-specific adsoption on the slow steps has been observed to our knowledge. Hottenhuis *et al.* investigated many other impurities as well, such as the mono- and di-cation transition metals and the larger organic impurity of benzoic acid, all of which showed no kinetic or morphological effects in KAP.[45] The authors attribute the differences in impurity activity to the frequency at which the impurities dehydrate, with those additives that take longer to

dehydrate being stronger step inhibitors. This indicates that greater step pinning activity is a result of the ions still being partially hydrated when overgrown, rather than being bare ions. The enthalpies of dehydration for various cations can be determined via the following empirical formula given by Philips and Williams:[46]

$$\Delta H = -699\frac{z}{r_{eff}}(kJ / mol) \tag{2.13}$$

where z is the cation valency (i.e., $z = 3$ for trivalent cations) and r_{eff} is the ionic radius of the cation and anion (r_{ion} + 0.85 Å).

In other studies by Kuznetsov *et al.*, growth *promoting* effects were observed for various low concentrations of organic additives (ethylene glycol, glycerol, PEG, EDTA, benzene, acetone, and some organic acids) in KAP, while at higher concentrations the behavior turned inhibitive.[47] They demonstrated that the initial growth promoting effects are not related to a decrease in the edge free energy, which would result in an increase in growth rate. Rather, they speculated that the tendency for these organic molecules to form complexes with unintentional impurities that inhibit step kinetics (e.g. trivalent cations) helps to reduce the competition between such impurities and the K^+ ions, thus increasing the density of adatoms on the growing surface and, hence, the growth rate. However, as the additive concentration was increased, the adsorption of these molecules on the surface became the dominant competitive impurity with KAP units, thereby changing from growth promoters to growth inhibitors.

Table 2.1. *Types of impurity adsorption sites in KAP.* Impurities are to be compared to K^+, which has an ionic radius of r = 1.33 Å and a dehydration enthalpy of H = -0.321.[44,45]

Adsorption Site	Morphological Influence	Impurities	Ionic Radius	Dehydration Enthalpy ($\times 10^{-6}$ J/mol)
Terrace	Impurities uniformly inhibit step growth causing a loss of polygonal features as spirals become rounded.[48] (Figure 2.9c)	Cr^{3+}, Rh^{3+}	r_{Cr} = 0.63 Å r_{Rh} = 0.68 Å	ΔH_{Cr} = -4.37 ΔH_{Rh} = -4.11
Step Edge	Impurities impede step movement, initially causing bunching, and eventually rounding out the steps to create a more circular spiral.	Al^{3+}	r_{Al} = 0.51 Å	ΔH_{Al} = -4.75
Kink Site (+c on fast step)	Fast steps become progressively misoriented towards $[10\bar{2}]$ with increasing impurity concentration, eventually causing the corner between the $(10\bar{1})$ and $(\bar{1}0\bar{1})$ fast steps to become sharper; spiral becomes longer along the c-axis; angle of boundary between fast and slow steps becomes acute towards +c direction; slow steps unaltered. (Figure 2.9a and b)	Ce^{3+}	r_{Ce} = 1.034 Å	ΔH_{Ce} = -3.21
Kink Site (-c on fast step)	Fast steps become progressively rounded with increasing impurity	Fe^{3+}	r_{Fe} = 0.64 Å	ΔH_{Fe} = -4.22

Table 2.1 - continued

	concentration, eventually causing the corner between the $(10\bar{1})$ and $(\bar{1}0\bar{1})$ fast steps to disappear; spiral becomes shorter along the c-axis; angle of boundary between fast and slow steps flattens out; slow steps unaltered. (Figure 2.9a and d)			

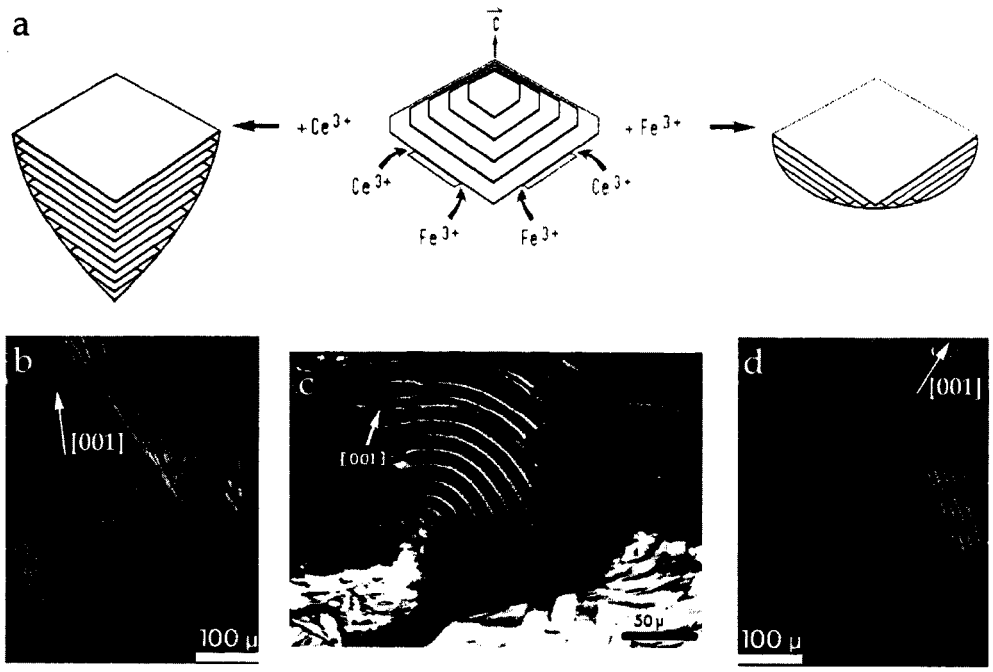

Figure 2.9. *Trivalent cations in KAP hillocks.* a) Schematic of anisotropic kink adsorption of Ce^{3+} and Fe^{3+} into +*c* and -*c* kink sites, respectively, on the fast steps of KAP hillocks and the morphological changes that result. b) Spiral morphology changes to KAP hillocks after the addition of 500 ppm of $CeCl_3 \bullet 6H_2O$. c) Loss of polygonal morphology to KAP hillocks after the addition of a terrace adsorbing impurity, $CrCl_3 \bullet 6H_2O$ at 16 ppm. d) Spiral morphology changes to KAP hillocks after the addition of 500 ppm of $FeCl_3 \bullet 6H_2O$. [Images taken by Hottenhuis, *et al.* and reproduced from Refs. 44 and 45].

2.4 Dyes Used to Label KAP Hillocks

As discussed in Sections 2.2.1 and 2.2.2, KAP orients and overgrows a remarkably wide variety of organic dye molecules into most major growth sectors, displaying both inter- and intra-sectoral zoning.[22] The behaviors of these various dyes in KAP are equally wide in range: some show strong habit modification while others show none, some repeatably go into only one growth sector while others go into many, of those that recognize the hillock slopes some have significant influence on spiral morphololgy whereas others have little to none. The differences lie primarily in the specificity of the host-guest chemical interactions upon adsorption, but as yet there is no straight forward set of rules that can be applied to these mixed crystal systems to predict how a particular guest molecule will influence the growing crystal. Despite the lack of a theoretical model to explain the dye-crystal interactions, the fact that the dyes selectively recognize specific growing faces and steps during growth from solution can be exploited as a tool for probing the formation and evolution of hillocks.

One of the first questions that may come to mind in using such an approach is, could the dye molecules act as sources for nucleating new dislocations? It was stated in Chapter 1 that to the best of our knowledge there is no evidence for molecular-sized impurities nucleating new dislocations. This is supported by the fact that even a conservative estimate of the total number of intrasectorally zoned dye molecules is on order of 10^{15} molecules present in a typical dyed KAP crystal. The number of hillocks, on the other hand, can reach the hundreds (in extreme cases) throughout the (010) face, but by no means does this compare to the number of dye molecules overgrown. Furthermore the hillock densities of

dyed KAP and pure KAP in the (010) sector are roughly the same, as observed by DIC.

There are 100's of dyes that display intrasectoral zoning within KAP hillocks, the large majority of them preferentially binding to the fast steps. Of these, three dyes were selected for this research based on the following criteria:

- Ease of incorporation into the fast slopes
- Minimal to no observable effects on hillock morphology at typical dye concentrations (10^{-6} – 10^{-5} M)
- High fluorescence intensity upon excitation by the available laser wavelengths used for confocal luminescence imaging (see Section 2.6)
- The need for two dyes with distinctly different emission peaks for distinguishing between seed and daughter hillock growth, i.e. one dye with say red fluorescence for the seed, and another dye for the daughter that fluoresces in the yellow-green region of the spectrum.

Those three dyes are light green SF yellowish (**1** or "LGSFY"), erioglaucine (**2** or "Erio"), both of which are of the triphenylmethane family of dyes, and a red xanthene dye called 2′,7′-dichlorofluorescein (**3** or "DCF"). A summary of the various characteristics of these dyes is given in Table 2.2.

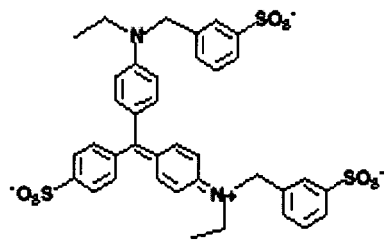

1
light green SF yellowish

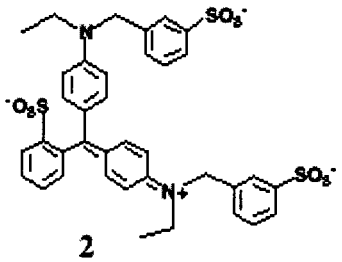

2
erioglaucine

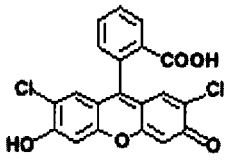

3
2',7'-dichlorofluorescein

Table 2.2. *Dye characteristics.*[49]

	LGSFY (1)	Erio (2)	DCF (3)
Mol. Formula	$C_{37}H_{34}N_2Na_2O_9S_3$	$C_{37}H_{34}N_2Na_2O_9S_3$	$C_{20}H_{10}Cl_2O_5$
Formula Weight	792.86 g/mol	792.86 g/mol	401.20 g/mol
Absorption λ_{max}	630 nm in water	625 nm in water	509 nm in ethanol + 1 drop 1N NaOH
Emission peaks in KAP crystals	655 nm	651 nm	530 nm
Good excitation wavelengths	400-455 nm, 565-640 nm	375-425 nm, 540-655 nm	440-520 nm
Appearance in powder form	deep purple	purple	light orange
Appearance in KAP	green	blue	clear with yellowish tint
Solubility	100 mg/ml in H_2O 100 mg/ml in EGME† 2 mg/ml in EtOH	30 mg/ml in H_2O 20 mg/ml in EGME† 3 mg/ml in EtOH	< 0.1 mg/ml in H_2O 80 mg/ml in EGME† 30 mg/ml in EtOH
Dye Family	Triphenylmethane	Triphenylmethane	Xanthene
Common Use	Fabric dye; printing ink; biological stain; plasma stain	Fabric dye; histology and cytology stain	Fluorescent pH indicator; limited laser dye use
Other Names	Acid Green 5	Acid Blue 9; Alphazurine FG; Brilliant Blue FCF	None

† EGME is 2-Methoxyethanol (also monomethyl ether of ethylene glycol)

2.4.1 *Triphenylmethane Dyes*

Triphenylmethane dyes tend to show an affinity for the fast slopes of the (010) KAP hillocks. Remarkably, these dyes have surprisingly little effect on the overall habit of the KAP crystal. However, in some cases even where the polyhedral volume of the whole crystal is hardly perturbed, the hillock morphology may be substantially altered by the dye, while with others of the same family there is no observable influence on hillock morphology. It is by no means obvious that such closely related compounds would have such distinct effects on the color and morphology of KAP crystals. Two closely related dyes of this family are light green SF Yellowish (**1**) [Colour Index #42095] and erioglaucine (**2**) [Colour Index #42090]. At typical dye concentrations (10^{-6} - 10^{-5} M) neither of them have any observable effect on the hillock morphology, as evidenced by DIC. It is only when dye concentration is increased by orders of magnitude (10^{-4} M and higher) that any significant morphological effects are observable. The only chemical difference between these two dyes is the location of the sulfonate in the third phenyl ring, where **1** has a *para* substition and **2** has an *ortho* substitution, as can be seen in the structure diagrams above.

Light green SF yellowish

The dyed regions of KAP/**1** crystals appear green in white light and emit in the red upon excitation (Figure 2.10). There is 1 dye molecule per 130,000 KAP molecules in whole crystals dyed at 10^{-5} M solution concentration.[50] The molar extinction coefficient of **1** in water or KAP solution is about 4.4×10^4 L mol^{-1} cm^{-1} at 635 nm. Absorption spectra show peaks at 425 nm and 633 nm in pure water, at 428 nm and 638 nm in aqueous KAP solution, and at 432 nm and 643 nm in KAP crystals, indicating a slight red-shift in absorbance due to the interactions

between the dye and crystal host (Figure 2.11). The fluorescence spectra in Figure 2.12 show that good excitation can be acheived with wavelengths ranging from 400-455nm and from 565-640nm, with emission at 655 nm for all excitations. The linear dichroism (LD) is slight but greater anisotropy can be seen in the fast slopes that contain most of the dye (Figure 2.13). The LD increases slightly, with the average dipole transition moment orientation aligning closer to the *a*-axis, for greater dye concentrations, ranging from about 42° to 39° from the *a*-axis (Figure 2.14). LD images were made by the rotating polarizer method in conjunction with a CCD camera[51] and the bulk ensemble orientations of the dye were identified using polarized absorption spectroscopy (see Section 2.5.1.2).

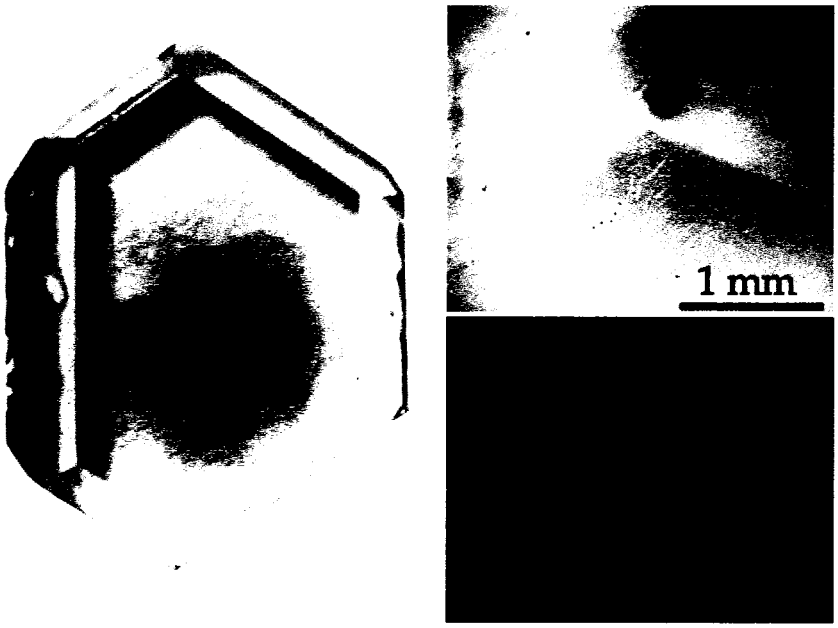

Figure 2.10. *KAP crystal and hillocks dyed with LGSFY (1) at 10^{-5} M concentration.* (a) Whole crystal image under white light. Crystal dimensions are 0.7 cm x 1.0 cm. (b) DIC image of crystal surface showing the correspondence between dye and hillock fast slope. (c) Fluorescence image of same hillocks as shown in (b).

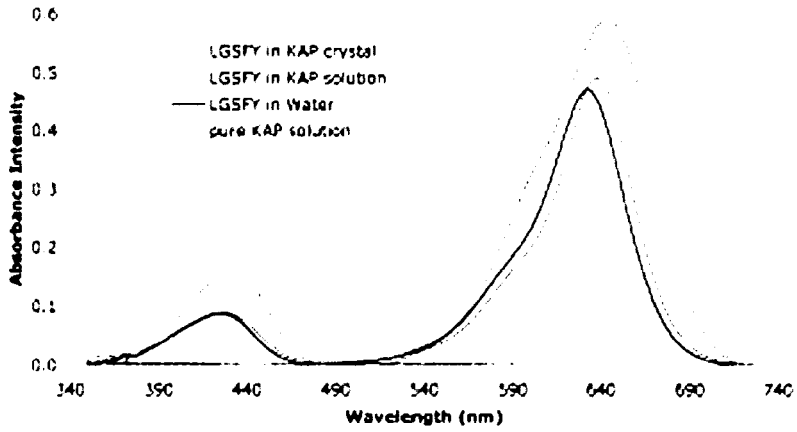

Figure 2.11. *Absorbance spectra for 1.* Slight spectral shifts occur from the dye interaction with KAP. Absorbance peaks are at 425 nm and 633 nm in pure water, at 428 nm and 638 nm in aqueous KAP solution, and at 432 nm and 643 nm in KAP crystals (10^{-5} M dye concentration in solution).

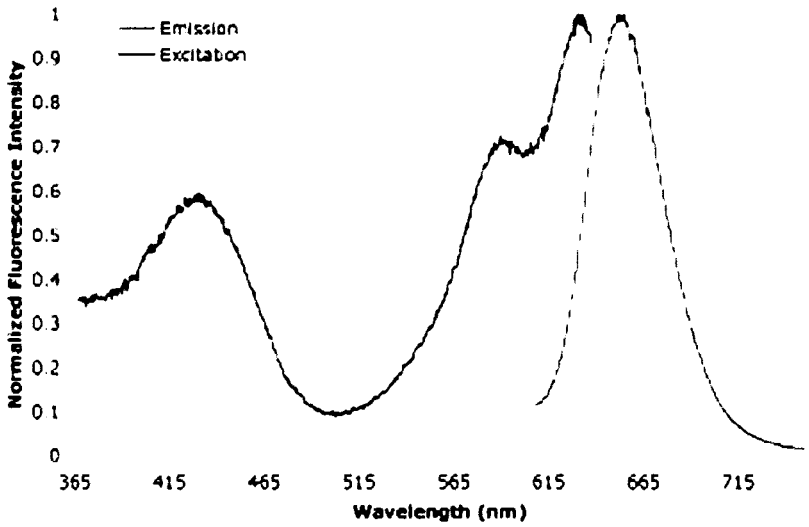

Figure 2.12. *Normalized fluorescence spectra for 1 in KAP crystals.* Emission peak at 655 nm for excitation wavelength of 592 nm (10^{-5} M dye concentration).

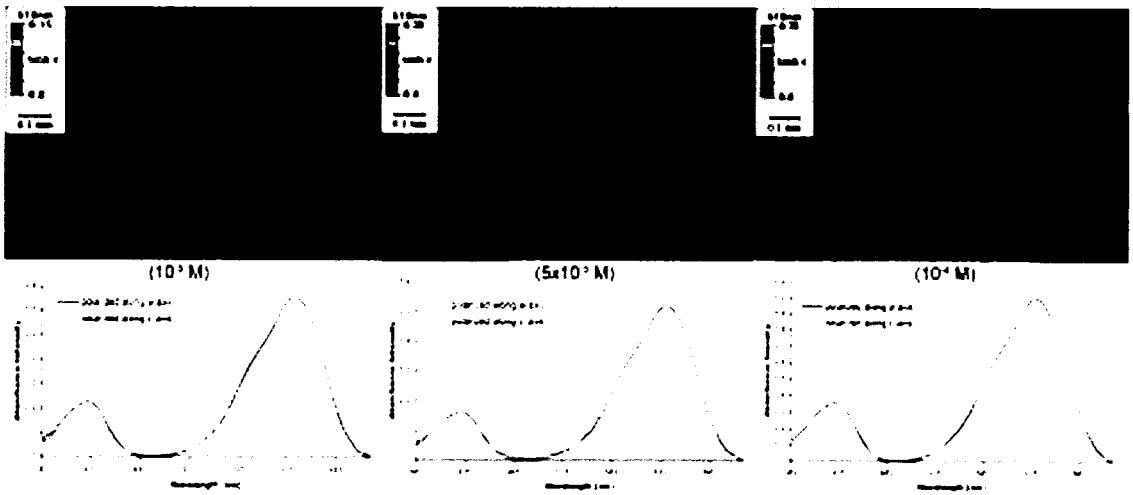

Figure 2.13. *Linear dichroism of 1 in KAP hillock fast slope at varying concentration.* Top row images taken with MetriPol at 610 nm.[51] The parameter $\tanh \varepsilon = (T_{\perp} - T_{\parallel})/(T_{\perp} + T_{\parallel})$, where $T_{\perp}$ and $T_{\parallel}$ are the transmission components for orthogonal orientations. Second row shows polarized absorption anisotropy taken with a spectral absorbance microscope. Absorption maxima are around λ = 640 nm for polarization along the *a*-axis and at λ = 635 nm for polarization along the *c*-axis. Average dipole transition moment orientations move progressively closer to the *a*-axis with increasing dye concentration, as shown in Figure 2.14).

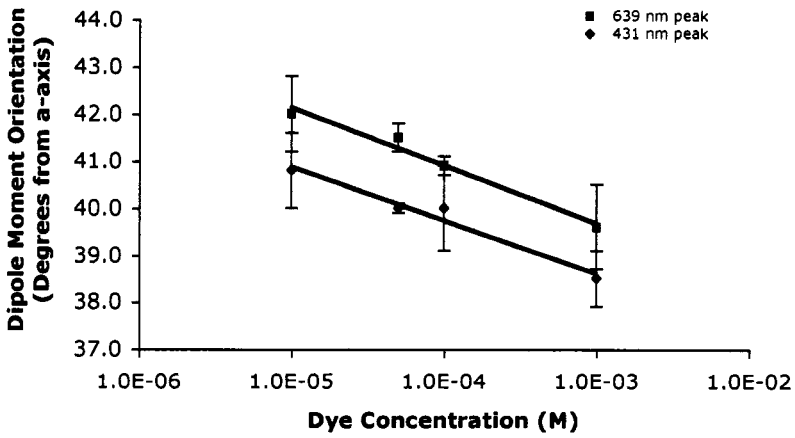

Figure 2.14. *Average dipole transition moment orientation of 1 in KAP at varying dye concentration.* Orientation shifts towards the *a*-axis as dye concentration is increased. Error bars obtained from the standard deviation of multiple measurements.

Erioglaucine

The dyed regions of KAP/**2** crystals appear blue in white light and emit in the red upon excitation at 575 nm (Figure 2.15). There is 1 dye molecule per 600,000 KAP molecules in whole crystals dyed at 10^{-5} M solution concentration.[50] The molar extinction coefficient of **2** in KAP solution is about 7.1×10^4 L mol^{-1} cm^{-1} at 633 nm. Absorption spectra show peaks at 407 nm and 629 nm in pure water, at 408 nm and 632 nm in aqueous KAP solution, and at 413 nm and 639 nm in KAP crystals, again indicating a slight red-shift in absorbance due to the interactions between the dye and crystal host (Figure 2.16). The fluorescence spectra in Figure 2.17 show that good excitation can be acheived with wavelengths ranging from 375-425 nm and from 540-650 nm, with emission at 651 nm for all excitations. The linear dichroism is *very* slight but again there is a greater anisotropy in the fast slopes that contain most of the dye (Figure 2.18). Average transition moment orientations stay close to 43° from the *a*-axis for all concentrations at the 639 nm absorbance peak, but the dye population with a peak at 414 nm varies in orientation as concentration is increased, as shown in Figure 2.19. LD measurements were imaged by the rotating polarizer method in conjunction with a CCD camera[51] and the bulk ensemble dipole transition moment orientations were identified using polarized absorption spectroscopy (see Section 2.5.1.2).

Miki Kurimoto, a previous graduate student of the Kahr research labs, in collaboration with DeYoreo *et al.* of Laurence Livermore National Labs showed via AFM studies of KAP crystals dyed with **2** that no changes to the overall hillock shape result from the presence of the dye (10^{-6}–10^{-5} M), however they did see some step roughening and a slight change in step kinetics due to kink blocking.[52] Kink blocking occurs when impurities adsorb into kink sites and halt their propagation. This reduces the kink density and therefore the kinetic

coefficient, slowing down the growth. The solution solubility is not influenced by this phenomenon, however, and steps can continue to grow around the impurity without any interuption or *dead-zone* in the overall crystal growth.[52]

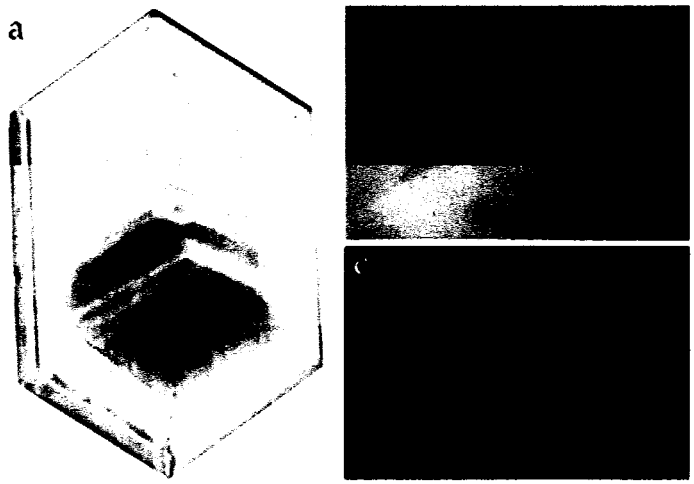

Figure 2.15. *KAP crystal and hillocks dyed with erioglaucine (2) at 10^{-5} M concentration.* (a) Whole crystal image under white light. Crystal dimensions are 1.2 cm x 1.8 cm. (b) DIC image of crystal surface showing the correspondence between dye and hillock fast slope. (c) Fluorescence image of same hillocks as shown in (b).

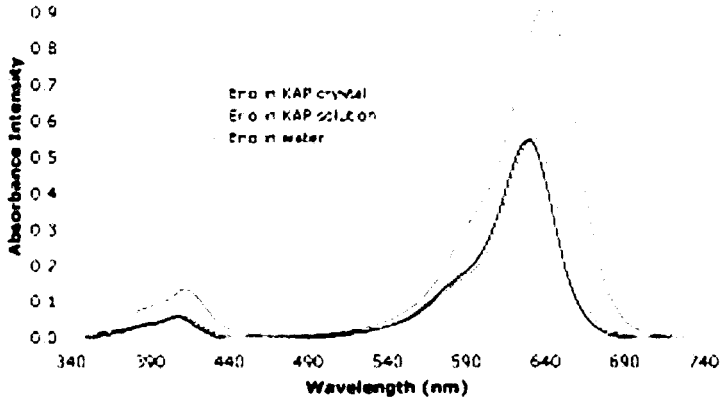

Figure 2.16. *Absorbance spectra for* 2. Slight spectral shifts occur from the dye interaction with KAP. Absorbance peaks are at 407 nm and 629 nm in pure water, at 408 nm and 632 nm in aqueous KAP solution, and at 413 nm and 639 nm in KAP crystals (10^{-5} M dye concentration in solution).

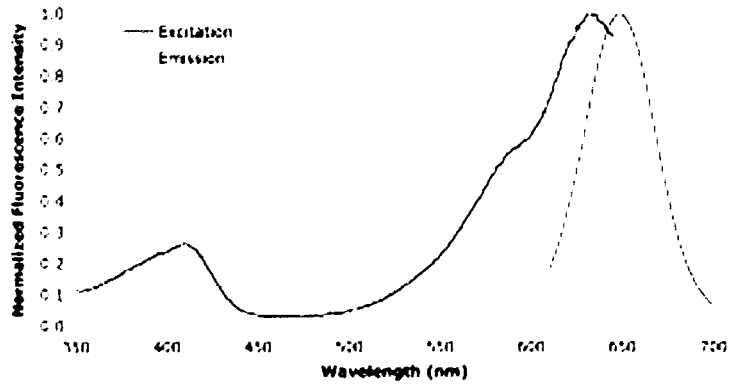

Figure 2.17. *Normalized fluorescence spectra for* 2 *in KAP crystal.* Emission peak at 651 nm for excitation wavelength of 590 nm (5×10^{-5} M dye concentration).

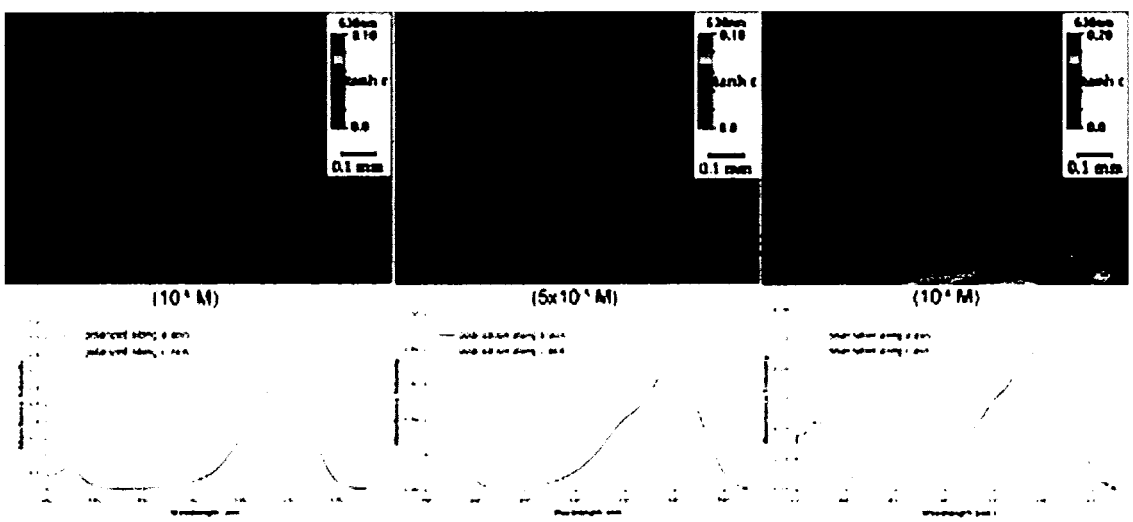

Figure 2.18. *Linear dichroism of* 2 *in KAP hillock fast slope at varying concentration.* Top row images taken with MetriPol at 630 nm.[51] The parameter $\tanh \varepsilon = (T_{\perp} - T_{\parallel})/(T_{\perp} + T_{\parallel})$, where $T_{\perp}$ and $T_{\parallel}$ are the transmission components for orthogonal orientations. Second row shows polarized absorption anisotropy taken with a spectral absorbance microscope. Absorption maxima are around $\lambda = 639$ nm for both polarizations. Average ensemble transition dipole moment orientations stays close to the 43° from the *a*-axis for all concentrations at the 639 nm peak, but vary for the smaller peak at 414 nm, as shown in Figure 2.19. [Note, differences seen in the

images above are partly due to KAP's birefringence, which is corrected for in determining the dipole transition moment orientations, as well as the more heavily dyed crystals absorbing more light.]

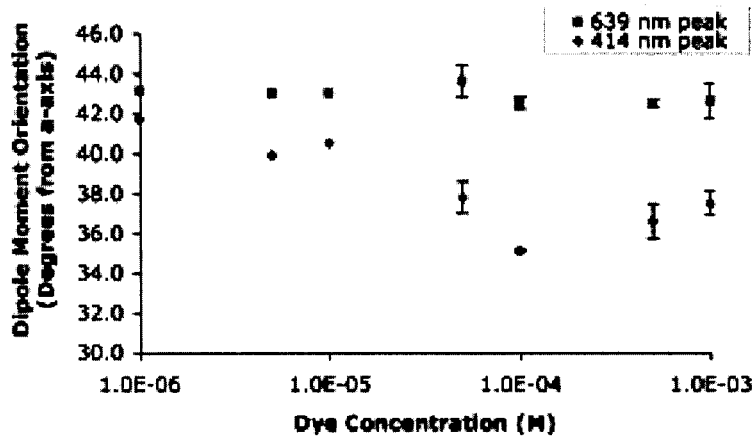

Figure 2.19. *Average dipole transition moment orientation of* **2** *in KAP at varying dye concentration.* Orientation stays close to the 43° from the *a*-axis for all concentrations at the 639 nm peak, but vary for the smaller peak at 414 nm. Higher dye concentrations lead to morphological changes to the hillocks and may also lead to dye aggregation, causing variations in orientation. Error bars obtained from the standard deviation of multiple measurements.

2.4.2 *2′,7′-Dichlorofluorescein*

2′,7′-Dichlorofluorescein (DCF, **3**) was selected for labeling hillocks during growth of crystals from seeds because it fluoresces brightly and is readily overgrown by KAP. This allows us to either use a much lower dye concentration or a reduced growth time for daughter crystals. There is 1 dye molecule per 20,000 KAP molecules in whole crystals dyed from a starting solution concentration of 10^{-4} M (it was difficult to obtain the dye:KAP ratio for lower concentrations due to weak absorbance).[50] The molar extinction coefficient of **3** in KAP solution (pH = 4.5) is about 1.8×10^4 L mol^{-1} cm^{-1} at 498 nm.

Absorption spectra show key peaks at 490 nm and 519 nm in pure ethanol, at 470 nm and 498 nm in aqueous KAP solution, and at 472 nm and 502 nm in KAP crystals (ε_{seg} = 0.0047), again indicating a slight shift in absorbance due to the interactions between the dye and crystal host (Figure 2.21). The fluorescence spectra in Figure 2.22 show that good excitation can be acheived with wavelengths ranging from 440-520 nm, with emission at 530 nm for all excitations. The linear dichroism is more pronounced in **3** than it was in dyes **1** and **2**, with greater anisotropy again in the fast slopes that contain most of the dye (Figure 2.18). Average orientation of the transition dipole moment in heavily-dyed ($\geq 10^{-5}$ M) KAP/**3** crystals is closer to the *c*-axis, ranging from 47-56° from [100] at both the 473 nm and 502 nm absorbance peaks, with the transition dipole moment of the 502 nm absorbing species being oriented slightly closer to *c*, as shown in Figure 2.19. LD measurements were imaged by the rotating polarizer method in conjunction with a CCD camera[51] and the bulk ensemble dipole transition moment orientations were identified using polarized absorption spectroscopy (see Section 2.5.1.2).

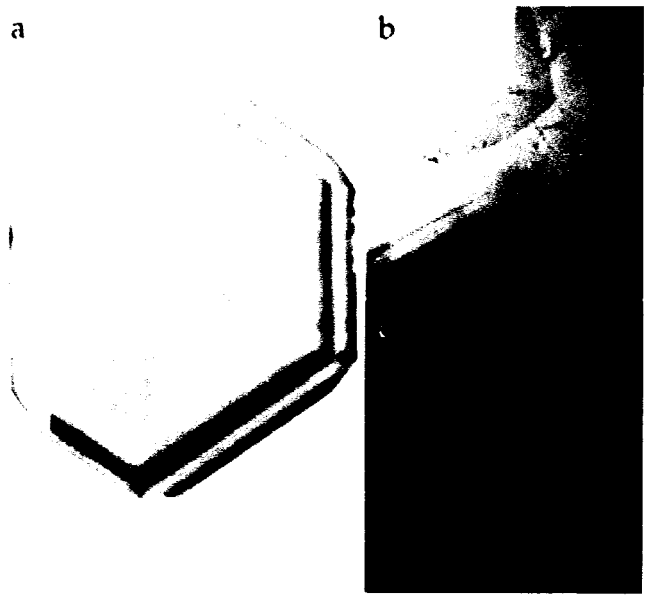

Figure 2.20. *KAP crystal and hillocks dyed with DCF (3) at 5×10^{-5} M concentration.* (a) Whole crystal image under white light. Crystal dimensions are 0.8 cm x 1.1 cm. (b) DIC image of crystal surface showing hillocks. (c) Fluorescence image of same hillocks as shown in (b), displaying the correspondence of dye and hillock fast slopes.

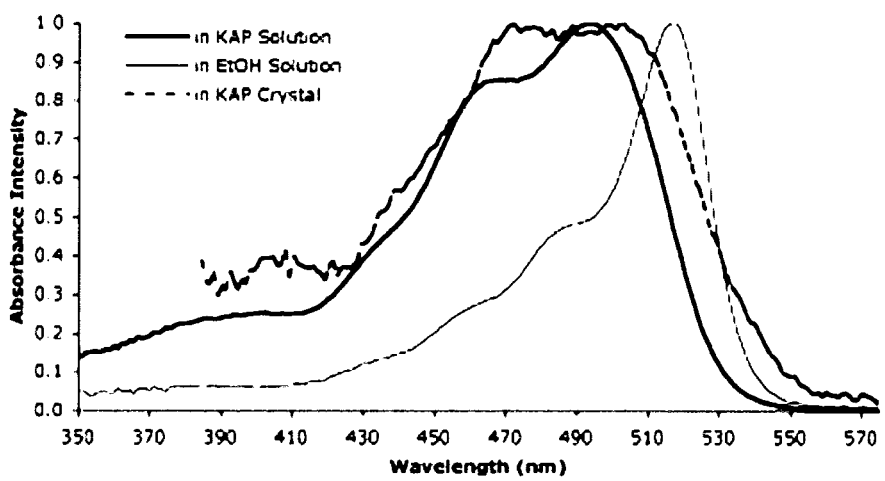

Figure 2.21. *Normalized absorbance spectra for 3.* Significant spectral shifts occur from the dye interaction with KAP, partly due to pH changes. Key absorbance peaks are at 490 nm and 519 nm in pure ethanol, at 470 nm and 498 nm in aqueous KAP solution, and at 472 nm and 502 nm in KAP crystals. (5×10^{-5} M dye concentration in solution).

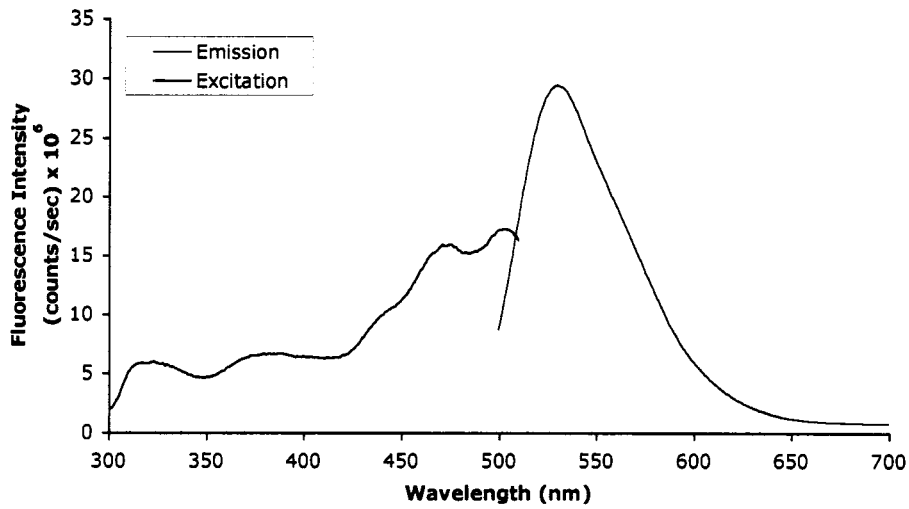

Figure 2.22. *Fluorescence spectra for 3 in KAP crystals.* Emission peak at 530 nm for excitation wavelength of 470 nm (5×10^{-5} M dye concentration).

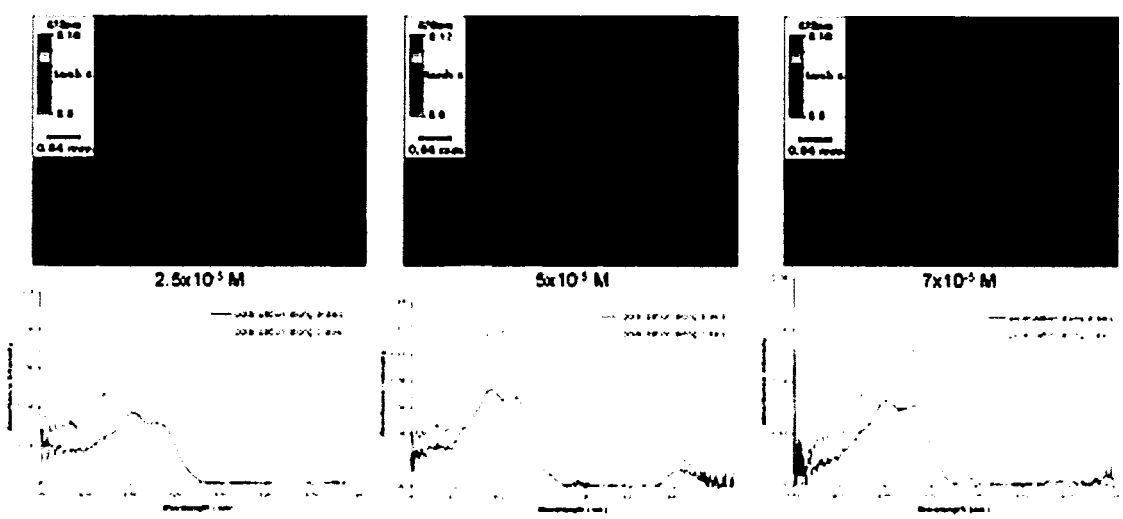

Figure 2.23. *Linear dichroism of 3 in KAP hillock fast slope at varying concentration.* Top row images taken with MetriPol at 470 nm.[51] The parameter $\tanh \varepsilon = (T_{\perp} - T_{\parallel})/(T_{\perp} + T_{\parallel})$, where $T_{\perp}$ and $T_{\parallel}$ are the transmission components for orthogonal orientations. Second row shows polarized absorption anisotropy taken with a spectral absorbance microscope. Absorption maxima are around λ = 473 nm and 503 nm for both polarizations. Average ensemble transition dipole moments are consistently closer to the *c*-axis at these heavily dyed concentrations, as shown in Figure 2.24.

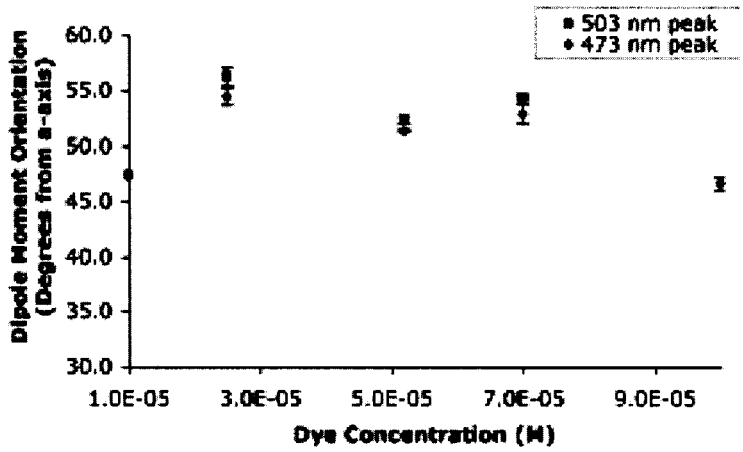

Figure 2.24. *Average dipole transition moment orientation of 3 in KAP at varying dye concentration.* Orientation is consistently closer to the *c*-axis for all dye concentrations shown. Error bars obtained from the standard deviation of multiple measurements.

Dye **3** is a diprotic acid subject to protonation in acidic solutions. It has been used as a fluorescent pH indicator with its transition interval ranging from weak yellow-green at pH 4.0 to bright yellow-green at pH 6.0.[49] Figure 2.25 shows the most likely path of protolytic conversions for **3** in water, where $pK_{a1} = 4.00 \pm 0.10$ and $pK_{a2} = 5.19 \pm 0.06$.[53] There is a second form that the mono-anion (Figure 2.25b) can take, where the hydrogen atom is removed from the phenolate rather than the carboxylic group, however COOH is much more easily de-protonated than OH (ie, the $pK_{a1,OH} > pK_{a1,COOH}$). Thus, in a water-based buffer solution such as KAP, with a pH around 4.2, it is unlikely that the second mono-anion form will be significant. (Throughout, an equilibrium mixture of the dye is hereafter referred to as DCF, while the neutral, mono-anionic, and di-anionic species are referred to separately as DCFH, DCF^-, and DCF^{2-}, respectively.)

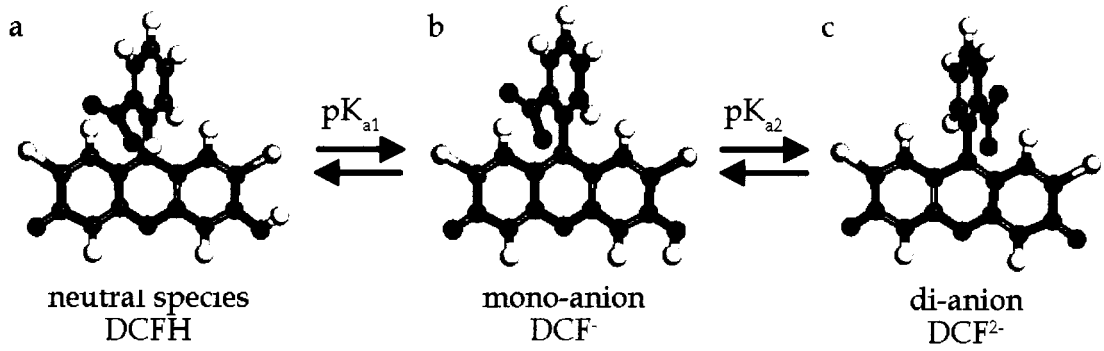

Figure 2.25. *Equilibria of 3.* Structure coordinates calculated for optimized geometry using Accelrys MS Modeling (see Section 2.5.2).

The species populations of **3** in KAP solution can be estimated by first determining the solution pH with the following formula:[54]

$$pH = -\log([H+]) = -\log\left(\sqrt{\frac{K_1K_2F + K_1K_w}{K_1 + F}}\right) \approx \frac{1}{2}(pK_1 + pK_2) \tag{2.14}$$

where F is the mole concentration of KAP, $K_1 = 1.12\times10^{-3}$, and $K_2 = 3.89\times10^{-6}$ are the ionization constants of phthalic acid, $K_w = 1\times10^{-14}$ at 25°C, and $pK_i = -\log(K_i)$ for $i = 1, 2$.[53,55] A supersaturated solution concentration of 127 g/L of KAP in water gives $F = 0.622$ mol/L (KAP formula weight = 204.23 g/mol). This results in a KAP pH = 4.18. Next, this pH is used along with the standard acid/base fractional composition equations[54] and the pK_a values reported in literature for DCF in water[53] to arrive at the following estimated population percentages in solution: 37.6% of the neutral species, 57.0% of the mono-anion species, 5.4% of the di-anion species, and negligible cationic species present.

Figure 2.26 shows absorbance spectra comparisons for **3** in ethanol solution and in KAP solution at diferent pH values. The ethanol/**3** solutions (Figure 2.26a and b) show three unique spectral profiles, one at very acidic pH = 0.47 with an absorbance maximum at 458 nm and a shoulder at 488 nm; a second one at basic

pH values ranging from 7.8-12.0 with an absorbance maximum at 511 nm and shoulder at 488 nm; a third intermediate spectral profile at pH = 4.52 with an absorbance peak at 519 nm and smaller peaks at 488 nm and 466 nm. The KAP/**3** solutions (Figure 2.26candd) show only two spectral profiles, one with spectral peaks at 493 nm and 466 nm for $3.3 \leq pH < 3.8$, and the other with a peak at 503 nm and 473 nm shoulder for $pH > 5$. Measurements below a pH of 3.3 could not be obtained for KAP solution because it would convert into phthalic acid and 'crash-out' of solution (phthalic acid's formula is C_6H_4-1,2-$(COOH)_2$ and it is not very soluble in water). These results are summarized in Table 2.3 and compared with data given in the literature for **3** in water.

The typical supersaturated KAP solution pH ranges from 3.7 - 4.5 (as measured by pH meter). In KAP/**3** crystals two absorbance peaks appear with approximately equal intensity, one at 472 nm (corresponding to the neutral form of the dye, DCFH) and the other at 502 nm (corresponding to the mono-anionic form of the dye, DCF^-). This red-shift from the peak values in a typical KAP solution could be due to the crystal pH being more basic, or it could be due to geometric stabilization of the dye and its interactions with the local environment in the crystal latice. It is common for the spectral profile of a dye to shift when it is fixed within a condensed medium such as a crystal, as was also seen for dyes **1** and **2**, so there is not enough evidence to attribute these shifts in **3**'s spectral profiles to a change in pH from solution to crystallization. Specific interactions of the KAP/**3** mixed crystal system will be detailed further in Chapter 3.

Table 2.3. *2′,7′-Dichlorofluorescein (3) species pK_a values, populations in KAP solution, and absorption peaks.*[49]

	Neutral, H_2A	Mono-anion, HA^-	Di-anion, A^{2-}
Polyprotic Conversions	$H_3A^+ \rightleftharpoons H_2A + H^+$	$H_2A \rightleftharpoons HA^- + H^+$	$HA^- \rightleftharpoons A^{2-} + H^+$
pK_a in Water[53]	0.35	4.00	5.19
Population in KAP Solution	37.6%	57.0%	5.4%
λ_{max} in Water[53]	460 nm, 485 nm	465-470 nm, 490 nm	502 nm
λ_{max} in Ethanol	458 nm, 488 nm	488 nm, 519 nm	511 nm
λ_{max} in KAP Solution	466 nm	493 nm	503 nm
λ_{max} in KAP Crystals	472 nm	502 nm	-

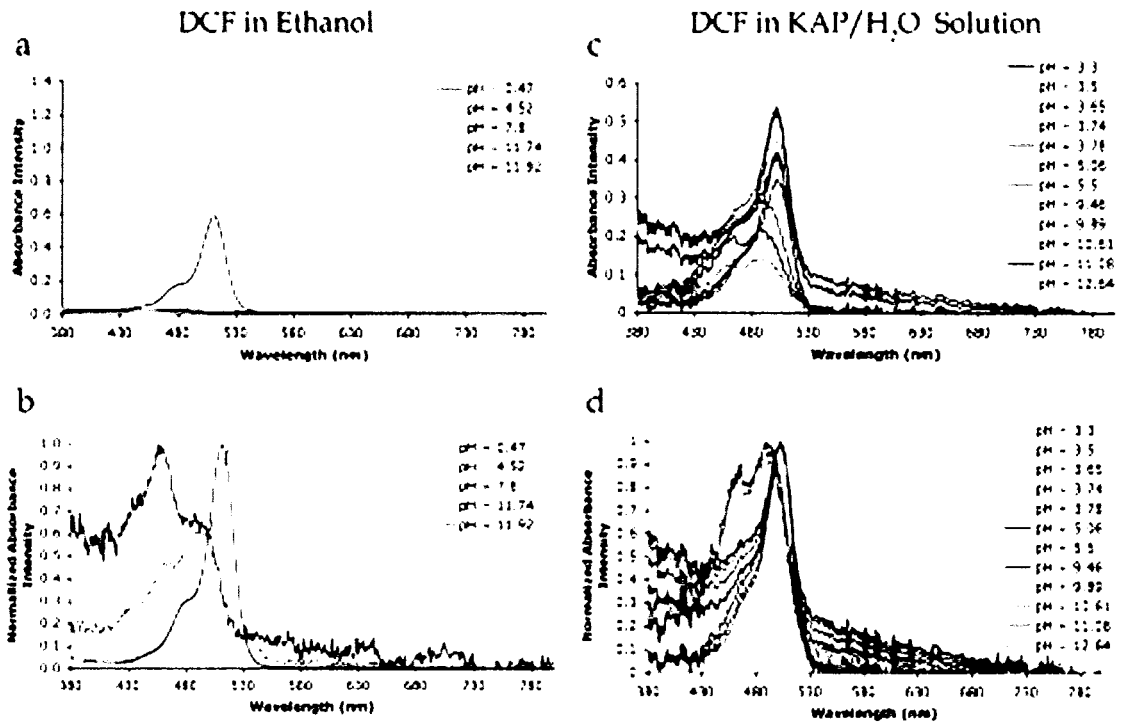

Figure 2.26. *Absorption spectra for 3 at different pH values (~10^{-5} M).* (a) DCF absorbance in ethanol solution shows decrease in intensity with decreasing pH. (b) Same as spectra shown in (a) but normalized for easier identification of peak positions. Three spectral profiles are observed, one at very acidic pH with an absorbance maximum at 458 nm and a shoulder at 488 nm; a spectral profile at basic pH with an absorbance maximum at 511 nm and shoulder at 488 nm; and an intermediate (pink) spectrum at mid-range pH with an absorbance peak at 519 nm and smaller peaks at 488 nm and 466 nm. (c and d) same thing for DCF in KAP solution. In this case only two spectral profiles were observed, one with peaks at 493 nm and 466 nm for $3.3 \leq pH < 3.8$, and the other with a peak at 503 nm for $pH > 5$. Below a pH of 3.3, KAP turns into phthalic acid and 'crash-out' of solution. The typical saturated KAP solution pH is in the range of 3.7 – 3.8. pH values are according to measurements taken in KAP solution with a pH meter.

2.5 Methods for Identifying Dye-Crystal Interactions

2.5.1 *Spectroscopy*

Various spectroscopic techniques and instruments are employed in our lab to probe dye-crystal interactions. This section describes the methods used to obtain the mole concentrations, spectra, and orientations of the various dyes reported in Section 2.4.

2.5.1.1 *Beer's Law*

The actual amount of dye that becomes overgrown within the crystal can be determined using the Beer's Law relationship between the absorbance, A, of a material and the concentration, c, of the light-absorbing species within that material:[54]

(2.15) $$A = \varepsilon l c$$

where l is the pathlength traveled by the light, and ε is known as the molar absorptivity or extinction coefficient with units of L/(mol·cm). Absorbance is defined as the negative log of the transmittance, T:[54]

(2.16) $$A = -\log T = \log_{10}\left(\frac{P_0}{P}\right)$$

where P_0 is the radiant power of incident light upon a sample, and P is the radiant power of emergent light that passed through the sample of thickness l. In these equations A, T, P, and ε are wavelength and chromophore dependent, and they can also be influenced by solvent.

The molar absorptivities of a dyes in KAP solution were determined experimentally by taking several absorption spectra of aqueous KAP solution samples at various known dye concentrations in cuvettes of known pathlength. The results were ploted as the absorbance maximum divided by the pathlength, $A(\lambda_{max})/l$, versus the dye concentration, c. According to Beer's Law this should give a linear relationship where the slope of the line is the molar absorptivity (see for example Figure 2.27). An SI Potonics model 440 UV/Vis spectrophotometer with a cuvette sampling bench was used to take absorption spectra of solutions. A "blank" was taken with pure water for background subtraction, and spectra were measured in the wavelength range 350-800 nm, for which pure KAP solution is non-absorbing.

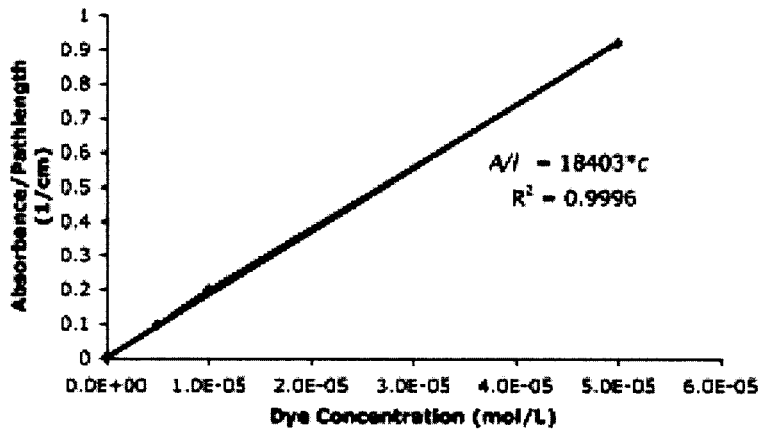

Figure 2.27. *Beer's law plot of* **3** *in aqueous KAP solution.* The slope of the line fit to the data gives molar absorptivity. R^2 value indicates the goodness of fit. Absorbance values measured at λ_{max} = 498 nm.

Once the molar absorptivity was obtained for the dyes in KAP solution, dyed single crystals were weighed and dissolved into small known volumes of pure water (typically 0.8-1.5 mL of water depending on the crystal mass)[50], and absorption spectra obtained. A sonicator helped dissolve crystals more rapidly. Applying Beer's Law was once more determines the dye concentration at the

absorption maximum for each dissolved crystal spectrum, as well as the respective molar absorptivity. The ratio of dye molecules to KAP molecules in each crystal was determined based on the crystal weight, the molecular formula weights, the dye concentration, and Avogadro's number. We repeated this procedure for several crystals grown from a particular starting concentration of dye in solution, and averaged the results to arrive at the reported values. The moles of dye included in the crystal divided by the moles of dye in the starting solution gives the segregation coefficient. When considering the amount of dye included in KAP hillocks, it is important to note that the results will vary based on the number and lifetime of growth active hillocks in a given crystal. These results also vary depending on the starting dye concentration in growth solution.

2.5.1.2 *Dipole Transition Moment*

The relative orientation of a chromophore's dipole transition moment can be determined through polarized microscopy measurements (Section 2.3.3). Since light is constrained to travel along the eigenmodes of the crystal, it is only possible to directly measure the projection of polarized light. Therefore a minimum of two measurements at orthogonal polarizations are needed to determine the relative orientation of the dye, which is given by:

(2.17)
$$\theta = \arctan\left(\sqrt{\frac{a_{\parallel}}{a_{\perp}}\beta}\right)$$

where $a_{\perp}$ and $a_{\parallel}$ are the absorbances for orthogonal orientations, and β is the birefringence correction factor given by:

(2.18)
$$\beta = \frac{|E_{\parallel}|^2}{|E_{\perp}|^2}$$

where $E_{\parallel}$ and $E_{\perp}$ are given by Equations (2.7) and (2.8), respectively. For KAP, $E_{\parallel}$ and $a_{\parallel}$ are assigned to the *c*-axis, while $E_{\perp}$ and $a_{\perp}$ correspond to the *a*-axis, giving θ to be the orientation of the dipole transition moment with respect to the *a*-axis. Using the data reported in the literature[33,37] for the indicies of refraction in KAP we can extrapolate the data to arrive at the following reference table for the birefringence correction as a function of wavelength:

Table 2.4. *Wavelength-dependent indices of refraction[33,37] and birefringence corrections for KAP.*

Energy	Wavelength	$n_c = n_{\perp}$	$n_a = n_{\parallel}$	Birefringence Correction, β
3.50 eV	354 nm	1.52	1.70	0.87
3.25 eV	382 nm	1.52	1.68	0.88
3.00 eV	413 nm	1.51	1.66	0.89
2.75 eV	451 nm	1.50	1.65	0.89
2.50 eV	496 nm	1.49	1.64	0.89
2.25 eV	551 nm	1.49	1.62	0.90
2.00 eV	620 nm	1.48	1.62	0.90
1.75 eV	708 nm	1.48	1.61	0.90

Linear dichroism measurements were taken with two different instruments. We obtained polarized absorption anisotropy spectra using a SI Potonics model 440 spectrophotometer coupled to an Olympus BX50 transmission microscope via a 200 mm fiber-optic. The extinction directions of the crystals were used to orient the sample relative to the input polarization. Measurements were taken at orthogonal polarizations for three different positions on the crystal *b*-face and for multiple crystals of the same dye concentration. The orientations were determined at the absorption maxima using Equation (2.17) for each position on the crystal, and the results were averaged together to give the final reported values.

Qualitative images were obtained using Metripol, a microscope that employs a rotating polarizer method.[51] By this method the linear dichroism is displayed as the hyperbolic tangent of the parameter $\varepsilon = (a_{\perp} - a_{\parallel})/2$. This function is also proportional to the scaled differential transmission, T, of light that has been linearly polarized along the crystal eigenmodes:

$$\tanh(\varepsilon) = \frac{T_{\perp} - T_{\parallel}}{T_{\perp} + T_{\parallel}} \tag{2.19}$$

Metripol images were collected at wavelengths near the absorption maximum for the dyes, according to the filters available.

2.5.1.3 *Luminescence Spectra*

Luminescence measurements are far more sensitive than absorbance. Emission spectra should resemble a mirror image of the absorbance spectra, but shifted to a lower energy.[54] Excitation spectra closely match absorbance profiles, though they are not a true profile due to variation in detector efficiency at different wavelengths. Excitation and emission spectra were taken using a monochrometer-equipped FluoroMax-2 by Instruments S. A., Inc. The fluorimeter was controlled remotely via a computer with DM3000F Instrument Control Center software version 3.3 by Jobin Yvon - Spex. Excitation spectra were best obtained using a sample holder in the cuvette bench with the excitation light incident upon the crystal *b*-face at an angle of about 45° from the negative *a*-axis, and emission likewise collected at 90° from the incident light. Emission spectra could additionally be collected using an inverted Olympus IMT-2 microscope coupled to the fluorimeter via fiber optic cables. The microscope was

attached to a Nikon AFX-IIA shutter, and excitation light was fitered from the detection beam path using a dichroic filter block.

2.5.2 *Force-Field Calculations*

Atomic and molecular systems are governed by the laws of quantum mechanics, however in large systems such as crystals or polymers quantum calculations are computationally intensive and can often be impractical. Classical simulation techniques[56] based on molecular mechanics are commonly used to model bulk properties of large systems. Given a set of initial atomic coordinates for a structure, these simulations make use of potential energy surfaces empirically fit by forcefields that have been parameterized to a small set of models and experimental data. By applying periodic boundary conditions (for crystals), using statistical averaging, and minimizing energies over the potential energy surface, molecular simulations can predict properties like equilibrium structures, relative energies, crystal morphology, diffusion coefficients, minimum energy conformations, Young's moduli, etc.

To better understand the selectivity of dyes for the KAP (010) hillocks, force-field calculations were used to generate stable stepped and kinked surfaces. Simulations were performed using the Accelrys[57] MS Modeling program suite. Crystal habits and energetically stable (010) faces of KAP were generated with the Morphology feature and crystallographic data imported from the Cambridge Structural Database.[14] Energy minimizations and geometry optimizations were performed using Forcite with a COMPASS forcefield.[58] COMPASS was chosen because it minimized the volume of the KAP unit cell to within 94.5%, 96.2%, and

99.9% for the *a*, *b*, and *c* lattice parameters, respectively, of those established by X-ray crystallography.[14] The force-field was set to a fine quality minimizer tolerance, i.e. 4×10^{-4} kJ/mol energy convergence criteria. Graphics were generated with the MS Visualizer.

DCF (**3**) was selected as the main dye to model for docking into KAP steps, because this dye was used in parallel studies by others in the Kahr research group, providing an overlap of data, and it has fewer conformational degrees of freedom than the triphenyls. The molecular coordinates and transition dipole moment orientation of DCF were derived from crystallographic data for a fluorescein derivative[59], and optimized with Gaussian03[60] program suite using the Pople 6-31G* basis set[60]. For simplicity, the long axis of DCF's π-system was estimated to be the transition electric dipole moment, which is within 5° of the calculated vector in the ground state (Figure 2.28).[61,62] As the orientation of this dipole will undoubtedly change with DCF conformation and local environment, we took the xanthene ring long axis as the dipole orientation in all computations.

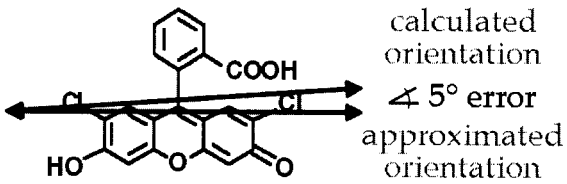

Figure 2.28. *Estimate DCF dipole transition moment orientation.* All orientations reported are from estimating the transition dipole moment to be the vector between chlorine atoms. This approximation is 5° off from that calculated using density functional theory on an optimized dye structure, as shown.[61] This difference is within the expected variance of the transition dipole moment orientation due to excited state conformational changes.

As mentioned in section 2.3.4, it has been suggested by Jetten[24] and reiterated by Hottenhuis *et al.*[44,45] that the rate-limiting step for KAP growth is the dehydration of the K^+ ions, which is relatively slow compared to the dehydration of the hydrogen phthalate ions. If this supposition is true, then the growing KAP (010) surface in solution will predominantly expose the carboxylate ends of the phthalate molecules, resulting in a negatively charged surface. Modeling of the minimum energy (010) surface in vacuum requires a neutral surface in order for it to be stable. According to Rohl *et al.*[63], the preferred surface termination is given by the cleave that results in the lowest surface energy (the energy difference between surface and bulk species, per unit surface area) and attachment energy (the energy liberated upon attaching a new layer to the surface).[64] The minimum energy (010) surface, as determined by the Morphology module, was terminated by the aromatic rings of the phthalate molecules. The preference for a C-H (010) termination was confirmed by the observation of smaller total surface (0.70 kJ/mol/Å^2) and attachment (-82 kJ/mol per unit cell) energies relative to the stable (010) surface with partial K^+ termination (surface energy = 3.11 kJ/mol/Å^2, attachment energy = (-367 kJ/mol per unit cell). Given the above arguments for a possible preference of either surface termination, both the aromatic ring terminated surface and the partial K^+/partial COO^- terminated surfaces were investigated.

Supercells with 2D periodic boundary conditions consisting of of 3 unit cells along [$\bar{1}$01], 5 unit cells along [101], and a depth of 3 unit cells in [010] were constructed and used for all simulations. This cell was created and split into two regions: region I contained surface atoms that could relax and interact with each other, while region II contained sufficient fixed atoms to reproduce the effect of the bulk properties on region I. Steps of unit-cell height were created to model the topography of the hillock surface with cuts corresponding to all possible step

orientations of (010) hillocks, namely the fast ([$\bar{1}1\bar{1}$] and [$\bar{1}0\bar{1}$]), slow ([111] and [101]), and intermediate (<100>) step directions on the (010) surface. Step cuts were made based on the lowest energy surface terminations of the {111} and {$11\bar{1}$} faces. Kink site docking was also simulated for the C-H (010) terminated surfaces. Kink sites were created in the upper half of the surface unit cell with two different configurations in the [$\bar{1}1\bar{1}$] fast step: kink sites that advance in either +*c* or -*c* fashion upon addition of a molecule. Kink locations were chosen based on the most natural docking configuration for the dye (i.e., position "A" in Figure 2.29), as indicated by the results from docking into step vacancies (discussed in Chapter 3, Section 3.4).

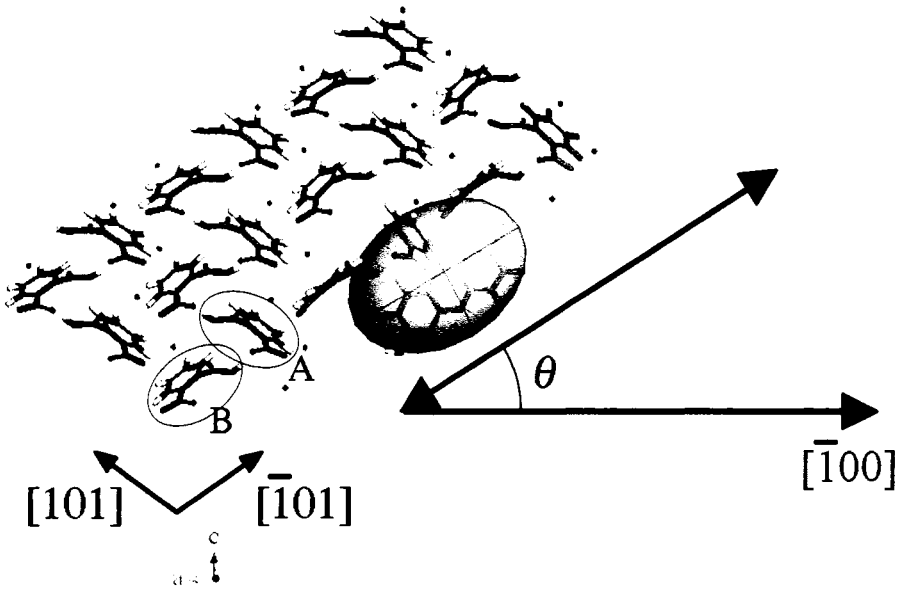

Figure 2.29. *Example docking locations for DCF into KAP (010) steps.* In position "A" the removed phthalate is oriented with its aromatic ring perpendicular to the step edge. In position "B", the aromatic ring of the phthalate is oriented parallel to the step edge. Position "A" provides a more natural docking configuration for DCF as will be discussed in Section 3.4. θ denotes the approximate transition dipole moment orientation of the dye (approximated as the vector between the chlorine atoms, as measured from the [$\bar{1}$00] or [100] directions.

The flat, stepped, or kinked surfaces were geometry optimized. For DCF$^-$ simulations, the straight or kinked step was relaxed, its energy (E_{step}) calculated, then a phthalate anion of minimized isolated energy $E_{Phthalate^-}$ was removed from the upper half of the step to create a docking site in either position "A" or "B" (Figure 2.29). Whereas in DCFH simulations, the straight or kinked step was relaxed with a full KAP unit already removed from position "A" or "B" to create the docking site, and thus $E_{step,"A"}$ and $E_{step,"B"}$ already account for the removal of a KAP unit, setting $E_{Phthalate^-} = 0$. In all other respects, the final KAP surfaces are the same. Table 2.5 lists the values for the initial parameters used in determining the reaction energies for docking into the fast steps, according to Equation (2.20). Note that $E_{step,"A"}$ and $E_{step,"B"}$ are both greater (less negative) than $E_{step} + E_{KAP}$, indicating that it takes work to remove a KAP unit from the step.

Next, the entire lattice was constrained, the dye was inserted ~5-20 Å from the docking sites, and the minimum energy configuration for the docked additive was calculated. In the case of kink-site docking, all neighboring KAP units surrounding the kink were also allowed to relax during optimization. After optimization, the resulting lattice was unconstrained and the final total energy calculated. Rohl and colleagues have demonstrated the validity and usefulness of the following type of formula for calculating the relative reaction energy of replacing a crystal unit with a dye molecule:[64]

$$E_{reaction} = E_f - E_i = \left(E_{step+dye} + E_{Phthalate^-}\right)_f - \left(E_{step} + E_{dye}\right)_i \tag{2.20}$$

Table 2.5. *Calculated energies for DCF⁻ and DCFH docking simulations into KAP (010) steps.* E_{step} values are averaged between the $[\bar{1}1\bar{1}]$ and $[\bar{1}0\bar{1}]$ fast steps for the straight steps, and between the +*c* and −*c* kink sites for the kinked steps. The uncertainties reported are the corresponding standard deviation of the mean.

Structure	For DCF⁻ Docking (kJ/mol)	For DCFH Docking (kJ/mol)
Straight Step (010) Supercell partial K⁺ termination	E_{step} = -284,041 ± 316	$E_{step,"A"}$ = -282,868 ± 325 $E_{step,"B"}$ = -282,875 ± 328
Straight Steps (010) Supercell C-H termination	E_{step} = -285,826 ± 1	$E_{step,"A"}$ = -284,665 ± 6 $E_{step,"B"}$ = -284,586 ± 17
Kinked Fast Step (010) Supercell C-H termination	E_{step} = -283,756 ± 2	E_{step} = -282,760 ± 1
Straight [100] Steps (010) Supercell C-H termination	$E_{step,"CO^{2-}"}$ = -186,728 $E_{step,"COOH"}$ = -186,550	$E_{step,"CO^{2-}"}$ = -185,595 $E_{step,"COOH"}$ = -185,480
Isolated KAP Unit	$E_{Phthalate^-}$ = -194	N/A → $E_{Phthalate^-}$ = 0
Isolated Dye Molecule	E_{dye} = -258	E_{dye} = -303

Many different combinations of flat, stepped, and kinked surfaces and docking sites were simulated, and the relative energies calculated to gain insight into the most likely docking locations and transition dipole moment orientations of DCF in KAP hillocks. Modeling results are reported in Chapter 3, Section 3.4. In considering the resulting reaction energies, it is important to keep in mind that all calculations were performed for vacuum conditions, not solvated. Therefore, the energies reported are not absolute, and they merely serve for making comparisons between simulations performed under similar conditions. It is expected that inclusion of solvation energies will result in less exothermic reaction energies. The solvent environment and partial hydration of the dye may

influence docking orientations, however, DCF is relatively water insoluble and does not favor the hydrated state.

2.5.3 *Observing Dyed Hillocks*

This Chapter began with an overview of the various techniques that are commonly used for viewing hillocks and screw dislocations. We often use reflected light differential interference contrast microscopy (DIC) as an initial qualitative diagnostic of the surfaces for grown KAP crystals. Due to the presence of the fluorophores we can also take complimentary fluorescence images to see the dye that marks out the fast slopes. More often than not, far more hillocks are seen with the fluorescence view than are visible on the surface through DIC. This is a consequence of the overgrowth of hillocks that do not emerge on the surface. A Leica DMLM polarizing microscope coupled to a digital camera (either a Diagnostic Instruments SPOT Camera or a Nikon D80 camera) was used to aquire DIC and fluorescence images. The DIC mode consisted of using reflected light under cross-polarizers and a prism for adjusting interference contrast, while fluorescence micrographs were made with a 100 Watt Hg arclamp powered by an LEP Ltd. power supply and a dichroic filter block (480 SPEC from Leica). Images were typically taken with a 5x objective.

As a rough indicator of hillock morphology changes due to the presence of added impurities, the angle spanned by the boundary line between the fast and slow slopes of the hillocks was measured. This angle is 125° for pure KAP crystals. When the morphology is altered this angle widens, as can be easily seen in the images from Hottenhuis *et al.* due to the presence of trivalent cation impurities (Figure 2.9). This diagnostic, however, only provides an initial indication of morphology changes due to the resolution limits of our DIC

microscope, therefore the use of atomic force microscopy (AFM) is needed for a more detailed analysis of hillock morphologies.

As was mentioned previously, probes like DIC and AFM are limited to surface detection. To better understand the global evolution of growth hillocks, it is necessary to observe *both* the bulk and surface defects throughout the entire crystal. Fluorescence microscopy allows us to see all hillocks that were once growth-active, because the dye leaves a "fossil record" of the growth history. Traditional fluorescence microscopes, however, image luminescence from the entire crystal bulk onto a 2D plane, this includes out-of-focus light that renders the images blurry. To remedy this, a new technique for observing hillocks using confocal microscopy was implemented (see Section 2.6).

2.6 Confocal Microscopy

2.6.1 Introduction

Confocal laser scanning microscopy (CLSM)[65,66] is a widely established research instrument in the fields of biology, medicine, and materials science. Known as a "point-probing scanner", CLSM irradiates samples and collectes emission in a point-by-point fashion. Furthermore, it eliminates out-of-focus light in fluorescence imaging by use of a pinhole at the intermediate imaging plane. To image an entire specimen, the laser beam is scanned relative to the sample, or vice versa. This is in contrast to conventional light microscopy that illuminates and images whole objects within a given field of view, often rendering them burred by out-of-focus light.

Airy Diffraction

One key way in which CLSM improves resolution is by blocking outer fringes of diffracted light interference patterns that result from the passage of light through a small circular aperture (microscope objective). The diffraction pattern from a circular aperture consists of a central diffuse circular disc, known as the Airy disc, surrounded by fainter concentric rings (Figure 2.30). In optical microscopy, every point in a sample is represented in the image focal plane by an Airy diffraction pattern of a finite spread. If the diffraction pattern from a single point source is larger than the system's resolution at the imaging plane, the process is said to be *diffraction-limited*, meaning the best resolution that can be achieved is determined by the aperture size. Two objects or points in an image can be resoved from each other if they meet the Rayleigh criterion: the center of the Airy ring for the first point source must occur at the first minimum, or beyond, in the Airy ring of the second point source. The diameter of the Airy disc is related to the wavelength of the source light and the size (f-number) of the circular aperture. As given by the Bessel function solutions for the diffraction amplitude of a point source, the first minimum occurs at:

(2.21) $$NA_{obj} = n \times \sin\ \theta = 1.22\lambda/d$$

where NA_{obj} is the numerical aperture of the objective, n is the refractive index of the medium, θ is the angle separating the center lines of the diffraction patterns from each point source (which intersect at the aperture), λ is the wavelength of the light, and d is the diameter of the aperture. The diameter of the central Airy disk to the first minimum at the intermediate imaging focal plane is called an Airy Unit (AU).

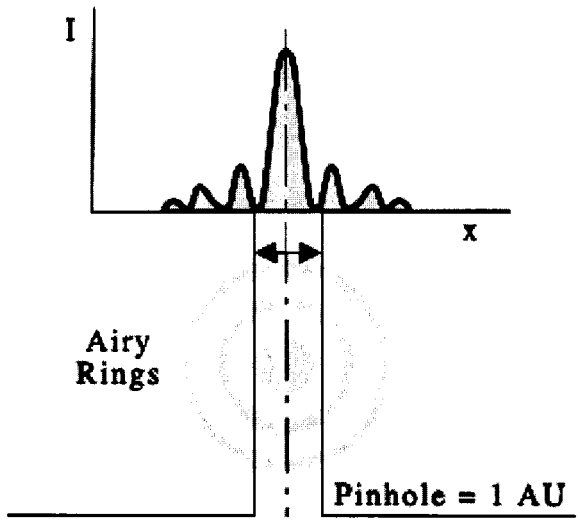

Figure 2.30. *Schematic of Airy diffraction pattern.* Depicts the interference fringes that result from light passing through a circular aperture. In confocal microscopy, a pinhole serves to eliminate outer fringes by setting its width to one Airy unit (AU). [Figure adapted from Zeiss].

The Confocal Method

The most unique feature of a confocal microscope is the pinhole aperture design that is positioned in the intermediate imaging focal plane (Figure 2.31). The detector is positioned behind the pinhole so that it can only collect light that passes through. The laser beam is focused to a diffraction-limited spot, illuminating one point at a time in the sample. The use of a pinhole helps to improve resolution by eliminating the outer rings of the Airy diffraction pattern from each point source, according to the width set for the pinhole. When the pinhole is set to 1 Airy Unit (AU), it only allows light from the central Airy disk to pass through to the conjugate imaging plane. The pinhole also serves to create depth-discrimination by eliminating light coming from object points that lie outside the focal volume. An entire slice of the object is then imaged by scanning

the laser beam relative to the object.[67] By varying the diameter of the pinhole the degree of confocality can be adapted to practical requirements; with the pinhole fully open all object light is collected, like a conventional microscope, whereas with a narrow pinhole stray light is suppressed and image contrast is improved due to limiting the amount of Airy diffraction imaged. The narrower the pinhole, the narrower the optical section that is imaged (however, while a pinhole width less than 1 AU will create thinner sections, it does not improve upon resolution, and it is advised that one switch to a better numerical aperture objective lense).

When the object focal plane is incrementally changed along the optical (*z*) axis, one can obtain a series of 2D optical slices at different depths. Once a *z*-series is aquired, the images can be compiled to make a movie or reconstructed into a 3D representation of the sample. The spatial (and in the case of crystal growth, temporal) structure of the object is obtained in this way. An optimal 3D reconstruction requires thin optical sections and a spacing between successive *z*-slices that is half the optical section thickness. With the enhanced specificity and contrast of light collection from only the focal plane, the details illuminated by fluorescent light become much more discernable than with a conventional microscope. CLSM can also be set up to simultaneously image different emission colors on multiple channels that can be viewed separately or overlayed for comparison.

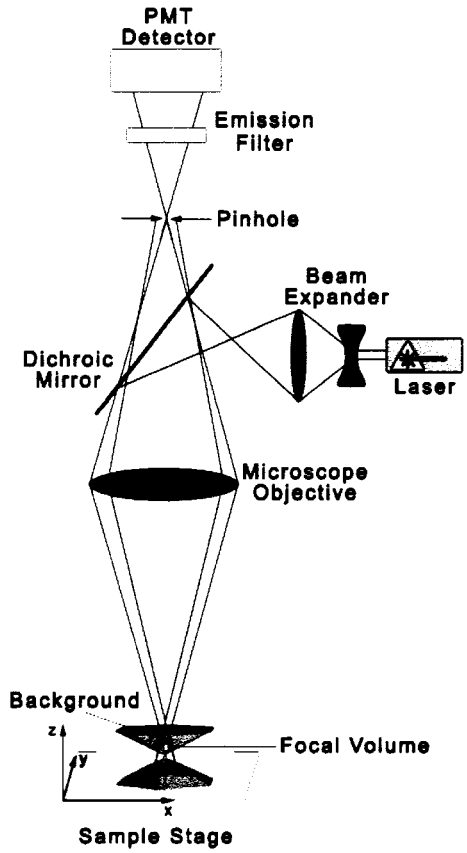

Figure 2.31. *Confocal microscopy diagram.* The use of a pinhole in CLSM helps to eliminate out-of-focus light. The pinhole is placed at the intermediate image focal plane, only allowing in-focus light to pass through to the detector, which lies in a plane conjugate to the object plane (i.e. the detected light is inflected from how it would show up at the intermediate imaging plane).

2.6.2 *Instrument Description and Settings Used*

We used confocal microscopy to image as-grown KAP crystals doped with fluorescent dyes at varying concentrations within the fast slopes of the {010}

growth hillocks. Whole-crystal images of heavily-dyed crystals were performed using an inverted confocal microscope.[67,68,69] Figure 2.32 shows a schematic of the beam path for this confocal microscope used in dual-channel mode, and Table 2.6 lists the settings used for imaging each of the dyes. Simultaneous multi-color imaging of KAP crystals dyed with **3** were excited with 488 nm illumination from a 30 mW Argon laser, while dyes **1** or **2** were excited with 543 nm light from a He-Ne laser. The excitation light was sent through a HauptFarbTeiler (HFT) dichroic beam splitter and focused to a diffraction-limited spot with a 10x dry objective (FLUAR 0.5 NA at 0.7 zoom). Emission from the sample was sent back through the objective, passed through a secondary dichroic beam splitter (NebenFarbTeiler, NFT), spectrally filtered with an emission filter, then spatially filtered with a confocal pinhole to give optical sections of between 12.5 - 20 μm (pinhole diameter is wavelength dependent so size varied for different emission channels). Emission was collected using a photomultiplier tube detector. Image quality was controlled via scan settings, including an average scan time of 4 seconds per frame using uni-directional line scans with averaging two scans per image. Many frames were imaged in a tiling fashion to automatically stitch together composite images of the entire (010) growth sector for each optical slice (or *z*-section).[67]

By scanning from the bottom to the top of a heavily-dyed crystal, the number and position of growth-active hillocks that form throughout the (010) sector are recorded. Figure 2.33 shows successive optical slices of KAP dyed with **3** in which the development of the (010) growth sector is seen in the evolving pattern of luminescence. The optical sections are thin enough such that the *z*-coordinate can roughly be taken as time of growth. By mapping hillock positions in each optical section, and by comparing them to the positions in previous and

subsequent sections, a sequence of hillock activation is obtained, as well as the stability of the defect pattern (see Chapter 4 for experimental results).

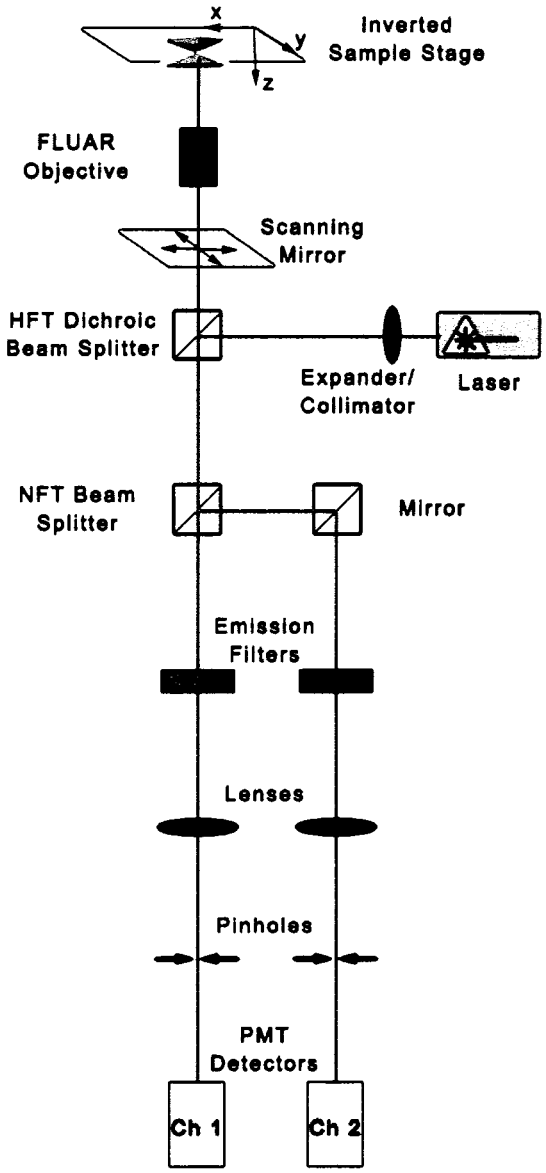

Figure 2.32. *Confocal beam path for multi-spectral imaging.*[68]

Table 2.6. *Confocal Settings.*[68]

Confocal Settings	LGSFY (1)[‡]	Erio (2)	DCF (3)
Laser	He-Ne @ 50%	He-Ne @ 50%	30 mW Argon @ 50%
Excitation Wavelength	543 nm	543 nm	488 nm
1st Dichroic Beam Splitter	HFT 488/543	HFT 488/543	HFT 488/543
2nd Dichroic Beam Splitter	NFT 545 longpass	NFT 545 longpass	NFT 515 longpass (single) NFT 545 longpass (multi)
Emission Filter	LP 560	LP 560	LP 505 (single) BP 505-530 (multi)
Sample Confocal Pinhole Sizes	~1 AU ≈ 47 μm for 10×/0.5 NA	~1 AU ≈ 47 μm for 10×/0.5 NA	~1 - 7 AU ≈ 48 - 295 μm for 10×/0.5 NA

[‡] LGSFY (1) was also imaged during early studies using a different confocal microscope than what is described here. See Endnote 69 for specs.

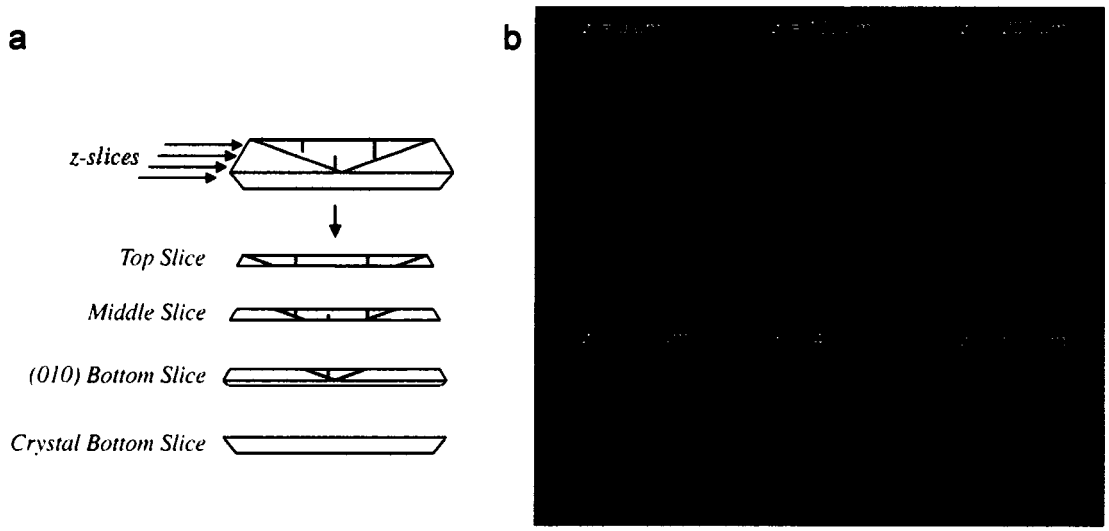

Figure 2.33. *Confocal slices of KAP with 3.* a) Cartoon depicting the *z*-sectioning process in KAP, which illuminates varying sizes of the *b*-face, depending on depth. b) Confocal Images read from the top of the crystal (upper left) to the bottom (lower right), depth in the *z*-series is indicated. Step size is 12.5 μm. Every eighth optical slice is shown. Luminescence develops on the fast slopes of (010) growth hillocks, with vertices marking the dislocation cores. Crystal size = 6.3 mm wide × 8.3 mm long × 0.7 mm thick.

2.7 Quantifying Information Content and 'Genetic Inheritance'

CS proposed the transfer of information in the patterns of screw dislocations through crystal growth. But, what is the nature of this information, and how can it be characterized? Crystal growth studies of defects have historically shown that it is not the *number* and *location* of dislocations present in the seed that remains constant but rather the *density* of dislocations.[70] In other words, as a seed crystal continues to grow in volume and in surface area, the number of dislocations will increase to maintain a certain dislocation density. This is contrary to the theory of crystal growth[70] that says the number and location of

dislocations present in a seed crystal should be preserved in the daughter crystal (as discussed in Chapter 1). An initial assessment of the stability versus mutation of genetic inheritance can be gained from a general statistical analysis of the appearance, dissappearance, and lifetimes of growth active hillocks, as determined from the confocal image stacks. Going a step further, the following 'information content parameters' are also employed and assessed for each crystal:

$$Transfer = \frac{\#\,previous - \#\,deaths}{\#\,previous} \times 100\% \tag{2.22}$$

$$Mutation = \frac{1}{2}\left(\frac{\#\,new}{\#\,active} + \frac{\#\,deaths}{\#\,previous}\right) \times 100\% \tag{2.23}$$

$$Info_Preserved = Transfer - Mutation \tag{2.24}$$

where *Transfer* is the percentage of events from the previous layer or crystal surface that are successfully transfered to the next layer or daughter crystal, *Mutation* gives a measure of loss (*deaths*) and addition (*new*) to the information content between layers, and *Info_Preserved* indicates the amount of information content preserved from one layer to the next (which can vary between 100%, indicating no deaths or births between layers, to -100%, indicating all hillocks from the *previous* layer died and all the currently *active* hillocks are new). In these studies, we frequently observed changes in the number of dislocations between the seed and daughter crystals, as well as between layers within a single crystal, leading to a series of studies to achieve greater control over the crystal growth conditions and thereby attempt to minimize such mutations (see Chapter 4).

Is it possible that the transferable information content is stored in some other form, such as the density of growth-active hillocks or the overall pattern of emergent dislocations itself, rather than a bit-wise information store? To answer

this question, a more involved quantification of the growth-active hillock patterns and densities was performed using correlation analyses (a form of fractal analysis). To the best of our knowledge this is the first application of fractal correlation analysis towards the assessment of growth hillock patterns in crystals. The methods used for these analyses are described in this section, while the results are given in Chapter 4.

2.7.1 *Fractal Analysis*

Fractal analysis can be used to quantify the information stored in the pattern of growth hillocks. Fractal geometry extends the classical concept of dimensional analysis to include a fractional (non-integer) number that describes the structure of complex systems in space-time. There are a variety of methods for computing fractal scaling, many of which rely upon covering a given structure with circles (or boxes) of varying sizes, r, counting the number, $N(r)$, of circles (boxes) it takes to enclose the object, and plotting the results on a log-log scale to draw out a power law, $N(r) \sim r^D$, where D is the fractal dimension of the object.[71] A more practical approach when dealing with scale-limited random fractals, abundant in naturally occurring patterns, is to use a density-density or pair-correlation function. 'Scale-limited random fractal' refers to physical fractals that possess a degree of randomness due to stochastic fluctuations, and therefore lack the high degrees of symmetry found in deterministic fractals generated through iterative mathematical methods.[71] The correlation function is as follows:

$$c(\vec{r}) = \frac{1}{V}\sum_{\vec{r}'} \rho(\vec{r}+\vec{r}')\rho(\vec{r}') \tag{2.25}$$

Here, $\rho(v)$ is the probability density distrbution of an event happening at the point defined by vector, v. The probability function is equal to one if the position, v, is occupied, or zero if it is empty. V is the amount of space (volume, area, or

length) the object covers. If an event has occured at position r', and another one at $r+r'$, then $c(r')$ will be non-zero. Thus, when summed over all positions, r', this equation gives the likelihood or expectation value that two events are correlated in space by the vector r.

An important component of fractal behavior is that the basic structural pattern (information) re-emerges at varying magnifications, a phenomenon known as scale-invariance. For an object to qualify as non-trivially scale-invariant, its correlation function must obey the following criteria when rescaled by an arbitrary amount b:

(2.26) $$c(br) \sim b^{-\alpha} c(r), \qquad 0 < \alpha < d$$

where α is a non-integer scaling constant between zero and the Euclidean dimension, d, in which the object is embedded. This criteria is only fulfilled by a power law function:[18]

(2.27) $$c(r) \sim r^{-\alpha}$$

For an isotropic object (i.e. direction independent), as most random fractals are, $c(r)$ becomes a measure of how the object's local density distribution scales with distance relative to any given point in the object. Under the power law condition, the local density will decay algebraically. In the isotropic case, one can see that integrating $c(r)$ over a sphere of radius R gives the number of particles $N(R)$ contained within the sphere:

(2.28) $$N(R) \sim \int_0^R c(\vec{r}) d^d r \sim R^{d-\alpha}$$

Comparing this to the typical power law formula, $N(R) \sim R^D$, where D is the fractal dimension of the object, one can see that the fractal dimension for the

density correlation analysis is expressed as $D = d - \alpha$, where d again is the Euclidean dimension enclosing the object.

In the present application of analyzing a confocal z-series of growth active hillocks, it cannot be assumed that we have an isotropic object. In fact, it is clearly seen by eye that this data is not isotropic. However, we can still simplify the functional form of $c(\vec{r})$ by assuming the variables are separable:

$$c(\vec{r}) = c(r,\theta,z) = f(r)g(\theta)h(z) \tag{2.29}$$

where each function, $f(r)$, $g(\theta)$, and $h(z)$ would independently need to statisfy the power law criteria if it is to be considered scale-invariant and analyzable via fractal methods. In this case, $f(r)$ takes on the same meaning of $c(r)$ for an isotropic object, i.e. a correlation in the planar separation between the appearance of hillocks in a growing crystal and a measure of the local density scale-invariance. The polar function, $g(\theta)$, is a measure of whether there is correlation in the relative direction between emergent dislocations. If there are specific directional correlations between hillocks, then it is likely that they are more discrete in nature rather than determined by a continuous power law scaling. For example they may relate to crystallographic directions or defect structure. In viewing the confocal sequences by eye, there seem to be clear correlations between screw dislocation cores along the a-axis, the c-axis, and the fast-slow boundary of the hillocks themselves. Such correlations cannot be quantified using fractal analysis, however similar counting methods can be applied and the results plotted on a histogram to quantify direction-specific correlations. These methods will be described shortly.

The final function, $h(z)$, would indicate a correlation in the number of new layers that must grow before new dislocations appear and become growth active. A meaningful correlation in z seems unlikely given that a hillock only has the potential to generate another dislocation on a layer where it is still growth-active. In other words, an overgrown hillock should not create enough strain to propagate through multiple layers of growth and provide sufficient energy to generate a *new* dislocation. Hence $h(z)$ has been treated as trivial for the confocal data and is not addressed further herein. Each confocal section is mapped out and treated as a separate two-dimensional pattern (i.e. $d = 2$), with the (x, y) hillock coodinates and (010) outlines being identified for further analysis. The actual numerical methods for applying these pair correlation functions to our data are described below.

Determination of $f(r)$ according to fractal analysis techniques involves choosing a hillock vertex and counting the number of other vertices that fall within a circular shell of radius $r + \delta r$, where δr is typically ten percent of r.[71] This calculation is repeated with each of the vertices as the origin, and for varying sizes of r (without double counting pairs). Using circular shells in this manner is equivalent to taking the derivative of $N(r)$, which essentially gives $f(r)$. The results are normalized according to the number of vertices and the areas of the circular shells for each scan. Vertices close to the outer edges are discarded as counting centers in order to avoid area truncation effects. This is reasonable since the fractal behavior of any real object is only valid within a limited scaling range determined by the object's size. Figure 2.34 displays a schematic of the method just described using the (010) outlines and hillock coordinates for all layers of a z-stack projected onto one plane. A useful feature of this method for calculating the fractal dimension is that it improves the counting statistics by averaging

distances between many points within a single cluster; there are $n(n-1)/2$ sample points rather than just n, where n is the number of vertices.

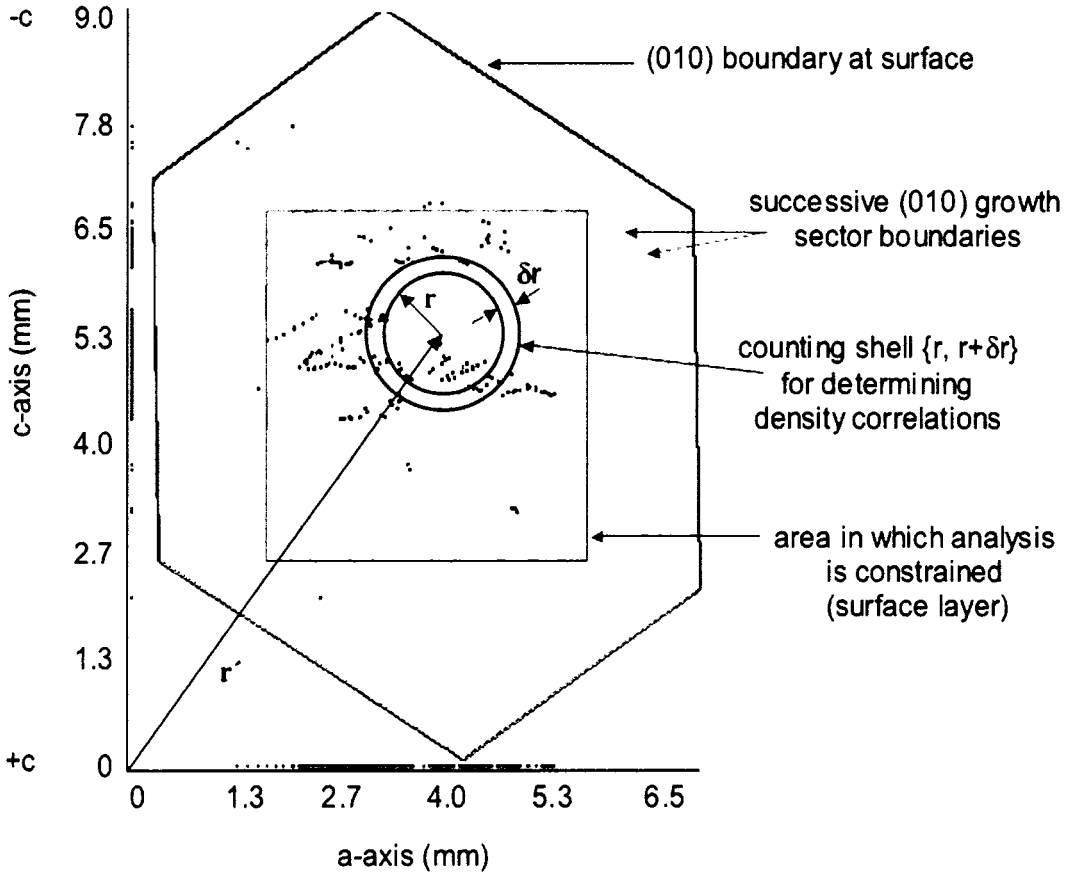

Figure 2.34. *Density correlation function analysis.* Hillock locations are denoted by black dots. Blue dots on the coordinate scales are the projections of the hillock locations onto the *a*-axis and *c*-axis of the crystal. Hexagonal outlines display the areas of the (010) face as the crystal grew between optical *z* slices where the innermost border is near the bottom of the (010) sector and the outermost (red) border is the fully-grown surface. The red box encloses the central 30-40% of the (010) section of interest (here shown for the surface layer). Any hillocks lying outside this box were discarded in the analysis to avoid area truncation effects. The blue ring gives an example of how pair correlations are counted for various *r*; all points falling within the ring are counted for that $r + \delta r$ from each center.

The fractal dimension is obtained by plotting $f(r)$, the normalized number of points that fall within the shell of radii r and $r + \delta r$, versus the shell radii used, r, on a log-log scale (Figure 2.35). The slope of this line within the appropriate length range gives the scaling parameter α, from which the fractal dimension is determined as $D = d - \alpha$, where d is the embedding Euclidean dimension (in this case $d = 2$). The fractal dimension, D_i, for the hillock patterns on each optical section is determined and can then be plotted versus height in the (010) sector to ascertain how this value, and hence the local density correlations, changes through crystal growth.

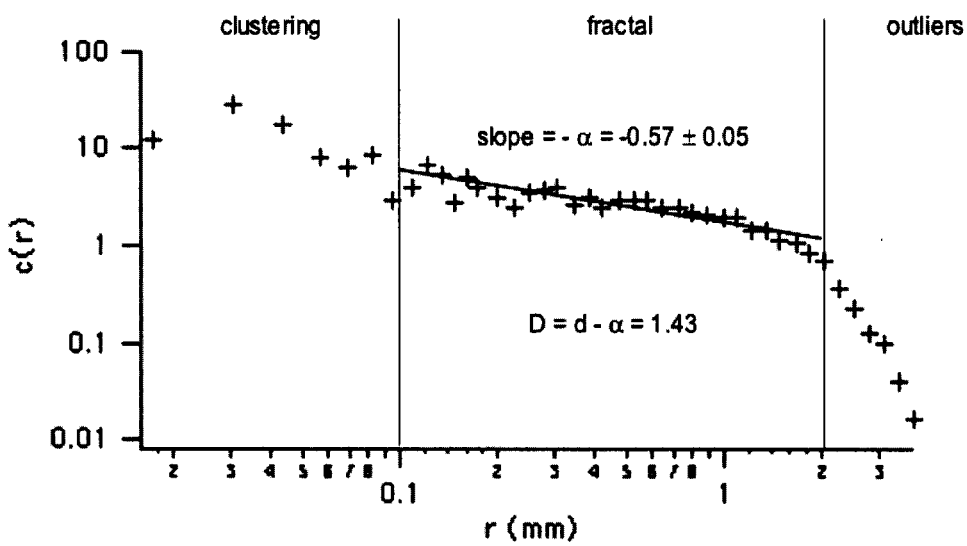

Figure 2.35. *Pair correlation plot for one optical z-section of hillock data.* Three distinct regions are identified. Within the range of 0.1 mm and 2 mm pair separations that display the characteristic power-law for a random fractal are observed. The region at large r tails off due to boundary effects, while the region at smaller length scales displays evidence of hillock clustering.

In the case of directional correlations, the fractal analysis method is not appropriate due to their more discrete nature. However, similar counting

techniques can be employed to look at the numbers of events that fall within a certain direction with respect to each counting center. In this case, instead of using circular shells of radii $r + \delta r$, counting is performed using a bow-tie shaped scanning window centered on θ and $\theta + 180°$ with angular spread $\delta\theta$ (typically set to an angular tolerance of 2°-4°). This calculation is again repeated with each of the vertices as the origin, all 360° scanned from each center, and the number of dislocations that fall within the bow-tie scanning range are tallied (without double counting pairs). Vertices close to the outer edges were again discarded as counting centers in order to avoid area truncation effects. Figure 2.36 displays the method just described for determining $g(\theta)$. The results are then displayed as a histogram of the number of dislocation pairs that are related by the various relative directions (see Chapter 4 for examples). Peaks in the histogram indicate which directions have correlations between emergent hillocks. Rather than analyze these results layer-by-layer, I chose to use the entire data set of all hillocks in a sample crystal projected onto one plane in order to maximize statistics and draw out the peaks from the background.

Finally, as a control data set for comparison with the crystal data, a Monte Carlo simulation was created to mimic the growth of the crystal with random events (or 'hillock' locations), limited to a rectangular[72] area derived from the boundaries of the growing (010) face. The simulation took the numbers of hillock "births" and "deaths" from the actual crystal optical sections. The positions of new hillocks and the selection of those to be removed were both randomized. The radial and angular correlations for all corresponding layers of the Monte Carlo simulation were analyzed and compared to the results from real hillock data. A copy of the computer code I wrote to perform these correlation analyses is given in Appendix A. Analyses for the mapping of active hillocks through the

growth of dyed KAP crystals and corrsponding Monte Carlo simulations are given in Chapter 4.

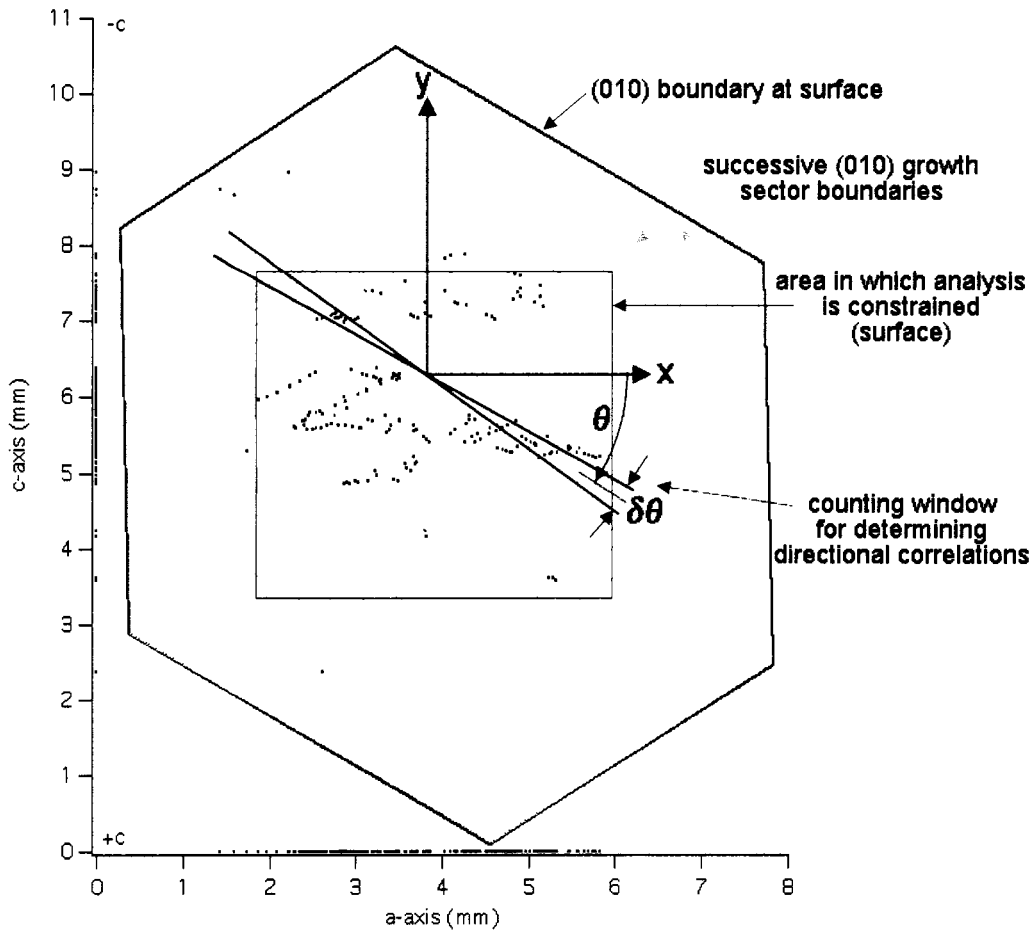

Figure 2.36. *Angular correlation analysis.* All hillock locations that appeared throughout the crystal growth are denoted by black dots. Blue dots on the coordinate scales are the projections of the hillock locations onto the *a*-axis and *c*-axis of the crystal. Hexagonal outlines display the areas of the (010) face as the crystal grew between optical *z* slices where the innermost border is near the bottom of the (010) sector and the outermost (red) border is the fully-grown surface. The red box encloses the central 30-40% of the (010) section of interest (here shown for the surface layer). Any hillocks lying outside this box were discarded in the analysis to avoid area truncation effects. The blue bow-tie gives an example of how pair correlations are counted for various directions θ; all points falling within the bow-tie are counted for that $\theta \pm \delta\theta/2$ from each center.

2.7.2 *Controlled Growth Experiments*

Chapter 1 discussed growth induced screw dislocations of varied origin, including those transfered from the seed, mechanical stress from trapped particulates, stacking errors, constitutional stress from significant impurity segregation, and random stresses from the laboratory environment. In order to test some of these possible sources for their relative degree of influence on the development of screw dislocations, controlled growth experiments must be performed where one growth parameter is systematically varied at a time. The relevant parameters that can be controlled include supersaturation, impurity type and concentration, temperature, solution flow, and solvent composition. Of these, the most important factors in growth hillock dynamics are the supersaturation and the influence of impurities, thus I chose to test these two parameters.

Supersaturation Studies

As discussed in Chapter 1, supersaturation influences the formation of screw dislocations because it is the main driving force of crystal growth from solution. It is expected that as supersaturation increases the number of new dislocations will also go up due to a greater number of accidents, such as impurity trapping or 2D nuclei creating stacking faults or step edge shearing. At some point the roughening transition will be encountered, resulting in a rather topographically complex growth interface. As supersaturation continues to increase, then 2D nucleation will take over the growth and the crystal face will smooth out and become more dislocation-free.

Controlling supersaturation requires precise control over temperature, solution flow, and solute concentration. We designed and built a closed-loop crystal growth flow system to perform supersaturation studies (Figure 2.37). The system is sealed from the atmosphere to avoid evaporation and ensure the original solvent concentration is maintained. KAP solution at a pre-determined concentration, given by the KAP solubility formula (Equation (2.11)), is stored in a reservoir and maintained at an elevated temperature via a hot plate to dissolve any pre-nucleation aggregates. This reservoir is placed on a shelf above the lab bench, employing gravity to smoothly and continuously flow solution down through silicon tubing (Nalgene silicon tubing sizes #16 and #17 connected via Cole-Parmer Nylon tubing adapters). The solution passes a coarse filter holder (Schleicher and Schull, FP 050) to remove any large particulates or dust, and then runs through a glass coil immersed in a temperature controlled water bath to reduce to the desired growth temperature. It is then directed into a glass tube ("growth cell") where laminar flow is achieved over 4 seed crystals mounted in series on glass posts afixed to silicon stoppers. A thermocouple (Omega precision fine wire T-type thermocouple) reads out the growth cell temperature to a digital meter. The solution recycles into a catch reservior where it is heated and then pumped back up to the source reservoir using a peristaltic pump (Omega, FPU-120, flow rate 230 mL/min) controlled by a liquid level sensor. The water bath temperature is read out with a thermocouple and regulated by a combination of a computer controlled heating element, an isolated glass tube with a constant supply of cold tap water running through it, and a stir rod to homogenize the temperature throughout the water bath. This set-up maintains a constant temperature to within 0.1°C if the source reservoir is not too hot (ie, less than 5.0°C above growth temperature). Solution flow speed is determined by the relative height difference, Δh, between the solution level of the source reservoir and the system outlet at the recycling reservoir. A height of about four feet is

sufficient to attain laminar flow (~216 mL/min) through the growth cell such that supersaturation gradients are overcome and all four crystals in series are equally supplied with solute, as determined by relative percent mass increase. The growth cell has an inner diameter of 0.5 cm and is 40.5 cm long, giving a cell volume of 31.8 cm^3 that holds 37 mL solution and has a cross-sectional area of 0.78 cm^2. The flow velocity is then determined by the following formula:

(2.30) $$\textit{Flow Velocity} = \textit{Flow Rate (mL/s)} \div \textit{Area (cm}^2\textit{)}$$

Thus, the flow velocity in this system is about 4.6 cm/s, which is sufficient up to about 5% supersaturation. We chose a gravity-driven design because we were unable to find any commercially available pumps without metal parts that produced low to medium volume, pulseless flow.

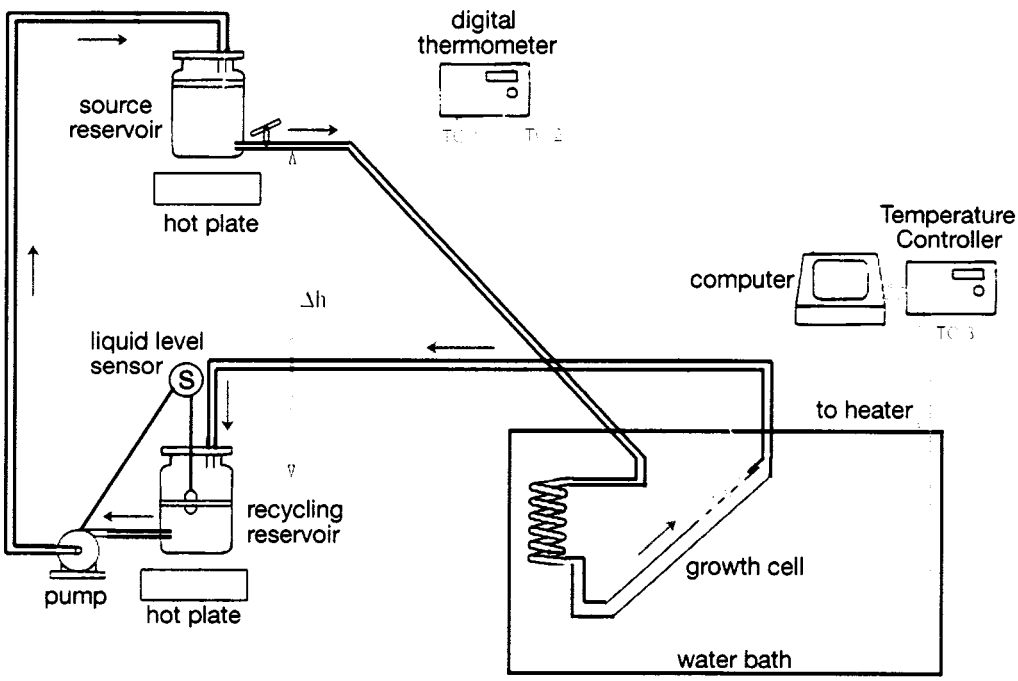

Figure 2.37. *Crystal growth flow system.* A closed-loop, gravity-fed solution flow system is used for growing from seeds at controlled supersaturation and constant temperature. The relative height between the source reservoir solution level and the outlet in the recycling reservoir determines the flow rate.

Using this flow system, we performed several experiments at varying starting concentrations of KAP solution dyed with 5×10^{-6} M of **3**. In all studies the growth temperature was maintained at 26.0 ± 0.1°C. Solutions were reused for experimental runs of the same supersaturation. Only seed crystals of KAP dyed with **1** or **2** that had clean surfaces were used for final studies. Surfaces were slightly etched using superheated solution for 5-10 minutes prior to immersing glass components into the water bath and cooling to growth temperature. Crystals grew for about 24 hours and were then harvested and dried with a jet of nitrogen air. Results of these studies are reported in Chapter 4, Section 4.1.2.1.

Impurity Studies

Impurity inclusions can cause dislocations either through step edge shearing, or if segregation occurs, by creating constitutional stress and regions with different expansion coefficients. The larger an impurity, the more likely it is to cause dislocations because it can achieve the critical local strain needed. Ionic impurities tend to produce a greater impact on KAP morphology than neutral ones.[45] To test the influence of impurities on hillock development we performed several studies by varying the size, type, and concentration of intentionally added impurities to KAP crystals grown from static solution. We looked at particulate inclusions using quantum dots and fluorescent polystyrene beads of varying sizes. We performed several studies with dyes at different concentrations, and we also investigated the effects of various trivalent cations in combination with dye **3** to better understand the specificity of the dye-hillock interactions. These studies and their results will be further described in Chapters 3 and 4.

2.8 Summary of Experimental Methods

To investigate the reliability of crystals to act as a primitive source of transferable information, the spatio-temporal evolution of growth-active hillocks is analyzed via a novel technique. Confocal microscopy is employed to image the "fossil-record" of intrasectorally-zoned fluorescent dyes within the growth-active hillocks of a well-defined model crystal system, namely KAP. Using local density and angular correlation analyses, along with statistical analysis to quantify the information content of the hillock patterns, the degree of transfer between successive generations of crystal growth is assessed. These results are compared with a Monte Carlo simulation designed to mimic the appearance and disappearance of growth-active hillocks in the crystal with boundary-limited randomized events. A variety of experiments are undertaken to control the transfer of the hillock patterns from seed to daughter crystals, and to minimize the appearance of new dislocations. Through a combination of experimental techniques and force-field calculations I also investigate dye-crystal interactions and the specificity of intrasectoral zoning in KAP. Beyond providing the first experimental test of the Cairns-Smith proposal, this work also applies towards improving our basic understanding of the nucleation, evolution, and impurity interactions of growth-induced screw dislocations, a fundamental and necessary ingredient for the growth of crystals at low supersaturation.

NOTES AND REFERENCES TO CHAPTER 2

1. D. Hull and D. J. Bacon; *Introduction to Dislocations* (Butterworth-Heinemann: Oxford, 2001).

2. M. Pluta, in: *Advanced Light Microscopy, vol. 2*, p. 146 (Elsevier: New York, 1989).

3. W. N. Unertl, in *Scanning Probe Microscopy and Spectroscopy: Theory, Techniques, and Applications*, p. 113, ed. D. Bonnell (Wiley-VCH: New York, 2001).

4. G. T. R. Palmore, T. J. Luo, T. L. Martin, M. T. McBride-Wieser, N. T. Voong, T. A. Land, and J. J. De Yoreo, *Transactions ACA*, **33** (1998), 45; J. J. De Yoreo, C. A. Orme, and T. A. Land, in: *Advances in Crystal Growth Research*, eds. K. Sato, Y. Furukawa, and K. Nakajima (Elsevier Science B. V.: Amsterdam, 2001).

5. (a) N. A. Booth, B. Stanojev, A. A. Chernov, P. G. Vekilov, *Rev. Sci. Instrum.* **73** (2002), 3540; (b) N. A. Booth, A. A. Chernov, P. G. Vekilov, *J. Mater. Res.* **17** (2002), 2059.

6. (a) X. Ma, M. Dudley, W. Vetter, and T. Sudarshan, *Jpn. J. Appl. Phys.* **42** (2003), 1077; (b) M. Dudley, *Mat. Res. Soc. Symp. Proc.* **307** (1993), 213. (c) H. Klapper, *Mat. Sci. Forum*, **276** (1998), 291.

7. W. M. Vetter, H. Totsuka, M. Dudley, and B. Kahr, *J. Cryst. Growth.* **241** (2002), 498.

8. L. Reimer, in: *Transmission Electron Microscopy: Physics of Image Formation and Microanalysis*, p. 344, eds. P. W. Hawkes, A. L. Schawlow, A. E. Siegman, K. Shimoda, T. Tamir, and H. K. V. Lotsch (Springer-Verlag: New York, 1993).

9. (a) J. Paquette and R. J. Reeder, *Geology*, **18** (1990), 1244; (b) J. Paquette and R. J. Reeder, *Geochim. Cosmochim. Acta*, **59** (1994), 735; (c) N. G. Hemming, R. J. Reeder, and S. R. Hart, *Geochim. Cosmochim. Acta* **62** (1998), 2915; (d) E. J. Elzinga and R. J. Reeder, *Geochim. Cosmochim. Acta*, **66** (2002), 3943.

10. H. W. Schutt, *Eilhard Mitscherlich: Prince of Prussian Chemistry*, translated by W. E. Russey (American Chemical Society: Washington, DC, 1997).

11. B. Kahr and R. W. Gurney, *Chem. Rev.*, **101** (2001), 893.

12. B. Kahr and S.-H. Jang, in *Encyclopedia of Supramolecular Chemistry*, vol. *D*, p. 1 (Dekker Encyclopedias by Taylor and Francis Group LLC: New York, 2004).

13. Y. Okaya, *Acta Cryst.* **19** (1965), 879.

14. T. A. Eremina, N. G. Furmanova, L. F. Malakhova, T. M. Okhrimenko, and V. A. Kuznetsov, *Kristallografiya* **38** (1993), 236.

15. A. Barbon, M. Bellinazzi, J. Benedict, M. Brustolon, S. Fleming, S.-H. Jang, B. Kahr, and A. Rohl, *Angew. Chem. Int. Ed.*, **43** (2004), 5328.

16. N. Zaitseva, L. Carman, I. Smolsky, R. Torres, and M. J. Yan, *J. Cryst. Growth*, **204** (1999), 512.

17. (a) R. W. Gurney, C. A. Mitchell, S. Ham, L. D. Bastin, and B. Kahr, *J. Phys. Chem. B*, **104** (2000), 878; (b) R. W. Gurney, M. Kurimoto, J. A. Subramony, L. D. Bastin, and B. Kahr, in: *Anisotropic Organic Materials: Am. Chem. Soc. Symp. Ser.* eds. R. Glaser and P. Kaszynsky (American Chemical Society, Washington, DC, 2001).

18. M. Kurimoto, P. Subramony, R. W. Gurney, S. Lovell, J. Chmielewski, and B. Kahr, *J. Am. Chem. Soc.* **121** (1999), 6952.

19. (a) R. A. Visser, *Neth. Milk Diary J.* **36** (1982), 167; (b) T. D. Dincer, G. M. Parkinson, A. L. Rohl, and M. I. Ogden, in: *Crystal. Growth Org. Mater. 4th International Workshop, vol. 4*, p. 25, eds. J. Ulrich (Shaker Verlag: Aachen, Germany, 1997); (c) T. D. Dincer, G. M. Parkinson, A. L. Rohl, and M. I. Ogden, *J. Cryst. Growth*, **205** (1999), 368.

20. M. Kurimoto, L. D. Bastin, D. Fredrickson, P. N. Gustafson, S.-H. Jang, W. Kaminsky, S. Lovell, C. A. Mitchell, J. Chmielewski, and B. Kahr, *Mat. Res. Soc. Symp.*, **620** (2000), M9.8.1.

21. W. J. P. van Enckevort and L. A. M. J. Jetten, *J. Cryst. Growth*, **60** (1982), 275.

22. T. Bullard, M. Kurimoto, S. Avagyan, S. H. Jang, B. Kahr, *ACA Transactions*, **39** (2004). Other examples of the use of confocal fluorescence microscopy to study impurity distributions in crystals include: Y. Iimura, I. Yoshizaki, H. Nakamura, S. Yoda, H. Komatsu, *Cryst. Growth Des.* **5** (2005), 301; and Y. Iimura, I. Yoshizaki, S. Yoda, H. Komatsu, *Cryst.*

Growth Des. **5** (2005), 295. Intrasectoral zoning in minerals by cathodoluminescence was pioneered by Reeder *et al.* See: J. Rakovan, R. J. Reeder, *Geochim. Cosmochim Acta,* **60** (1996), 4435 and references therein.

23. Groth, P., *Chemische Krsytallographie*, **4** (1917), 724.

24. L. A. M. J. Jetten, *Thesis,* (University of Nijmegen, 1983).

25. Graphical display was generated with Materials Studio Visualizer by Accelrys.

26. T. M. Okhrimenko, G. S. Belikova, L. M. Avdonina, *et al., Growth of Crystals, vol. 15,* p. 102 [in Russian], (Nauka, Moscow, 1986).

27. a) G. R. Ester, R. Price, and P. J. Halfpenny, *J. Cryst. Growth,* **182** (1997), 95; b) G. R. Ester and P. J. Halfpenny, *Phil. Mag. A,* **79**(3) (1999), 593; c) G. R. Ester, R. Price, and P. J. Halfpenny, *J. Phys. D: Appl. Phys.*, **32** (1999), A128.

28. J. Benedict, T. Bullard, W. Kaminsky, and B. Kahr, *Acta Cryst. C: Crystal Structure Communications,* **60** (2004), m551.

29. J. L. Jones, K. W. Paschen, and J. B. Nicholson, *J. Appl. Optics,* **2** (1963), 955.

30. G. S. Belikova, V. V. Korneev, I. Ya. Nikiforov, *et al., Sov. Tech. Phys. Lett.*, **7** (1981), 308.

31. S. Haussuhl, *Zeitschrift fur Kristallographie*, **196** (1991), 47.

32. a) L. M. Belayev, G. S. Belikova, A. B. Gil'varg, M. P. Golovei, I. N. Kalinkina, and G. I. Kosurov, *Opt Spectrosc.* (USSR) **29** (1970), 522; b) L. M. Belayev, G. S. Belikova, A. B. Gil'varg, and I. M. Sil'vestrova, *Sov. Phys. Crystallogr.*, **4** (1970), 544.

33. D. Comoretto, L. Rossi, A. Borghesi, *J. Mater. Res.*, **12**(5) (1997), 1262.

34. W. S. Graswinckel, F. J. van den Bruele, W. J. P. van Enckevort, and E. Vlieg, *Cryst. Growth and Design,* **7**(2) (2007), 243.

35. B. Kahr, A. Shtukenberg, and Y. O. Punin, *Optically Anomalous Crystals*, ed. B. Kahr (Springer Verlag, New York, 2007).

36. E. A. Wood, *Crystals and Light: An Introduction to Optical Crystallography, 2nd ed.*, (Dover Publications, Inc., New York, 1977).

37. Ref. 33 gives a detailed analysis of the optical properties of KAP for a range of wavelengths. They cite typical values at 1200 nm light to be n_c = 1.45 and n_a = 1.62, and then they give many plots of data for the full range of wavelengths tested, from which the values reported herein are drawn.

38. J. Michl, and E. W. Thulstrup, *Spectroscopy with Polarized Light*, (Wiley-VHC Publishers: New York, 1995).

39. E. Hecht, *Optics, 2nd ed.*, (Addison-Wesley Publishing Company: Massachusetts, 1987).

40. Z. Solc, J. Kvapil, J. and Vlcek, *Kristall Tech.*, **8** (1973), 59.

41. a) Q. L. Zhao and Y. S. Huang, *Acta Phys. Sin.*, 38 (**1989**), 1134; b) Q. L. Zhao, *J. Appl. Cryst.*, **27** (1994), 283.

42. K. Sangwal, K. Wojcik, and J. Borc, *Cryst. Res. Technol.*, **38**(7-8) (2003), 684.

43. Note also that dislocations of this spacing (< 1.26 μm), that produce cooperative growth spirals, would be seen as a single hillock in our confocal images (which usually have a resolution of 2-10 μm/pixel). The apices of cooperative spirals may be sharp or they might blur over several pixels.

44. M. H. J. Hottenhuis and C. B. Lucasius, *J. Cryst. Growth*, **94** (1989), 708.

45. a) M. H. J. Hottenhuis and C. B. Lucasius, *J. Cryst. Growth*, **78** (1986), 379; b) M. H. J. Hottenhuis, J. G. E. Gardeniers, L. A. M. J. Jeten, and P. Bennema, *J Cryst. Growth*, **92** (1988), 171; c) M. H. J. Hottenhuis and A. Oudenampsen, *J. Cryst. Growth*, **92** (1988), 513.

46. C. S. G. Philips and R. J. P. Williams, in: *Inorganic Chemistry: Principles and Non-Metals*, p. 159 (OUP: Oxford, 1965).

47. V. A. Kuznetsov, T. M. Okhrimenko, and M. Rak, *J. Cryst. Growth*, **193** (1998), 164.

48. N. Cabrera and D. A. Vermilyea, in: *Growth and Perfection of Crystals*, eds. R. H. Doremus, B. W. Roberts, and D. Turnbull, (Wiley Publishing: New York, 1958).

49. F. J. Green, *The Sigma-Aldrich Handbook of Stains, Dyes and Indicators*, (Aldrich Chemical Company: Milwaukee, 1990).

50. Molar ratios given of dye inclusion in KAP crystals is with respect to whole crystals rather than just the dyed sector. A more precise measurement would entail cutting out the dyed sector (in this case the (010) sector) and identifying the number of dye molecules per number of KAP molecules in that section. Note also that in the case of dying hillocks, this molar ratio will change crystal by crystal due to its dependence on the number of hillocks that appear through the growth of a particular crystal.

51. (a) A. M. Glazer, J. G. Lewis, and W. Kaminsky, *Proc. R. Soc. Lond. A*, **452** (1996), 2751; (b) M. A. Geday, W. Kaminsky, J. G. Lewis, and M Glazer, *J. Microscopy*, **198** (2000), 1.

52. Reported by J. J. De Yoreo and P. G. Vekilov, in *Reviews in Minerology and Geochemistry: Biomineralization, Vol. 54*, p. 87, eds. P. M. Dove, J. J. De Yoreo, S. Weiner, and J. J. Rosso, (Mineralogical Society of America, 2003).

53. a) N. O. Mchedlov-Petrossyan, M. I. Rubtsov, L. L. Lukatskaya, *Dyes Pigm.*, **18** (1992), 179; b) N. O. Mchedlov-Petrossyan, N. V. Salamanova, N. A. Vodolazkaya, Y. A. Gurina, and V. I. Borodenko, *J. Phys. Org. Chem.*, **19** (2006), 365.

54. D. C. Harris, *Quantitative Chemical Analysis, 5th ed.*, (W. H. Freeman and Company: New York, 1999).

55. R. A. Robinson and R. H. Stokes, *Electrolyte Solutions*, (Butterworths: London, 1959).

56. Accelrys, *Materials Studio Online Help*, (Accelrys Software, Inc.: San Diego, 2006).

57. Accelrys, *Materials Studio Getting Started, Release 4.0*, (Accelrys Software, Inc.: San Diego, 2006).

58. COMPASS stands for Condensed-phase Optimized Molecular Potentials for Atomistic Simulation Studies. Accelrys, *Materials Studio Getting Started, Release 4.0*, (Accelrys Software, Inc.: San Diego, 2006).

59. K. Yamaguchi, Z. Tamura, and M. Maeda, *Acta Crysta. C*, **C53** (1997), 284.

60. M. J. Frisch, G. W. Trucks, H. B. Schlegel, G. E. Scuseria, M. A. Robb, J. R. Cheeseman, J. A. Montgomery, J. T. Vreven, K. N. Kudin, J. C. Burant, J. M. Millam, S. S. Iyengar, J. Tomasi, V. Barone, B. Mennucci, M. Cossi, G.

Scalmani, N. Rega, G. A. Petersson, H. Nakatsuji, M. Hada, M. Ehara, K. Toyota, R. Fukuda, J. Hasegawa, M. Ishida, T. Nakajima, Y. Honda, O. Kitao, H. Nakai, M. Klene, X. Li, J. E. Knox, H. P. Hratchian, J. B. Cross, V. Bakken, C. Adamo, J. Jaramillo, R. Gomperts, R. E. Stratmann, O. Yazyev, A. J. Austin, R. Cammi, C. Pomelli, J. W. Ochterski, P. Y. Ayala, K. Morokuma, G. A. Voth, P. Salvador, J. J. Dannenberg, V. G. Zakrzewski, S. Dapprich, A. D. Daniels, M. C. Strain, O. Farkas, D. K. Malick, A. D. Rabuck, K. Raghavachari, J. B. Foresman, J. V. Ortiz, Q. Cui, A. G. Baboul, S. Clifford, J. Cioslowski, B. B. Stefanov, G. Liu, A. Liashenko, P. Piskorz, I. Komaromi, R. L. Martin, D. J. Fox, T. Keith, M. A. Al-Laham, C. Y. Peng, A. Nanayakkara, M. Challacombe, P. M. W. Gill, B. Johnson, W. Chen, M. W. Wong, C. Gonzalez, J. A. Pople, *Gaussian Development Version, revision D.02*, (Gaussian, Inc.: Wallingford, 2004).

61. The transition dipole moment was calculated using density functional theory (DFT) with the B3LYP functional.[62] Calculations were performed by Christine Isborn at the University of Washington, starting from molecular coordinates obtained from a crystal structure of fluorescein[59] in the Cambridge Databse and adding the chlorine atoms. This molecular structure was then optimized in order to calculate the transition dipole moment. The theoretical ground state transition electric dipole moment orientation was calculated to be 5° off from the approximated vector between the two chlorine atoms (representing the long axis of DCF's π-system). However, there is also an expected variance of about ±5° as the dye changes to excited state conformations in order to dock into the KAP lattice. Thus, in all reported orientations, the approximated vector between chlorine atoms was used.

62. a) A. D. Becke, *J. Chem. Phys.*, **98** (1993), 5648; b) C. T. Lee, W. T. Yang, R. G. Parr, *Phys. Rev. B*, **37** (1988), 785.

63. D. H. Gay and A. L. Rohl, *J. Chem. Soc. Faraday Transactions*, **91** (1995), 925.

64. a) A. L. Rohl, D. H. Gay, C. R. A. Catlow, R. J. Davey, and W. C. Mackrodt, *J. Chem. Soc., Faraday Discuss.*, **95** (1993), 273; b) A. L. Rohl, D. H. Gay, R. J. Davey, C. R. A. Catlow, *J. Am. Chem. Soc.*, **118** (1996), 642; c) D. J. Carter, A. L. Rohl, J. D. Gale, A. M. Fogg, R. W. Gurney, and B. Kahr, *J. Mol. Struct.* **647** (2003), 65; d) D. J. Carter, M. I. Ogden, A. L. Rohl, *J. Phys. Chem. C*, **111** (2007), 9283; e) Also suggested to us by A. L. Rohl in private consultation.

65. S. Wilhelm, B. Gröbler, M. Gluch, and H. Heinz, *Principles of Confocal Laser Scanning Microscopy*, (Carl Zeiss, Inc.: New York).

66. S. W. Paddock, *Mol. Biotech.*, **16** (2000), 127.

67. In CLSM, either the laser or the sample stage can be scanned to obtain a complete image within the field of view using the point-probing method. If the sample is larger than the field of view, then the sample stage can be moved in *x-y* to stitch or tile together images from multiple scans. In our research, two different confocal microscopes were utilized, both of which scanned the laser across the object. Earlier studies were performed with a Leica CLSM at the UW KECK Center.[69] Later studies used a Zeiss CLSM at the UW NTUF.[68] The former required manual stitching of images (using Adobe Photoshop™) to obtain a complete optical slice of the crystal, while the later could be set up to automatically tile the images together.

68. Zeiss LSM 510 NLO (Axiovert 100 M) inverted confocal microscope at the University of Washington Nanotechnology User Facility, a member of National Nanotechnology Infrastructure Network supported by NSF. http://depts.washington.edu/ntuf/. Typically, a 10x/0.5D FLUAR objective and 488 nm excitation light from an Argon laser was used for exciting DCF (**3**), while 543 nm light from a He-Ne laser was used to excite LGSFY (**1**) or Erio (**2**).

69. Leica TCS SP/NT on a DMIRBE incident-light inverted microscope at the University of Washington W. M. KECK Center for Advanced Studies in Neural Signaling. http://depts.washington.edu/keck/. Only KAP/LGSFY crystals were imaged on this microscope through a 5x objective, pinhole width of 1 Airy unit, and with 568 nm excitation light from a 25mW krypton ion laser.

70. F. R. N. Nabarro, *Theory of Crystal Dislocations*, (Oxford University Press: Oxford, 1967).

71. T. Vicsek, *Fractal Growth Phenomena, 2nd Ed.*, (World Scientific Publishing: New Jersey, 1992).

72. Monte Carlo events were generated within a rectangular area on the (010) face rather than within the boundaries of the entire (010) face for ease of programming. As the scanning window is also rectangular, any events occuring in the upper or lower triangular areas of the hexagonal (010) face would have been excluded anyhow.

CHAPTER 3 – ROLE OF KINKS IN DYEING CRYSTALS: DICHLOROFLUORESCEIN IN KAP

3.1 Concentration Dependent Linear Dichroism

Large potassium hydrogen phthalate crystals grown in the presence of the well-known fluorofluor and pH indicator, 2′,7′-dichlorofluorescein (**3**, DCF), show spatially localized patterns of luminescence characteristic of selective inter- and intra-sectoral zoning. As described in Section 2.4.2, linear dichroism measurements of heavily-dyed KAP/DCF crystals showed the average orientation of the transition dipole moment to be closer to the *c*-axis, ranging from 47-56° from [100] at both the 473 nm (DCFH) and 502 nm (DCF^-) absorbance peaks, with the mono-anion (DCF^-) being oriented slightly closer to *c*. Figure 3.1a presents polarized absorption spectra for KAP/DCF grown from 2.5×10^{-5} M dye, exhibiting dichroic ratios of 2.0 and 2.2 corresponding to average orientations of $54.4 \pm 1.0°$ and $56.3 \pm 1.1°$ relative to [100] for DCFH and DCF^-, respectively. Corresponding transmission and linear dichroism images made using the rotating polarizer technique[1] (as described in section 2.5.1.2) are presented in Figure 3.1b and c, respectively. As expected, KAP/DCF demonstrates the greatest absorption anisotropy in the fast slope that contains most of the dye, and the ensemble-averaged transition dipole moment orientation is closer to [001].

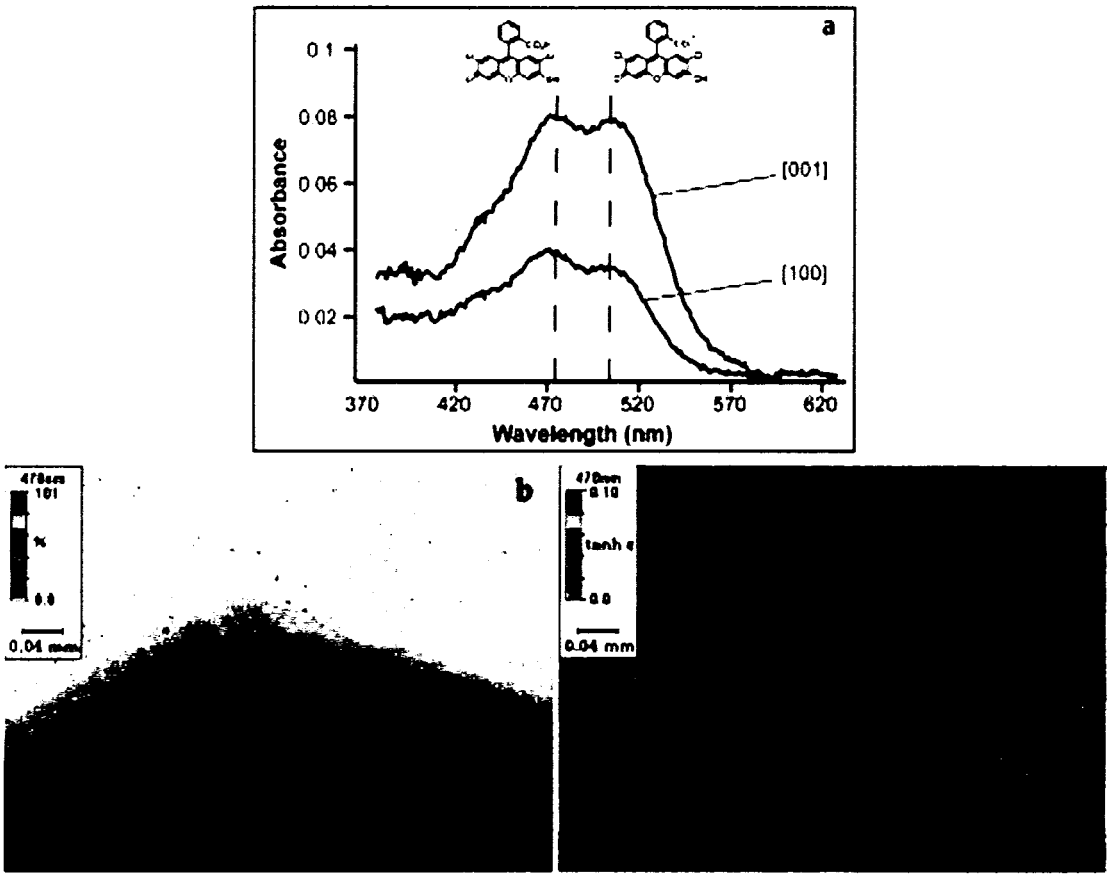

Figure 3.1. *Absorption dichroism of DCF (2.5×10^{-5}M) in the fast slopes of KAP hillocks.* (a) Polarized absorption anisotropy taken with a microabsorption spectrophotometer. Absorption maxima are observed at 473 nm (DCFH) and 503 nm (DCF^-) for both the [001] and [100] polarizations. (b) $\times10^{-5}$M) crystalLinear dichroism image where $\tanh\varepsilon = (T_\perp - T_\parallel)/(T_\perp + T_\parallel)$, with $T_\perp$ and $T_\parallel$ being the transmission components for orthogonal orientations..

Through parallel studies in our laboratories, performed by Kristin Wustholz, the photophysical properties of DCF in KAP at the single-molecule level were examined.[2] Interestingly, the orientations of included dyes obtained from ensemble-averaged dichroism measurements in heavily-dyed crystals and the average orientations of the corresponding single-molecule distributions grown

from more dilute dye solutions were at variance. The polarization dependence of the luminescence at the single molecule level indicated broad orientational distributions consistent with non-selective mixed crystal growth mechanisms. In an effort to reconcile this apparent dichotomy, KAP crystals were grown from solutions containing 10^{-9} to 10^{-4} M DCF and examined using confocal luminescence microscopy and polarized absorption spectroscopy. The linear dichroism and fluorescence excitation dichroism were found to be strongly dependent on the concentration of the luminophore, suggesting that different mixed crystal growth mechanisms were at work in different guest concentration regimes. A detailed analysis of the dependence of molecular orientation on solution dye and additive concentrations, combined with thermodynamic force-field calculations, herein shows for the first time that the selective recognition of kink sites by the luminophores is a critical step in the mechanism of crystal dyeing and in establishing dye alignment.

3.1.1 Ensemble-Averaged DCF Orientations

Linear dichroism measurements were performed on crystals with varying concentrations of DCF ($\geq 10^{-5}$ M) using conventional polarized light absorbance microscopy. To obtain orientations at dye concentrations below the detection limit of the absorbance microscope, confocal fluorescence microscopy[3] was used instead. Average orientations from confocal measurements were obtained by averaging the excitation dichroism from several 10×10 μm^2 areas in one or more crystals. Table 3.1 summarizes the average orientations and corresponding standard deviations from the mean obtained from a series of KAP/DCF crystals grown from 10^{-7} M to 7×10^{-5} M dye. From excitation dichroism measurements using 532-nm illumination, the average orientation of DCF^-, for heavily dyed

crystals where DCF ≥ 10^{-6} M, was found to be 52.1 ± 4.0° from [100]. From corresponding absorption dichroism measurements, the average orientations of DCF were determined to be 50.9 ± 3.2°, 51.9 ± 4.1°, and 57.8 ± 5.6° from [100] at 475nm, 502nm, and 532nm, respectively. As the dye concentration is decreased, the average orientation is significantly modified and becomes closer to [100]. In fact, crystals grown from 10^{-7} M dye exhibited an average orientation for DCF^- of 34.7 ± 3.2° from [100]. These results suggest that different mixed crystal growth mechanisms are at work in different guest concentration regimes.

Table 3.1. *Ensemble-averaged orientations of DCF in KAP.* Average absorption transition dipole moment orientations in KAP/DCF measured using confocal fluorescence microscopy[3] (excitation dichroism at 532 nm) and polarized absorption microscopy (absorption dichroism). [DCF] is the dye concentration in the starting crystal growth solution. Average orientations with corresponding standard deviations from the mean are reported relative to [100] in the *ac*-plane.

[DCF]	Excitation Dichroism[3] 532 nm	Absorption Dichroism 472 nm	Absorption Dichroism 502 nm	Absorption Dichroism 532 nm
1.0×10^{-7} M	34.7 ± 3.2°	n/a	n/a	n/a
5.0×10^{-7} M	41.1 ± 1.1°	n/a	n/a	n/a
1.0×10^{-6} M up to 7.0×10^{-5} M	52.1 ± 4.0°	50.9 ± 3.2°	51.9 ± 4.1°	57.8 ± 5.6°

3.1.2 *Single Molecule Studies of DCF Orientations in KAP*

The observed variation in orientation with dye concentration motivates the question: to what extent is DCF aligned in the fast steps of KAP hillocks at the

limit where interluminophore interactions are negligible? The breadth of the orientational distribution measured at the single-molecule level can reveal information about the amount of environmental heterogeneity in the host and the distribution of inclusion sites. Wustholz *et al* have previously described the use of single-molecule techniques to examine the molecular orientation and photophysics in dyed salt crystals.[2] In the collaborative experiments described herein, single-molecule fluorescence microscopy was used to measure the average orientation of DCF in KAP at extremely dilute dye concentrations and determine the extent of chromophore alignment. Figure 3.2a and b shows a typical single-molecule dataset, consisting of false-color images of the fluorescence from KAP/DCF grown from a solution containing 5×10^{-9} M dye, with images corresponding to excitation along the [100] and [001] eigenmodes of the crystal. Molecules that are brighter with excitation polarization parallel to [100] and [001] have absorption dipole moments oriented closer to the *a*- and *c*-direction, respectively. For single-molecule experiments employing 405-nm illumination, corresponding to excitation of DCFH, the average orientation of 180 molecules in KAP was found to be 42.6 ± 18.3° from [100], with values ranging from 5.8° to 86.5° (Figure 3.2). The single-molecule measurements were repeated using 532-nm illumination, corresponding to excitation of DCF^-, yielding an average orientation for 151 molecules of 38.6 ± 15.5° from [100], with the orientational distribution ranging from 9.3° to 70.9° (Figure 3.2). The FWHM of the orientational distributions following 405-nm and 532-nm excitation were ~55° and ~50°, respectively.

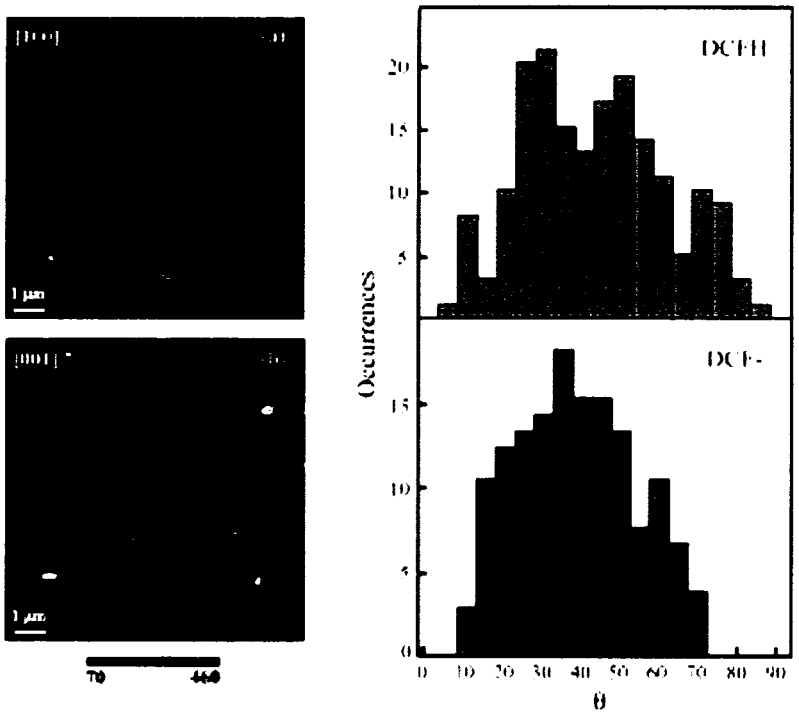

Figure 3.2. *Single molecule distribution of DCF in KAP.* False-color 10×10 μm^2 images of the fluorescence from a KAP crystal grown from 5×10^{-9} M DCF obtained from 532-nm excitation along orthogonal eigenmodes, (a) [100] and (b) [001]. Color scale corresponds to counts per 100 ms. (right) Corresponding single-molecule orientational histograms for 180 molecules employing 405-nm excitation (DCFH), measured as an angle between 0° and 90° from [100]. The average was found to be 42.6 ± 18.3° from [100]. For 151 molecules excited at 532 nm (DCF^-), the average orientation was 38.6 ± 15.5° from [100]. (Reproduced with permission by Wustholz *et al*)[2]

The single-molecule data demonstrate three important results. First, the average of the single-molecule orientations, measured on crystals containing nanomolar quantities of DCF in the growth solution, is significantly different from ensemble-averaged measurements on heavily-dyed crystals (grown from 10^{-6} M to 7×10^{-5} M dye), consistent with the results summarized in Table 3.1. Next, the breadth of the orientational distributions demonstrates that single

molecules are poorly aligned in the crystal host and adopt a wide variety of molecular orientations, despite the fact that heavily-dyed crystals demonstrate specific chemical zoning that directs dyes primarily to the fast slopes of growth hillocks. For cases in which dyes in the crystals have narrow distributions, the dichroism is consistent with a single structurally well-defined site,[2,4,5] the single-molecule orientational distribution is narrow (FWHM ~10°). Therefore, the observation of extremely wide orientational distributions for KAP/DCF suggests that dyes incorporate into multiple conformations. This could indicate that either there are several acceptable inclusion sites in the {010} hillocks, or there are a few primary inclusion sites that provide enough room for the dye to adopt a number of different orientations upon integration. Lastly, using two excitation wavelengths for single-molecule measurements reveals that both the neutral and monoanionic forms of DCF are incorporated within {010} in similarly wide orientational distributions, despite previous optical and EPR studies on the acid base indicator diaminoacridine that exhibited differences in the states of dye protonation and orientation in the different growth sectors of KAP.[6] Overall, single-molecule measurements of molecular orientations of DCFH and DCF^- in KAP/DCF suggest a significant amount of environmental heterogeneity in the host and a wide variety of inclusion sites.

3.2 Dye Impact on Hillock Morphology

What is the origin of concentration-dependent orientation in KAP/DCF? Some impurities are known to modify the habit and morphology of KAP crystals. For instance, as described in Section 2.3.4, Hottenhuis *et al* observed drastic alterations to KAP step kinetics and hillock morphology due to the presence of various trivalent cationic additives during growth from solution.[7] The impurities were found to slow step movement through pinning and

competition with KAP building units for available binding sites, consistent with site-specific adsorption of the impurities.[7] Therefore, the main categories of impurity adsorption in KAP hillocks were expanded to encompass inclusion on the terrace, at a step edge, in a vacancy along the step edge, and in two non-equivalent kink sites within the hillock fast steps.[7]

One hypothesis why changing dye concentration in solution impacts average orientation in the crystal is that DCF may modify KAP hillock morphology at high dye concentrations. In particular, the addition of DCF may influence both the kink density and growth kinetics of the fast steps where the dye is incorporated, generating a greater diversity of binding sites. To a first approximation using differential interference contrast (DIC) and fluorescence microscopies, morphological changes to a hillock are observable through the angle spanning the boundary between its fast and slow slopes (also seen as the apices of the hillock 'chevrons', see Figure 3.1b and c for example). At a more detailed level, morphology changes can be observed through atomic force microscopy (AFM) imaging. Therefore, to test the hypothesis that DCF may modify KAP morphology, we measured the angles of the fast-slow boundary of the hillocks, as well as the various step orientations of the hillocks on a series of KAP/DCF crystals grown from different dye concentrations.

For the ideal KAP habit, where the step edges are defined by the crystallographic directions <101> and $<10\bar{1}>$, the fast and slow steps of the {010} hillocks are oriented at ±34° from [100] and the angle spanned by the fast-slow boundary is 124°.[8] These values for pure KAP morphology have been confirmed by DIC and AFM measurements (Table 3.2).[10,11] For KAP/DCF crystals the average slow step orientation, as seen by AFM[9], remained unchanged, while the

fast step orientation experienced slight modification and was found to be 42 ± 2° (Figure 3.3 and Table 3.2). AFM images of KAP/DCF hillocks also showed a rounding out of the junction between the fast and slow steps, due to the presence of and step pinning in the <100> intermediate steps (Figure 3.3). This curved region of deviation from straight steps was significantly greater in the presence of DCF, with an average angular span of 37 ± 4°, than in pure KAP whose <100> steps are straight and only span a region of 6 ± 4° (Table 3.2). Overall, AFM images indicate slight morphological changes due to the *presence* of DCF, but these changes appear to be independent of dye *concentration.*

At a macroscopic scale, DIC measurements showed a small change to the fast-slow boundary of KAP/DCF cyrstals, giving an average angle of 127 ± 2°. At the highest dye concentrations (≥ 5×10^{-5} M) the fast-slow boundary angle approached 130°, indicating a small concentration dependence. However, this is a relatively modest change compared to the impact of trivalent cations on hillock morphology.[7] For example, the fast-slow boundary approaches as wide as 180° in the presence of Fe^{3+} and as sweeping as 359° at high concentrations of Ce^{3+} (Figure 3.4).[7] Since the observed morphology changes to KAP hillocks were modest even at high dye concentrations, we tested the extreme cases of morphological influences on dye orientations by adding Ce^{3+} and Fe^{3+} cations to the crystal growth solutions.

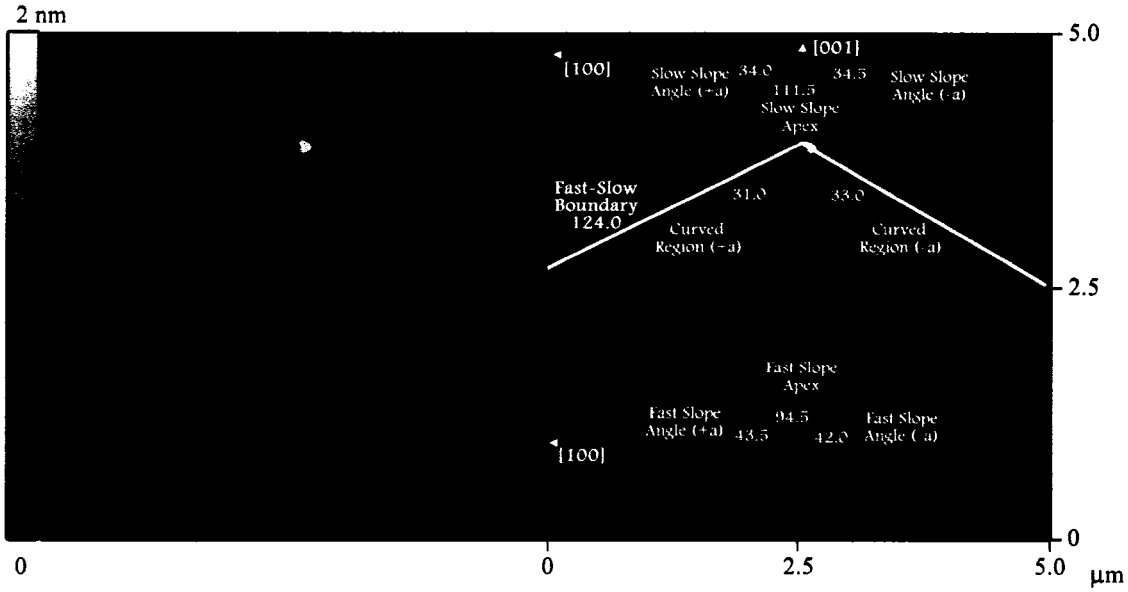

Figure 3.3. *AFM image of KAP/DCF hillock.* Image on the left is the raw AFM data of a sample KAP/DCF (10^{-5} M) hillock, while the image to the right is the same hillock with various step and morphology features outlined and angular measurements labeled. Table 3.2 gives the resulting measurements for a number of sample crystals at varying DCF concentrations. (AFM image taken by and reproduced with permission of John Freudenthal)[9]

Table 3.2. *Hillock morphology measurements from AFM and DIC images.* The fast slope orientations shift slightly closer to [100] for KAP/DCF crystals compared to pure KAP, while the slow slopes remain unaltered. The curved region also becomes more pronounced in KAP/DCF crystals compared to pure KAP. AFM images indicate that the morphological changes appear to be dependent upon dye presence but independent of concentration above 10^{-7} M. At a macroscopic scale, however, DIC images of the fast-slow boundary indicate a small concentration dependence at heavily dyed concentrations (right-most column).

[DCF]	# Samples	Fast Slope Angle	Slow Slope Angle	Curved Region	Fast-Slow Boundary
Idealized KAP	n/a	34°	34°	0°	124°
Pure KAP (DeYoreo)[10]	1	34 ± 1°	34 ± 1°	2 ± 1°	124°
Pure KAP (Kurimoto)[11]	1	38 ± 1°	34 ± 1°	10 ± 1°	124°
1×10^{-7} M	2	43 ± 1°	35 ± 1°	44 ± 2°	125 ± 1°
5×10^{-7} M	3	41 ± 1°	34 ± 1°	40 ± 3°	125 ± 1°
5×10^{-6} M	2	43 ± 3°	36 ± 3°	38 ± 2°	126 ± 1°
1×10^{-5} M	10	43 ± 3°	34 ± 2°	36 ± 4°	126 ± 3°
2.5×10^{-5} M†	4	-	-	-	128 ± 1°
$\geq 5\times10^{-5}$ M†	7	-	-	-	130 ± 1°

† DIC measurements only (no AFM data was taken at these concentrations)

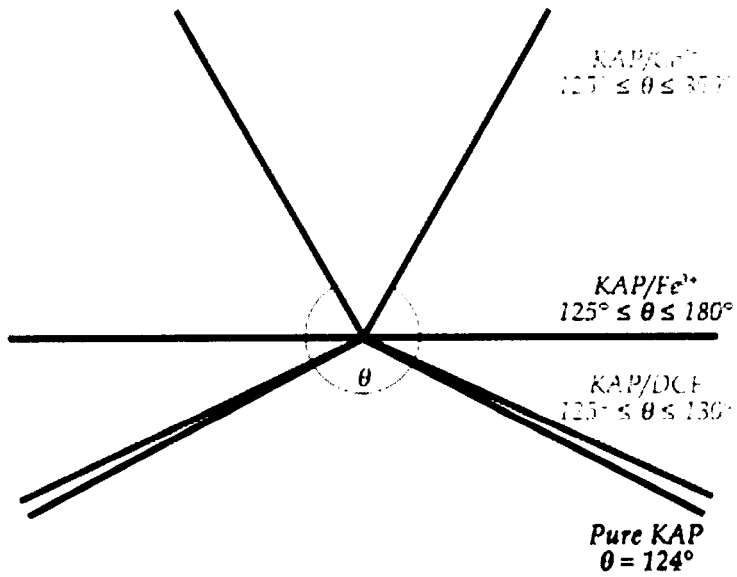

Figure 3.4. *Angle spanned by the boundary between the fast and slow steps of KAP hillocks.* Pure KAP hillocks have an angle (θ) of 124°. When DCF is added the angle varies between 125° and 130° for high dye concentrations. Trivalent cations such as Fe^{3+} and Ce^{3+} can alter the hillock morphology significantly, causing the angle between the fast and slow steps to become as wide as 180° and 359°, respectively, at high impurity concentrations.

3.3 Experiments with Trivalent Cationic Additives

In a series of studies, Hottenhuis *et al* demonstrated that partially hydrated Ce^{3+} and Fe^{3+} function as specific kink-blocking impurities in KAP, producing dramatic dichotomous changes in hillock morphology (see also Section 2.3.4).[7] As KAP's polar *c*-axis causes a differentiation between fast and slow steps of the {010} hillocks, the kink sites along these steps are also different in structure. Thus, two unique adsorption sites exist: one on the +*c* side of a step where the kink site advances in the <101> directions upon addition of a new unit, the other on the -*c* side of a step where the kink site advances in the $<10\bar{1}>$ directions (Figure 3.5). Upon the addition of Ce^{3+} to growth solutions, the fast steps of KAP

were observed to become progressively misoriented towards $[10\bar{2}]$ until the corner between the $[10\bar{1}]$ and $[\bar{1}0\bar{1}]$ fast steps became sharply pointed.[7] Spirals were elongated along [001] relative to pure KAP, the angle of the boundary between the fast and slow steps became acute toward the +*c* direction, and the slow steps were unaltered. Therefore, the authors determined that Ce^{3+} binds preferentially to the +*c* kink sites, blocking the further addition of KAP units to the +*c* binding sites and only allowing for continued growth into the -*c* kinks and along the step edges, resulting in an elongation of the fast slopes towards $[00\bar{1}]$, and a narrowing along [100]. With the addition of Fe^{3+}, the fast steps became progressively rounded until the corner between the $[10\bar{1}]$ and $[\bar{1}0\bar{1}]$ fast steps disappeared.[7] Spirals were shortened along [001], and the angle of the boundary between the fast and slow steps flattened out along [100]. From these observations, Hottenhuis *et al* concluded that Fe^{3+} prefers the -*c* kink sites, blocking further addition at these sites and forcing future growth at the +*c* kinks and along the step edges, resulting in a rounding and shortening of the fast slope along $[00\bar{1}]$ and widening in [100]. Figure 3.5 presents a schematic of the kink blocking scenarios and the resulting spiral hillock morphologies.

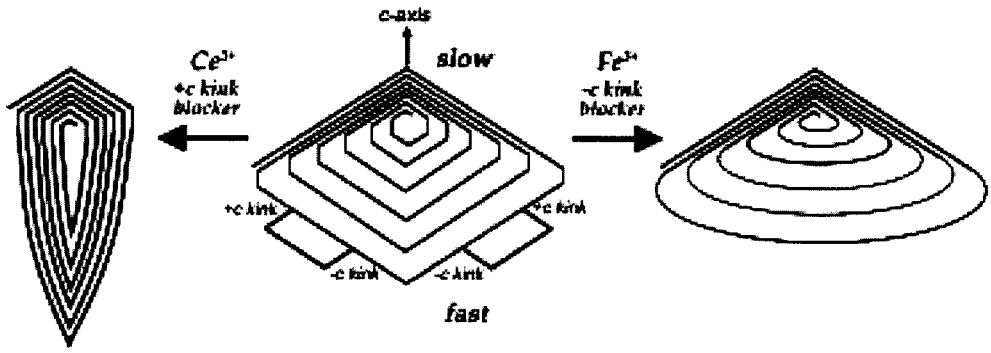

Figure 3.5. *Selective kink adsorption of impurities into KAP hillock fast steps.* +*c* kink blockers such as Ce^{3+} (left) narrow and elongate hillock fast slopes, misorienting steps towards $[10\bar{2}]$. -*c* kink blockers like Fe^{3+} (right) widen and round out hillock fast steps. Figure adapted after Hottenhuis *et al.*[7]

The influence of hillock morphology on dye incorporation was investigated by adding trivalent cations into the crystal growth solutions. Various concentrations of cerium chloride (0.1 to 15 ppm $CeCl_3 \cdot 7H_2O$ with respect to KAP) or ferric nitrate (5.0 to 20 ppm $Fe(NO_3)_3 \cdot 9H_2O$, with respect to KAP) (J. T. Baker) were added to the crystal growth solution, which was then filtered to remove undissolved particulates, and subsequently grown by slow evaporation, as described in Chapter 2. This work was performed by REU student Miranda Robertson, under my supervision.

3.3.1 Fe^{3+} Additive

To examine with greater certainty the interplay between hillock morphology and dye orientation, we studied KAP crystals grown in the presence of DCF as well as the kink blockers, Ce^{3+} and Fe^{3+}. First, varying amounts of Fe^{3+} were added to KAP/DCF growth solutions in order to determine how DCF behaves when the $-c$ kink sites are occupied and the resulting hillocks are broadened and rounded. We observed that crystals of KAP/DCF/Fe^{3+} were half as bright as non-ferric KAP/DCF crystals obtained under the same growth conditions. For example, crystals grown at 10^{-5} M DCF and 10 ppm Fe^{3+} showed an average emission intensity (normalized by crystal thickness) of $7.3 \pm 0.6 \times 10^4$ counts/sec/mm. In contrast, crystals grown at 10^{-5} M DCF with no cations emitted $1.2 \pm 0.2 \times 10^5$ counts/sec/mm. The observation of less dye incorporation suggests that DCF is adverse to the $+c$ kink sites, of which there are many available due to the corresponding morphology changes, and that Fe^{3+} competes with DCF for other preferred binding sites. The DCF emission peak was also blue shifted by about 10 nm in the presence of Fe^{3+}. The average dye orientation in KAP/DCF/Fe^{3+} crystals as a function of ion content was found to be $41.2 \pm 2.7°$ from [100] for DCFH and $42.0 \pm 2.4°$ from [100] for DCF^-, as determined by both

polarized absorbance and excitation dichroism measurements (Figure 3.6). The dye orientation was statistically equivalent for crystals grown from various dye (10^{-6} M to 5×10^{-5} M) or cationic-impurity (5 to 20 ppm) concentrations. The apparent indifference of dye orientation to cation concentration suggests that the dye is constrained to a very limited number of docking configurations, unrelated to kink sites, in the presence of Fe^{3+}. In fact, this orientation is close to what might be expected if the dye's transition dipole moment were aligning close to the $[10\bar{1}]$ fast step edges in KAP hillocks, which are ideally oriented at 34° from [100] (see Section 3.4.3). That dye orientation was constant regardless of dye content was surprising, considering earlier observations of concentration-dependent orientations for KAP/DCF crystals grown without any cationic additives.

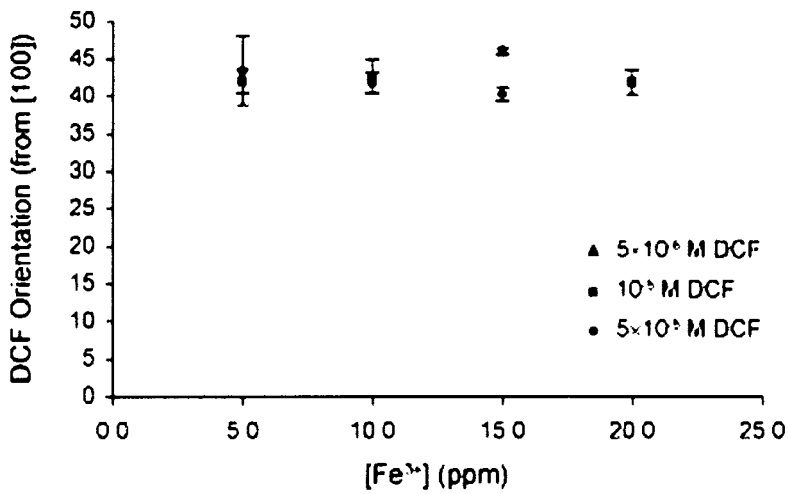

Figure 3.6. *Average DCF orientation as a function of Fe^{3+} dopant.* Error bars correspond to the standard deviation from the mean. Average dye orientation remains the same at 41.2 ± 2.7° from [100] for DCFH and 42.0 ± 2.4° from [100] for DCF^-, regardless of Fe^{3+} and dye concentrations. Note: for clarity, only DCF^- data is shown.

3.3.2 Ce^{3+} *Additive*

To test the hypothesis that DCF prefers the *-c* kink site in KAP we grew crystals of KAP/DCF containing various concentrations of Ce^{3+}, a *+c* kink blocker. Crystals of KAP/DCF/Ce^{3+} ($\geq 10^{-6}$ M DCF) were about 31 times more luminescent ($3.6 \pm 0.5 \times 10^6$ counts/sec/mm) than crystals obtained using the same growth conditions but without any cationic additives. Additionally, the DCF emission peak was blue shifted by 5 nm in the presence of Ce^{3+}. These results are indeed consistent with the hypothesis that DCF prefers the *-c* kink site in the fast slopes of KAP hillocks. Figure 3.7 presents the average orientation of DCF obtained using polarized absorption and excitation measurements in crystals of KAP/DCF/Ce^{3+} as a function of Ce^{3+} concentration. For crystals grown from three different concentrations of DCF, it is clear that dye alignment is sensitive to Ce^{3+}-induced morphological changes, but independent of DCF concentration. At low Ce^{3+} concentration the dye orientation is similar to that of heavily dyed KAP/DCF crystals without any cations. As the Ce^{3+} concentration is increased up to 5 ppm (where 1 ppm = 0.056 μmol/mL), the dye orientation moves progressively closer to $25.2 \pm 2.8°$ from [100] for DCFH and $21.0 \pm 2.5°$ from [100] for DCF^-, indicating a switch in orientation from closer to [001] to closer to [100]. The data suggest that the dye increasingly adopts an orientation associated with the *-c* kink site, as a greater number of *-c* kinks are created and freely available for DCF adsorption due to the morphological changes induced by Ce^{3+}. Thus, the dichroism resulting from *-c* kink site incorporation increasingly dominates the signal over that from other incorporation sites.

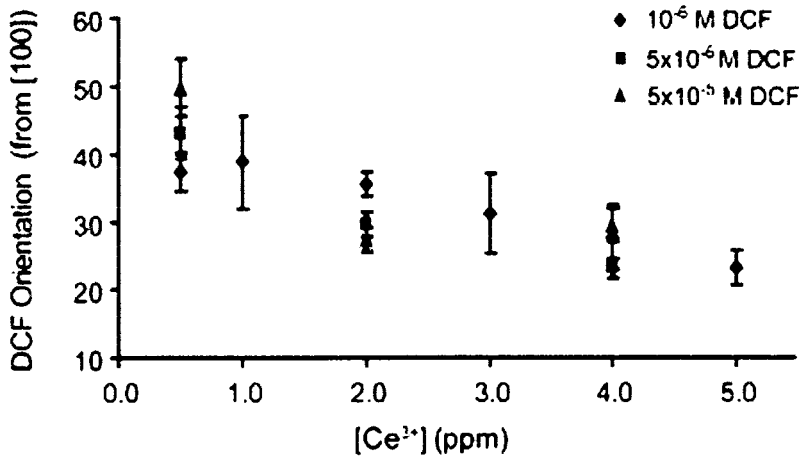

Figure 3.7. *Average DCF orientation as a function of Ce^{3+} dopant.* Error bars correspond to the standard deviation from the mean. Average dye orientation shifts progressively closer to [100] for both DCFH and DCF^- with increasing Ce^{3+} concentration, irrespective of dye concentration. Note: for clarity, only DCF^- data is shown.

Due to their bright fluoresecence, we also took emission spectra for the KAP/DCF/Ce^{3+} cyrstals at 10^{-6} M DCF as a function of Ce^{3+} concentration. The peak emission intensity was recorded for several (5-9) crystals at each Ce^{3+} concentration and normalized by crystal thickness, as measured via micron-scale calipers (Figure 3.8). Coupled with visual inspection of the crystals and their resulting dye inclusion, it became clear that the initial increase in normalized emission intensity was due to greater dye inclusion within the (010) sector. This resulted from the morphological changes induced by Ce^{3+}, where the fast-slow boundary gradually increased its angluar spread, allowing the fast slopes to dominate more of the (010) face. The measure of this angle increased from 132 ± 2° at 0.1 ppm of Ce^{3+}, flattening to 182 ± 3° at 2ppm, turning acute towards [001] by 5ppm with an angular spread of 220 ± 18°, and nearly engulfing the entire hillock spiral with an angular spread of 355 ± 3° at ≥ 7 ppm (Figure 3.9). Simultaneously, the centers of the hillocks shifted progressively closer towards

the +*c* end of the (010) face. However, after 5 ppm it also became clear that the continued increase of Ce^{3+} concentration became a significant impediment to continued growth and dye inclusion, presumably due to step pinning. For example, dye inclusion could be seen in early stages of growth but there was almost no visible dye inclusion in later growth (see 10 ppm crystal in Figure 3.9). Furthermore, the crystals became exceedingly thin at high Ce^{3+} concentrations.

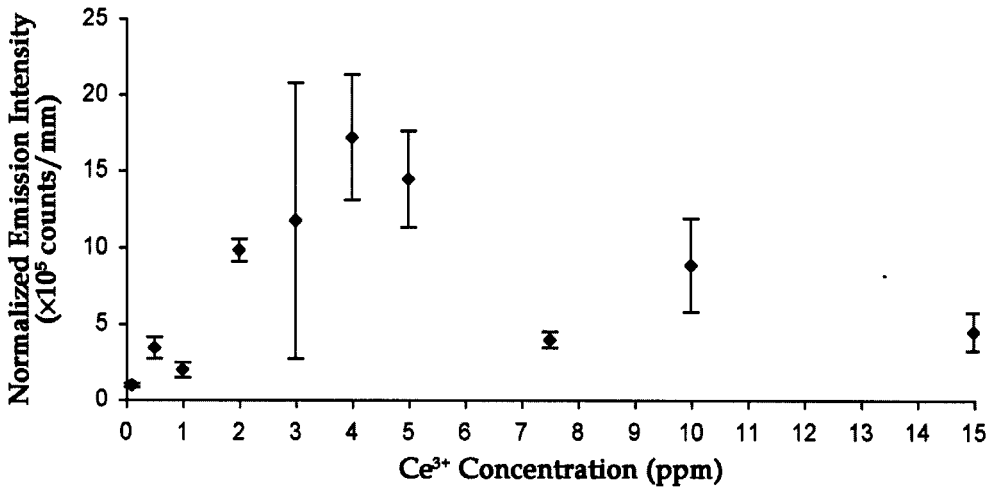

Figure 3.8. *Normalized emission intensity as a function of Ce^{3+} concentration for KAP/DCF/Ce^{3+} (10^{-6} M).* Bulk fluorescence intensity is normalized by crystal thickness. Intensity initially increases for Ce^{3+} concentrations up to 4ppm, as a result of greater dye inclusion within the (010) face. At concentrations greater than 4ppm, normalized emission intensity decreases due to less dye inclusion and thinner crystals resulting from severe growth inhibition by the Ce^{3+}.

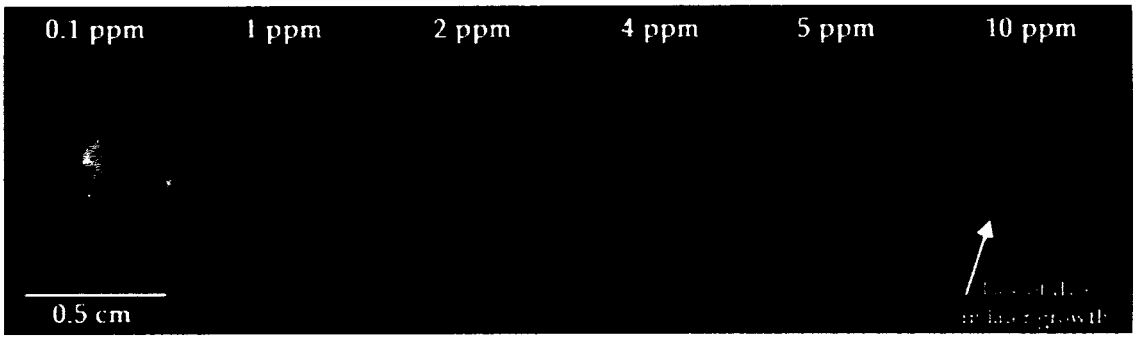

Figure 3.9. *KAP/DCF/Ce^{3+} images at different Ce^{3+} concentrations.* These sample crystals show the progressive widening of the fast-slow boundary angle and increased dye inclusion within the (010) face as Ce^{3+} concentration is increased. The 10 ppm sample also shows the inhibition of dyeing during the later stages of growth, indicated by the dark outer region, however the entire (010) face was dyed in early growth.

In summary, our observations suggest that DCF binds preferentially to the *-c* kink site. Morphological changes to the hillocks as a result of cation additives are clear from DIC and fluoresecence measurements. At high impurity concentrations significant step pinning and growth inhibition are observed, resulting in thinner crystals and no dye inclusion in later growth. Even at low concentrations, the presence of Fe^{3+}, a *-c* kink blocker, inhibits dye incorporation from all but a small number of vacancies in the step edges, consistent with an average dye orientation of 41.2 ± 2.7° from [100] for DCFH and 42.0 ± 2.4° from [100] for DCF^-, regardless of dye or ion concentration. Given the large number of available *+c* kink sites and yet the noticeable lack of dye incorporation when Fe^{3+} is present, it is clear that the dye does not favor the *+c* kink sites. In contrast, the addition of Ce^{3+}, a *+c* kink blocker, encourages greater dye incorporation relative to KAP/DCF by creating more *-c* kinks through morphological changes to the hillocks, confirming that DCF indeed favors *-c* kink-site adsorption. At low Ce^{3+} concentration the dye orientation is similar to that found in KAP crystals containing DCF as the only additive. As the ion concentration is increased and

the morphological changes to the hillocks are amplified, the average dye orientation progressively approaches a value of 25.2 ± 2.8° from [100] for DCFH and 21.0 ± 2.5° from [100] for DCF^-. This orientation is presumably that adopted by DCF upon incorporation into the -*c* kink sites. To predict the theoretical transition electric dipole moment orientations of DCF that would correspond to the various docking sites (terrace, step-edge, step-vacancy, and two non-equivalent kink sites), I performed force-field calculations for the stable (010) KAP surfaces.

3.4 Force-Field Calculations

Force-field calculations[12] were empolyed to help illucidate the apparent dichotomy of broad single molecule orientational distributions and yet high specificity indicated by intrasectoral zoning and selective kink recognition of DCF in KAP. The thermodynamically favorable molecular orientations of DCF^- and DCFH in the stepped and kinked (010) KAP surfaces that contribute to the observed orientations were modeled (see Section 2.5.2 for experimental details of the simulation set-ups). The DCF- and DCFH ground state conformations were obtained from geometry optimizating the isolated dye molecules (beginning from initial coordinates as described in Section 2.5.2). DCF^- is distinguished from DCFH in that the carboxylate group is coplanar with the phenyl ring, whereas it makes a dihedral angle of 4° in the protonated congener. The angle between the phenyl and xanthene rings is 83° and 90° in DCF^- and DCFH, respectively. The most significant quantities obtained from modeling the docking of an additive into a given site within a crystal lattice are the transition dipole moment orientation, approximated as the vector between the two chlorine atoms,[13] and the relative reaction energy ($E_{reaction}$) or the change in energy upon docking the dye in place of a KAP unit. Rohl and coworkers have demonstrated the validity

and usefulness of the following type of formula for calculating the relative reaction energy of replacing a crystal unit with a dye molecule:[14]

$$E_{reaction} = E_f - E_i = \left(E_{step+dye} + E_{Phthalate^-}\right)_f - \left(E_{step} + E_{dye}\right)_i \tag{3.1}$$

where E_{step} is the total energy of either the relaxed straight or kinked step for the stable (010) surfaces, $E_{step+dye}$ is the optimized total energy of the straight or kinked step with a dye molecule docked in place of a KAP unit, $E_{Phthalate^-}$ is the internal energy of the minimized isolated phthalate anion removed in the case of DCF^- (for DCFH docking this parameter is set to zero because the phthalate and K^+ are already removed from the E_{step} calculation. See Experimental Section 2.5.2), and E_{dye} is the internal energy of the optimized isolated dye molecule. Table 2.5 in the experimental description of Chapter 2 lists the calculated values for these parameters. The primary differences in initial simulation setup for DCF^- and DCFH were due to charge neutrality restrictions and are also described further in Section 2.5.2. Due to these differences in simulation conditions, as well as the absence of solvation energies in the calculations, the reaction energies for DCF^- and DCFH cannot be directly compared relative to each other. The transition dipole moment orientations and reaction energies of many combinations of stepped or kinked surfaces and docking sites were calculated for both the aromatic hydrocarbon terminated (Figure 3.10a) and partial-K^+ terminated (Figure 3.10b) neutral surfaces, totaling over a hundred simulations all together. In general, exothermic reaction energies were produced from the adsorption of the dye's carboxylate (or carboxylic acid) group to a K^+ ion (and sometimes an oxygen in a phthalate anion) in a similar manner that a phthalate would fit into the KAP lattice.

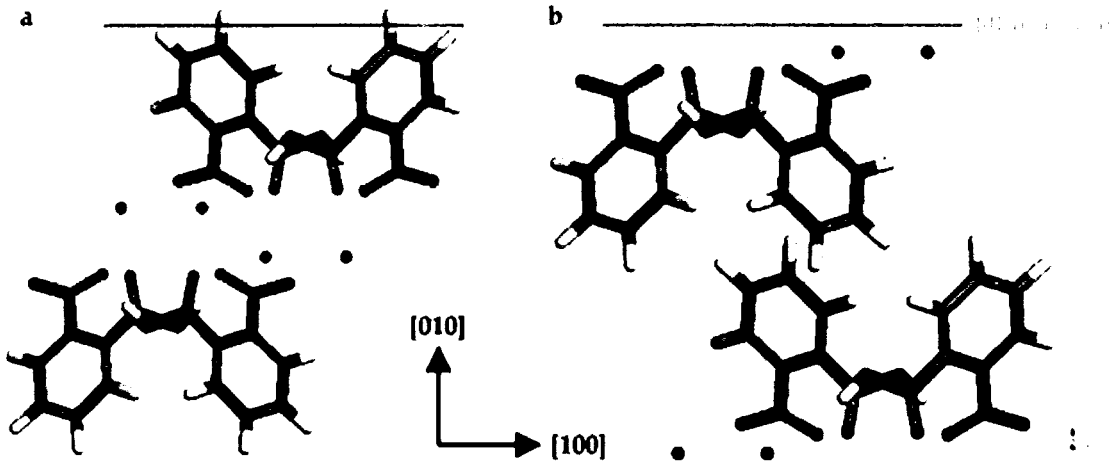

Figure 3.10. *Stable (010) surface terminations.* a) Hydrocarbon (C-H) surface termination with aromatic rings sticking up from the surface, and a total surface energy of 0.697 kJ/mol per unit cell. b) Partial-K^+ surface termination, where each unit cell of surface area is half covered with K^+ ions, while the other half exposes oxygens from the carboxylate and carboxylic acid groups of the phthalates. The total surface energy is 3.113 kJ/mol per unit cell, which is thermodynamically less stable than the C-H termination (in vacuum). In both images the green line represents the surface level.

3.4.1 Terrace Docking

Recall that the main sites for impurity adsorption (or "docking") in KAP hillocks include: on a terrace, at a step edge, in a vacancy along the step edge, and in two non-equivalent kink sites within the hillock fast steps.[7,15] Simulations for docking DCF onto a neutral (010) terrace gave mixed results.[16] For the hydrocarbon surface termination, which is the most stable (010) surface in vacuum with a total surface energy of 0.70 kJ/mol/Å^2 and attachment energy -82 kJ/mol per unit cell, no terrace docking occured. The minimum energy configuration always prefered to dock the dye up against a step edge rather than on a terrace (see Section 3.4.2). When a flat (non-stepped) hydrocarbon surface

termination was modeled the reaction energy for docking the dye was endothermic.

The partial-K^+ terminated surface (total surface energy of 3.11 kJ/mol/Å^2 and attachment energy of -367 kJ/mol per unit cell), on the other hand, was amenable to docking DCF on the terrace. The final energy configurations for docking DCFH resulted from the carboxylic acid group of the dye bonding with one or two K^+ ions and a neighboring oxygen from a phthalate, while the two oxygen atoms at either end of the xanthene wings also prefered to bond with accessible K^+ ions on the surface. There are only two possiblities for pairs of nearest neighbor K^+ ions to which both oxygens of the carboxylic acid group can bind simultaneously. The inter-ion separation of these neighboring K^+ ions is 4.32 Å, and they are related by mirror symmetry about the *a*-axis at an angle of ±48.5° from $[\bar{1}00]$ (Figure 3.11). Due to the variable dihedral angle between the carboxylic acid group and the phenyl ring, a wide range of DCFH orientations resulted. In this combination of bonds between the surface and dye, the average transition dipole moment orientation from 15 different simulations was 37 ± 25° from [100]. Terrace docking on a stepped surface was always endothermic, however docking to a flat surface, surprisingly, gave exothermic reaction energies.

Despite favorable docking results for DCF onto the flat partial-K^+ terminated surface, it is unlikely to be one of the primary mechanisms for DCF inclusion in KAP. If it were, the entire (010) face would be colored by the dye. Terrace docking does not discriminate between fast and slow slopes of the hillock and therefore would not result in the intrasectoral zoning observed. Recent theoretical studies by Carter *et al.*[17] in comparison with experimental studies by

Gurney *et al.*[18] of potassium sulfate (K_2SO_4) dye inclusion crystals also suggest that the docking of additives onto terraces is too simplistic of a process to accurately explain dye incorporation, even in the case of intersectoral zoning. However, these simulations may indicate that the dye will more likely adsorb onto and difuse around the growing surface when K^+ ions are present at the (010) termination, rather than with a strictly C-H termination. On the other hand, the discrepancy between the experimental and theoretical results may indicate that, while both surface terminations are present during growth, the C-H terminated surface is indeed the most stable and exposed (010) surface, even in solution, hence there is minimal terrace docking by DCF. However, whether DCF competes with KAP units on the surface that is long-lived or short-lived remains an open question.

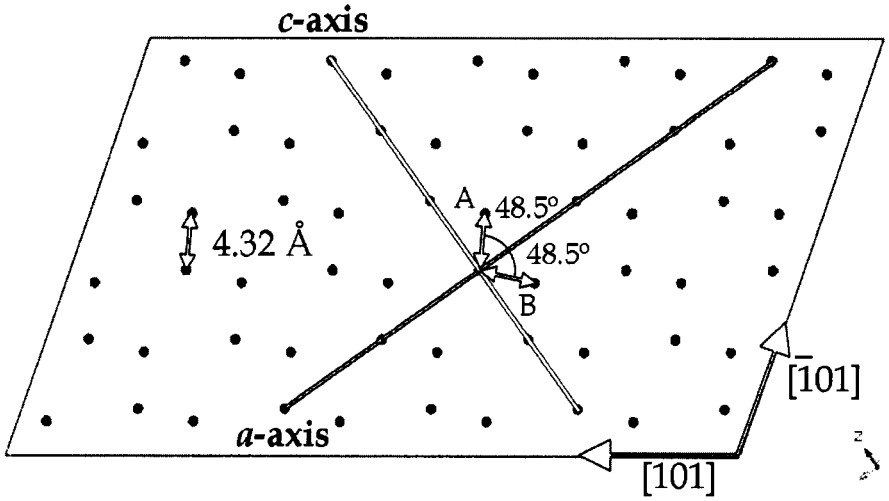

Figure 3.11. *Arrangement of K^+ ions on the partial-K^+ terminated (010) KAP surface.* There are two pairs of nearest neighbor K^+ ions separated by 4.32 Å and oriented at ±48.5° from [$\bar{1}$00], to which the carboxylate (or carboxylic acid) group of DCF^- (or DCFH) binds in a minimum energy configuration. This configuration results in an average dye orientation of 67 ± 2° from [100].

3.4.2 *Step-Edge Docking*

DCF's selective affinity for the fast slopes of KAP (010) hillocks is indicative of chemically specific interactions with the $<10\bar{1}>$ steps. Thus, even more likey than terrace docking, which should not discriminate between fast and slow slope inclusions, is step-edge docking. Once more, due to the charge neutrality requirement, only DCFH docking at step edges on both the C-H (Figure 3.12a) and partial-K^+ (Figure 3.12b) terminated surfaces was modeled. In all simulations, step-edge docking resulted in exothermic reaction energies for both the fast and slow steps (Table 3.3). Docking at the fast step edges, however, was relatively more thermodynamically favorable than docking at slow step edges. Additionally, given that step kinetics (not included in the calculations) also favor the fast steps, we can conclude that both thermodynamics and step kinetics collaborate to capture DCF within the fast slopes of KAP (010) hillocks.

In general, modeling results gave a variety of docking configurations at the step edge. For the hydrocarbon termination, the accessible K^+ ions are all sandwiched between phthalates in the middle of the step face (Figure 3.12a). Thus, the primary docking mechanism at both the fast and slow steps was for the carboxylic acid group of the dye to attach to either one or two K^+ ions in the middle of the step face, often with its hydrogen atom also coupling to an oxygen of a neighboring phthalate. In these simulations, the dye always traveled over to a step edge during energy minimization, rather than docking on the flat terrace, confirming that there is little to no interaction between the aromatic hydrocarbon rings and the dye. Dye orientations ranged from 7° to 20° from [100], with an average orientation of 14 ± 6° for the fast steps, and ranging from 32° to 80° from [100], with an average of 56 ± 24° for the slow steps (Table 3.3).

In the simulations for step-edge docking with the partial-K^+ (010) termination, it was common for the oxygen atoms at either end of the xanthene ring to bond with K^+ ions on the surface. This led to a wider variety of docking configurations for the dye. When both oxygens on the sides of the xanthene bonded to K^+ ions at the terrace, then the carboxylic acid group of the dye ended up pointing at the middle of the step face or parallel to it, but was not strongly bonded, due to the middle of the step being a sandwich of aromatic rings governed only by van der Waals forces. On the other hand, when the dye's carboxylic acid group played a key role in the bonding at the step edge, by affiliating with a phthalate at the upper part of the step (near the surface), then only one oxygen from the xanthene could reach the lower terrace to bond with a K^+ ion (as shown in Figure 3.12b). Dye orientations varied from 1° to 5° from [100], averaging to 3 ± 2° for the fast steps, and from 54° to 80° from [100], with an average of 67 ± 13° for the slow steps (Table 3.3). Terrace docking was also common in these simulations, with the dye adopting similar bonding configurations and orientations to those given in Section 3.4.1.

Insight into DCF's preference for step edge adsorbtion versus terrace adsorbtion for the partial-K^+ termination can be gained by comparing the reaction energies from various simulations of docking DCFH onto the same stepped surface. As shown in Table 3.3, the average energy for docking at the fast step edge was -194 ± 1 kJ/mol, whereas when simulations with the same surface cut resulted in the dye docking to the lower terrace, an average reaction energy of 892 ± 10 kJ/mol resulted. This stark difference in reaction energies between the same surface cut and dye molecule indicates that it is more favorable for the dye to adsorb to a step edge than to a flat terrace.

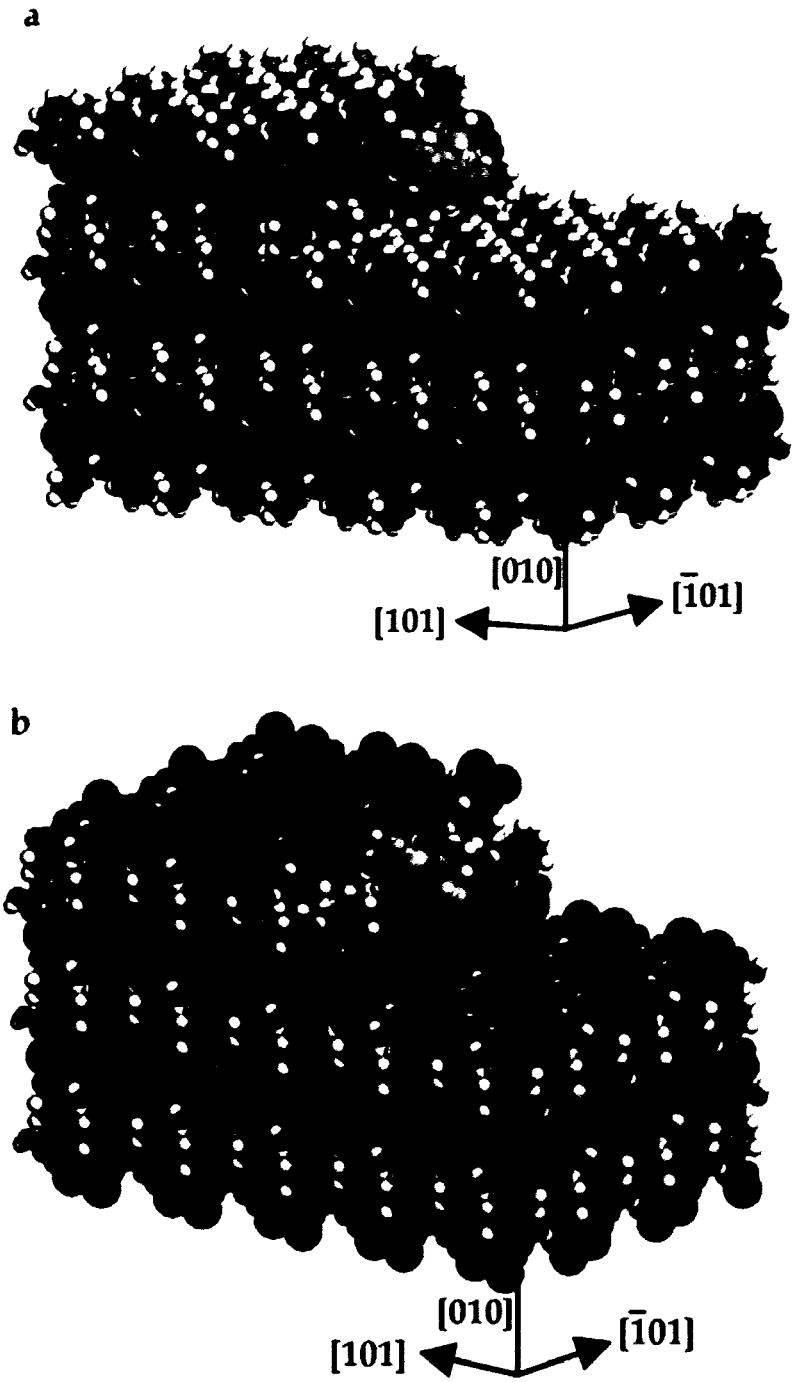

Figure 3.12. *Step edge docking of DCFH.* a) DCFH attaches its carboxylic acid group to a K^+ and O^- of a phthalate in the middle of the fast step edge on the C-H terminated (010) KAP surface when no specific

docking site is created. With this termination, DCFH always prefers to adsorb at the step edge and never on the flat terrace. b) In the case of the partial-K^+ terminated (010) KAP surface, DCFH attaches its H from the carboxylic acid group to an O from a phthalate in the middle of the fast step edge, with one or both oxygens from the xanthene ring attaching to K^+ ions accessible on the lower terrace. Sometimes it will also dock completely on the terrace by attaching to a K^+ and phthalate on the (010) surface. In these images K^+ ions are colored purple, O atoms are red, C atoms are grey, and H atoms are white.

Table 3.3. *Docking of DCFH at step edges.* Uncertainties reported are from averaging between simulations run for two different step cuts, namely the $[\bar{1}1\bar{1}]$ and $[\bar{1}0\bar{1}]$ fast steps as well as the [111] and [101] slow steps.

Step Edge	C-H Termination		Partial-K^+ Termination	
DCFH Docking	$E_{reaction}$ (kJ/mol)	Dye Orientation (from [100])	$E_{reaction}$ (kJ/mol)	Dye Orientation (from [100])
Avg. Fast Step	-178 ± 1	14 ± 6°	-194 ± 1	3 ± 2°
Avg. Slow Step	-157 ± 6	56 ± 24°	-99 ± 26	67 ± 13°
Avg. Terrace Docking	n/a	n/a	892 ± 10	37 ± 25°

3.4.3 *Step-Vacancy Docking*

A growing step edge is often rough, with many kinks and vacancies along the step front. These empty sites create greater potential for bonding due to more nearest-neighbor interactions that hold the impurity in place if it can fit into the site. This section descibes the modeling results for docking DCF^- and DCFH into *vacancies* in both the upper and lower halves of a step for the C-H terminated

(Figure 3.10a) and partial-K^+ terminated (Figure 3.10b) neutral surfaces. Results were generally shown to be unfavorable if a K^+ ion was not readily accessible in the docking site, giving endothermic reaction energies. Thus, for simplicity and clarity, only results for docking into the *upper* half of a C-H terminated step and the *lower* half of a partial-K^+ terminated step, where the primary bonding mechanism is the preferred COO^- (or COOH) to K^+, are reported.

As discussed in Chapter 2, Section 2.5.2, the structure of the fast and slow step edges allows for two distinct types of vacancies, or docking sites, to be created: one where the removed phthalate's aromatic ring is oriented perpendicular to the step edge (labled "A" in Figure 3.13), and the other created by removing a phthalate that is parallel to the step edge (labeled "B" in Figure 3.13). Given that KAP carboxylate for DCF carboxylate substitution appears to be the principal replacement motif, docking into the "B" vacancy is chemically unreasonable, forcing the dye to jam its xanthene ring system into the step. Simulations of "B" site docking led to either endothermic reaction energies or physically unreasonable xanthene ring bending[19] and distortion of C-C bonds.[20] Position "A" docking, however, led to favorable results, always giving exothermic reaction energies. Thus in the final analysis only "A" site docking was considered.

Exothermic reaction energies were produced, again, from adsorption of the dye's carboxylate (or carboxylic acid) group to a K+ ion (and sometimes a phthalate anion) in a similar maner that a phthalate would fit into the KAP lattice. In the fast step vacancies, K^+ ions are readily accessible to the dye at the step edge, whereas the slow steps expose phthalates and the K^+ ions are buried several angstroms within the layer. Slow step vacancy docking often led to bent

conformations[19,20] of the dye.[21] This difference in step structure in addition to growth kinetics are presumably the reasons DCF does not incorporate into the slow steps. Given the various indications mentioned, from both modeling and experimental observation, that DCF does not readily incorporate into the slow steps, I did not perform any further simulations with the slow slopes beyond those mentioned above.

Calculations for step-vacancy docking that resulted in reasonable configurations and exothermic energies (i.e. "A" position of the fast steps) are summarized in Table 3.4. For the C-H (010) fast steps, docking into position "A" resulted in the transition dipole moment of DCF^- and DCFH to be oriented at 39 ± 3° and 38 ± 6° from [100], respectively, essentially along the step edge (see Figure 3.13). The partial-K^+ terminated fast step docking gave similar orientations of 41 ± 1° and 42 ± 2° from [100] for DCF^- and DCFH, respectively. These results are consistent with the average of the single-molecule orientation distribution reported in Section Figure 3.2, as well as the average orientation adopted by DCF when Fe^{3+} cations were also present during crystal growth (Section 3.3.1). Energetically, DCFH shows greater preference for the C-H terminated step configuration (where the vacancy is in the upper half of the step), while DCF^- prefers the partial K^+ termination (where the vacancy is in the lower half of the step, which is rich in positively charged potassium ions at the step-terrace junction). These differences in docking preference are likely due to the interactions between the Coulombic forces surrounding each vacancy and the charge of the dye molecule.

Table 3.4. *Docking of DCF⁻ and DCFH into an "A" site vacancy in the upper half of straight KAP (010) fast steps.* Uncertainties reported are from averaging between simulations run for two different step cuts, namely the $[\bar{1}1\bar{1}]$ and $[\bar{1}0\bar{1}]$ fast steps as well as the [111] and [101] slow steps. Note that reaction energies for DCF⁻ and DCFH cannot be directly compared due to different simulation set-ups (See Section 2.5.2).

Docking Site	C-H Termination		Partial K^+ Termination	
Docking into "A" position	$E_{reaction}$ (kJ/mol)	**Dye Orientation** (from [100])	$E_{reaction}$ (kJ/mol)	**Dye Orientation** (from [100])
Avg. DCF⁻ in Fast Step	-20 ± 2	39 ± 3°	-58 ± 6	41 ± 1°
Avg. DCFH in Fast Step	-366 ± 32	38 ± 6°	-266 ± 1	42 ± 2°

3.4.4 *Kink Site Docking*

To examine the supposition of Hottenhuis *et al.*, that the kink sites within the KAP fast steps are non-equivalent, thus allowing for kink-specific impurity adsorbtion, and to identify the theoretical orientation DCF would adopt upon incorporating into each of these kink sites, simulations for docking into kinked $<11\bar{1}>$ fast steps on the C-H terminated (010) surface were performed. Modeling confirmed that the kink sites are indeed stereo chemically distinct. In the +*c* kink site, the carboxylic acid groups of the phthalate anions are exposed and the kink is angled at 70° with respect to the $[\bar{1}01]$ direction. In contrast, the carboxylate group of the phthalates are exposed in the -*c* kink site that is angled at 110° with respect to the $[10\bar{1}]$ direction. Since the kink sites provide more space into which the DCF molecule can situate, the position of the OH group on the DCF xanthene ring can have a significant influence on the simulated molecular orientation.

Thus, kink docking was performed for the enantiomers of DCFH and DCF$^-$. Reaction energies and orientations were averaged between these results, and are reported with the corresponding standard deviation from these means.

The docking of DCF$^-$ and DCFH into the kink sites was thermodynamically favorable in all simulations (Table 3.5). Surprisingly, the average reaction energies for dye incorporation into the +*c* kink (-170 ± 11 kJ/mol for DCF$^-$ and -196 ± 3 kJ/mol for DCFH) were more exothermic than for the -*c* kink (-105 ± 35 kJ/mol for DCF$^-$ and -133 ± 21 kJ/mol for DCFH). Experimental observations from the KAP/DCF/cation studies suggested the opposite, that the dye prefers the -*c* kink site (Section 3.3). However, recall that these simulations do not account for solvent interactions and growth kinetics (i.e., the +*c* kinks and -*c* kinks presumably propagate at different rates due to their stereo-chemical distinctions). The average orientation for docking into the +*c* kink was 64 ± 8° from [100] for DCF$^-$ and 54 ± 1° from [100] for DCFH, while that for the -*c* kink was 25 ± 8° from [100] for DCF$^-$ and 20 ± 15° from [100] for DCFH (Figure 3.13).

Table 3.5. *Docking of DCF$^-$ and DCFH into a kink in the [$\bar{1}1\bar{1}$] fast step on the C-H terminated (010) KAP surface.* Uncertainties reported are from averaging between simulations run for enantiomers of the dye. Note that reaction energies for DCF$^-$ and DCFH cannot be directly compared due to different simulation set-ups (See Section 2.5.2).

Docking Site	DCF$^-$		DCFH	
C-H Terminated Surface	$E_{reaction}$ (kJ/mol)	Dye Orientation (from [100])	$E_{reaction}$ (kJ/mol)	Dye Orientation (from [100])
Ave. +c Kink Site	-170 ± 11	64 ± 8°	-196 ± 3	54 ± 1°
Ave. -c Kink Site	-105 ± 35	25 ± 8°	-133 ± 21	20 ± 15°

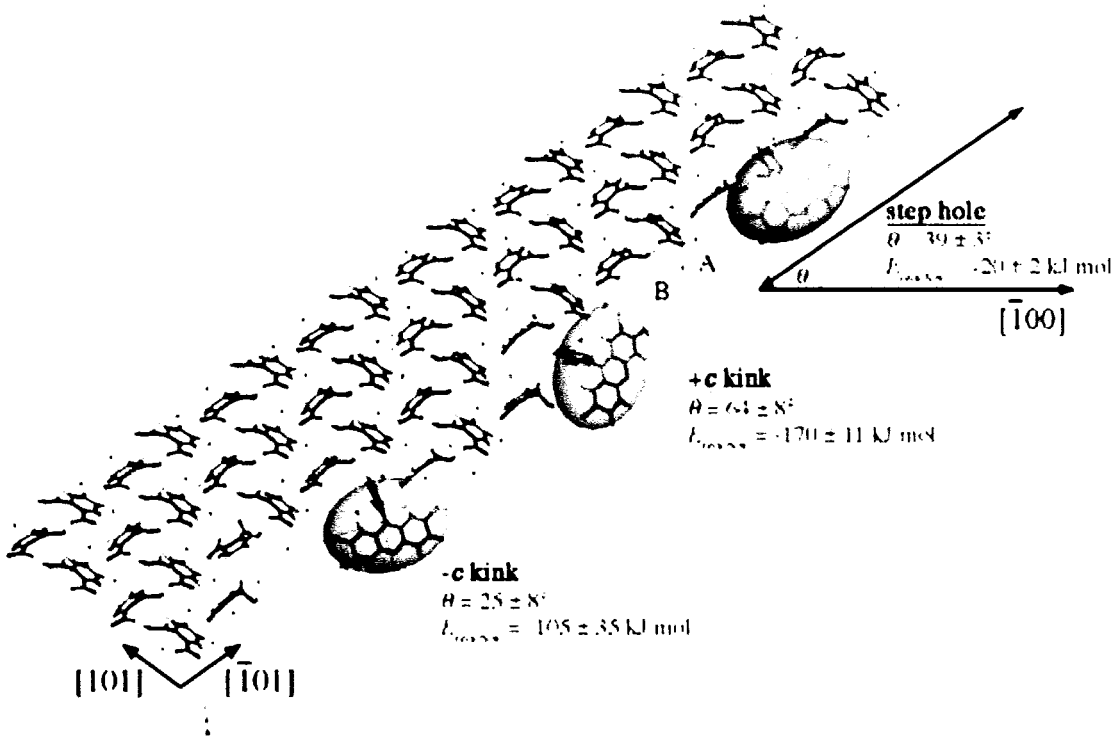

Figure 3.13. *Docking sites for DCF in KAP.* Dye orientation changes according to docking site, always preferring to replace a phthalate in position "A" within the KAP lattice rather than position "B". The -*c* kink and +*c* kink orient DCF closer to [100] and [001], respectively, and the dye docked into a vacancy in the step edge is oriented with its transition dipole moment along the fast step, ($\bar{1}$01). Orientations reported in the image are for DCF$^-$.

The combined simulation results for docking DCF into the +*c* and -*c* kink sites as well as the step-edge vacancy support the experimental results for KAP/DCF grown in the presence of Fe^{3+} and Ce^{3+}. In particular, when docked into the -*c* kink site, the dye is oriented at roughly 25° from [100], consistent with our observations for crystals grown from high Ce^{3+} concentrations. When docked into the +*c* kink site, simulations suggest that the dye adopts an orientation between 54° and 64° from [100]. However, our experimental observations suggested that Fe^{3+} inhibits the dye from docking into all but the

step-edge holes, limiting its orientation to a narrow range of conformations at about 42 ± 2° from [100], consistent with the simulation results for docking DCF into a vacancy in the step edge.

3.4.5 *[100] Step Docking*

Despite the success of these findings in illuminating the importance of specific kink recognition in crystal dyeing, the original question of KAP/DCF orientational dependence on dye concentration remains to be addressed. One mechanism whereby DCF orients progressively closer to [001] with increasing dye concentration is the appearance of and inclusion into the <100> intermediate steps of the {010} hillocks. For example, Hottenhuis *et al.* observed the appearance of <100> macrosteps in almost all pure KAP growth experiments.[7] AFM data showed the range covered by these steps is very small in pure KAP, however the <100> step region expands upon addition of DCF (Section 3.2). Furthermore, in the fluorescence and CLSM images of several heavily dyed (≥ 2.5 $\times 10^{-5}$ M) KAP/DCF crystals, we noticed bright, angled, bow-tie regions of dye outlining the fast-slow boundary of the hillocks, corresponding to <100> step incorporation. In many cases, these areas were more luminescent relative to the rest of the (010) fast step inclusions (Figure 3.14a). We even found one rare but spectacular example where only the <100> steps were dyed in earlier stages of growth (Figure 3.14b). Moreover, upon closer inspection, linear dichroism images indicated an enhanced dichroism towards [001] in this region relative to the fast slopes containing dye (Figure 3.1b and d).

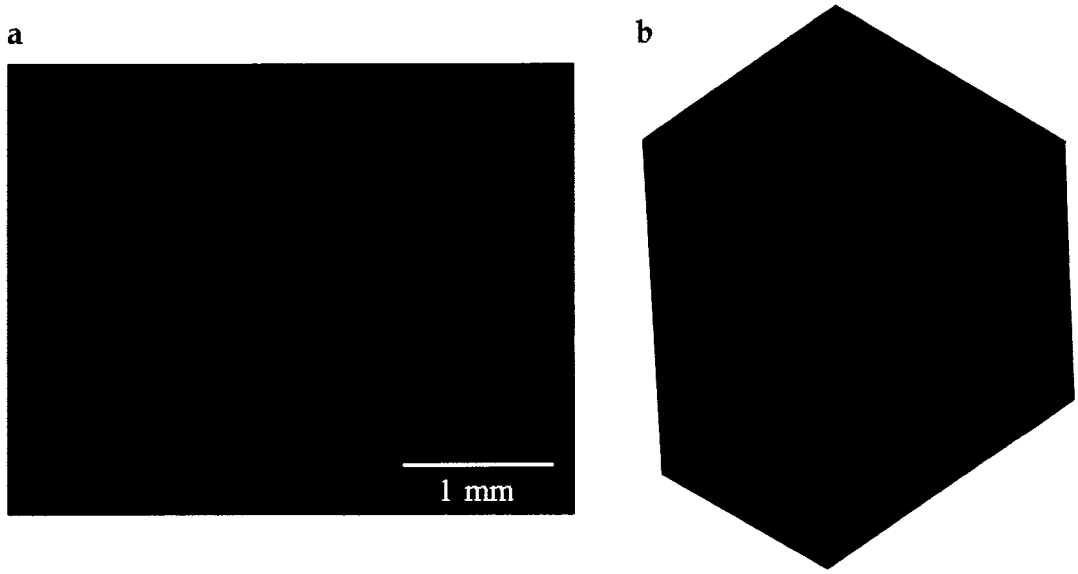

Figure 3.14. *<100> step inclusion of DCF in KAP at high dye concentrations.* a) Fluorescence image of KAP/DCF (2.5×10^{-5} M) showing the greater amount of dye in the <100> steps relative to the dye included in the fast slopes. b) Confocal luminescence image of an *anomalous* KAP crystal spectacularly showing DCF primarily in the <100> steps (crystal dimensions are 7.4 mm × 8.3 mm).

Since steps propagating in the <100> directions present step edges aligned along [001], DCF adsorbed to these steps may adopt orientations closer to [001]. Isolating the <100> step inclusion experimentally has proven to be difficult, as it is always accompanied by signal from the fast step inclusion, resulting in a convolution of signals when orientation measurements are attempted.[22] However, we performed simulations of docking DCF^- and DCFH into the <100> steps to test the hypothesis that their orientations will be closer to [001].

Two alternate terminations were modeled for the <100> step cuts on the C-H terminated (010) surface: one where the carboxylate groups of the phthalates emerge at the step edge, while the carboxylic acid moieties are exposed in the other. Figure 3.15 gives two examples of the <100> step cuts with DCF^- docked

into a vacancy. For all simulations, the orientations of DCF^- and DCFH ranged from 60° to 85° relative to [100], indicating that the dyes will orient closer to [001] if they are overgrown along the <100> steps (Table 3.6). Docking into the carboxylic acid-terminated step was more energetically favorable and the resulting orientations were closer to [001] than for the carboxylate-terminated step cut. These results support the hypothesis that increased dye inclusion into the <100> steps will shift the ensemble average orientation of DCF closer to [001].

Table 3.6. *Docking for DCF^- and DCFH into the [$\bar{1}$00] intermediate step on the (010) C-H terminated KAP surface.* Uncertainties reported are from averaging between simulations run for enantiomeric versions of the dye molecule. Note that reaction energies for DCF^- and DCFH cannot be directly compared due to different simulation set-ups (See Section 2.5.2).

Docking Site	DCF^-		DCFH	
C-H Terminated Surface	$E_{reaction}$ (kJ/mol)	**Dye Orientation** (from [100])	$E_{reaction}$ (kJ/mol)	**Dye Orientation** (from [100])
COOH Step Termination	-25 ± 3	69° ± 1°	-208 ± 9	65 ± 1°
COO^- Step Termination	-94 ± 5	77° ± 4°	-220 ± 2	77 ± 2°

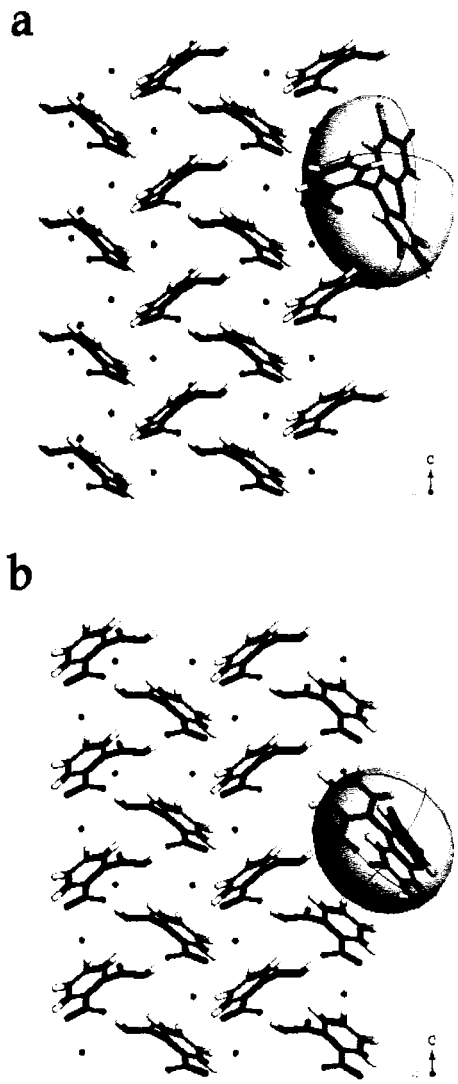

Figure 3.15. *DCF⁻ docking into KAP [$\bar{1}$00] step.* a) In the COOH-terminated step cut, the carboxylate group of DCF⁻ positions itself in a similar fashion as that of a phthalate, with the transition dipole moment of the dye aligned along the [$\bar{1}$00] step edge. b) In the COO⁻-terminated step cut, the transition dipole moment is oriented nearly perpendicular to (010), with its projection into the *ac*-plane close to the *c*-axis.

3.5 Summary

Crystals of KAP/DCF exhibited dye-concentration dependent molecular orientation. Heavily-dyed crystals displayed average orientations closer to [001] while crystals containing nanomolar quantities of dye exhibited disperse single-molecule orientations and an average value closer to [100]. To explore the possibility that DCF-induced morphological changes to the crystal hillocks were responsible for changing dye orientation, we measured the angles of hillock steps using DIC and AFM microscopy. Only slight modifications to hillock morphology were detected in the fast and intermediate steps in the *presence* of DCF, and appeared to be independent of dye *concentration* ($\geq 10^{-7}$ M). Alternative explanations for dye-concentration dependent orientations were examined using a combination of experimental and theoretical approaches. Below is a list of key results and conclusions drawn from these studies:

- Single-molecule measurements of molecular orientations suggested a significant amount of environmental heterogeneity in KAP and a wide variety of DCF inclusion sites.
- Force-field calculations verified the wide distribution of orientations and inclusion sites for docking DCF into KAP steps, kinks, and terraces.
- Force-field calculations support the hypothesis that the main driving force for DCF incorporation into KAP is carboxylate for carboxylate (or carboylic acid for carboxylic acid) substitution, rather than a purely Coulombic interaction.
- Simulations of DCF docking into the KAP slow steps were equivocal due to step structure and the lack of accessibility of K^+ ions to the dye.

- Experimental evidence supported by force-field calculations revealed preferential kink site recognition to be the dominant mechanism whereby DCF becomes overgrown within the fast steps of KAP (010) hillocks. This is the first time selective kink integration, a more refined type of intra-sectoral zoning, plays a significant role in the process of dyeing crystals.
- The orientation of DCF in KAP hillocks could be modulated by the addition of specific kink-blocking trivalent cations Fe^{3+} or Ce^{3+} to growth solutions.
- Addition of Ce^{3+} to growth solutions demonstrated that DCF prefers to incorporate into the $-c$ kink sites, progressively pushing the dye orientation closer to [100] as the Ce^{3+} concentration was increased, with both a calculated and measured transition dipole moment orientation around 20° - 25° from the *a*-axis.
- Addition of Fe^{3+} blocked the $-c$ kink sites, forcing DCF to incorporate into other less favorable sites, producing faintly luminescent crystals relative to KAP/DCF, and resulting in an average dye orientation, independent of Fe^{3+} concentration, that was similar to modeling results for docking into a vacancy along the fast step edge (38° - 42° from the *a*-axis).
- The combined experimental and computational investigations led to the discovery that DCF selectively recognizes the $-c$ kink sites in preference to the $+c$ kink sites within the KAP fast steps.
- However, DCF also shows thermodynamically favorable docking into vacancies in the fast step edges, as well as docking sites in the <100> steps (resulting in calculated transition dipole moment orientations closer to [001]).

- Force-field calculations of DCF docking into the various KAP steps and kinks also showed surprising indifference in orientation with respect to the dye's charge.
- The primary difference between the DCF^- and DCFH bonding motifs is that the extra hydrogen on the carboxylic acid group of DCFH additionally bonds to an oxygen from a neighboring phthalate anion in the lattice.

In comparing resulting reaction energies from the various force-field calculations, the preferred docking configurations for DCF^- and DCFH are given as follows:[23]

DCF-

1. +*c* kink site (-170 kJ/mol)
2. –*c* kink site (-105 kJ/mol)
3. $[100]_{COO^-}$ step *vacancy* (-94 kJ/mol)
4. $[10\bar{1}]$ fast step *vacancy* on partial-K^+ terminated surface (-58 kJ/mol)
5. $[100]_{COOH}$ step *vacancy* (-25 kJ/mol)
6. $[10\bar{1}]$ fast step *vacancy* on C-H terminated surface (-20 kJ/mol)

DCFH

1. $[10\bar{1}]$ fast step *vacancy* on C-H terminated surface (-366 kJ/mol)
2. $[10\bar{1}]$ fast step *vacancy* on partial-K^+ terminated surface (-266 kJ/mol)
3. $[100]_{COO^-}$ step *vacancy* (-220 kJ/mol)
4. $[100]_{COOH}$ step *vacancy* (-208 kJ/mol)
5. +*c* kink site (-196 kJ/mol)
6. $[10\bar{1}]$ fast step *edge* on partial-K^+ terminated surface (-194 kJ/mol)
7. $[10\bar{1}]$ fast step *edge* on C-H terminated surface (-178 kJ/mol)
8. $[10\bar{1}]$ slow step *edge* on C-H terminated surface (-157 kJ/mol)
9. -*c* kink site (-133 kJ/mol)
10. $[10\bar{1}]$ slow step *edge* on partial-K^+ terminated surface (-99 kJ/mol)
11. *Terrace* of the partial-K^+ terminated surface (+892 kJ/mol)

This ranking shows an almost reverse order of docking preferences for DCF^- and DCFH (excluding step *edge* and terrace docking, for which there are no DCF^- results to compare). Thus, while orientational configurations of the docked molecules show little difference for similar docking locations, there is indication that the selectivity of these two protonation states for DCF may be different. The differences in selectivity, however are still restricted to the various intrasectoral zoning options within the KAP (010) hillocks, and are not nearly as dramatic as the differences shown by the protonation states of acid-base indicator 2,7-diaminoacridine in KAP.[6] Bear in mind that the calculated docking energies do not account for step kinetics or solvation energies. Step kinetics favor fast steps over slow steps, and may also favor $-c$ kink propagation over $+c$ kink propagation (although this has not been experimentally determined). Addition of solvation energies are expected to make reaction energies less exothermic, however the changes will be different for the DCFH and DCF^- calculations.

Other issues requiring further investigation are:

- The role that step kinetics play in dye entrapment and overgrowth within the kinks and steps of KAP (010) hillocks.
- Why KAP/DCF shows dye-concentration dependent orientations, although there is indication that it is in part due to <100> step incorporation at high dye concentrations ($\geq 2.5 \times 10^{-5}$ M).
- The ensemble orientation of DCF in the <100> steps, and the degree to which this influences the overall orientation measurements in heavily dyed KAP/DCF crystals.

Recommended future work, therefore, entails excitation dichroism measurements of the <100> step inclusions using polarized confocal microscopy that can pinpoint the dyed region of interest with precise planar and depth discrimination to avoid the convolution of signals from the fast step inclusions.[22]

Single molecule studies on KAP/DCF/Fe^{3+} can be performed to verify the narrower distribution of orientations due to a more limited set of docking sites available to the dye. KAP/DCF/Ce^{3+} crystals can also be studied at the single molecule level to see how the orientation distribution moves as a function of Ce^{3+} concentration. Finally, computational modeling of rate constants, attachment energies, and kink concentrations may quantify the influence of kinetics on selective kink integration.

NOTES AND REFERENCES TO CHAPTER 3

1. a) A. M. Glazer, J. G. Lewis, and W. Kaminsky, *Proc. R. Soc. Lond. A*, **452** (1996), 2751; b) M. A. Geday, W. Kaminsky, J. G. Lewis, and M Glazer, *J. Microscopy*, **198** (2000), 1.

2. a) K. L. Wustholz, B. Kahr, and P. J. Reid, *J. Phys. Chem. B.*, **109**(34) (2005), 16357; b) K. L. Wustholz, E. D. Bott, C. M. Isborn, X. Li, B. Kahr, and P. J. Reid, *J. Phys. Chem. C*, **111** (2007), 9146; c) T. V. Bullard, K. L. Wustholz, M. Robertson, J. Freudenthal, P. J. Reid, and B. Kahr, to be published (2008).

3. Bulk polarized confocal fluoresecence microscopy measurements were performed by Kristin Wustholz, another graduate student in Bart Kahr's group with a joint position in Phil Reid's research group at the UW Chemistry Department.

4. L.D. Bastin and B. Kahr, *Tetrahedron*, **56**(36) (2000), 6633.

5. R. W. Gurney, C. A. Mitchell, S. Ham, L. D. Bastin, and B. Kahr, *J. Phys. Chem. B.*, **104**(5) (2000), 878.

6. M. Bellinazzi, A. Barbon, B. Kahr, J. B. Benedict, and M. Brustolon, *Phys. Chem. Chem. Phys.*, **8**(3) 2006, 379.

7. a) M. H. J. Hottenhuis and C. B. Lucasius, *J. Cryst. Growth*, **78** (1986), 379; b) M. H. J. Hottenhuis, J. G. E. Gardeniers, L. A. M. J. Jeten, and P. Bennema, *J Cryst. Growth*, **92** (1988), 171; c) M. H. J. Hottenhuis and A. Oudenampsen, *J. Cryst. Growth*, **92** (1988), 513; d) M. H. J. Hottenhuis and C. B. Lucasius, *J. Cryst. Growth*, **94** (1989), 708.

8. These values for the ideal hillock morphology are based on KAP habit and lattice parameters, as well as an assumed fast:slow step kinetic ratio of 10:1, as is given by Hottenhuis, *et al.*[7]

9. Atomic force microscopy (AFM) imaging on KAP/DCF hillocks were performed by John Freudenthal, a graduate student in the Kahr research group, using a Veeco Dimension 3100 SPM with Nanoscope IV controller at the University of Washington Nanotechnology User Facility. The AFM data was collected under ambient atmosphere in tapping mode. The morphology changes and orientations of the hillock steps with respect to the [100] direction and the angle spanned by the fast-slow boundary were measured by Theresa Bullard.

10. J. J. DeYoreo and P. Vekilov, in *Biomineralization*, pp. 57-93, Fig 29a., eds. P. M. Dove, J. J. De Yoreo, and S. Weiner, (Mineral Soc. Am.: Washington, DC, 2003)

11. Unpublished AFM image taken by Kurimoto, M., a former graduate student of the Kahr research group at the University of Washington Department of Chemistry.

12. COMPASS stands for Condensed-phase Optimized Molecular Potentials for Atomistic Simulation Studies. Accelrys, *Materials Studio Getting Started, Release 4.0*, (Accelrys Software, Inc.: San Diego, 2006).

13. a) The transition dipole moment was calculated using density functional theory (DFT) with the B3LYP functional.[13b,c] Calculations were performed by Christine Isborn at the University of Washington, starting from molecular coordinates obtained from a crystal structure of fluorescein[13d] in the Cambridge Databse and adding the chlorine atoms. This molecular structure was then optimized in order to calculate the transition dipole moment. The theoretical ground state transition electric dipole moment orientation was calculated to be 5° off from the approximated vector between the two chlorine atoms (representing the long axis of DCF's π-system). However, there is also an expected variance of about ±5° as the dye changes to excited state conformations in order to dock into the KAP lattice. Thus, in all reported orientations, the approximated vector between chlorine atoms was used. b) A. D. Becke, *J. Chem. Phys.*, **98** (1993), 5648; c) C. T. Lee, W. T. Yang, and R. G. Parr, *Phys. Rev. B*, **37** (1988), 785; d) K. Yamaguchi, Z. Tamura, M. Maeda, *Acta Crysta. C*, **C53** (1997), 284.

14. A. L. Rohl suggested in private conversation. See for example: A. L. Rohl, D. H. Gay, R. J. Davey, and C. R. A. Catlow, *J. Am. Chem. Soc.*, **118** (1996), 642.

15. It is unlikely or impossible for large impurities such as a dye molecule to dock in a vacancy on the terrace, thus this option has been excluded from the various DCF docking simulations.

16. DCF^- docking onto the flat partial K+ terminated surface was performed, but due to the need for charge neutrality an embedded phthalate needed to be removed to perform these caluclations, thus skewing the reaction energy. These energy results are therefore not included, however, the

orientational results still seemed significant and relevant, thus these are included.

17. D. J. Carter, M. I. Ogden, A. L. Rohl, *J. Phys. Chem. C*, **111** (2007), 9283.

18. R. W. Gurney, *Dyeing Crystals*, Ph.D. Thesis, (Purdue University: West Lafayette, IN, 2000).

19. The unreasonable bending in conformation that resulted from some of the simulations is likely due to force-field parameters for the intra-molecular bonds being too flexible. In an effort to avoid this bending, we tried restricting the dye molecule to be treated as a rigid motion group (ie, translations permitted but not changes in conformation). These rigid-dye molecule simulations did not converge. This is a clear limitation of the force-field calculation approach, given that it can allow for non-physical results. Thus, in final analysis, it is assumed that simulations resulting in significantly bent[20] conformations of the dye were unfavorable docking configurations, even if they led to exothermic reaction energies (ie, they are considered false-positives and thrown out by default of their non-physical nature).

20. R. A. Pascal, Jr., *Chem. Rev.*, **106** (2006), 4809.

21. Fast and slow step-edge cuts were created according to the lowest energy surfaces for the {111} and {11-1} growth sector faces, as determined by the Accelrys Morphology feature. (Accelrys, *Materials Studio Getting Started, Release 4.0*, Accelrys Software, Inc.: San Diego, 2006).

22. Bulk spectroscopy measurements result in a convolution of signals from dye included within the entire crystal. The home built confocal microscope used for polarized excitation dichroism is not able to identify exactly where in the crystal measurements are being taken. The confocal microscope used for macroscopic imaging of hillock evolution through crystal growth does not have the ability to do polarized excitation spectroscopy. Thus to-date we have been limited in our ability to measure the <100> step inclusion dichroism.

23. DCF^- and DCFH reaction energies cannot be compared to each other due to different simulation conditions.

CHAPTER 4 - INFORMATION CONTENT AND TRANSFER THROUGH CRYSTAL GROWTH

4.1 Information Transfer Through Crystal Growth

As described in Chapter 1, Graham Cairns-Smith (CS) proposed that defect patterns in crystals may act as primitive sources of 'genetic' information that are transferred and inherited through crystal growth.[1] Herein, the first known experimental investigations[2] of CS's 'crystals-as-genes' hypothesis are described in the context of the arrangement and evolution of screw dislocations in successive generations of crystals. Figure 4.1 shows a cartoon of crystal reproduction in order to recapitulate the idea that generation of screw dislocations in a crystal, followed by cleavage and growth, can lead to the propagation of information. Here, the 2D spatial positions of hillocks are explicitly indicated as the 'bits' of information.

4.1.1 Daughter Growth from Cleaved Surfaces

Parent KAP crystals were grown by spontaneous nucleation and harvested as described in Chapter 2, Section 2.3.2. Figure 4.2 shows a sample crystal grown with DCF (**3**) that was cut into successive 200 μm slices by placing the edge of a sharp razor parallel to the cleavage plane as did Borc and Sangwal.[3] In this way, the development of the luminescent (010) growth sector and its hillocks were revealed in cross sections. The (010) cleavage would be characterized by the descriptive crystallographer as 'perfect'. Layers of sliced KAP crystals were then

used as seeds for subsequent growth to establish if the defect patterns are inheritable, that is, passed on to daughter fragments.

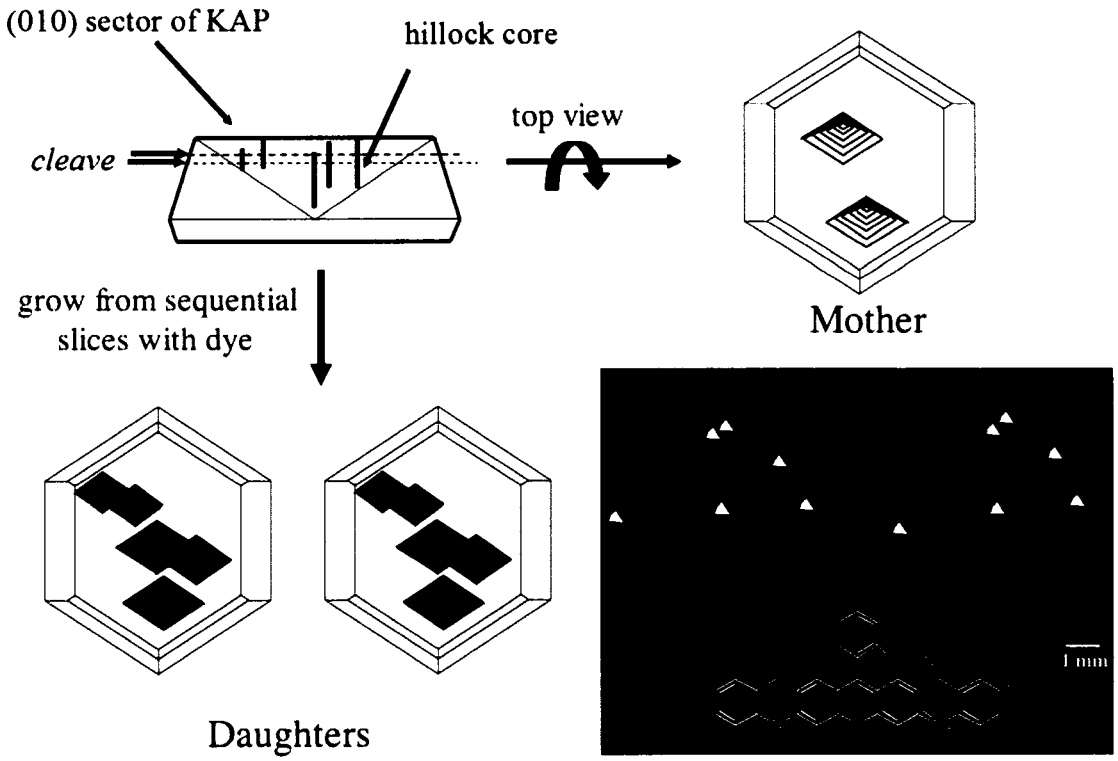

Figure 4.1. *Information transfer through crystal growth.* KAP has 'perfect' (010) cleavage perpendicular to the screw dislocation cores. Cleavage and subsequent growth generates daughter crystals that in principle retain their mother's genes (cartoon). Inherited dislocations are indicated in the photomicrographs by the lower right corners of the white triangles in the patterns of luminescence from dopant violamine R.[4] (Image reproduced from the Royal Society of Chemistry.[5])

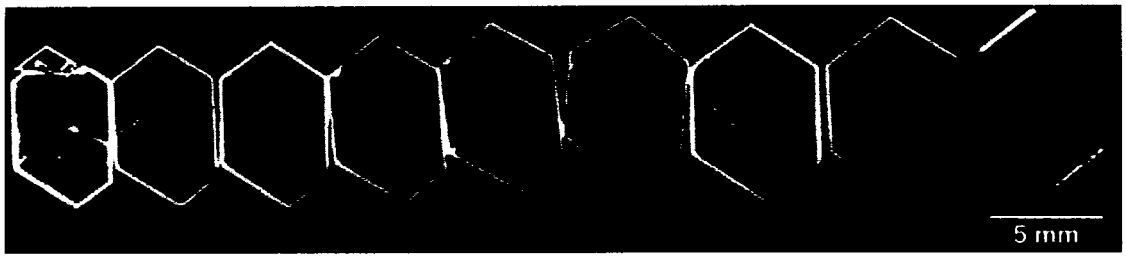

Figure 4.2. *Cleaved KAP/3.* Successive slices (~200 μm) of KAP dyed with **3** from top surface (left) to bottom (right) of a (010) growth sector. Cross sections reveal the development of the luminescent dye inclusion. In this case, two hillocks are seen in the early stages of growth (two right-most slices), but later growth was dominated by a single hillock. (Image reproduced from the Royal Society of Chemistry.[5])

In KAP, screw dislocations passing through cleavage planes will expose corresponding high-energy cores in successive slices following cleavage. As KAP has a diad axis parallel to *c*, complementary cores may be related by symmetry. It was expected that the defects that exist on the exposed surfaces of cleaved seeds would propagate during further growth and be readied for observation by luminescence microscopy after a hillock recognizing dye was added to the growth solution.[6] Early studies performed by Serine Avagyan qualitatively verified that screw dislocations can indeed be transferred through cleavage and subsequent growth.[4] Pure KAP crystals were cleaved into 13 slices of about 150 μm thickness each. These slices were then used as seeds to grow daughter crystals from a KAP solution doped with 4×10^{-5} M violamine R at supersaturation 0.8% in 26° C ambient conditions. The resulting daughter crystals were imaged using fluorescence microscopy. The photo inset in Figure 4.1 shows two of the daughters grown from sequential slices of a parent crystal. Indeed, seven labeled hillocks, identified at the lower right corners of the triangles in Figure 4.1, were shared by each of the daughter crystals. That said, CS's proposition that the information encoded as the spatial disposition of screw

dislocations can be transferred from one crystal to another has been demonstrated. However, a greater number of new hillocks, 'mutations', were also observed that were apparently not present or active in the parent or in the twin daughters. Furthermore, other daughters from the same parent showed fewer corresponding hillocks, indicating a loss of information. For this work to be a compelling stimulus to other scientists, the number of preserved hillocks in the daughter crystals must exceed the number of new and lost hillocks. In other words, for KAP crystals to resemble genes, there must be more inheritance than mutation in successive generations. The great number of mutations led to parallel experiments[5], performed by Theresa Bullard and John Freudenthal[7], aimed at the elucidation of the fundamental mechanisms that give rise to the birth, evolution, and death of growth active hillocks.

Real crystals often grow through the emergence, competition, and poisoning of many hillocks. In order to ensure that the seeds used for subsequent growth share the same 'genes' ('punches' or screw dislocations) J. Freudenthal[5,7] grew daughter crystals from *complementary* surfaces produced from a single slice, rather than sequential surfaces (Figure 4.3), so as to produce enantiomorphous twins. Daughters were grown for four hours from a KAP solution (supersaturation 1.0% at 23° C) doped with 10^{-5} M violamine R. Complementary surfaces resulted in even more mutation than sequential surfaces. This is true even when extra care is taken to not expose the fresh cleaved surfaces to atmosphere, by cleaving the parent crystal in solution and thereby avoiding the collection of particulates that might nucleate new dislocations. We therefore examined surfaces of cleaved KAP.

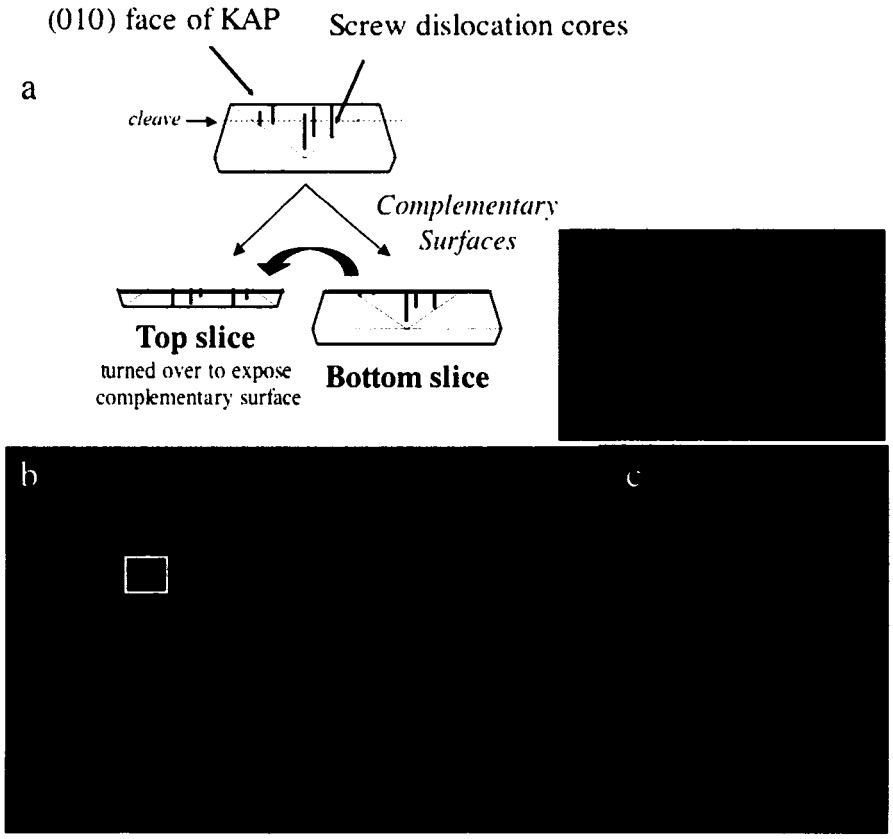

Figure 4.3. *Information transfer from complimentary surfaces.* (a) Cartoon of complementary surfaces from 'perfect' cleavage. Complementary surfaces expose the same screw dislocation cores on each surface and should result in exact replication of growth active hillocks during subsequent growth of daughters. (b) Daughters grown with violamine R from complementary surfaces. Blue and green dots mark the hillock cores. (c) Superposition of green and blue dots showing there is little if any correspondence between daughters. Inset above (c) shows a magnified section of the crystal on the left indicated by the box. Crystals = 6 mm × 9 mm. (Image reproduced from the Royal Society of Chemistry.[5])

KAP crystal layers separate as easily as those in mica. However, the razor places stresses on the separating halves. After cutting the crystals, J. Fruedenthal[5,7] examined the surfaces by differential interference contrast (DIC) microscopy and atomic force microscopy[8] (AFM). The images of cleaved surfaces

showed ridges and terraces of unit cell height or greater, indicating that the cleavage process is inherently imperfect at the nanometer scale (Figure 4.4). AFM showed similar surface features to those observed previously by Borc and Sangwal:[3] disorganized breakage, terraced macrosteps, and V-shaped elementary steps oriented along low-index crystallographic directions.

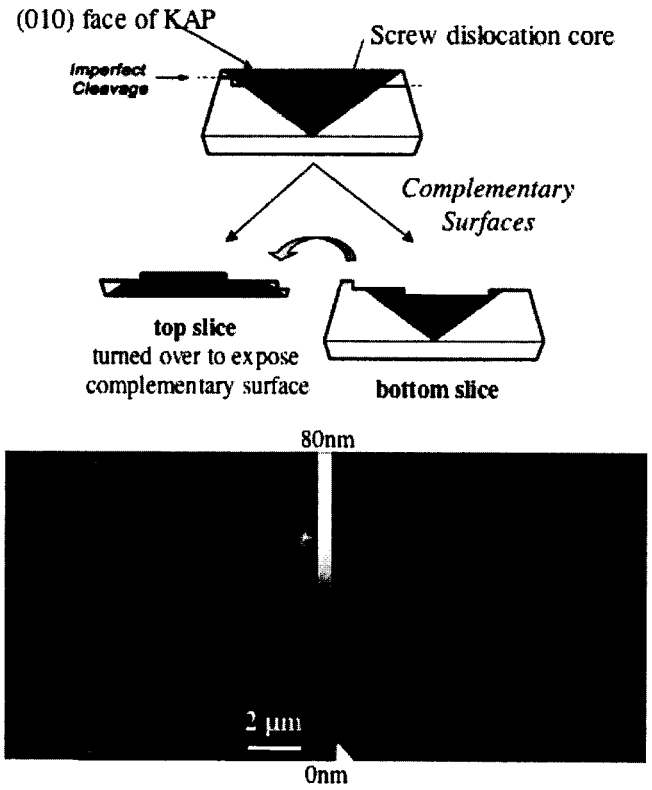

Figure 4.4. *Complementary surfaces from imperfect cleavage.* Surfaces exposed by cleavage will have, in principle, complementary topographies. Hills will have abutted valleys and vice versa. This is shown, imperfectly, by complementary AFM[8] images at bottom, taken by J. Freudenthal[7]. (Image reproduced with permission by the Faraday Society[5])

Complementary halves will leave a screw dislocation emergent on a hill on one surface and in a valley on the other. Thus, mass transport will undoubtedly be affected by differences in fluid dynamics associated with these topographical

features. Furthermore, hillocks in valleys are more easily subject to overgrowth from macrosteps, whereas dislocations emerging on higher terraces have a greater chance of surviving. After re-growth, these unavoidable macrosteps become a prolific source of new dislocations and false positive inheritance or mutation. After just two minutes of re-growth from a cleaved surface in a 1% supersaturated pure KAP solution, DIC micrographs show that new hillocks form along newly created macroedges (Figure 4.5), principally on the upper terraces. Daughter growth from imperfectly cleaved, complementary surfaces is doomed to fail. Cleavage by its very nature serves to generate new, and non-reciprocal hillocks.

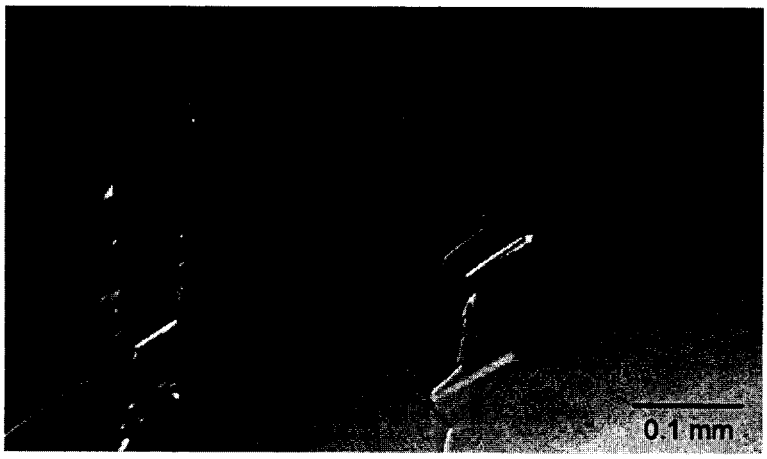

Figure 4.5. *DIC image of KAP re-growth after cleavage.* Newly formed hillocks are mainly on the upper terraces running along cracks and macrosteps induced by the cleave. The jagged macrosteps seen to the left of the columns of hillocks is the growth front that propagated from the newly formed macro-edges. (Image reproduced with permission by the Faraday Society[5])

4.1.2 *Daughter Growth from Unadulterated Surfaces*

Given the inherent flaws in the cleaving mechanism, I attempted to grow daughters from as-grown, unadulterated seeds, so as to minimize the generation of new dislocations. To accomplish this, seeds were freshly harvested from a growth solution at 30°C and immediately transferred to a new solution at the same temperature. Seeds did not undergo any cleavage or exposure to air. In order to clearly discern which hillocks in the daughter crystal were transferred from the seed and which ones resulted from mutations, the seed crystal was grown with a red fluorescing, hillock-recognizing dye (**1**). Growth was continued by slow evaporation in a dry temperature controlled (30°C) chamber for 1-2 hours from a solution (starting $\sigma = 0.8\%$) containing green fluorescing **3**, as in Figure 4.6. Results from over 35 experimental batches with 180 seeds showed positive information transfer (1-10%), but still more mutation than inheritance.

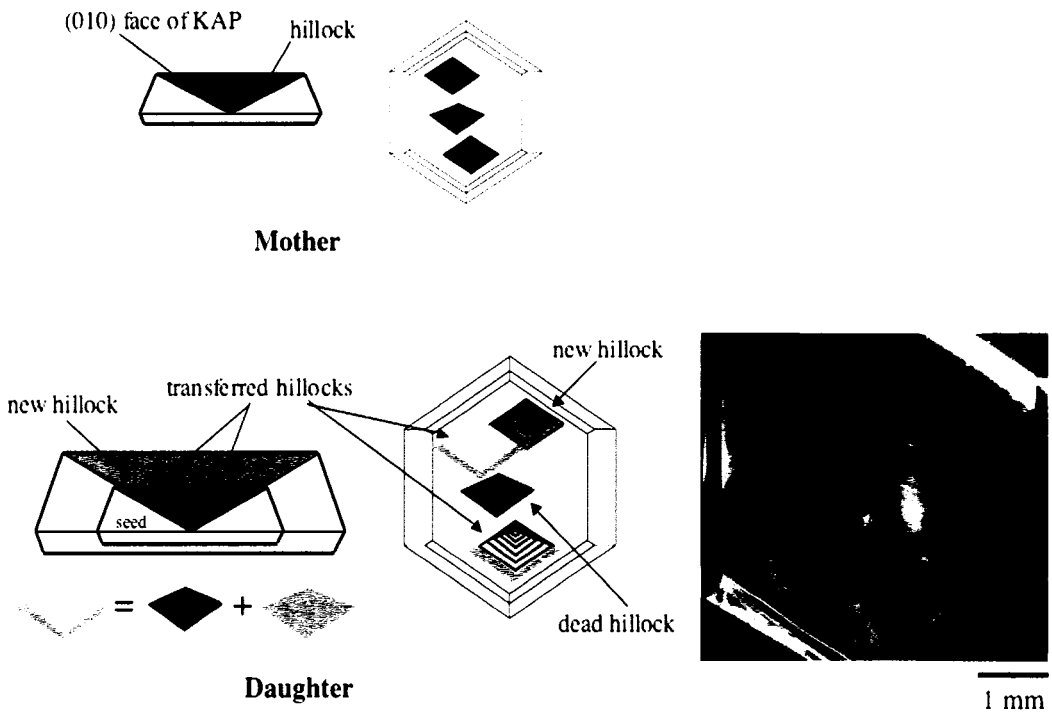

Figure 4.6. *Inheritance without cleavage.* Hillocks in the parent crystal were labeled with a red fluorescent dye (**1**). Subsequent growth from a solution containing a green fluorescent dye (**3**) allowed for the distinction between transferred hillocks (information preserved), buried hillocks (information lost), and new hillocks (mutations or information added) based on color. (Image reproduced with permission by the Faraday Society[5])

4.1.2.1 Solution Flow and Controlled Growth

As discussed in detail in Chapter 1 (Section 1.2.2.3), the degree to which various experimental growth parameters, such as temperature, supersaturation, solution flow, solvent, additives, etc. can be controlled plays an important role in our ability to preserve information content during the transfer of a particular pattern of defects from a crystal seed to its daughter. Crystals grown by slow evaporation or at varying temperatures do so under fluctuating supersaturation

conditions. In order to control the growth of crystals in solution it is imperative to attain a high enough *laminar* solution flow that will overcome any diffusion layer gradients at the surface. Thus, in an attempt to gain greater control over the crystal growth conditions and minimize mutation rates, a closed loop crystal growth flow system was designed and built (see Chapter 2, Section 2.7.2 for design details).

Due to various complications the flow system went through about 3 or 4 redesigns[9], with the final design derived from Lin *et al.* with some modification.[10] The main differences between our design and that of Lin *et al.* were the gravity controlled solution flow rather than a pump to achieve a pulseless flow rate, our growth cell tube had slightly different dimensions, several seeds were mounted in series with the faces of interest (the (010) face) oriented parallel to the flow direction so as to minimize the disturbance to the laminar flow, and temperature control in the growth cell was maintained by immersing the glass tube into a temperature controlled water bath. Unfortunately, after numerous experiments, repairs, and attempts at fine tuning the system we were still not able to achieve usable results. In the end, an impasse was reached when we could not attain robust temperature control using the water bath immersion technique. In part this was due to the solubility of KAP being very sensitive to temperature fluctuations, and in part it was due to poor control of lab temperatures and their influence on our system. Of those experiments that resulted positive growth rather than dissolution, daughter crystals often had macrostep features, large fluid inclusions, secondary nucleations and twinning, or not enough dye inclusion to be analyzed via fluorescence.

4.1.2.2 *Particulate Inclusion*

As discussed in Chapters 1 and 2, impurity inclusions can cause dislocations either through step edge shearing, or if segregation occurs, by creating constitutional stress and regions with different expansion coefficients. Despite the greatest of care taken to not expose fresh seeds to atmosphere, and even in the absence of cleavage, new hillocks still abounded. In order to directly test whether these newly formed hillocks resulted from the inclusion of foreign particles, I grew KAP in the presence of water soluble red-fluorescing CdSe quantum dots (30-50 nm)[11] and red-fluorescing rhodamine-coupled polystyrene microspheres[12] (200 nm and 1 μm). Growth was continued from unadulterated fresh seeds by slow evaporation (starting $\sigma = 0.1\%$) in a dry, 30 ± 0.02 °C chamber with 2×10^{-5}M **3** to label the hillocks and 10^{-9} M or less of the luminescent particulate. Particulates were introduced to growth solution via a needle syringe 5-10 minutes after seeds were placed in growth solutions. If the particles generated hillocks (see Chapter 1, Section 1.2.2.2), then we would see bright red luminescing spots at the hillock cores (luminescent vertices). Beads and quantum dots were indeed embedded within the crystal, as seen by confocal fluorescence microscopy, but there was no correspondence between particulate inclusion positions and dyed hillocks, even for the 1 μm beads (Figure 4.7). For example, in a crystal grown for 22 hours at $\sigma = 0.1\%$ from a 0.7 cm × 1.0 cm seed, over 130 microbeads (1 μm) were found to be embedded in the crystal at various depths. Far more than could be reliably counted of the 200 nm beads and quantum dots were found embedded in other crystals. In these daughter crystals, there were about 20-50 hillocks found in post-seed growth, none of which corresponded with any of the embedded particulate locations.

While the data in Figure 4.7 do little to support the notion that particulate impurities nucleate screw dislocations, there is evidence that larger bulk fluid inclusions act as sources for the appearance of new dislocations (see Section 1.2.2.3 and Section 2.3.4).[13] Indeed, in many of the crystals grown from seed there were visible fluid inclusions at the seed-daughter growth interface and borders. To investigate these possible dislocation sources further and to see if other types of defects (such as edge dislocations) were generated from the included particulates we worked with a collaborator[14] to perform X-ray topography imaging of our crystals.

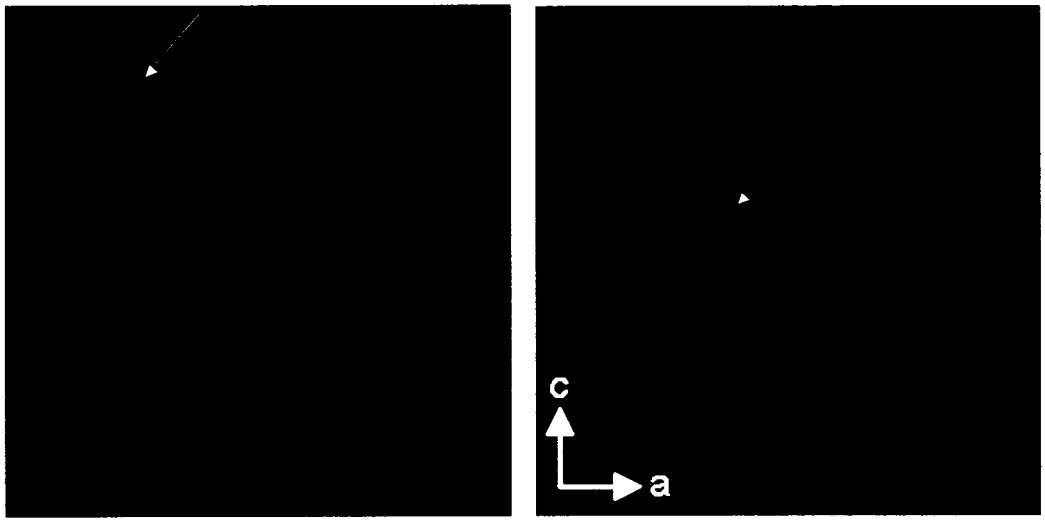

Figure 4.7. *Confocal images of crystal grown with 1 μm red fluorescent polystyrene beads.* Arrow points to an embedded microbeads. There is no correspondence between beads and hillocks. Crystallographic axes, as marked, apply to both images. Image sizes = 230 μm × 230 μm. (Image reproduced from the Royal Society of Chemistry[5])

4.1.2.3 *X-ray Topography of Dyed KAP*

X-ray topography[15] imaging of single crystals was performed by Alexey Voloshin at the Russian Academy of Sciences using the Lang Method[16] from $MoK_{\alpha 1}$ irradiation via the 400 reflection through the (010) face.[14] Sample preparation for X-ray topography can often be a tedious task involving etching and polishing of the crystals to relax surface strain. Any strain in the crystal will darken the resulting topograph, obscuring contrast from dislocations. Such is the case when crystals are cleaved, as we discovered in our first round of imaging samples that had previously been studied via confocal microscopy for cross-correlation of results. However, Halfpenny *et al.* reported good results from imaging pure KAP crystals as-grown by slow evaporation, without any cutting or polishing.[13] Thus, the second round of samples sent to Dr. Voloshin[14] were prepared in a similar manner as Halfpenny *et al.*

Due to the acquisition time[17] for X-ray topography by the Lang method[16], which involves scanning the sample to mimic the extended beam obtained instantly with synchrotron sources, we were limited to imaging only a few crystals with the following compositions:

- One pure KAP crystal, as grown from spontaneous nucleation by slow evaporation.
- One dyed KAP/DCF (10^{-5} M) crystal, as grown from spontaneous nucleation by slow evaporation.
- Two KAP crystals with 1 μm beads embedded in them, as grown from seeds by slow evaporation.

Unfortunately, good X-ray topographs require crystals of the highest quality. Of the samples we sent, only one of them displayed a clear and orderly single crystal image, while the others were blurred by distortions. Nonetheless, insights can be gained from the results for all four samples, and are thus included herein.

In general, our topographs display features similar to those obtained by Halfpenny *et al.*[13] for pure KAP, as-grown by spontaneous nucleation (see Chapter 2, Section 2.3.4). Namely, the majority of dislocations (*D*) appear in the $\{11\bar{1}\}$ sectors, arising from either bulk solvent inclusions (*I*) as bunches of single dislocations or as pairs of diverging dislocations originating at isolated points. These dislocations are of mixed character, the majority of which have a Burgers vector [001], while a smaller number have <101> Burgers vectors.[13] Dislocations in the {111} sectors are also visible, however they do not arise from bulk solvent inclusions, and most of them come in pairs. Dislocation contrast is more diffuse in these sectors, making it difficult to characterize the defects, however there is indication that the Burgers vectors are similar to those for dislocations found in the $\{11\bar{1}\}$ sectors.[13] Far fewer dislocations are observed in the lateral {110} sectors, but those that do arise were characterized by Halfpenny *et al.* to have Burgers vectors [001] and [100].[13] Some growth sector boundaries (*S*) are also observable in our topographs, as are zonal inhomogeneities or striations (*Z*). Striations and other similar stripes parallel to the side faces likely arise from competition between step sources on the {110} and {111} faces during growth.

Figure 4.8 shows corresponding white light photograph (a) and X-ray topograph (b) of a pure KAP crystal grown by spontaneous nucleation at 30°C. This crystal contained a long fluid inclusion or void (*I*) in the $(\bar{1}1\bar{1})$ sector that can be seen in both images. Several dislocations (*D*) nucleate from this inclusion, emerging on the $(\bar{1}1\bar{1})$ face. A few dislocations in the {111} and {110} growth sectors appear to originate from the crystal nucleus (dark spot at center of crystal in the topograph). Sectoral boundaries (*S*) and zonal inhomogeneities or striations (*Z*) can also be seen in the topograph. The features labeled *R* in the photographs are from uneven growth on the $(0\bar{1}0)$ face that was in contact with

the bottom of the crystallization dish during growth. These ridges do not have a direct connection to any defect structures visible in the topographs (the same is true for the other samples discussed below). DIC images of this pure KAP crystal showed eight hillocks had propagated to the (010) surface. However, due to the general blurriness and strong distortions at the center of this crystal, no vicinal features from the (010) surface could be identified through X-ray topography.

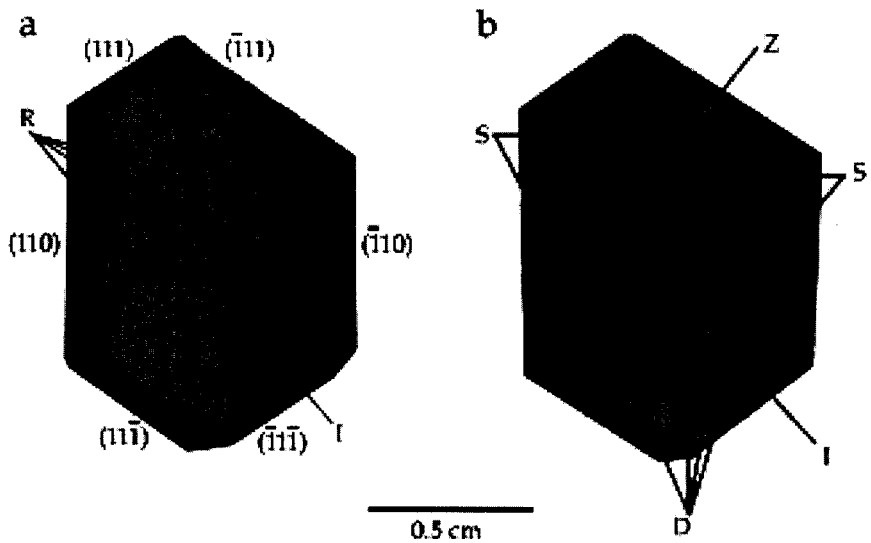

Figure 4.8. *Spontaneously nucleated pure KAP. Photo (a) and X-ray topograph of 400 reflection (b).* There is a large fluid inclusion or void (*I*) in the ($\bar{1}1\bar{1}$) sector, from which several dislocations (*D*) nucleate to emerge on the ($\bar{1}1\bar{1}$) face. Other dislocations appear to originate at the crystal nucleus (dark area in center). Sectoral (*S*) and zonal inhomogeneities (*Z*) are also visible indicating strain at growth sector boundaries and competing step sources, respectively.

Figure 4.9 shows corresponding photograph (a) and a very clean topograph (b) resulting from a KAP/DCF (10^{-5} M) crystal grown by spontaneous nucleation at 30°C. This heavily dyed crystal had clear sectoral (*S*) and zonal (*Z*) structures. There were several large fluid inclusions or voids (*I*) in the ($\bar{1}1\bar{1}$) sector, as well

as a few small inclusions (*i*) present. These inclusions acted as sources for dislocation bunches (*D*) that emerge on the $\{11\bar{1}\}$ faces. The more or less intensive striation (*Z*) in each growth sector is evidence of several existing step sources (vicinal hillocks) on each face of the sample during the growth, including a few that are visible on the (010) face, appearing as a contrast in color between the fast and slow vicinal slopes of the hillocks (similar to those apices recognized in DIC images). DIC and fluorescence imaging of this crystal showed 19 visible hillocks in the (010) sector. There is no kinematical contrast associated with strain from the dye's presence in the crystal (which would be seen as *darker* areas where the dye is included more heavily), indicating that the dye-inclusion crystals are equivalent in quality to pure, un-dyed crystals. Similar results were obtained by Vetter *et al.* in X-ray topography studies of hourglass inclusions of the dye acid fuchsin in potassium sulfate (K_2SO_4) single crystals.[18]

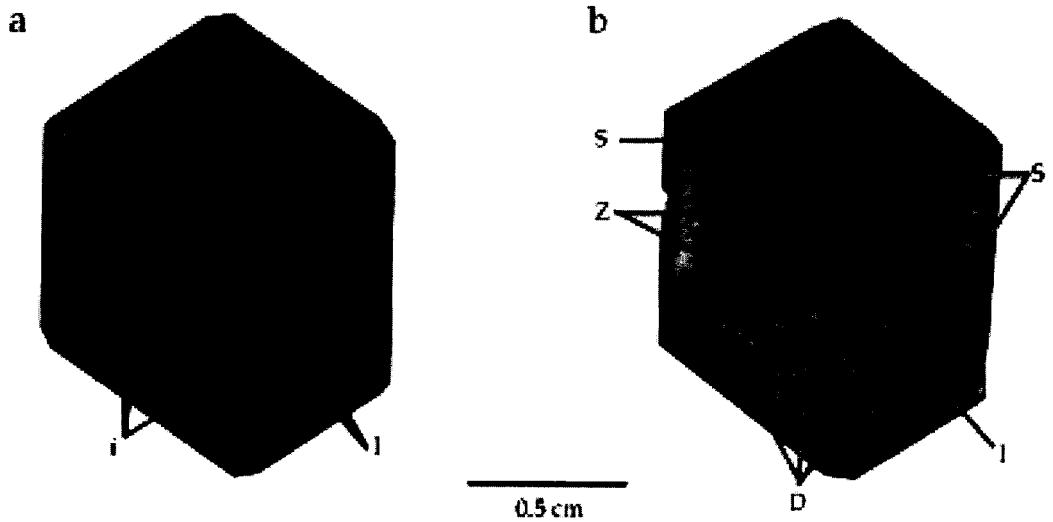

Figure 4.9. *Spontaneously nucleated KAP/DCF (10^{-5} M). Photo (a) and X-ray topograph of 400 reflection (b).* There is a series of large fluid inclusions or voids (*I*) in the $(\bar{1}1\bar{1})$ sector and a few smaller inclusions (*i*), from which several dislocation bunches (*D*) nucleate to emerge on the $\{11\bar{1}\}$ faces. Sectoral (*S*) and zonal inhomogeneities (*Z*) are again visible indicating strain at growth

sector boundaries and competing step sources, respectively. Strain from competing vicinal hillock steps on the (010) surface is also visible, however there is no kinematical contrast due to the presence of the dye, indicating the dyed crystals are no less perfect than pure KAP crystals in terms of structural integrity.

Figure 4.10 and Figure 4.11 show corresponding photographs (a) and topographs (b) resulting from un-dyed KAP crystals with 1 μm beads (10^{-9} M) embedded in them, as grown from seeds by slow evaporation at 30°C and 0.01% starting supersaturation. Unfortunately, these topographs are less informative due to their poor quality, especially in the area covered by the seed, indicating a high degree of strain introduced at the seed/daughter interface. Defects such as inclusions or voids (*I*) can be seen in large quantities around the seed border. Several dislocations (*D*) are also seen to originate at the seed/daughter interface. Zonal and sectoral structures are obscured by the general strain in the crystal.

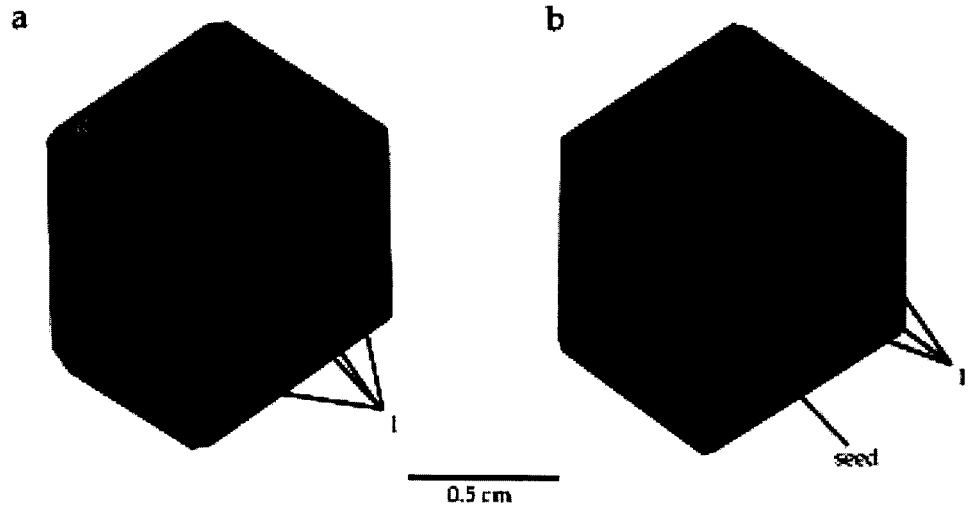

Figure 4.10. *Seed-grown KAP with 1 μm polystyrene beads included. Photo (a) and X-ray topograph (b).* Large inclusions (*I*) are seen surrounding the seed border, but all other contrast is washed out by strain at the seed/daughter interface.

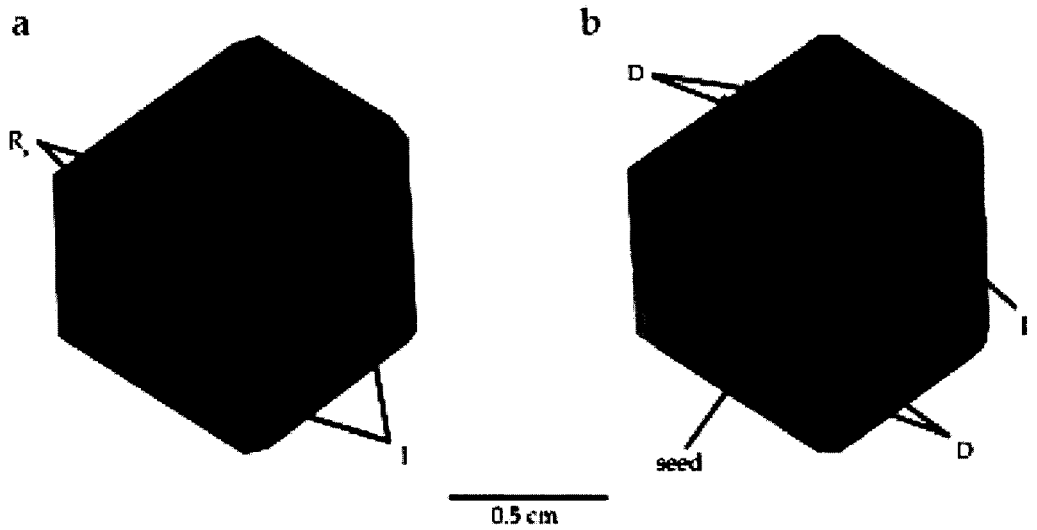

Figure 4.11. *Seed-grown KAP with 1 μm polystyrene beads included. Photo (a) and X-ray topograph (b).* Again, large inclusions (*I*) as well as some dislocation bunches (*D*) are seen originating at the seed border, but all other contrast is washed out by strain at the seed/daughter interface.

One possible explanation for the high degree of strain at the seed/daughter interface is the presence of many small inclusions introduced by the microbeads. When looked at in detail under an optical microscope (Figure 4.12), a significant number of chains or trails of bubbles spanning one to several microns can be seen. These long trails typically result from the presence of small solid particles at the growing crystal front that surf along for a while, leaving voids in their wake, until they are eventually trapped and overgrown. Although the volume density of these particulates within the crystals is low, the fact that they leave long trails of voids in the lattice can lead to distorted X-ray fields inside the crystal across the entire seed/daughter interface, rendering blurry topographs.

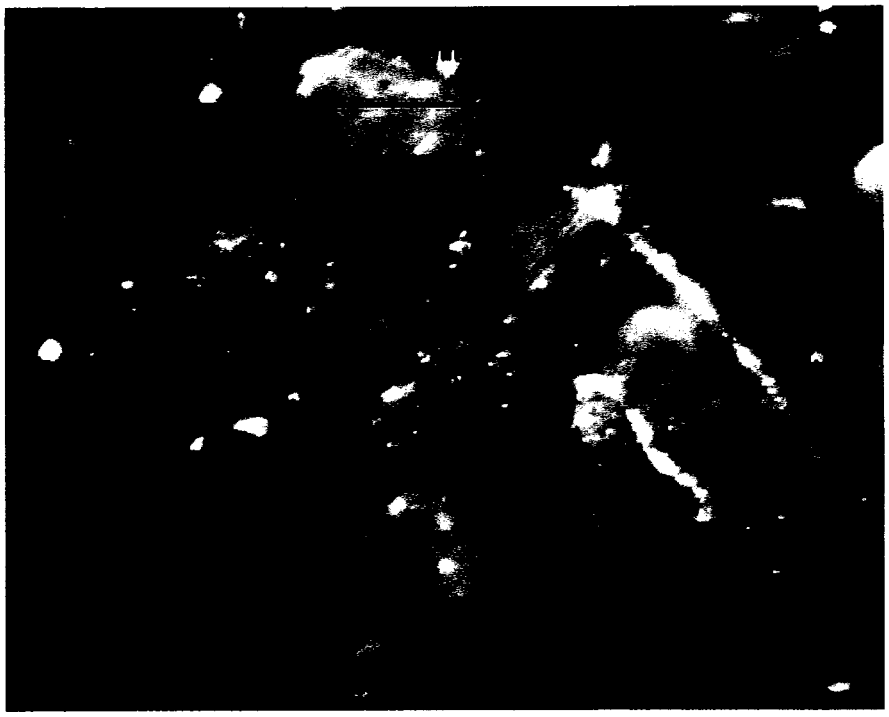

Figure 4.12. *Photo of tails or channels of bubbles typically resulting from capture of small solid particles during growth of crystal.* These channels create strain in the lattice and distort the X-ray fields inside, thus obscuring the topographic images. Tails resulting from individual particulate inclusions go in slightly different directions, thus illuminating them requires a change in the sample orientation relative to the light beam. Hence, on this photograph not all tails present are visible.

Another possible explanation for the significant strain in crystals grown from seed is the presence of stacking faults at the seed/daughter interface. For example, Sanchez and colleagues observed the formation of stacking disorder in sublimation-grown silicon carbide at the initial stages of growth from high quality Lely seeds.[19] Utilizing a combination of synchrotron X-ray topography, transmission electron microscopy (TEM), atomic force microscopy (AFM), and KOH etching they measured the correlation between the location and number of these stacking faults with the dislocation density (both edge and screw type). The

stacking faults at the seed daughter interface appeared as dark (strained) areas in X-ray topographs, and were also observed directly via TEM.[19,20] The majority of dislocations appeared to nucleate at the strained regions in pairs, likely having opposite Burgers vectors.[19] Other factors that influenced the dislocation density were the growth rate and the surface cut of the seed; dislocation densities increased for higher growth rates and decreased when seeds were slightly miscut off-axis to create a vicinal surface.[19] The authors proposed a mechanism whereby 2D islands containing basal plane stacking faults nucleate at the seed surface, and upon coalescence lead to the formation of partial dislocations in the basal plane.[19] Hence there is a direct correlation between strain at the seed/daughter interface, the formation of new dislocations, and the disorder that occurs in the early stages of growth from seed. While more investigation of growth dynamics and defect formation at the seed/daughter interface is needed, there seems to yet again be indication that information transfer from seed, with minimal mutation, is doomed to fail due to the complex nature of the growth of real crystals.

What about the defect structure of the {010} sectors? Similar to Sanchez *et al.*, we have also observed, via confocal microscopy, growth hillocks on the (010) face that arise in pairs. In KAP, these pairs often align themselves along the *a*-axis (see Figure 4.7 for example). Such pairs are consistent with the X-ray topographic and AFM analyses of Halfpenny *et al.* for the characterization of {010} dislocations (see Chapter 2, Section 2.3.4).[13] They observed a minority of mixed screw/edge dislocations (Burger's vectors = <110>) nucleated in V-shaped pairs with about 20° between arms that were equally inclined with respect to [010] and that lie in the (001) plane. These V-shaped pairs originated at isolated points lying at different depths, for which the sources were invisible in the X-ray topographs. While these pairs of dislocations represent a minority[21] of the hillocks appearing on the (010) face, they can still have a significant influence on

growth dynamics, as discussed in Chapter 1, Section 1.2.2.3. We will return to the appearance and significance of these dislocation pairs in Section 4.2.

In addition to the V-shaped mixed dislocation pairs in the (010) sector, Halfpenny *et al.* report "numerous instances" of dislocations bending into the (010) sector from underlying lateral sectors, as seen by a change in line direction at growth sector boundaries. In particular dislocations from the $\{11\bar{1}\}$ sectors with Burgers vector [001] that bend into (010) emerge as edge dislocations on the (010) face. Such dislocations are not likely to have as much of an influence on growth dynamics as those of mixed or pure screw type. Unfortunately, (010) dislocations with pure screw component are difficult to distinguish amongst the convolution of signals from underlying growth sectors in X-ray topographs. This results from Burgers vectors close to [010] appearing as short line segments in topographic projections. It is possible that pure screw type dislocations represent a significant contribution to the (010) hillocks, however X-ray topography falls short in identifying their presence. Needless to say, there remains much that can still be learned about dislocation nucleation and structure in KAP, which is indeed essential in using it to evaluate the 'crystals-as-genes' hypothesis.

4.2 Identifying Screw Dislocation Patterns and Evolution

Despite the challenges met in attempting to transfer defect patterns from parent to daughter crystals, we can still ascertain the information content and hillock evolution from crystals grown by spontaneous nucleation. In particular, the parent crystals themselves can be analyzed for the transfer of their defect patterns from one layer of growth to the next. For example, even in a 20 μm section of KAP, there are more than 15,000 replicated layers. Confocal laser scanning microscopy (CLSM)[22] can be used to image these 'fossil-records' of dyes

intrasectorally zoned within KAP crystals (as described in detail in Chapter 2, Section 2.6). With this technique, the spatio-temporal evolution of growth-active hillocks and the transfer of "genetic" information stored within crystal defect patterns can be investigated in as-grown crystals. The hillock patterns are analyzed using statistical analysis to assess the birth, death, and stability of growth-active hillocks, and fractal analysis is used to quantify the information content (see Chapter 2, Section 2.7 for details on analytical methods).

CLSM was used to image crystals doped with either **1**, **2**, or **3** at approximately 1 molar part dye per 100,000 parts KAP, within the fast slopes of the {010} growth hillocks. By scanning from the bottom to the top of a crystal, the number and position of the hillocks that form throughout the (010) growth sector were recorded. Figure 4.13 and Figure 4.14 show successive optical slices of KAP dyed with **3** and **1**, respectively, in which the development of the (010) growth sector can be seen in the evolving patterns of luminescence.[23] The optical sections are thin enough such that the *z*-coordinates can roughly be taken as time of growth. By mapping hillock positions in each optical section, and by comparing them to the positions in previous and subsequent sections, sequences of growth-active hillocks were obtained.

Figure 4.13. *Confocal slices of KAP with 3.* a) Cartoon of confocal *z*-sectioning of KAP (010) sector (green) containing screw dislocations (vertical lines). b) Confocal images read from top (left) to bottom (right) of the crystal, depth in the *z*-series is indicated. Step size is 15.0 μm. Every fifth optical slice is shown. Luminescence develops on the fast slopes of (010) growth hillocks, with vertices that mark the

dislocation cores. Crystal size = 5.5 × 9.2 × 1.0 mm. Each optical slice is composed of 5 frames wide by 10 frames high, where each frame is about 1 mm^2. These optical slices were automatically 'stitched together' by the Zeiss LSM 510 confocal control software.

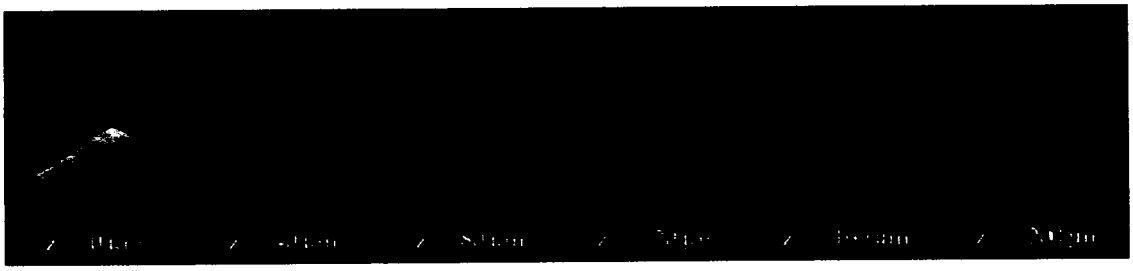

Figure 4.14. *Confocal*[24] *slices of KAP with* ***1***. Images read from top (left) to bottom (right) of the crystal, depth in the *z*-series is indicated. Step size is 20 μm. Every other optical slice is shown. Luminescence develops on the fast slopes of (010) growth hillocks, with vertices that mark the dislocation cores. Crystal size = 4.5 × 6.0 × 0.5 mm. Each optical slice is composed of 2.5 frames wide by 3 frames high, where each frame is about 2 mm^2. These optical slices were manually 'stitched together' and blended using image processing software[25].

4.2.1 *Locating Screw Dislocations*

Once an assembled mosaic of confocal tiles is obtained for each optical *z*-section,[26] a sequence of active hillocks throughout the growth history of the crystal can be identified. Screw dislocations are located by the apices of hillock chevrons. Figure 4.15 shows an example with a high density of dyed KAP hillocks. The points corresponding to the hillock generating dislocations were very sharp even at high magnifications. In most cases, they maintained the same *xy* coordinates through successive optical slices. Both of these observations are consistent with pure screw dislocations emergent on the (010) faces.

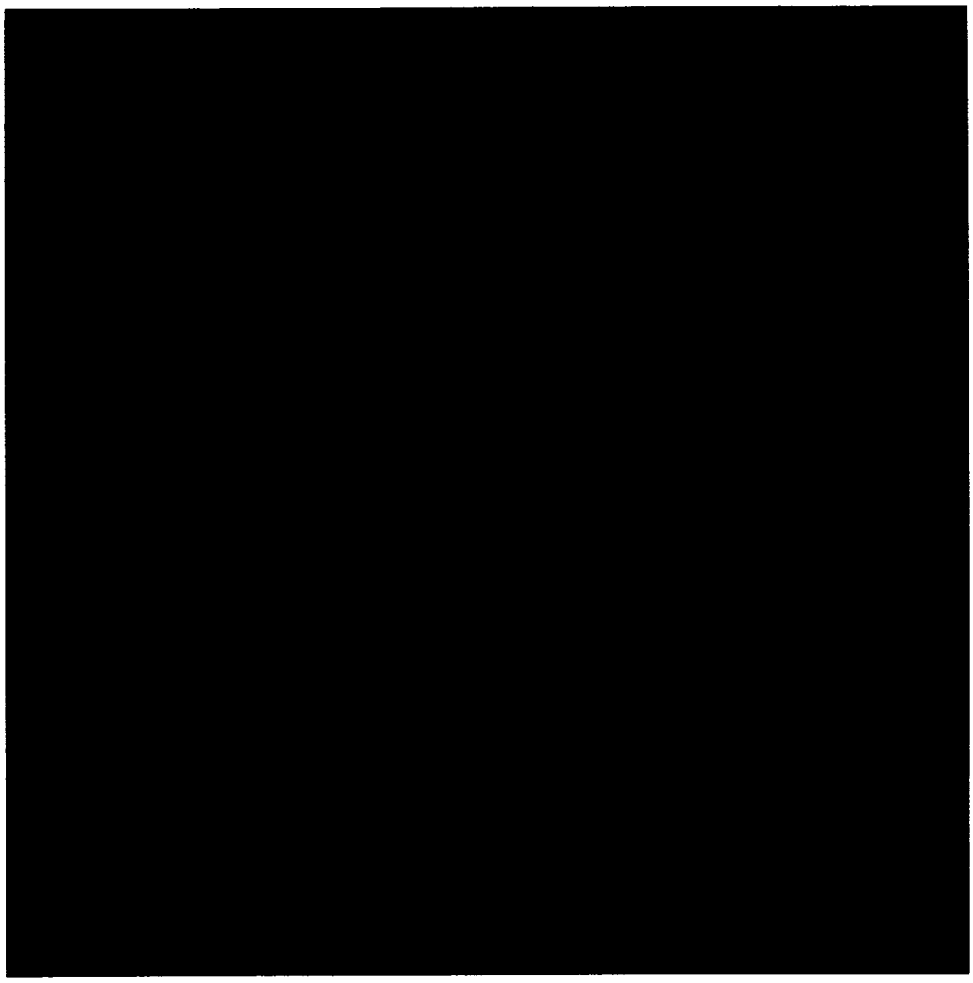

Figure 4.15. *Confocal imaging frame of KAP with 3.* This image shows details of luminescence that have developed in the fast slopes of the (010) growth hillocks. Vertices mark dislocation cores. Image size = 0.9 mm × 0.9 mm. (Image reproduced with permission by the Royal Society of Chemistry.[5])

Once fully formed, a hillock apex is easily isolated by eye with a precision of ±1 pixel in both x and y. Given the pixel resolution dictated by confocal scanning parameters used, this corresponds to anywhere between a 2 - 9 μm uncertainty in x and y for identifying screw dislocation locations. Furthermore, in the early stages of hillock formation, less dye is incorporated and its luminescence is faint, leading to greater uncertainty in the exact location of the apex in its earlier

sections. Dislocations with considerable edge character would undoubtedly move in the *xy* (or crystallographic (010)) plane between optical *z*-slices. In this way, the vertices of the luminescent chevrons would appear more diffuse at lower pixel resolutions. Were dislocations to emerge at an angle of just 20° with respect to (010), as is indicated by the V-shaped pairs found by Halfpenny *et al.*, the vertices would spread across ~4 μm in one 20 μm optical slice. Given that this is within our pixel resolution, it is possible that vertices would still appear sharp even for mixed dislocations. Indeed, on a minority of the hillocks mapped throughout the layers of our confocal *z*-stacks, there are some vertices that move about 1-2 pixels per optical slice. This is in agreement with a small population of mixed dislocations giving rise to some of the luminescent hillocks in our data. Further evidence for this inherently changing pattern of defects through the presence of mixed dislocation pairs on the (010) KAP face is given in the data analysis of the hillock growth sequence and evolution (see Section 4.2.2).

Results shown in the following section are from analyses performed on confocal data that was manually mapped[27] by myself or by undergraduate students, Serine Avagyan or Joyce Chen, who worked with me. The process of manually identifying hillock apices and birth/death sequence took about an hour per layer of the *z*-stack, where a *z*-stack typically had anywhere from 20 up to 80 optical sections depending on confocal scanning parameters used. With a physical tolerance of five consecutive hours, three days in a row to do this work, mapping out a single crystal could easily eat up one month. Due to this severe bottleneck created by having to manually map out hillock locations, we also explored the possibility of using machine vision programs to automatically identify hillocks within the confocal images. This avenue initially showed promise, however challenges were met in creating a feature detector robust enough to identify hillocks of varying contrast amidst the image noise, which

meant that we could not use a technique that depended on a threshold. Unfortunately, I abandoned machine vision. However, I do feel that this would be a profitable undertaking for future students who are drawn to this work, thus I have included supplemental information and examples of what we tried in Appendix B.

4.2.2 *Data Analysis Results*

By mapping hillock positions in each optical section of a confocal z-series, and by comparing them to the positions in previous and subsequent sections, a sequence of growth-active hillocks is obtained for a crystal sample. In addition to the growth sequence, the stability of the defect pattern is ascertained by recording the birth and death of growth-active hillocks in the (010) sector. Coordinates for the (010) outlines are also identified for each confocal layer in order to determine hillock density statistics, as well as to perform the density-density and angular correlation analyses (as described in Chapter 2, Section 2.7.1). This section gives the results obtained for five sample crystals all grown under similar conditions by slow evaporation at 30 °C. The samples reported were chosen because they had an above average number of hillocks in their (010) sectors, a necessary element for good counting statistics in these analyses. Table 4.1 summarizes the results for all five samples.

Crystal #1

The first sample of interest is one that had an exceptionally large number of hillocks on it, especially given its rather mediocre size. In fact, there were so many hillocks that it was very difficult to discern between neighboring hillocks in a cluster at the regular confocal imaging resolutions (5-10 μm/pixel). In

addition, it would have been a painstaking process to manually map out all imaged layers and track the birth/death sequence between layers. Yet, the sample was too beautiful to just pass up, given that its large number of hillocks made it a perfect candidate for testing proof-of-concept regarding the use of fractal analysis on a hillock pattern versus a random pattern. Thus, I mapped and analyzed only the surface layer of this crystal (imaged[23] at a higher resolution of 1.8 μm/pixel, requiring a greater acquisition time of course). The picture in Figure 4.15 shows a detailed section of this crystal's high population of hillocks.

This crystal was grown with 10^{-5} M DCF/**3** by slow evaporation in a dry temperature controlled chamber held at 30 °C. On the surface layer alone, there were 182 ± 10 active growth hillocks (the most I had seen prior to this was about 67 active hillocks on one layer), resulting in a density of 17.3 hillocks/mm^2 for the (010) surface. Since only one layer was mapped, no birth, death, lifetime, or information transfer statistics were obtained for the hillocks in this sample. The hillock pattern for the surface layer was analyzed via the density-density and angular correlation methods described in Chapter 2, Section 2.7.1. For comparison, 182 random events were generated within the bounds of the crystal *b*-face[28] and analyzed by the same methods.

Figure 4.16 shows the resulting log-log plots for the density-density correlation analysis of the hillock pattern (a) and the random pattern (b). The resulting fractal dimensions for the range of length scales showing power law behavior were 1.47 ± 0.03 for the hillocks, and 1.66 ± 0.06 for the random events. Some marked differences are immediately distinguishable between these two patterns (seen in the right side insets of Figure 4.16). The first thing to notice between these two patterns is that all but 8 hillock events fall within the blue

scanning area, whereas the random pattern is more spread out and has significantly more excluded events falling outside of the scanning area. Secondly, the hillocks seem to cluster, while the random events do not. This can also be seen in the correlation plots at smaller length scales, $r \leq 0.011$ mm, where the hillocks show an appreciable amount of pair-separations in this region, while the random events show none. The physical mechanisms governing clustering do not obey power-law scaling, therefore they must be non-random and non-fractal in nature. Hillock pairs at these small-scale separations were not included in the fractal dimension calculations. Within the power law scaling range (0.011 mm < r < 0.6 mm for the hillocks, and 0.016 mm < r < 1.0 mm for the random events), the hillock data is governed by a smaller scaling exponent (fractal dimension) than are the random events, again indicating a divergence from a purely random pattern. Both data sets show an "outliers" region where the power law scaling again drops off. This is due to the limitations of real data being boundary limited; the events falling near the edges of the pattern skew the results towards larger pair separations (in an unbounded pattern this would not be seen).

To further investigate the clustering nature of hillocks, histograms of nearest neighbor distances for both the hillock and random events were created. The hillock distribution showed a peak at small nearest neighbor separations between 11 - 22 μm. Whereas, the random distribution had a primary peak from 22 - 32 μm and a secondary one from 100 – 122 μm (Figure 4.17). This confirms that there are strong correlations between emergent dislocations on the (010) surface. It is likely that many of these dislocations are nucleated in pairs having opposite Burger's vectors. This will be addressed further in the discussion.

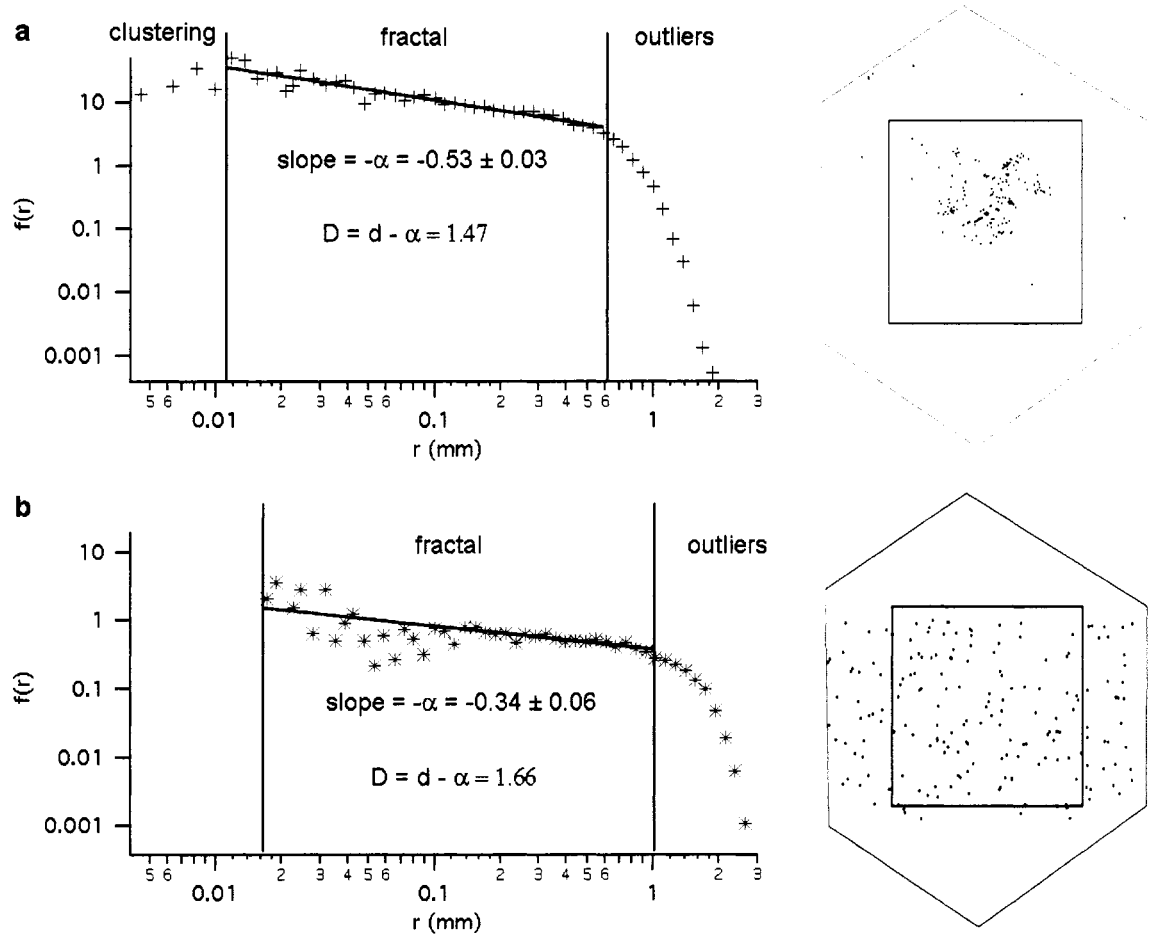

Figure 4.16. *Pair correlation plots for hillock pattern (a) and random pattern (b) relating to crystal #1.* Three distinct regions can be identified in each of the plots. Within the range of 0.011 mm and 0.6 mm for the hillocks (a) and from 0.016 to 1.0 mm for the random events (b), pair separations display the characteristic power-law behavior for a random fractal. The two data sets, however, result in different fractal dimensions, as shown. The regions at large *r*'s tail off due to boundary effects, while the regions at smaller length scales displays evidence of clustering in the case of the hillocks (a) and a lack of events in the case of the random data (b). The insets to the right of each plot are the corresponding patterns that were analyzed (dimensions for the (010) face were 3.7 mm along the *a*-axis and 4.6 mm along the *c*-axis).

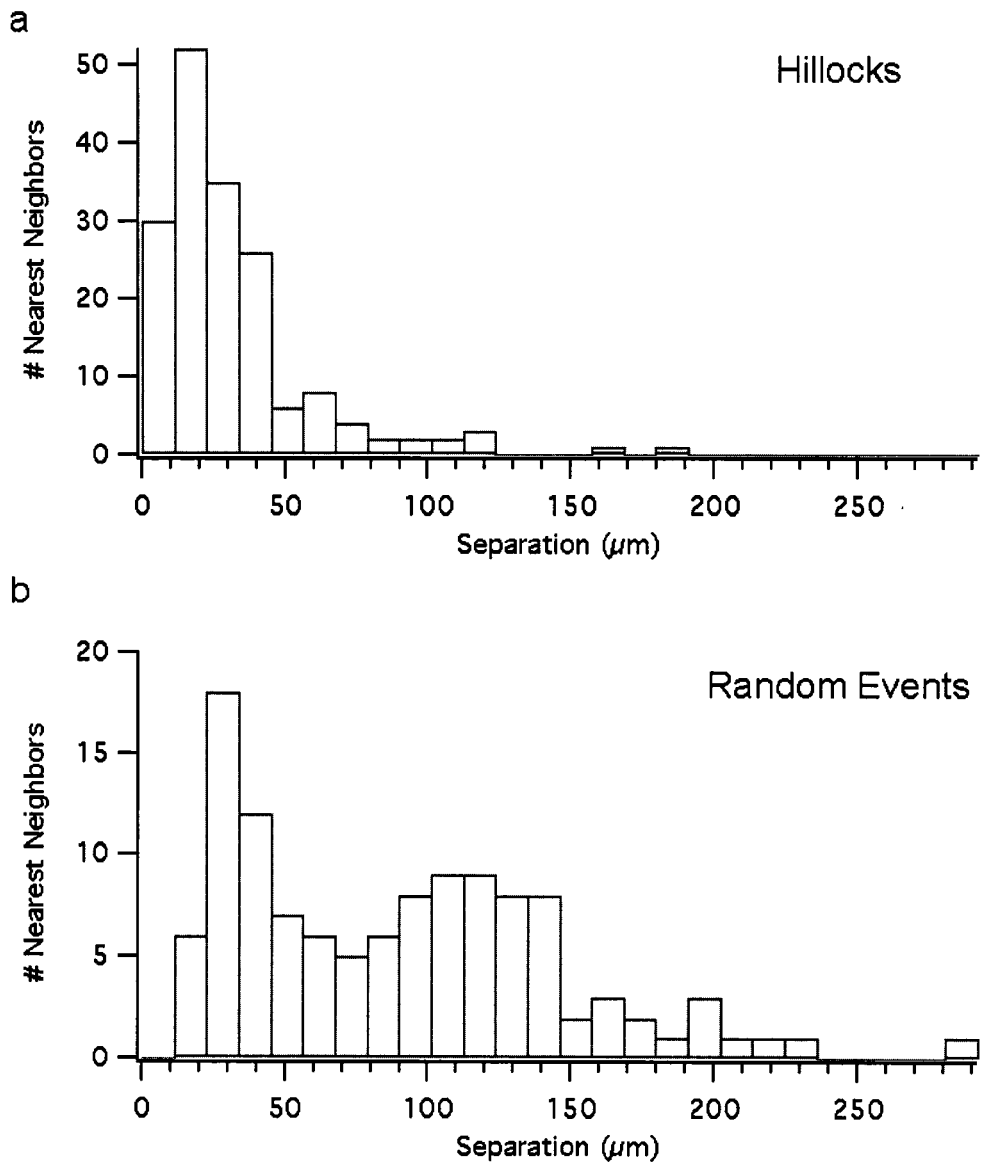

Figure 4.17. *Nearest neighbor distributions for crystal #1.* a) Hillock distributions show smaller nearest neighbor distributions, in general, with a peak at 16.2 ± 5.4 μm, indicating strong clustering tendencies at pair separations less then 22 μm. b) Random distributions show a primary peak at 27.5 ± 5.4 μm, and a secondary, more Gaussian-shaped peak around 112.0 ± 5.4 μm. Bin widths are 6 pixels or 10.8 μm each.

To probe other mechanisms by which the hillock pattern diverges from a random pattern, I analyzed directional correlations via two methods. The first method involved projecting the hillock locations onto the *a*-axis (non-polar) and *c*-axis (polar). Through this, a large number of hillock cores were observed to run in 'channels' along [001] and [100], respectively. This was measured as a pair-separation of zero in the projected views. Out of the 174 hillocks located within the scanning area, 14 of them were found to be in [001] channels and 16 were in [100] channels. Only 3 of these hillocks qualified as 2D clusters with $r < 7.2$ μm (4 pixels) that might have contributed to these results. The rest indicate longer-range [100] and [001] directional correlations between hillock locations. However, the hillocks found in [100] channels only accounted for 9% of the total active hillocks, likewise those in [001] channels accounted for about 8%.[29] By comparison, these correlations are completely absent in the randomly generated data along either channel.

Given that the crystallographic directions of [100] and [001] were distinctly correlated to the appearance of chains of hillocks, I performed further angular correlation analysis to test what other directions might influence the appearance of new hillocks (method described in Chapter 2, Section 2.7.1). Figure 4.18 shows the resulting distributions from performing the angular correlation analysis on the hillock data (thick black line) and the random distribution (dashed red line). The random data results in a flat[30] distribution, as it should be, for it represents an isotropic object. The hillock data, on the other hand, show multiple angular correlation peaks emerging at 25°± 4°, -11° ± 2°, -34°± 2°, -57°± 4°, and the largest one between -20 to -29° from the *a*-axis. The peaks centered around ±25° (including the largest peak) are well aligned with the boundaries between the

fast and slow slopes of the hillocks (measured angle is usually between ±25-29° from the *a*-axis, also seen as the angle at the apex of the dyed hillock chevrons with respect to [100]). These correlations are easily seen upon inspecting the confocal images of dyed hillocks by eye (see Figure 4.15). New hillocks often emerge precisely along the line extended by the dyed hillock apex. One would expect there to be a mirror symmetric distribution on both sides of these hillock fast-slow boundaries, however in this case there is a surplus of hillocks correlated to the [100] side of the hillocks. The -34° peak is perfectly aligned with the [101] and $[\bar{1}0\bar{1}]$ directions along which the fast and slow steps themselves orient and propagate. One would again expect to see a corresponding peak at +34° to indicate the mirror directions to these ($[10\bar{1}]$ and $[\bar{1}01]$), however this is absent in this data set. The -57° peak is interesting in that it is close to the [102] direction (calculated to be 53.4° from [100]), towards which the fast steps are said to occasionally misalign under significant selective kink blocking by impurities such as Ce^{3+} (as discussed in Chapter 3).[31] It is possible that the -11° peak arises from clustering in these directions as it is not associated with any particular crystallographic direction or defect structures that I am aware of. The peaks that would be expected at 0° and 90° corresponding to the [100] and [001] correlations are too small here to rise out from the background counts (the [100] channels had 116 pairs, while the [001] channels had only 97 pairs in this crystal).

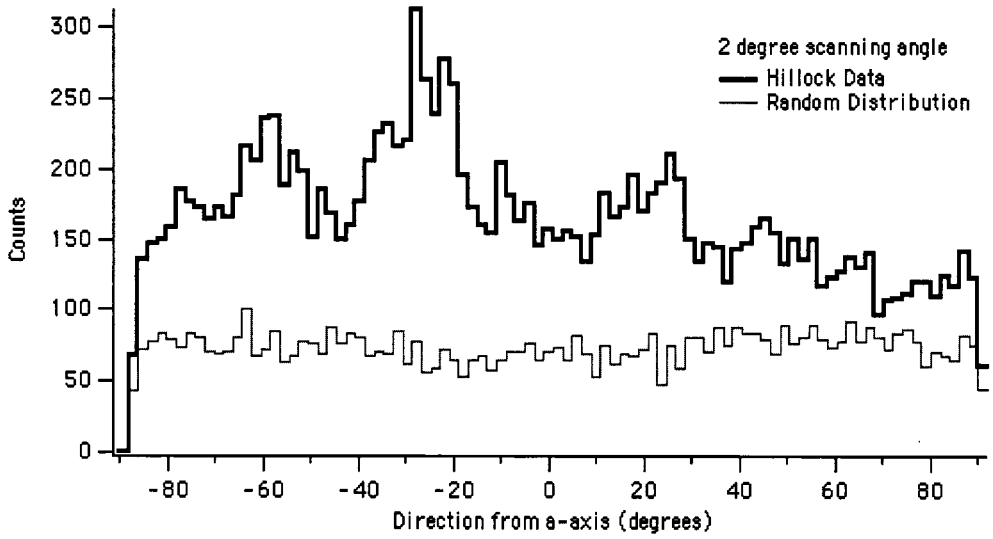

Figure 4.18. *Angular correlations for crystal #1.* The hillock directional correlations (thick black line) show peaks at 25°± 4°, -11° ± 2°, -34°± 2°, -57°± 4°, and the largest one between -20 to -29° from the *a*-axis. The purely random distribution of points (thin red line) shows no directional correlations, as is expected for an isotropic object.

Crystal #2

Sample 2 was grown with 10^{-5} M LGSFY/**1** by slow evaporation in a temperature controlled water bath held at 30 °C. The confocal imaging[24] showed 830 μm of (010) growth, throughout which I identified 189 hillocks. 54 of these hillocks propagated to the surface, a rather large population of hillocks compared to most of the crystals grown (with the exception of sample #1 described above) (Figure 4.19d). The lifetimes of the hillocks varied from ~20 μm (seen in only two sections) to ~520 μm (visible in 52 optical sections), with an average of ~130 μm. Figure 4.19 shows (a) the number of active hillocks and (b) the change in hillock density on the growing (010) surface, as well as (c) the total number of deaths that occured throughout the sector's growth. The hillock density reached a maximum at 2.2 hillocks/mm^2 for the whole *b*-face before

dropping back down. In general, this crystal displayed steady growth and increase in the number of active hillocks between 200 - 730 μm. Each new growth layer is ~13.33 Å high, the KAP *b* lattice constant. Thus even in a 20 μm section of KAP, there are more than 15,000 replicated layers. The assessment of information content parameters (see Chapter 2, Section 2.7.1) for this crystal, from one optical section to the next, showed an average *Transfer* = 95 ± 6%, *Mutation* = 7 ± 6%, and *Info_Preserved* = 89 ± 11%. This indicates a high degree of information content transferability and preservation through the 15,000 replicated layers between

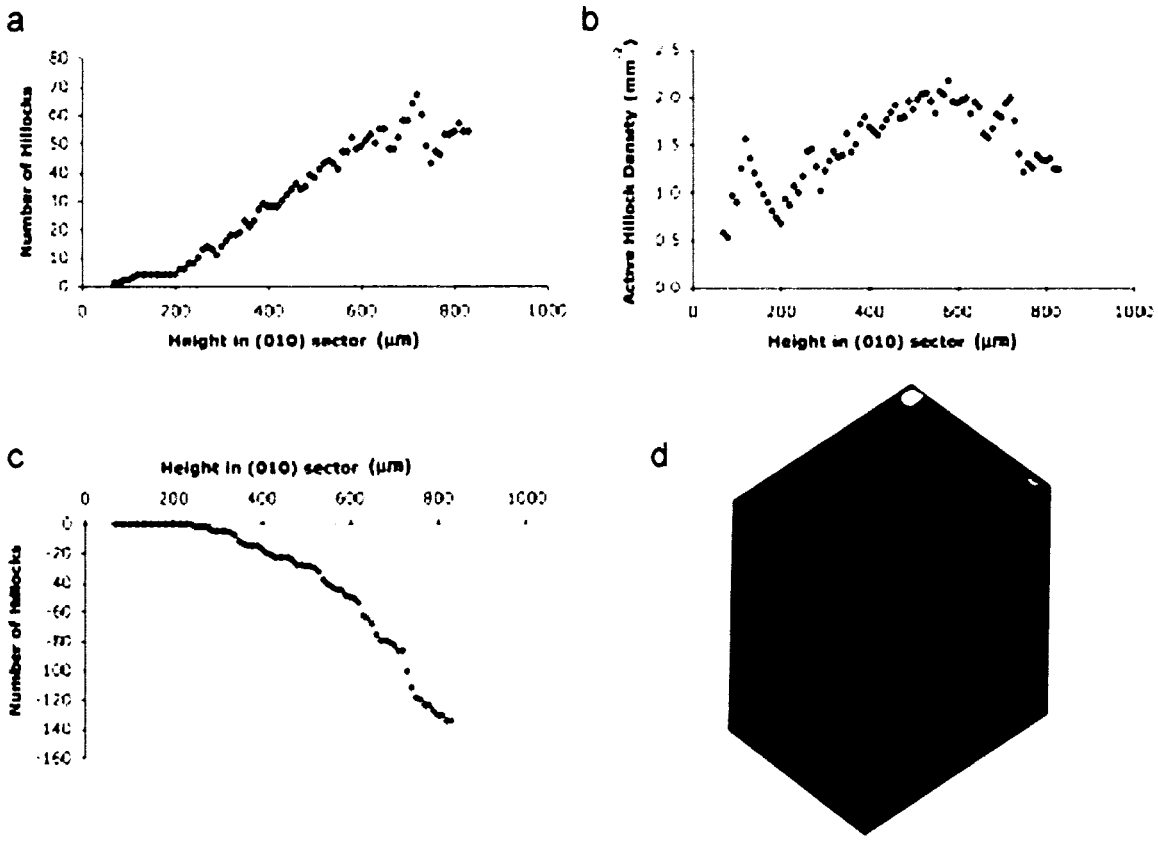

Figure 4.19. *Growth statistics for crystal #2.* a) Shows the total number of growth-active hillocks on each layer of the confocal z-series. b) Density of growth-active hillocks as a function of amount of (010) growth. c) Number of hillock "deaths" during growth. d) Confocal image of this crystal after 780 μm of (010) growth (crystal size is 8 mm × 10 mm. The circular obstruction in the image is due to a drop of solution that dried on the surface after harvesting).

optical sections. However, the integrity of this preservation degraded through time as the crystal grew, with the later stages of growth possessing almost none of the original information content, and with two to three instances where a largely new pattern emerged during the crystal's growth history.

After loading the sequence of hillocks for all layers of this *z*-series into the density-density correlation analysis code, the fractal dimensions, D_i, for the hillock patterns on each optical section (i) were determined (e.g. Figure 4.16a). The resulting plot of the fractal dimensions for all the layers in our crystal showed an average $D = 1.36 \pm 0.10$, with surprisingly little change between layers, even when 'dead hillocks' were removed from the sequence and new ones added (Figure 4.20a).

Figure 4.20b shows the resulting plot of the fractal dimensions for all corresponding layers of the Monte Carlo simulation that mimicked the growth of this crystal layer-by-layer (as described in Chapter 2, Section 2.7.1). In this case the simulated data continue to fill more space as the growth progresses, gradually increasing towards an average fractal dimension of 1.60 ± 0.05 at the later stages of growth. It is expected that if the simulation were to continue and the number of events increased, this fractal dimension would continue to rise towards $D = 2$, the Euclidean dimension that encloses the pattern. The comparison of these data indicates that there is a form of stability in the information content of the developing pattern for this crystal's hillocks and their local density correlations, even if the individual locations are not predetermined and the number of growth active hillocks varies from layer to layer.

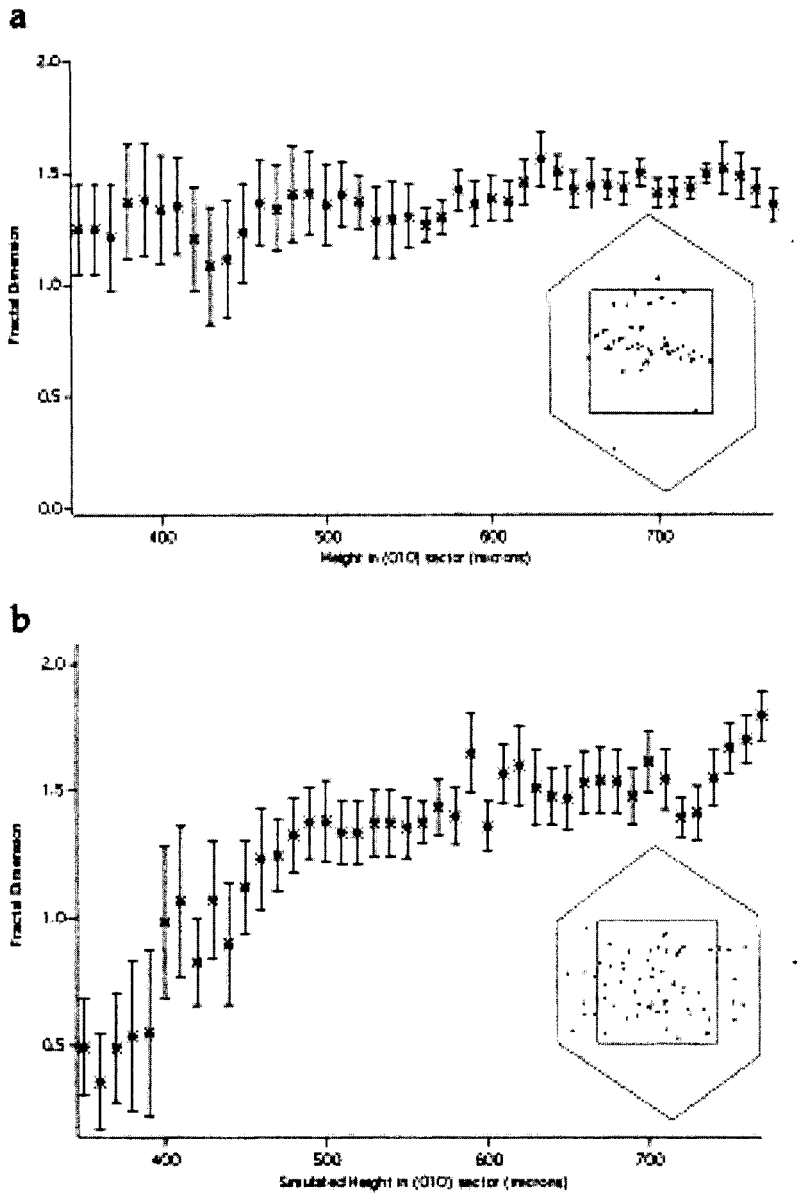

Figure 4.20. *Fractal dimensions for all optical sections of crystal #2.* The fractal dimension and its uncertainty, determined from fitting the slope of the pair correlation plots, is shown as a function of vertical growth of the (010) sector for both (a) the hillock data and (b) the Monte Carlo data. The fractal dimension consistently hovers around 1.4 ± 0.1 throughout the plot for the hillock data (a), whereas it gradually increases up to 1.6 ± 0.1 and beyond for the Monte Carlo data (b). The insets in (a) and (b) are examples of the hillock locations on a single layer of the actual crystal and from the Monte Carlo simulation, respectively.

To investigate this further, nearest neighbor distributions were plotted in a histogram for the various layers of both the hillock data and the Monte Carlo data for comparison. As expected, the hillock distributions showed peaks at small nearest neighbor separations between 0 - 30 μm. Whereas the Monte Carlo distributions had peaks around 30-50 μm (Figure 4.21). Furthermore, the simulated data showed 35% fewer 2D clusters (< 20 μm separation) than the hillock data for this crystal. This again confirms hillock clustering.

The [001] and [100] projections showed a large number of hillock cores running in these 'channels'. In general the number of active hillocks found in these channels fluctuated significantly between layers. However, there was an average of 4.7 ± 2.8 times more pairs aligned along the [100] channels than along the [001] channels. Of these, only about 12% of the [100] channels were attributable to hillock clusters of less than 4 pixel (20 μm) separation in the 2D pattern, the rest indicate longer range [100] directional correlations between hillock locations. On the other hand, around 46% of the [001] channel pairs were found in 2D clusters of hillocks. However, even on the layer with the greatest number of such channels, the hillocks found in [100] channels still only accounted for 23% of the total active hillocks, while those in [001] channels accounted for only 16%.[32] By comparison, these correlations are about 4-6 times less frequent in the Monte Carlo data along either channel.

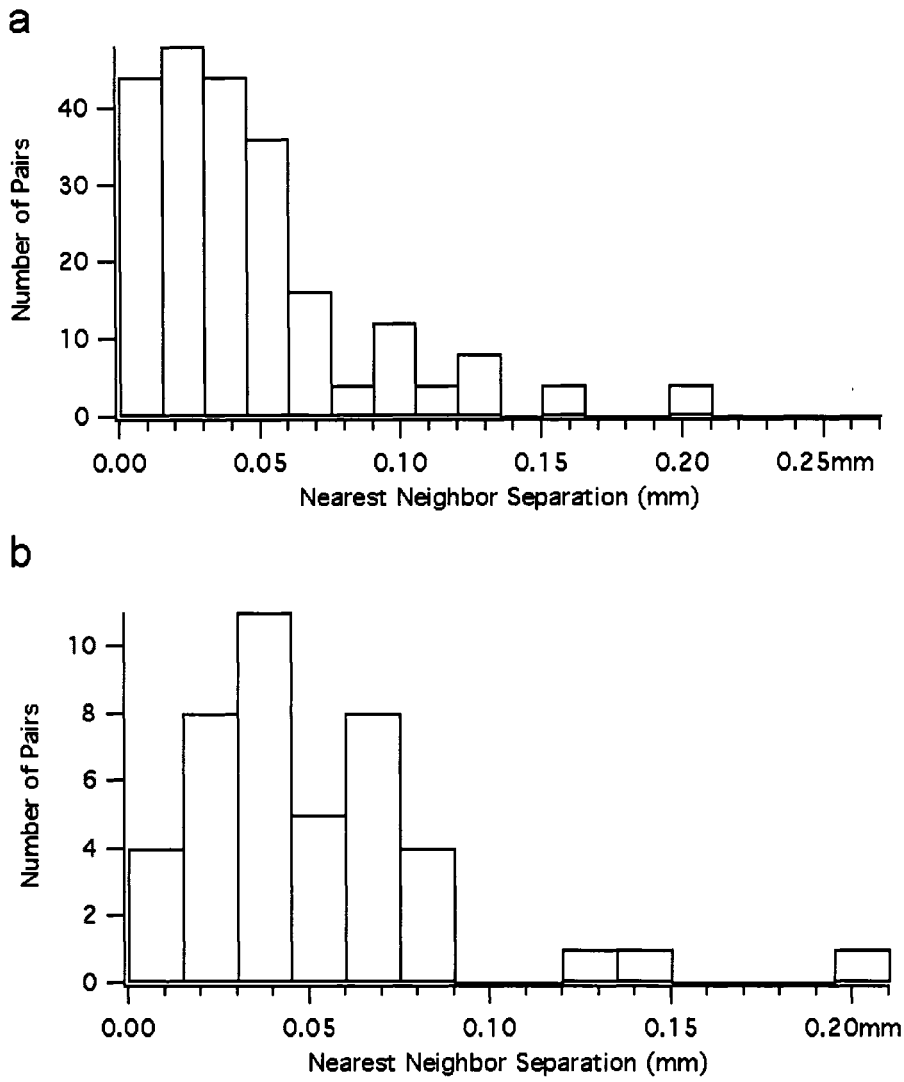

Figure 4.21. *Nearest neighbor distribution for hillock (a) and Monte Carlo (b) data of crystal #2.* a) Hillocks show clustering with a peak in the nearest neighbor distribution at smaller separations of 0 - 0.03 mm. b) Simulated data however does not reach its peak until a nearest neighbor separation of 0.03 - 0.05 mm. These distributions are for a confocal section of this crystal with 64 active hillocks, imaged at 710 μm of (010) growth.

Figure 4.22 shows the resulting distributions from performing the angular correlation analysis on the hillock data (thick black line), the Monte Carlo data (thin blue line), and on a purely random distribution of 189 points (i.e. not mimicking birth/death of events through growth as the Monte Carlo simulation does; dashed red line). The hillock data have more points included in the distribution because most of the hillocks again fell within the scanning area. Likewise, the Monte Carlo data had more of its events constrained to the inner portions of the simulated (010) sector than did the purely random distribution, thus the random distribution has the least amount of data included in the final analysis.

The random data resulted in a flat distribution, as expected for an isotropic object. The Monte Carlo data, on the other hand, is more Gaussian shaped with a peak at $-12.1 \pm 0.9°$ from the *a*-axis and a FWHM of $39.0 \pm 1.8°$. Again, because the Monte Carlo data simulates boundary-limited random events, where the (010) area is changing in time from small to large, it is expected that the pattern will have some non-isotropic characteristics and will therefore have angular correlations, depending on the frame of reference. However, these correlations are different from those of the hillock data for this crystal, which show multiple angular correlation peaks emerging above the threshold[33] of 250 counts at $-7° \pm 4°$, $-24° \pm 2°$, and $\pm 33° \pm 3°$ from the *a*-axis. This crystal had a slight off-axis rotation in the cofocal images, thus it is likely that the $-7°$ peak arises from a combination of [100] channel correlations as well as clustering in these directions. The $-24°$ peak is very close to what would be expected for new hillocks emerging along the boundary between the fast and slow slopes of a previous hillock (measured angle is $\pm 27°$, also seen as the angle at the apex of the dyed hillock chevrons with respect to [100]). In this case it would be on the [100] side of the hillock. One would expect there to be a mirror symmetric correlation on the

[$\bar{1}$00] side of the hillock fast-slow boundary as well, however such a peak does not appear in this data set. The ±33° peaks, are perfectly aligned with the <101> crystallographic directions, along which the fast and slow steps themselves align and propagate.

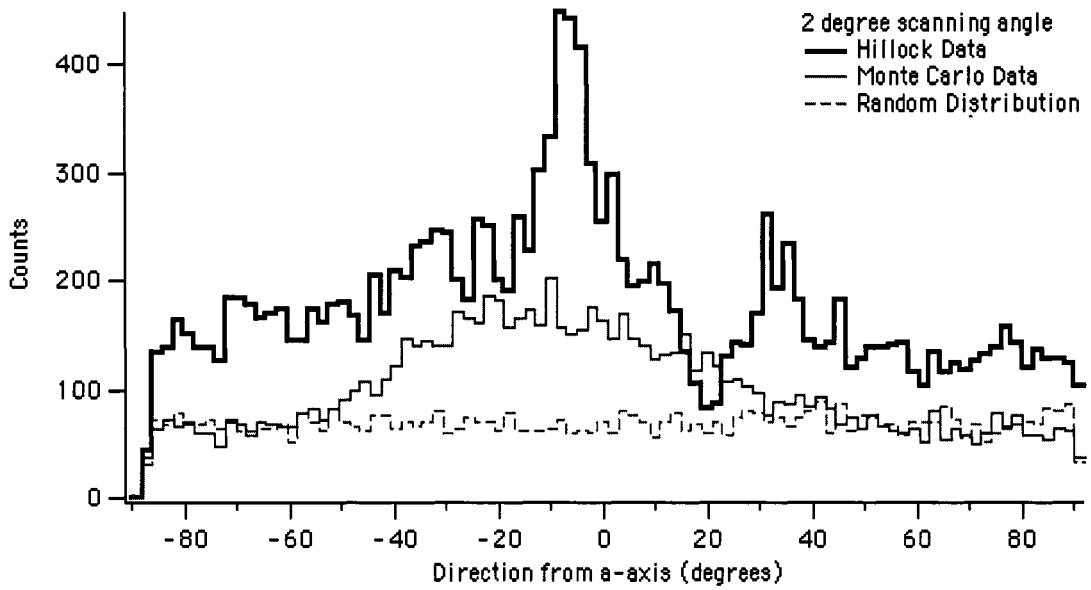

Figure 4.22. *Angular correlations comparison for crystal #2 and simulated data.* The hillock directional correlations (thick black line) show peaks above the threshold[33] of 250 counts at -7° ± 4°, -24° ± 2°, and ±33°± 3° from the *a*-axis. The Monte Carlo data (thin blue line) displays a Gaussian distribution of directional correlations, centered at -12.1 ± 0.9° from the *a*-axis and a FWHM of 39.0 ± 1.8°. The purely random distribution of points (dashed red line) shows no directional correlations, as is expected for an isotropic object.

Crystal #3

Sample #3 (Figure 4.23d) was grown with 10^{-5} M LGSFY/**1** by slow evaporation in a temperature controlled water bath held at 30 °C. Only 320 μm

worth of the (010) sector was imaged[24] via confocal microscopy. In that portion of the sector, 61 growth active hillocks were found, of which 32 propagated to the surface. The lifetimes of the hillocks varied from ~20 μm (seen in only one section) to ~320 μm (visible in all 16 optical sections imaged), with an average of ~140 μm. Figure 4.23 shows (a) the number of active hillocks and (b) the change in hillock density on the growing (010) surface, as well as (c) the total number of deaths that occurred throughout the sector's growth. The hillock density reached a maximum at 3.0 hillocks/mm^2 for the whole *b*-face before dropping back down slightly. In general, this crystal displayed steady growth and increase in the number of active hillocks, however the growth seemed to fluctuate a bit more than in sample #2. The assessment of information content parameters (see Chapter 2, Section 2.7.1) for this crystal, from one optical section to the next, showed an average *Transfer* = 94 ± 5%, *Mutation* = 11 ± 5%, and *Info_Preserved* = 84 ± 7%. This indicates a high degree of information content transferability and preservation through the 15,000 replicated layers between optical sections (20 μm optical section thickness). However, the integrity of this preservation gradually degraded through time as the crystal grew, with the later stages of growth possessing much less of the original information content.

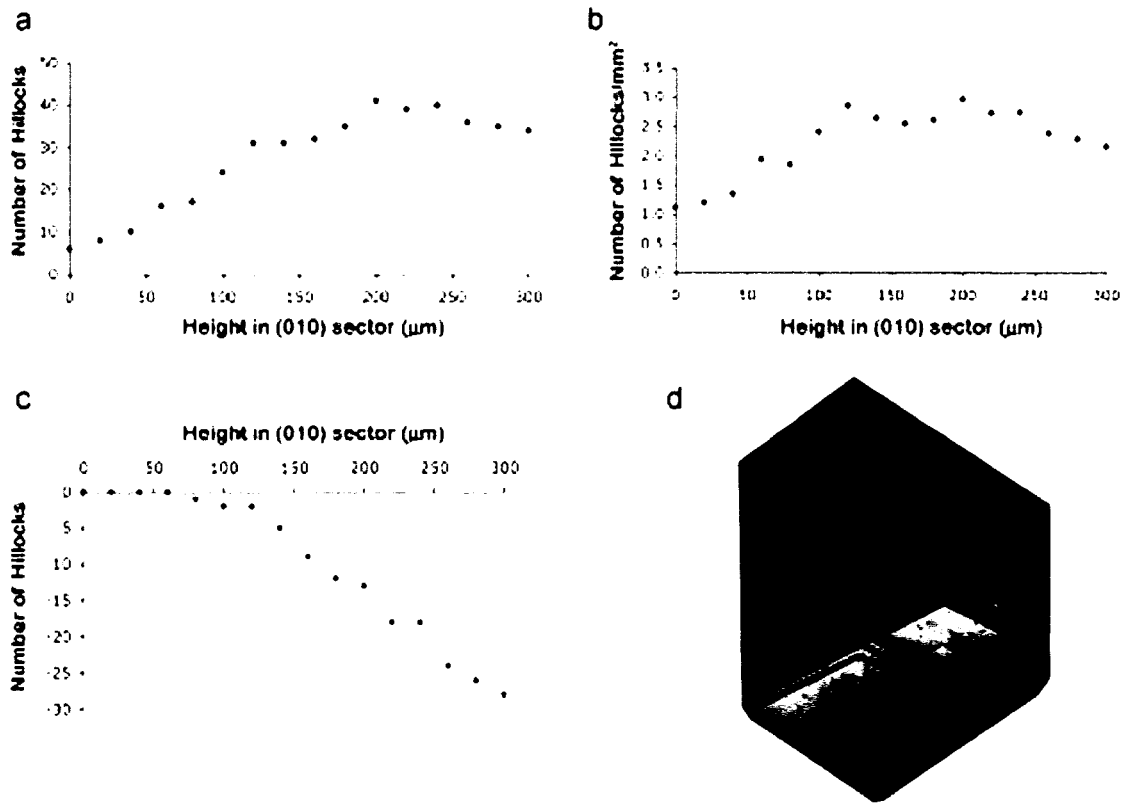

Figure 4.23. *Growth statistics for crystal #3.* a) Shows the total number of growth-active hillocks on each layer of the confocal *z*-series. b) Density of growth-active hillocks as a function of amount of (010) growth. c) Number of hillock "deaths" during growth. d) Confocal image of this crystal at (010) surface (crystal size is 4 mm × 5.5 mm).

After loading the sequence of hillocks for all layers of this *z*-series into the density-density correlation analysis code, the fractal dimensions, D_i, for the hillock patterns on each optical section (i) were determined (e.g. Figure 4.16a). The resulting plot of the fractal dimensions for all the layers in our crystal showed it reaching a maximum of 1.6 ± 0.1 and then retracing to an average value of D = 1.44 ± 0.12 (Figure 4.24a). There was more variation in this crystal's density correlation dimensions than in sample #2.

Figure 4.24b shows the resulting plot of the fractal dimensions for all corresponding layers of the Monte Carlo simulation that mimicked the growth of this crystal, layer-by-layer (as described in Chapter 2, Section 2.7.1). In this case the simulated data is not too different from the hillock data early on, but as growth continued, the fractal dimension gradually increased to and steadied out at an average value of 1.54 ± 0.10. It is expected that if the simulation were to continue and the number of events increased, this fractal dimension would continue to rise, while the hillock pattern would likely have continued to fluctuate around its average value of 1.4. The comparison of these data again indicates that the hillock pattern diverges from randomly generated growth, though in this case, due to fewer statistics, the difference is smaller than that shown in crystals #1 and #2.

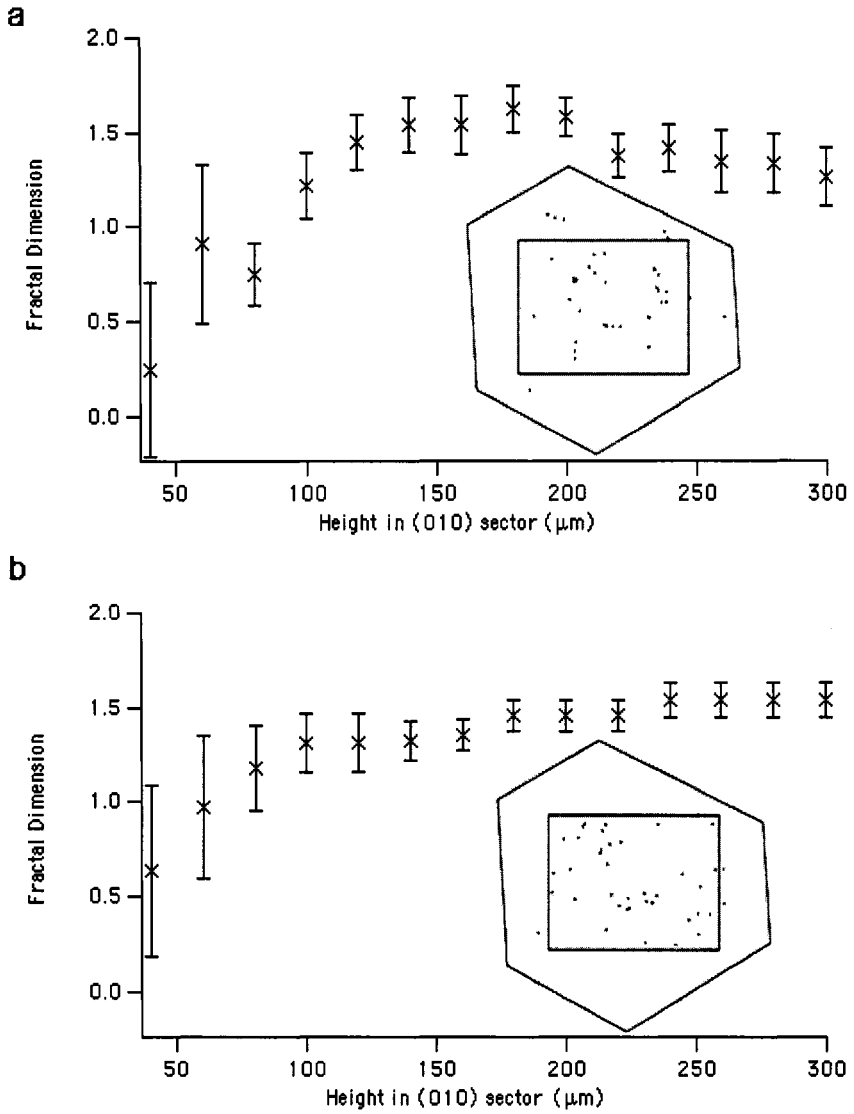

Figure 4.24. *Fractal dimensions for all optical sections of crystal #3.* The fractal dimension and its uncertainty, determined from fitting the slope of the pair correlation plots, is shown as a function of vertical growth of the (010) sector for both (a) the hillock data and (b) the Monte Carlo data. The fractal dimension reaches a maximum of 1.6 ± 0.1 and then retraces to an average value of 1.44 ± 0.12 for the hillock data (a), whereas for the Monte Carlo data (b) the fractal dimension gradually increases up to and steadies out at 1.54 ± 0.10 and is poised to continue its climb. The insets in (a) and (b) are examples of the hillock locations on a single layer of the actual crystal and from the Monte Carlo simulation, respectively.

Again, nearest neighbor distributions for the various layers of both the hillock data and the Monte Carlo data were inspected (Figure 4.25). While the statistics were somewhat poor, the hillock distributions did show a peak at small nearest neighbor separations between 0 - 50 μm. Whereas the Monte Carlo distributions were more Gaussian-shaped peaking around 144 - 200 μm. Furthermore, the simulated data showed 35% fewer 2D clusters (< 38 μm separation) than the hillock data for this crystal. This again confirms that one of the primary mechanisms whereby the hillock data are governed by non-random nucleation mechanisms is in their tendency to cluster and in their pair correlations.

The [001] and [100] projections again showed a significant number of hillock cores running in these 'channels'. In general the number of active hillocks found in these channels fluctuated between layers. However, there was an average of 1.4 ± 0.4 times more pairs aligned along the [001] channels than along the [100] channels in this crystal. Of these, 49% of the [001] channels and about 36% of the [100] channels were attributable to hillock clusters of less than 4 pixel (38 μm) separation in the 2D pattern, the rest indicate longer range directional correlations between hillock locations. However, even on the layer with the greatest number of such channels, the hillocks found in [001] channels still only accounted for 27% of the total active hillocks, while those in [100] channels accounted for only 21%.[32] By comparison, these correlations are about 3 times less frequent along [001] and 1.5 times less frequent along [100] in the Monte Carlo data along either channel. This crystal is one example for which there were more correlations along [001] than [100], typically it is the opposite.

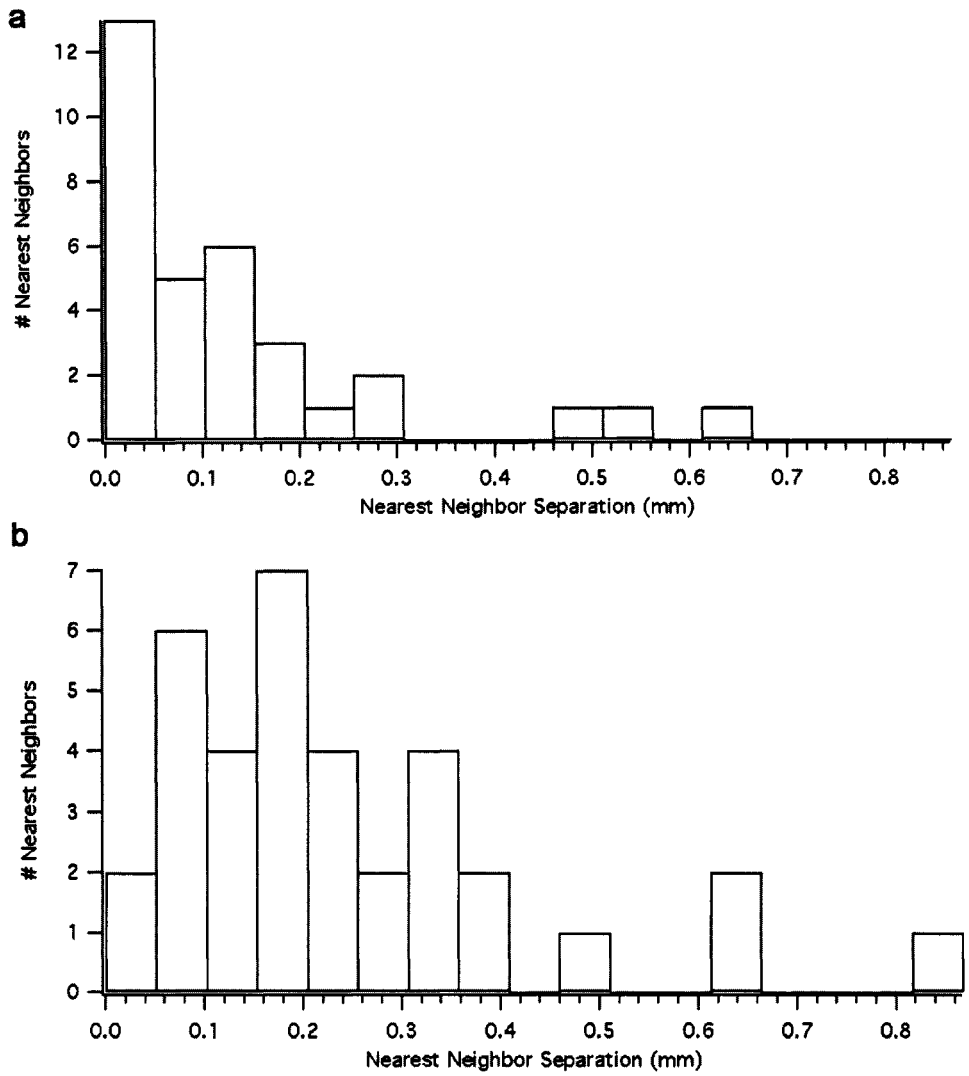

Figure 4.25. *Nearest neighbor distribution for hillock (a) and Monte Carlo (b) data of crystal #3.* a) Hillocks show clustering with a peak in the nearest neighbor distribution at smaller separations of 0 - 0.05 mm. b) Simulated data however does not reach its peak until a nearest neighbor separation of 0.14-.20 mm. These distributions are for a confocal section of this crystal with 41 active hillocks, imaged at 100 μm deep from the (010) surface.

Figure 4.26 shows the resulting distributions from performing the angular correlation analysis on the hillock data (thick black line), the Monte Carlo data (thin blue line), and on a purely random distribution of 61 points (i.e. not

mimicking birth/death of events through growth as the Monte Carlo simulation does; dashed red line). The hillock data have more points included in the distribution because most of the hillocks again fell within the scanning area. Likewise, the Monte Carlo data had more of its events constrained to the inner portions of the simulated (010) sector than did the purely random distribution, thus the random distribution has the least amount of data included in the final analysis. With all three data sets, the number of events that occurred in this crystal were small by comparison to crystal samples #1 and #2, thus the angular correlation histograms are not as well formed due to limited counts, hence the need for using a threshold[33] to discriminate peaks from noise is more necessary here.

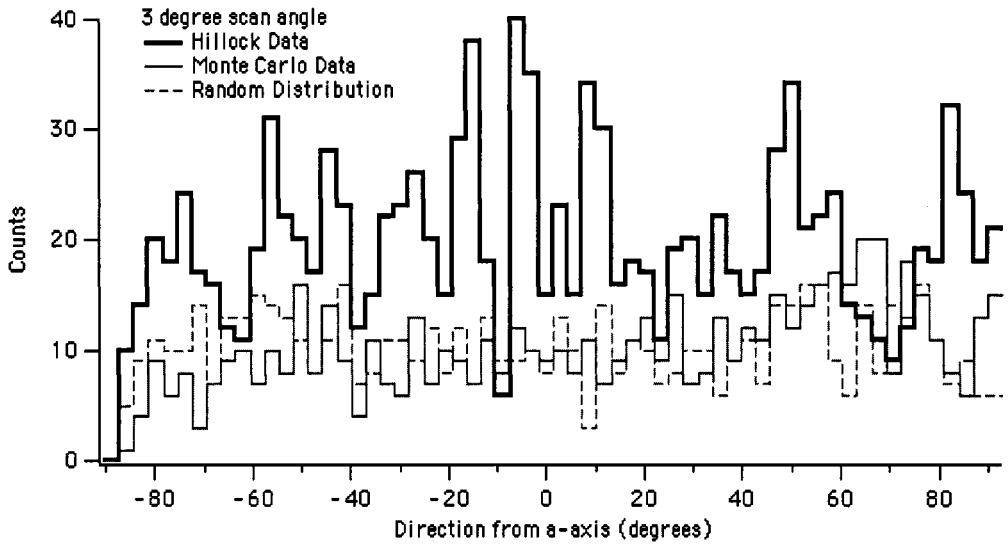

Figure 4.26. *Angular correlations comparison for crystal #3 and simulated data.* The hillock directional correlations (thick black line) show spikes above a threshold[33] value of 26 counts at -58° ± 2°, -46° ± 2°, -28° ± 2°, -16° ± 2°, -6° ± 2°, 1.5° ± 2°, 9° ± 2°, 47° ± 2°, 81° ± 2°, and 90° ± 2° from the *a*-axis. The Monte Carlo data (thin blue line) displays similar behavior to the random distribution (dashed red line) with the exception of a small peak that rises up around 65 ± 2° from the *a*-axis. The purely random distribution of points (dashed red line) shows no directional correlations, as is expected for an isotropic object.

The random data resulted in a flat distribution, as expected for an isotropic object. The Monte Carlo data closely followed the random distribution until it reached 65 ± 2° from the *a*-axis, where it formed a small Gaussian-shaped peak. However, these correlations are again different from those of the hillock data for this crystal, which show multiple angular correlation peaks or spikes emerging above a threshold[33] value of 26 counts at -58° ± 2°, **-46° ± 2°**, **-28° ± 2°**, -16° ± 2°, -6° ± 2°, **1.5° ± 2°**, 9° ± 2°, **47° ± 2°**, 81° ± 2°, and **90° ± 2°** from the *a*-axis. The directions in bold print have potential crystallographic and structural correspondences as described below, while the others are not as apparent. This crystal had a slight off-axis rotation of about 2° in the cofocal images, thus it is likely that the small 1.5° ± 2° peak arises from the [100] channel correlations. The -46° and +47° peaks are possibly related to misoriented hillock fast steps (which can be anywhere between 34°-54°). The -28° peak is very close to what would be expected for new hillocks emerging along the boundary between the fast and slow slopes of a previous hillock (measured angle is ±27°, also seen as the angle at the apex of the dyed hillock chevrons with respect to [100]). In this case it would be on the [100] side of the hillock. One would expect there to be a mirror symmetric correlation on the $[\bar{1}00]$ side of the hillock fast-slow boundary as well, however such a peak does not appear in this data set. The 90° peak, is obviously aligned with the [001] directional correlations. There are no peaks that correspond to the <101> crystallographic directions in this crystal, along which the fast and slow steps are expected to be aligned. If indeed the fast steps are misoriented in this crystal due to anisotropic kink adsorption, the lack of a peak at ±34° would indicate there is no correlation between hillock nucleation and the slow steps (which usually do not misorient easily).

Crystal #4

Sample #4 (Figure 4.27d) was grown with 10^{-5} M DCF/**3** by slow evaporation in a temperature controlled water bath held at 30 °C. As seen by confocal microscopy[23], the (010) sector was 915 μm deep, throughout which 80 growth active hillocks were found, with 34 propagating to the surface. The lifetimes of the growth hillocks varied from ~15 μm (seen in only one section) to ~600 μm (lasting through 40 sections), with an average of ~195 μm. Figure 4.27 shows (a) the number of active hillocks and (b) the change in hillock density on the growing (010) surface, as well as (c) the total number of deaths that occurred throughout the sector's growth. The active hillock density in this crystal oscillated drastically, with a maximum at 1.1 hillocks/mm^2 and a mean of 0.7 ± 0.2 hillocks/mm^2 for the whole *b*-face. In general, this crystal displayed fluctuating growth with several birth and death spurts. This kind of fluctuation is reminiscent of what might occur under widely varying local supersaturation conditions.

With each new growth layer being ~13.33 Å high, a 15 μm section of KAP has more than 11,000 replicated layers. The assessment of information content parameters (see Chapter 2, Section 2.7.1) for this crystal, from one optical section to the next, showed an average *Transfer* = 96 ± 8%, *Mutation* = 7 ± 7%, and *Info_Preserved* = 89 ± 13%. This indicates a high degree of information content transferability and preservation through the 11,000 replicated layers between optical sections. However, the integrity of this preservation degraded through time as the crystal grew, with the later stages of growth possessing none of the original information content, due to at least one instance where an entirely new pattern emerged during the crystal's growth history.

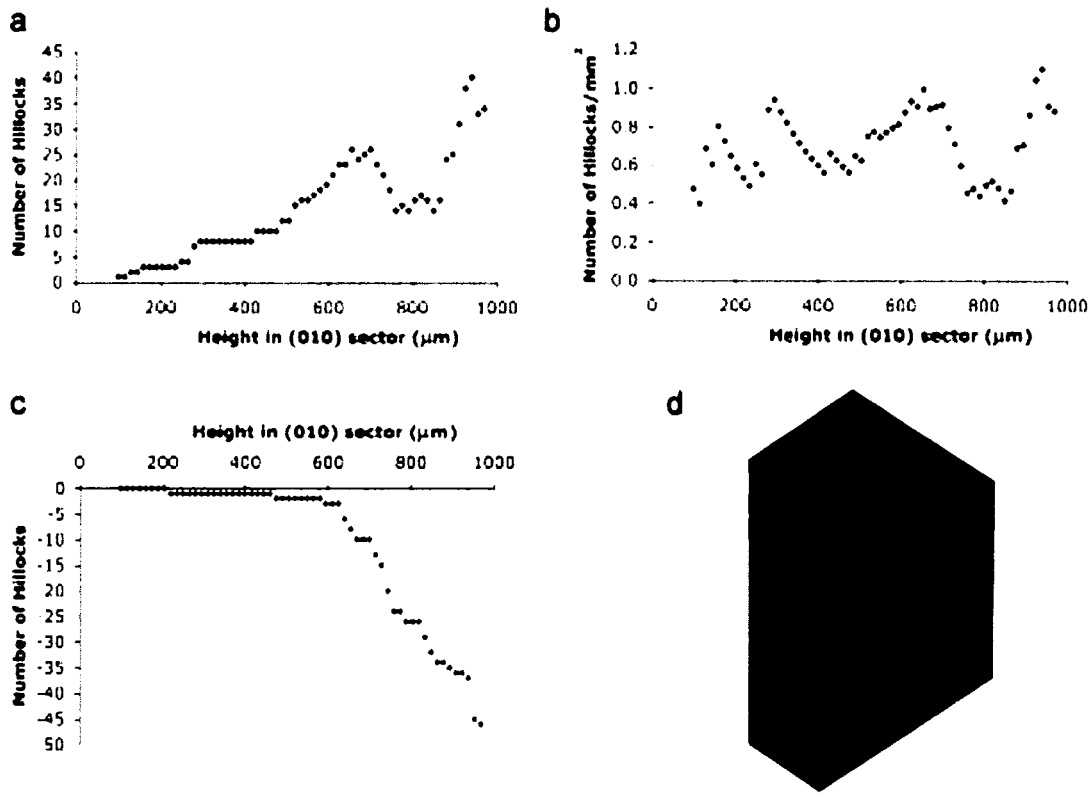

Figure 4.27. *Growth statistics for crystal #4.* a) Shows the total number of growth-active hillocks on each layer of the confocal *z*-series. b) Density of growth-active hillocks as a function of amount of (010) growth. c) Number of hillock "deaths" during growth. d) Confocal image of this crystal at (010) surface (crystal size is 5.54 mm × 9.23 mm).

After loading the sequence of hillocks for all layers of this *z*-series into the density-density correlation analysis code, the fractal dimensions, D_i, for the hillock patterns on each optical section (i) were determined (e.g. Figure 4.16a). Unfortunately, this crystal was not a good candidate for fractal analysis due to its large fluctuation in the number of active hillocks per layer through growth. The 'mass extinctions' that occurred drastically reduced the number of hillocks in the middle-to-late stages of growth (as can be seen by the sudden drop in Figure 4.27a). The resulting plot of the fractal dimensions for all the layers in this crystal was therefore not much different than that generated by the Monte Carlo

simulation that mimicked the growth of this crystal with random events (Figure 4.28a, black circles represent hillock data while red squares represent simulated data). The fractal dimension rose to an average value of $D = 1.5 \pm 0.1$ for the later stages of hillock development, and a value of $D = 1.4 \pm 0.1$ for the final stages of simulated event development. This crystal also had a significant portion of its hillocks emerge in the $+c$ side of its (010) face during later growth, causing an unusually high number of hillocks to be excluded from the fractal analysis by the outlier-filtering method. Thus, I also ran the analysis without the filtering as a comparison, the results of which are shown in Figure 4.28b. Though these non-filtered results showed some difference in behavior between the hillocks and the Monte Carlo data, the divergences are still slight. In this case, the later stages of hillock data gave an average fractal dimension of 1.6 ± 0.1, while those of the Monte Carlo gave $D = 1.5 \pm 0.1$. Figure 4.28c and d show examples of the patterns on one layer of this crystal's growth (c) and the corresponding simulated events (d).

While the fractal analysis showed little difference between this crystal and the Monte Carlo data, nearest neighbor distributions again showed a tendency for hillocks to cluster, but no clustering was seen in the simulated data. The hillock distributions had a peak at small separations between 0 - 50 μm (Figure 4.29a). Whereas the Monte Carlo distributions were more Gaussian-shaped peaking around 230 - 350 μm (Figure 4.29b). Moreover, the simulated data showed virtually no 2D clusters (< 33 μm separation) while the hillock data for this crystal had several. Thus, while the statistics on this crystal and its unusual birth/death spurts render it essentially equivalent to a random pattern as determined by density correlation analysis, the nearest neighbor distributions again confirm an element of non-randomness in the hillocks' tendency to cluster.

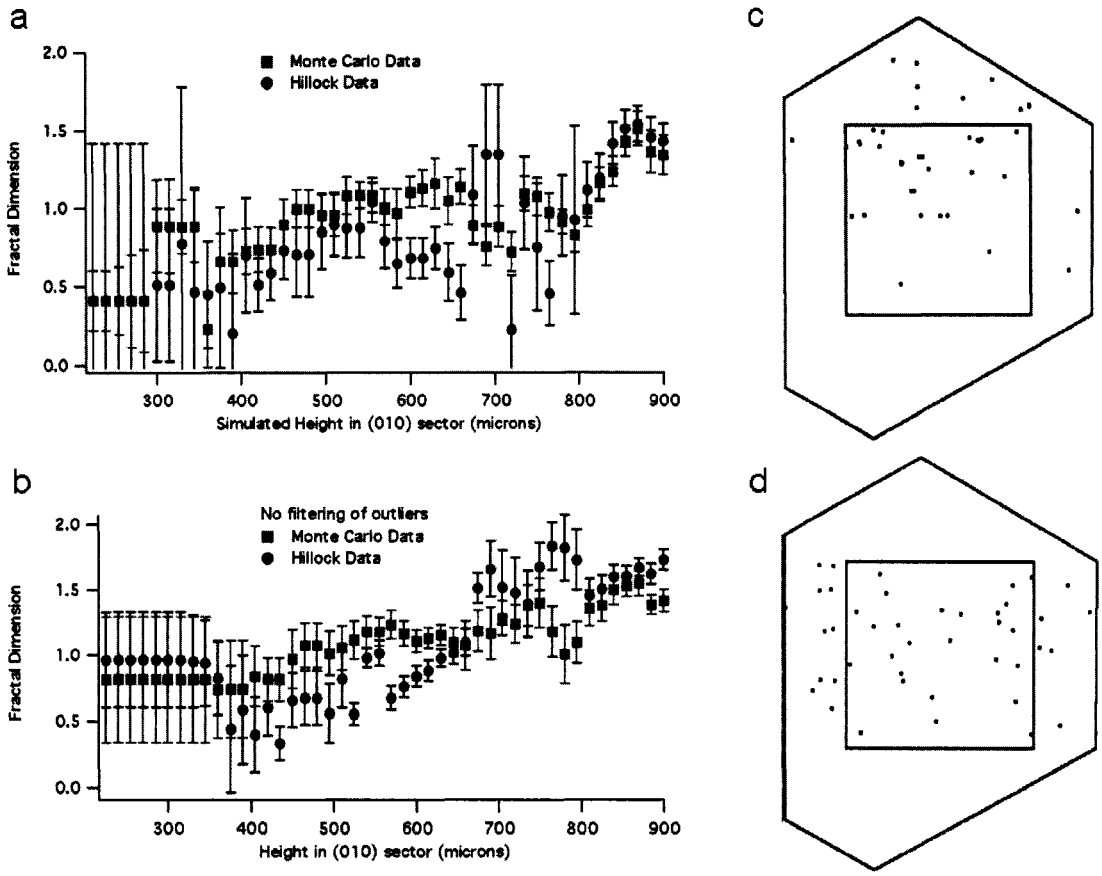

Figure 4.28. *Fractal dimensions for all optical sections of crystal #4.* The fractal dimension and its uncertainty, determined from fitting the slope of the pair correlation plots, is shown as a function of vertical growth of the (010) sector for both the hillock data (black circles) and the Monte Carlo data (red boxes) for when events lying outside the scanning area are filtered (a) and not filtered (b) in the counting analysis. In both cases there is not a significant difference between the two sets of data. (c) and (d) are examples of the hillock locations on a single layer of the actual crystal and from the Monte Carlo simulation, respectively, where the blue box represents the scanning area for that layer.

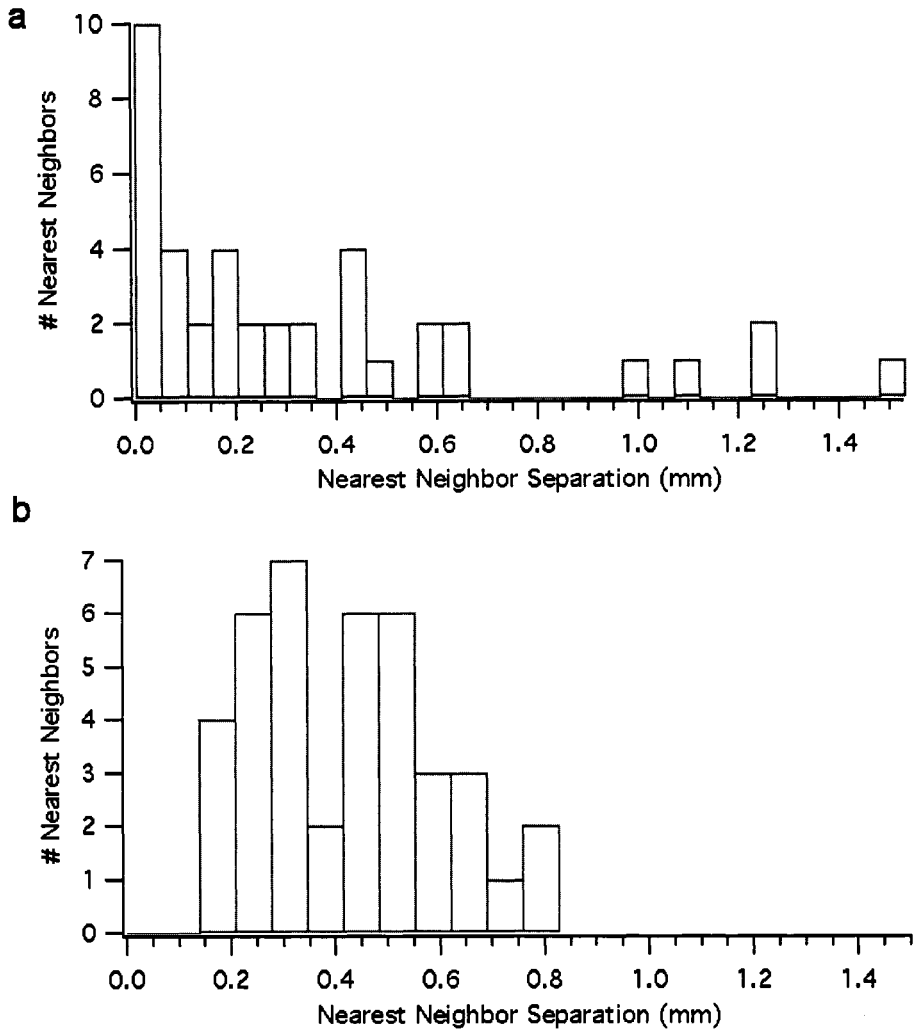

Figure 4.29. *Nearest neighbor distribution for hillock (a) and Monte Carlo (b) data of crystal #4.* a) Hillocks show clustering with a peak in the nearest neighbor distribution at smaller separations of 0 - 0.05 mm. b) Simulated data however does not reach its peak until a nearest neighbor separation of 0.23-.35 mm. These distributions are for a confocal section of this crystal with 40 active hillocks, imaged at 870 μm of (010) growth.

The [001] and [100] projections again showed fluctuation in the number of active hillocks found in these channels on the various crystal layers. On average, the number of pairs aligned along either channel in this crystal were essentially

the same. Of these, however, 78% of the [001] channels and only 50% of the [100] channels were attributable to hillock clusters of less than 4 pixel (33 μm) separation in the 2D pattern, the rest indicate longer range directional correlations between hillock locations. However, even on the layer with the greatest number of such channels, the hillocks found in [001] channels still only accounted for 11% of the total active hillocks, while those in [100] channels accounted for only 13%.[32] By comparison, there were no such correlations in the Monte Carlo data along either channel.

Figure 4.30 shows the resulting distributions from the angular correlation analysis on the hillock data (a), the Monte Carlo data (b), for both the filtered and unfiltered data sets.[34] With both data sets, the number of events that occurred in this crystal were small by comparison to crystal samples #1 and #2, thus the angular correlation histograms are not as well formed due to limited counts, and it was necessary to use a threshold[33] for discriminating peaks from noise.

The unfiltered Monte Carlo data (thick blue line in Figure 4.30b) shows a Gaussian distribution centered at 8.8° ± 2.2°. In part, this is an artifact of the boundary conditions for the generated data being wider along [100] than [001]. This Gaussian shape is missing from the filtered data (thin purple line), which shows a more flat distribution. The purely random data of 80 points (not shown) again resulted in a flat distribution, as expected for an isotropic object. The correlations for the hillock data on the other hand, show multiple peaks or spikes emerging above a threshold[33] value of 88 counts for the unfiltered data (thick black line in Figure 4.30a), and above 49 counts for the filtered data (thin gray line). These angular correlations occur at -72° ± 2°, **-52° ± 2°**, **-45° ± 2°**, **-29° ± 2°**, -16° ± 4°, **0° ± 2°**, **33° ± 2°**, **47° ± 4°**, 61° ± 2°, 72° ± 2°, and **88° ± 2°** from the *a*-axis. The directions in bold type have potential crystallographic and structural

correspondences as described below, while the others are not as apparent. The small 0° peak arises from the [100] channel correlations, of which there are not many in this crystal, thus the peak is small and does not even pass the threshold in the unfiltered data. The -45° and +47° peaks are possibly related to misoriented hillock fast steps (which can be anywhere between 34°-54°). The largest angular correlation appears at 52° in both the filtered and unfiltered data sets. This corresponds to the <102> direction (on the [100] side only), again indicating fast-step misorientation. A small peak also shows up at 33°, corresponding to the <101> directions ([$\bar{1}$00] side only). If the fast steps are misoriented in this crystal, then the 33° peak must correlate to the slow steps, otherwise it could be either the fast or slow steps. The -29° peak is close to what would be expected for new hillocks emerging along the boundary between the fast and slow slopes of a previous hillock (measured angle is ±25°, also seen as the angle at the apex of the dyed hillock chevrons with respect to [100]). In this case it would be on the [100] side of the hillock. One would expect there to be a mirror symmetric correlation on all of these directions just mentioned, however such a peaks do not appear in this data set (except for the ±45-47°, as well as the ±72° peaks that do not have crystallographic correspondences that I am aware of). The 88° peak, is obviously aligned with the [001] directional correlations, of which there are few in this crystal, hence the peak is small.

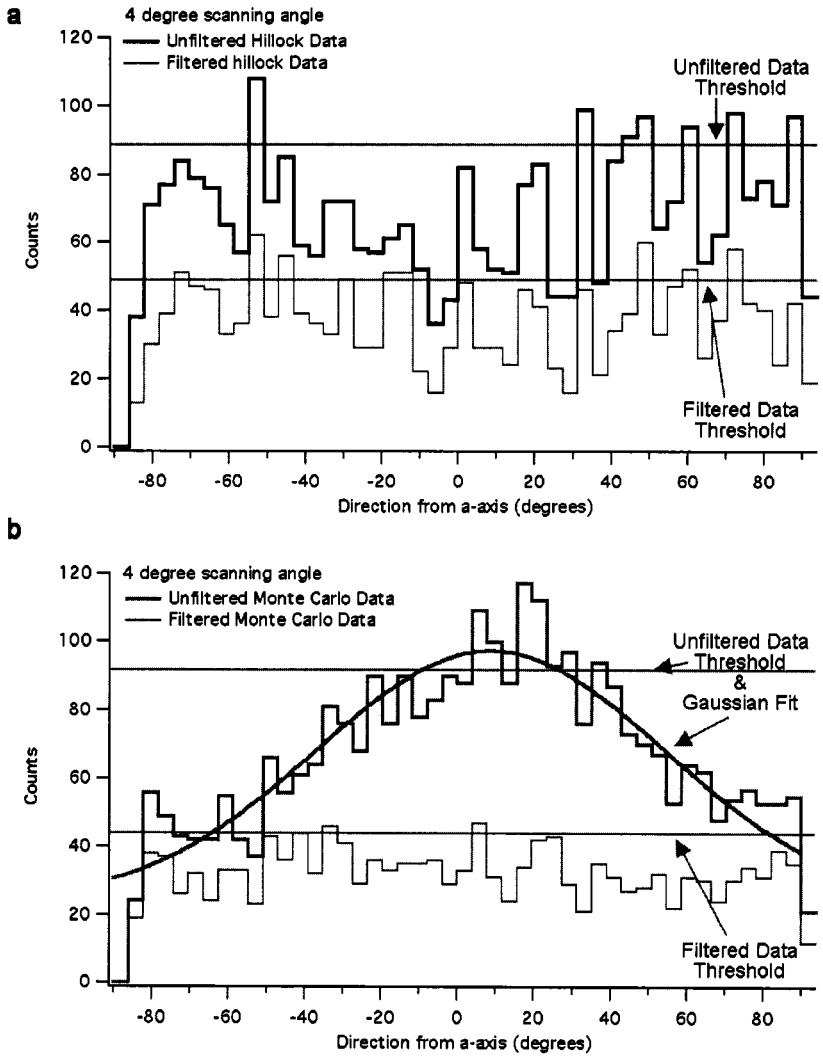

Figure 4.30. *Angular correlations comparison for crystal #4 (a) and simulated data (b).* a) The unfiltered hillock directional correlations (thick black line) show spikes above a threshold[33] value of 88 counts at -52° ± 2°, 33° ± 2°, 47° ± 4°, 61° ± 2°, 72° ± 2°, and 88° ± 2° from the *a*-axis. The filtered hillock data (thin gray line) shows similar peaks rising above its threshold of 49 counts, with additional small peaks at -72° ± 2°, -45° ± 2°, -29° ± 2°, -16° ± 4°, and 0° ± 2°. b) The unfiltered Monte Carlo data (thick blue line) shows a Gaussian distribution centered at 8.8 ± 2.2, as shown. In part, this is an artifact of the boundary conditions for the generated data being wider along [100] than [001]. This Gaussian shape is missing from the filtered data (thin purple line), which shows a more flat distribution. In both plots, red horizontal lines represent threshold values for each data set, as marked.

Crystal #5

Sample #5 (Figure 4.31d) was grown with 10^{-5} M DCF/**3** by slow evaporation in a temperature controlled water bath held at 30 °C. As seen by confocal microscopy[23], the (010) sector was 650 μm deep, throughout which 56 growth active hillocks were found, with 34 propagating to the surface. The lifetimes of the growth hillocks varied from ~12.5 μm (seen in only one section) to ~325 μm (lasting through 26 sections), with an average of ~130 μm. Figure 4.31 shows (a) the number of active hillocks and (b) the change in hillock density on the growing (010) surface, as well as (c) the total number of deaths that occurred throughout the sector's growth. The active hillock density in this crystal oscillated around 0.5 hillocks/mm^2 until it hit a period of rapid growth after 500 μm through (010), reaching a maximum at 1.4 hillocks/mm^2 before retracing slightly. The assessment of information content parameters (see Chapter 2, Section 2.7.1) for this crystal, from one optical section to the next, showed an average *Transfer* = 95 ± 11%, *Mutation* = 9 ± 9%, and *Info_Preserved* = 86 ± 16%. This indicates a reasonable degree of information content transferability and preservation through the 18,000 replicated layers between optical sections (25 μm optical section thickness). However, the integrity of this preservation again degraded through time as the crystal grew, with the later stages of growth possessing none of the original information content, due to at least one instance where an entirely new pattern emerged during the crystal's growth history.

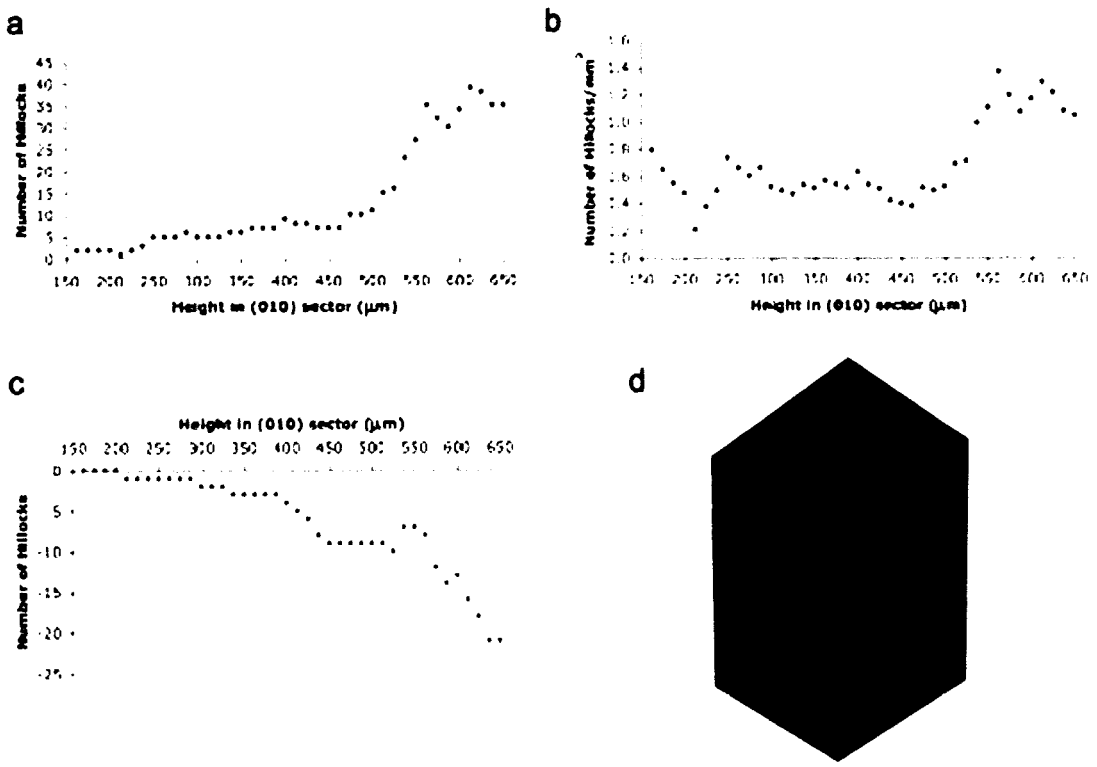

Figure 4.31. *Growth statistics for crystal #5.* a) Shows the total number of growth-active hillocks on each layer of the confocal *z*-series. b) Density of growth-active hillocks as a function of amount of (010) growth. c) Number of hillock "deaths" during growth. d) Confocal image of this crystal at 625 m worth of (010) growth (crystal size is 8.3 mm × 6.3 mm).

It is clear from Figure 4.31a that the number of active hillocks per layer of the confocal *z*-series is small for this crystal until after 500 μm of (010) growth. Thus, the fractal analysis for layers deeper than this gave poor results. However, analysis of the patterns after 500 μm of growth show divergence between the hillock and simulated patterns (Figure 4.32a, black circles represent hillock data while red squares represent simulated data). The fractal dimension reached a maximum of $D = 0.8 \pm 0.1$ and then retraced to an average value of $D = 0.6 \pm 0.2$ for the final stages of hillock development, while the Monte Carlo data leveled

out at a value of $D = 1.2 \pm 0.1$ in the final stages. This crystal also had a significant portion of its hillocks emerge near the borders of the (010) face during later growth, causing an unusually high number of hillocks to be excluded from the fractal analysis by the outlier-filtering method. Thus, similar to the analysis of sample #4, I ran the analysis without the filtering for comparison, the results of which are shown in Figure 4.32b. The non-filtered results showed less of a difference in behavior between the hillocks and the Monte Carlo data, though the difference is still statistically significant. In this case, the hillock data leveled out an average fractal dimension of 1.1 ± 0.1 in the final stages, while the Monte Carlo data converged to an average value of $D = 1.4 \pm 0.1$. Figure 4.32c and d show examples of the patterns on one layer of this crystal's growth (c) and the corresponding simulated events (d).

To complement the difference shown by fractal analysis between the crystal data and the Monte Carlo data, nearest neighbor distributions again showed a tendency for hillocks to cluster but not the simulated data. The hillock distributions had a peak at small separations between 0 - 80 μm (Figure 4.33a). Whereas the Monte Carlo distributions were more Gaussian-shaped peaking around 330 - 370 μm (Figure 4.33b). Moreover, the simulated data showed virtually no 2D clusters (< 27 μm separation) while the hillock data for this crystal had several. These data once again confirm an element of non-randomness in the hillock pattern development.

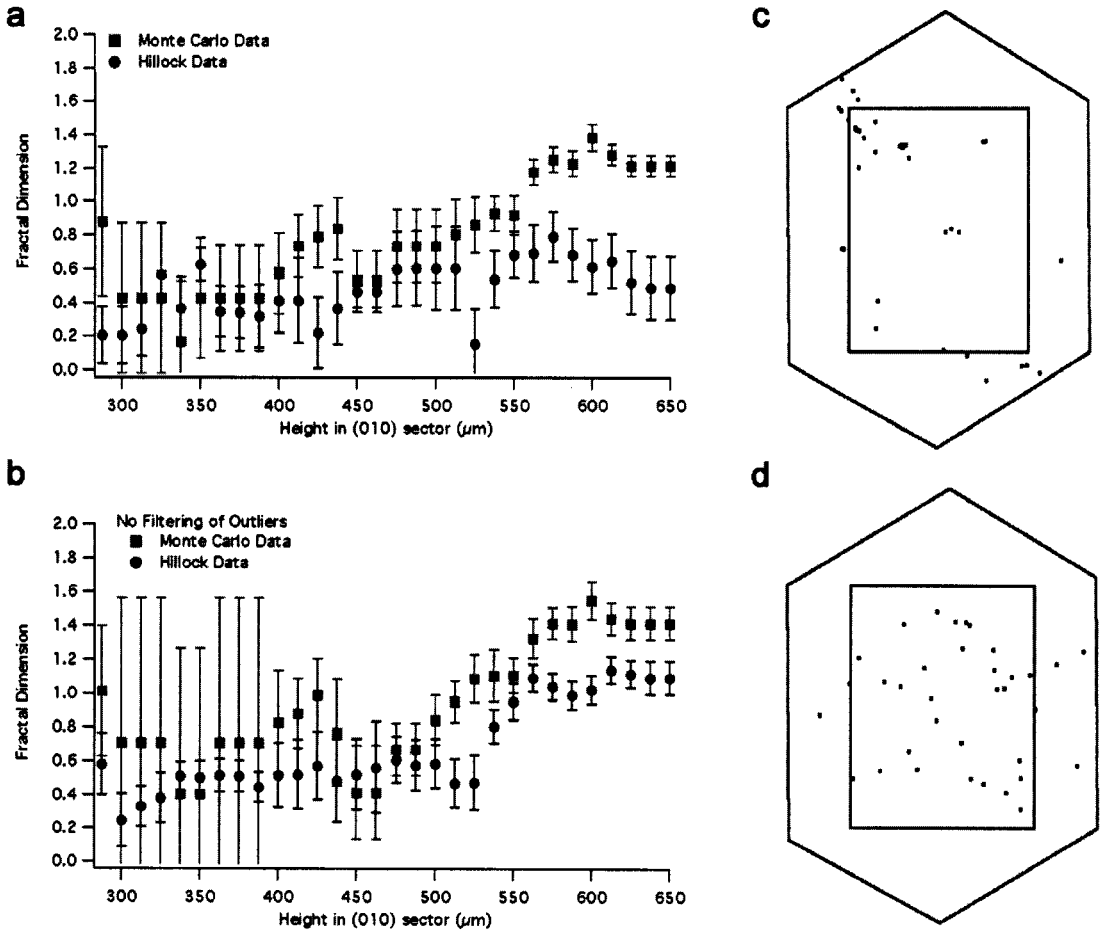

Figure 4.32. *Fractal dimensions for all optical sections of crystal #5.* The fractal dimension and its uncertainty, determined from fitting the slope of the pair correlation plots, is shown as a function of vertical growth of the (010) sector for both the hillock data (black circles) and the Monte Carlo data (red boxes) for when events lying outside the scanning area are filtered (a) and not filtered (b) in the counting analysis. Early stages of growth do not have enough events to show good statistical differences, but there is divergence between the two patterns in later stages of growth. (c) and (d) are examples of the hillock locations on a single layer of the actual crystal and from the Monte Carlo simulation, respectively, where the blue box represents the scanning area for that layer. Again, the clustering nature of hillocks is readily apparent in (c), which has equal numbers of events as (d), but a very different distribution of points across the (010) face.

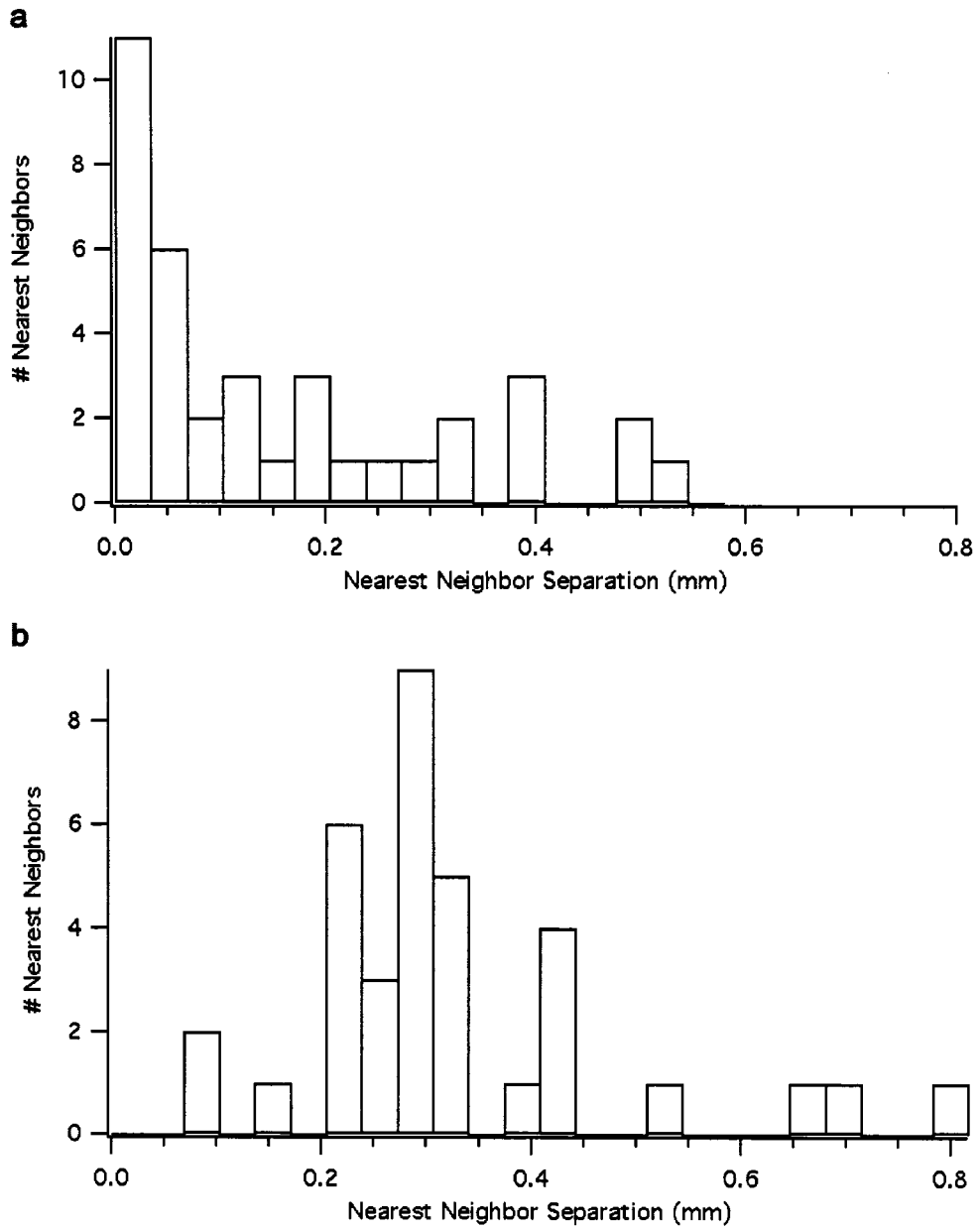

Figure 4.33. *Nearest neighbor distribution for hillock (a) and Monte Carlo (b) data of crystal #5.* a) Hillocks show clustering with a peak in the nearest neighbor distribution at smaller separations of 0 - 0.08 mm. b) Simulated data however does not reach its peak until a nearest neighbor separation of 0.33-.37 mm. These distributions are for a confocal section of this crystal with 38 active hillocks, imaged at 613 μm of (010) growth.

The [001] and [100] projections again showed fluctuation in the number of active hillocks found in these channels on the various crystal layers. On average, there were about twice as many pairs aligned along [100] channels than along [001] channels in this crystal (on some layers it was far more than this). Of these, 73% of the [001] channels and 52% of the [100] channels were attributable to hillock clusters of less than 4 pixel (27 μm) separation in the 2D pattern, the rest indicate longer range directional correlations between hillock locations. However, even on the layers with the greatest number of such channels, these hillocks only accounted for about 10-14% of the total active hillocks.[32] By comparison, there were no such correlations in the Monte Carlo data along either channel.

Figure 4.34 shows the resulting distributions from performing the angular correlation analysis on the hillock data (a) and the Monte Carlo data (b) (these are separated for clarity and ease of inspection). The Monte Carlo data shows a flat distribution, indicating a more isotropic pattern. The purely random data of 56 points (not shown) likewise resulted in a flat distribution, as expected. The correlations for the hillock data on the other hand, show multiple peaks or spikes emerging above a threshold[33] value of 43 counts (one standard deviation above the mean). These angular correlations occur at -76° ± 2°, **37° ± 2°**, **53° ± 2°**, 63° ± 4°, and **88° ± 2°** from the *a*-axis, with smaller spikes that don't pass the threshold but are easily identifiable by eye at -57° ± 2°, **0° ± 4°**, and **25° ± 2°**. The directions in bold type have potential crystallographic and structural correspondences as described below, while the others are not as apparent. The small 0° peak arises from the <100> channel correlations, of which only account for about 10% of the events in this crystal, thus the peak is small and doesn't pass the threshold. The -53° peak corresponds with the <102> directions and is possibly related to

misoriented hillock fast steps (on the [100] side only). The peak at 37° is close to the <101> directions along which the fast and slow steps align and propagate ([$\bar{1}$00] side only). The 25° peak is close to what would be expected for new hillocks emerging along the boundary between the fast and slow slopes of a previous hillock (measured angle is ±26°, also seen as the angle at the apex of the dyed hillock chevrons with respect to [100]). In this case it would be on the [100] side of the hillock. One would expect there to be a mirror symmetric correlation on all of these directions just mentioned, however such a peaks do not appear in this data set. The 88° peak, is obviously aligned with the <001> directional correlations.

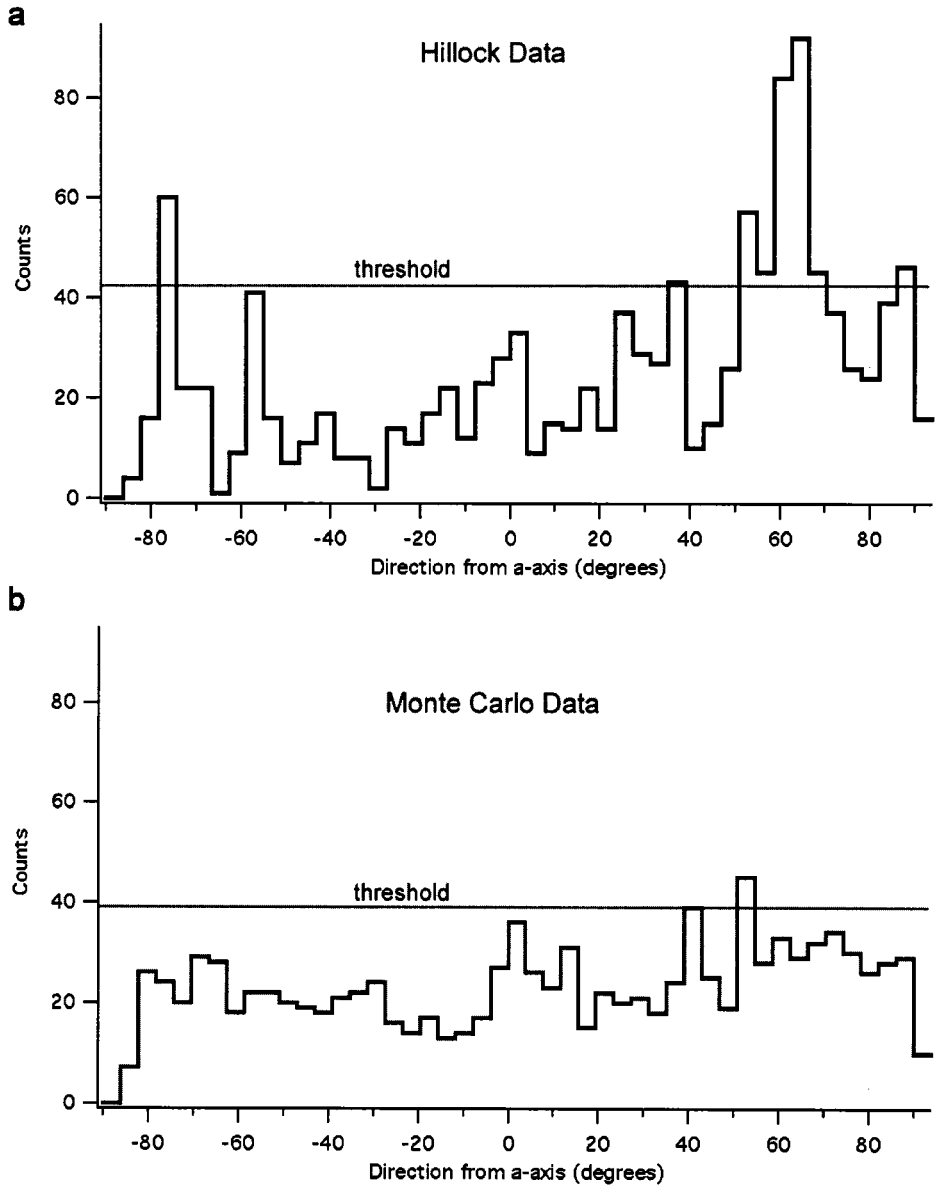

Figure 4.34. *Angular correlations comparison for crystal #5 (a) and simulated data (b).* a) The hillock directional correlations show spikes above a threshold[33] value of 43 counts at -76° ± 2°, 37° ± 2°, 53° ± 2°, 63° ± 4°, and 88° ± 2° from the *a*-axis, with smaller spikes that don't pass the threshold but are easily identifiable by eye at -57° ± 2°, 0° ± 4°, and 25° ± 2°. b) The Monte Carlo data shows a more flat distribution. In both plots, red horizontal lines represent threshold values for each data set, as marked (the hillock threshold is one standard deviation above the mean, while the Monte Carlo threshold is two standard deviations above the mean due to its relatively small variance).

4.2.3 *Discussion*

Table 4.1 summarizes the analysis results from all five crystals just discussed. For KAP crystals to resemble genes, we needed more inheritance than mutation in successive generations. This was quantified for inter-layer transfer of information through the growth of a single crystal by the 'information content parameters' *Transfer*, *Mutation*, and *Info_Preserved* (as defined in Chapter 2, equations 2.21, 2.22, and 2.23). All five sample crystals showed about 95% positive transfer between optical sections with about 7-11% mutation (loss and/or addition), resulting in an average preservation of information content between 84-89%. Given that there are tens of thousands of replicated layers of KAP growth within a single optical section, this demonstrates a high degree of genetic inheritance between layers for the growth of a single crystal, as would be expected. The weighted average hillock lifetime for all the samples discussed was 145 ± 27 μm, whereas most crystals grew to almost 1mm thickness in the (010) section. Additionally, the active hillock densities fluctuated significantly through growth.[35] Thus, while there was good short-term inheritance, the long-term inheritance experienced severe degradation over time, presumably due to fluctuating local supersaturation that resulted from growth by slow evaporation in static solutions. In most cases, the pattern of hillocks in the final stages of growth retained none of the original growth active hillocks from the nucleus.

Table 4.1. *Summary of data analysis results.* Crystal 1 was only mapped for the surface layer, while crystals 2-5 were mapped for the entire confocal *z*-series.

	Crystal 1	Crystal 2	Crystal 3	Crystal 4	Crystal 5
Dye	DCF/**3**	LGSFY/**1**	LGSFY/**1**	DCF/**3**	DCF/**3**
Sample Size (mm)	3.7 x 4.6 z = 0.015	8 x 10 z = 0.83	4 x 5.5 z = 0.32	5.54 x 9.23 z = 0.92	8.3 x 6.3 z = 0.65
#Sections	1	83	16	61	52
#Events	182	189	60	80	56
#Events on Surface	182	54	32	34	35
#Movers†	n/a	4	0	2	5-6
Avg. Lifetime	n/a	130 μm	140 μm	195 μm	130 μm
Max Lifetime	n/a	20 μm	20 μm	15 μm	12.5 μm
Max Lifetime	n/a	520 μm	320 μm	600 μm	325 μm
Avg. Density (hillocks/ mm²)	n/a	1.4 ± 0.4	2.2 ± 0.6	0.7 ± 0.2	0.5 ± 0.3
Max Density (hillocks/ mm²)	17.3	2.2	3.0	1.1	1.4
Avg. Transfer Between Layers	n/a	95 ± 6 %	94 ± 5 %	96 ± 8 %	95 ± 11 %

† This refers to the number of hillocks whose coordinates consistently changed between layers (usually by ~2 pixels in x and/or y), as determined by manual inspection.

Table 4.1. - continued

Avg. Mutation Between Layers	n/a	7 ± 6%	11 ± 5 %	7 ± 7 %	9 ± 9 %
Avg. Info Preserved Between Layers	n/a	89 ± 11 %	84 ± 7 %	89 ± 13 %	86 ± 16 %
Hillock Fractal Dim	1.47 ± 0.03 surface layer	1.36 ± 0.10 converged	1.44 ± 0.12 retracing	1.4 ± 0.1 oscillatory w/ max of 1.54 ± 0.11	0.6 ± 0.2 retraced from max of 0.8 ± 0.1
MC Fractal Dim	1.66 ± 0.06	1.60 ± 0.05 rising to 2.0	1.54 ± 0.10 rising	1.4 ± 0.1 w/ max of 1.5 ± 0.1	1.2 ± 0.1 converged w/ small rise
Nearest Neighbor Peak	11 – 22 μm	0 - 30 μm	0 – 50 μm	0 - 50 μm	0 – 80 μm
MC Nearest Neighbor Peak	22 - 32 μm 2nd peak @ 100 – 122 μm	30 - 50 μm	144 – 200 μm	230 – 350 μm	330 - 370 μm
Max % in [100] channels	9%	23%	21%	13%	14%
Max % in [001] channels	8%	16%	27%	11%	11%
Max % 2D clusters (≤4 pixels in r)	2%	9%	13%	8%	9%
MC Max % in [100] channels	0% for random distribution	9%	11%	0%	0%

Table 4.1. - continued

MC Max % in [001] channels	0% for random distribution	8%	15%	0%	0%
MC 2D clusters (≤4 pixels in r)	0% for random distribution	5%	6%	0%	0%
Angular Corr. Peaks as measured from x-axis	[-11° ± 2°] [±25° ± 4°] [-34° ± 2°] [-57° ± 4°]	[-7° ± 4°] [-24°± 2°] [±33°± 2°] needs 1° rot	[-6° ± 2°] [-16° ± 2°] [-28° ± 2°] [-46° ± 2°] [-58° ± 2°] [1.5° ± 2°] [9° ± 2°] [47° ± 2°] [81° ± 2°] [90° ± 2°] needs 2° rot	[-16° ± 2°] [-29° ± 2°] [-45° ± 2°] [-52° ± 2°] [-72° ± 2°] [0° ± 2°] [33° ± 2°] [47° ± 2°] [61° ± 2°] [72° ± 2°] [88° ± 2°]	[-57° ± 2°] [-76° ± 2°] [0° ± 4°] [25° ± 2°] [37° ± 2°] [53° ± 2°] [63° ± 4°] [88° ± 2°]
Predicted Angular Corr. Peaks as measured from [100]	0° <100> 90° <001> ~ ±25-29° f-s ±34° <101> ±53.4° <102>	0° <100> 90° <001> ~ ±27° f-s ±34° <101> ±53.4° <102>	0° <100> 90° <001> ~ ±27° f-s ±34° <101> ±53.4° <102>	0° <100> 90° <001> ~ ±25° f-s ±34° <101> ±53.4° <102>	0° <100> 90° <001> ~ ±26° f-s ±34° <101> ±53.4° <102>
MC Angular Peaks	n/a	-12.1° ± 0.9° Gaussian FWHM (39° ±2°)	~65° ~Gaussian Could not fit	8.8° ± 2.2° Gaussian (unfiltered) Flat (filtered)	flat
Random Dist Angular Peaks	Flat	Flat	Flat	Flat	Flat

As an attempt to identify other forms of information content that the hillock patterns might contain (i.e., beyond a simple bit-wise information store), various correlation analyses were employed and compared to random patterns generated via a Monte Carlo growth simulator. The density-density correlations showed fractal scaling behavior for the hillock patterns, within a limited scaling range (> 0.05 mm), typically governed by a fractal dimension of $D \sim 1.4$. This diverged from the fractal dimension for the simulated patterns (usually $D \sim 1.6$), given enough events were present for good statistical comparison. At smaller length scales the hillocks showed a tendency to cluster, whereas the Monte Carlo data showed a lack of such activity.

Nearest neighbor distributions consistently showed peaks at small hillock separations (usually < 50 μm), while the simulated data did not. One explanation for these short nearest neighbor distances is the appearance of dislocation pairs that nucleate together with opposite Burgers vectors. For example, as discussed previously, Halfpenny *et al.* observed mixed dislocation pairs with Burgers vectors <110> emerging on the (010) surface from nucleation points in the (010) sector that were invisible in their X-ray topography micrographs.[13] These V-shaped pairs are reported to have about 20° between arms, are equally inclined with respect to [010], and lie in the (001) plane. Given this configuration, such pairs should separate by 8 μm along the *a*-axis (the <100> directions) for every 20 μm of growth. Such movement in the growth active hillock locations from one optical section to another is not seen enough to indicate that such mixed dislocation pairs make a significant contribution to the observed peak at small nearest neighbor separations.[36] In fact, the large majority of growth active hillocks observed maintain their exact positions throughout their lifetime. Projections of hillock coordinates onto the *c*-axis and *a*-axis showed that around 10-25% of active hillocks fell in either [100] or [001] channels, respectively (the

Monte Carlo data by comparison showed between 0-10% in either projection). Thus, if these mixed dislocation pairs observed by Halfpenny *et al.* attribute to the growth active hillock patterns recognized by our dyes, then they account for only a small, yet meaningful, portion of the total active hillock density. However, given the apparent lack of travel in the hillock locations through multiple optical sections, it appears that the large majority of growth active hillocks are due to pure screw dislocations (which have poor contrast in X-ray topographs and were thus unobserved by Halfpenny *et al.*).

Halfpenny *et al.* also reported low dislocation densities (~5 cm^{-2}) for the KAP (010) sector.[13] This measurement included all edge and mixed dislocations emerging on the (010) face. The contribution to the dislocation density by pure screw dislocations was not reported. Our results indicate a minor contribution to the defect density by dislocations having a screw component that emerge on the (010) surface (usually a cross-sectional density between 0.5 - 4.0 growth active hillocks/mm^2).[37] Even in the most extreme cases, such as crystal #1, the dislocation density is still under 20 hillocks/mm^2. (For a discussion on defect densities the reader is referred back to Chapter 1, equations 1.2 and 1.3).

In addition to the [001] and [100] correlations between hillock locations, there were several more prominent angular correlations discovered. Many of these angular correlations corresponded with crystallographic directions (<101> and <102>), as well as defect structures such as misoriented hillock fast steps and the boundary between the fast and slow slopes of a hillock. Along with these directional correlations, there was often a curious absence of mirror symmetry. Analogous angular correlations were lacking from the Monte Carlo data. To the best of my knowledge, this is the first time that such macroscopic pattern analysis has been performed on the angular and local density correlations

between hillocks resulting from growth-induced screw dislocations. It is clear that such correlations play a significant role in the appearance of new dislocations through growth, and cause the overall pattern of hillocks on a growing crystal surface to be non-random.

4.3 Summary

Herein, the first known experimental investigations[2] of CS's 'crystals-as-genes' hypothesis have been described in the context of the arrangement, evolution, and transfer of screw dislocations through crystal growth. It was shown that when KAP crystals were cleaved, luminescence labeling of the daughter slices showed that during subsequent growth a number of hillocks from the mother crystal were retained. That said, the proposition of Cairns-Smith, that the information encoded as the spatial disposition of screw dislocations can be transferred from one crystal to another, has been demonstrated. While in principle CS's hypothesis is sound, and patterns of dislocations are preserved through successive generations of crystals (as they should be, according to the theory of dislocations), the growth of real crystals is complicated by several factors that introduce mutations. For example, daughter growth from cleaved surfaces is doomed to fail (whether growing from sequential or complementary surfaces), because cleavage by its very nature serves to generate new hillocks. It was also seen via x-ray topography that large amounts of strain and fluid inclusions often occur at the seed/daughter interface, with direct correlations to the formation of new dislocations. Disorder at the seed/daughter interface, bulk inclusions, and bending of dislocations from other growth sectors are all probable sources for the dislocations that emerge on the (010) surface. Particulate inclusions up to 1 μm, however did not generate dislocations. Mixed dislocation pairs and pure screw dislocations also appear,

however their sources are often invisible to X-ray topographic detection, and in the case of growth by spontaneous nucleation at low supersaturations, stacking disorders are less likely.

The presence of mixed dislocations on the (010) surface is yet another inherent problem whereby the preservation of information content through crystal growth is doomed to fail. Mixed dislocations automatically give rise to mutation due to the movement of their apex across the growing surface, i.e. the information stored in the pattern of dislocations is not static. Perhaps in the end, KAP, by the nature of its defects, turned out to not be such a good model system for testing GT. KAP has a constantly changing surface template, due to the *xy* spread of its (010) face through growth, and a minor though still significant population of mixed dislocations. A better model system would require a crystal that cleaves "perfectly", that only grows in one dimension through the screw dislocation mechanism, and that gives rise to only pure screw-type dislocations. Unfortunately, no such crystals exists.

Growth hillock activity and pattern development was significantly influenced by fluctuating supersaturations resulting from growth by slow evaporation in static solutions. Attempts to control growth via a closed-loop temperature controlled flow system were unsuccessful due to various mechanical set-backs and a design flaw in the temperature controlling mechanism. Another substantial factor influencing the overall pattern development of hillocks, as shown by local-density and angular correlation analyses, is the appearance of new hillocks that are correlated with the locations and structural features of previous hillocks. In other words, hillocks show a strong tendency to cluster, as well as to appear in channels corresponding with crystallographic directions (<100>, <001>, <101>, <102>) and surface defect structures, such as the fast step directions and the

junction between the fast and slow steps of a hillock. These directional correlations combined with the appearance of dislocation pairs results in a divergence from a purely random distribution of hillocks. These non-random elements contained within the hillock distributions validate that a higher level of complexity exists within the information content of crystal defect patterns.

For many of the directional correlations, there was an unexpected absence of mirror symmetry. One possible explanation for this could be related to the chiral nature of the hillock spirals themselves. If, for example, new hillocks are more likely to be generated on the $-c$ moving sweep of a spiral turn rather than the $+c$ moving sweep of a turn, then right handed screws would tend to have correlations on their $[\bar{1}00]$ side, while left-handed screws would have them on their [100] side. If there were an abundance of one handedness over another on the growing surface, then this would lead to an asymmetry in the correlations as well. Another possible explanation may be the presence of impurity molecules in the crystal and the influence they can have on the thermodynamic and kinetic growth properties. Even small amounts of the 'right' impurities can play a significant role in the early stages of crystal nucleation, influencing the appearance and morphology of defects and, thereby, the overall crystal properties throughout the remainder of its growth. This has been seen, for example, in the growth and dissolution rate differences between enantiomorphous *D*- and *L*-crystals in the presence of unintentional *D*- and *L*-amino acid impurity occlusions.[38] For crystals that are sensitive to the influences of specific chiral impurities, it would be impossible for their crystallization to not be influenced by the chiral molecules that abound in this world filled with biological life.[39] Whether or not such influences apply to KAP and could account for the observed symmetry breaking of directional correlations between hillocks remains to be determined.

NOTES AND REFERENCES TO CHAPTER 4

1. a) A. G. Cairns-Smith, *Genetic Takeover and the Mineral Origins of Life*, (Cambridge University Press: Cambridge, 1982). These ideas were first articulated in the following: b) A. G. Cairns-Smith, *J. Theor. Biol*, **10** (1966), 53; c) A. G. Cairns-Smith, in *Towards a Theoretical Biology, I. Prolegomena*, ed. C. H. Waddington, (Edinburgh University Press: Edinburgh, 1968); d) A. G. Cairns-Smith, *The Life Puzzle: On Crystals and Organisms and the Possibility of a Crystal as an Ancester*, (Oliver and Boyd: Edinburgh, 1971); e) A. G. Cairns-Smith, *Proc. Roy. Soc. B*, **189** (1975), 249; f) A. G. Cairns-Smith, *Origins of Life*, 1975, **6**, 2657; g) A. G. Cairns-Smith, *Frontiers of Life, vol. 1*, p. 169, eds. D. Batlimore, R. Dulbecco, F. Jacob, and R. Levi-Montalcini, (Academic Press: Sand Deigo, 2001); h) A. G. Cairns-Smith, *Seven Clues to the Origin of Life*, (Cambridge University Press: Cambridge, 1985).

2. In 1981 Armin Weiss published a document claiming to have found evidence for replication and evolution in layered silicates (A. Weiss, *Angew. Chem. Int. Ed. Engl.*, **20** (1981), 850.). However, when asked to provide further evidence to the scientific community so that the experiments could be replicated, he did not respond. This led to a public statement published by key origin of life researchers announcing Weiss' claims as inadequate and, until further evidence could be provided, that his claims should be "accepted with caution." (G. Arrhenius, A. G. Cairns-Smith, H. Hartman, S. L. Miller, L. E. Orgel, *Angew. Chem. Int. Ed. Engl.*, **25**(7) (1986), 658.) No further evidence was ever provided.

3. J. Borc and K. Sangwal, *Surf. Sci.*, **555** (2004), 1.

4. KAP daughter crystals doped with violamine R were grown and imaged by Serine Avagyan, an undergraduate student who worked with the Kahr research group at the University of Washington in 2003.

5. T. Bullard, J. Freudenthal, S. Avagyan, and B. Kahr, *Faraday Discussions*, **136** (2007), 231.

6. L. N. Rashkovich, E. V. Petrova, O. A. Shustin, and T. G. Chernevich, *Phys. Solid State*, **45** (2003), 400.

7. John Freudenthal is a graduate student of the Kahr research group at the University of Washington who worked with Theresa Bullard on the Cairns-Smith 'crystals-as-genes' project in 2006-2007. He performed in-depth studies of cleaved KAP surfaces with both differential interference

contrast (DIC) microscopy and atomic force microscopy (AFM). John also attempted to reproduce Serine Avagyan's[4] results of information transfer through crystal cleavage and subsequent growth.

8. Cleaved KAP crystals were examined with a Veeco Dimension 3100 SPM with Nanoscope IV a controller from the University of Washington Nanotechnology User Facility (NTUF), a member of National Nanotechnology Infrastructure Network supported by NSF. The AFM data was collected under ambient atmosphere in tapping mode.

9. The first several redesigns and testing of the flow cell system took place over the course of a year before a final design was implemented. Complications involved the need for flow control that was smooth at bulk flow rates, impurity control by having no metalic parts touching solution, using a flow cell that would allow for multiple seeds to be grown from simultaneously, maintaining solution level in the source and catch reservoires, acheiving a leakproof system, and controlling temperature to within 0.2 °C for accurate supersaturation control.

10. Ch. H. Lin, N. Gabas, J. P. Canselier, and N. Hiquily, *J. Cryst. Growth*, **166** (1996), 104.

11. Quantum Dot Corporation water soluble fluoresecent Qtracker non-targeted quantum dots were used. CdSe core with ZnS shell, polyethylene glycol derivatized and polyacrylic acid coated. Excitation light used was 543 nm, emission at 655 nm.

12. Invitrogen Microprobes water soluble FluoSpheres were used. Carboxylate modified polystyrene beads with rhodamine dyes chemically attached. Excitation light used was 543 nm, emission at 605 nm.

13. a) G. R. Ester, R. Price, and P. J. Halfpenny, *J. Phys. D: Appl. Phys*, **32** (1999), A128; b) G. R. Ester and P. J. Halfpenny, *Phil. Mag. A*, **79** (1999), 593.

14. X-ray topographs were taken by Dr. Alexey Voloshin who works in the Lab of X-ray Topography at the Shubnikov Institute of Crystallography, Russian Academy of Sciences (Leninsky prosp., 59 119333 Moscow, Russia. Tel./fax:+7-(495)-330-7883. Email: voloshin@ns.crys.ras.ru). This collaborative work was performed in 2006.

15. (a) D. Hull and D. J. Bacon, *Introduction to Dislications*, (Elisevier Butterworth-Heinemann: Oxford, 2001); (b) X. Ma, M. Dudley, W. Vetter, and T. Sudarshan, *Jpn. J. Appl. Phys.*, **42** (2003), 1077; (c) M. Dudley, *Mat. Res. Soc. Symp. Proc.*, **307** (1993), 213-224. (d) H. Klapper, *Mat. Sci. Forum*, **276** (1998), 291.

16. A.R. Lang, *Acta Cryst.*, **12** (1959), 249.

17. X-ray topographs obtained via the Lang Method take a couple hours to acquire and only one reflection direction at a time is imaged, whereas Synchrotron White Beam X-ray Topography (SWBXT) has a much shorter acquisition time of about 5 seconds and can be done for multiple reflections simultaneously.

18. W. M. Vetter, H. Totsuka, M. Dudley, and B. Kahr, *J. Cryst. Growth*, **241** (2002), 498.

19. E. K. Sanchez, J. Q. Liu, M. De Graef, M. Skowronski, W. M. Vetter, and M. Dudley, *J. Appl. Phys.*, **91** (2002), 1143.

20. W. Huang, S. Wang, and M. Dudley, *Mater. Res. Soc. Symp. Proc.*, **342** (1995), 67.

21. Halfpenny *et al.*[13] did not report what percentage of hillocks appear in pairs as opposed to isolated spirals. Presumably this is because they were limited to fields of view dictated by atomic force microscopy.

22. S. W. Paddock, *Mol. Biotech.*, **16** (2000), 127.

23. Confocal image made with a Zeiss LSM 510 NLO microscope at the University of Washington Nanotechnology User Facility (NTUF), a member of National Nanotechnology Infrastructure Network supported by NSF. A 10x/0.5D FLUAR objective and with 488 nm excitation light from an Argon laser were used.

24. This crystal was imaged using a Leica TCS SP/NT on a DMIRBE incident-light inverted microscope through a 5x objective, pinhole width of 1 Airy unit, and with 568 nm excitation light from a 25mW krypton ion laser at the University of Washington W. M. KECK Center for Advanced Studies in Neural Signaling. http://depts.washington.edu/keck/

25. Manual assembly of confocal mosaics was performed using Adobe Photoshop™. Initially, each layer was manually stitched and blended (~2 hours per layer). Later, the process was streamlined by assembling the first layer (2 hours) while recording actions performed utilizing the Action Manager. The action set was then replayed to assemble the remaining layers (2 minutes per layer). This was further sped up by writing a simple javascript to automatically load files and play the action manager, freeing me to do other things while the computer worked.

26. Originally, confocal imaging was performed at the UW KECK Center[24] and each optical section required manual stitching of several frames to create a mosaic of the entire *b*-face. This manual assembly of confocal layers took approximately 2 hours per layer and was an extremely tedious task. Later I discovered the "Action Manager" module in Adobe Photoshop™ which allowed for the recording of actions performed that could then be repeated for all subsequent layers. I then created a javascript to automatically run subsequent layer files through the recorded action set. This reduced the time for assebling one crystal's confocal sections to a couple hours per crystal, whereas before it could be a minimum of 40 hours worth of work to get one crystal ready for mapping. Once the NTUF[23] confocal microscope became available this task was reduced even further by the option to scan the entire *b*-face layer in "tiling mode" rather than in "z-sectioning mode". This way the *b*-face was automatically stitched together and the depth of the optical section in *z* was managed manually. In the end, the time to image and assemble the confocal layers for one crystal was reduced from over 45 hours down to 3 hours or less per crystal for crystals less than 0.7 cm × 1.0 cm × 1 mm in size.

27. Manual mapping of cofocal images consisted of loading the image into a software program such as Photoshop, ImageJ, or Gimp, altering contrast as necessary to ehance features of interest, and using the pointer to identify x, y coordinates in pixel scaling. All analysis was performed in units of pixels and rescaled at the end appropriately.

28. Random events generated for the Monte Carlo simulations and for the purely random distributions were restricted to the largest rectangular area that would fit within the (010) border for the layer of interest. Programming the random number generator to treat the entire (010) area rather than just a rectangle would have taken considerably more effort. Furthermore, the events included in the final analysis of both hillock and simulated data were also restricted to a rectangular area that enclosed the

inner 40% of the (010) face, which was smaller than the area bounding the randomly generated events.

29. Keep in mind that hillocks belonging to [100] channels may also lie in [001] channels, so these percentages of how many hillocks lie along these channels, with respect to the total active hillocks on a layer, are not mutually exclusive and may have overlapping contributions to the total number of active hillocks.

30. In some instances the randomly generated distributions were not exactly flat in the angular correlation histograms, but rather had a *very slight* sinusoidal trend to them. This is an artificial divergence from an isotropic distribution that results from the scanning area being rectangular rather than circular. As you can see from these plots, however, the correction to the data as a result of this artifact is very small.

31. a) M. H. J. Hottenhuis and C. B. Lucasius, *J. Cryst. Growth*, **78** (1986), 379; b) M. H. J. Hottenhuis, J. G. E. Gardeniers, L. A. M. J. Jeten, and P. Bennema, *J Cryst. Growth*, **92** (1988), 171; c) M. H. J. Hottenhuis and A. Oudenampsen, *J. Cryst. Growth*, **92** (1988), 513; d) M. H. J. Hottenhuis and C. B. Lucasius, *J. Cryst. Growth*, **94** (1989), 708.

32. Keep in mind that hillocks belonging to [100] channels may also lie in [001] channels, so these percentages of how many hillocks lie along these channels, with respect to the total active hillocks on a layer, are not mutually exclusive and may have overlapping contributions to the total number of active hillocks.

33. The threshold was determined by taking the average value of the data shifted up by about one standard deviation. A spike was only considered to be a peak if at least one neighboring division of the histogram was also high (ie, not a random, isolated spike). The only exception to this is the reporting of the angular correlation peaks along the [100] and [001] directions, which are typically a smaller subset of the data yet clearly exist, as determined by other methods. In the cases where the standard deviation was small, the threshold was set to the average plus two standard deviations to make sure peaks were significantly out of the noise.

34. "Filtered" and "unfiltered" here means with or without removing events that lie outside the scanning border. This was only done for sample #4 because this crystal had a significant number of hillocks appear in the +*c*

area of the (010) face during later stages of growth. Thus it became important to consider the unfiltered data to get better statistics.

35. Fluctuating active hillock densities do not necessarily indicate changes to the total dislocation densities, as dislocations may still exist in an inactive state (as dictated by the rule that dislocations may not end inside the bulk of a crystal, only at the surface, growth sector boundaries, or large bulk inclusions - see Chapter 1).

36. In some cases the lack of observation of hillock core movement may be due to limited pixel resolution in the confocal images, however, even when observing coordinates over many optical sections there is still very little movement. Furthermore, those that are seen to move are not typically in pairs, but rather are isolated hillocks (these may be attributable to mixed dislocations that have bent into the (010) sector from one of the other growth sectors).

37. This assumes that most or all dislocations emerging on the (010) surface with a screw component produce growth-active hillocks at some point during the crystal growth.

38. M. Lahav, I. Weissbuch, E. Shavit, C. Reiner, G. J. Nicholson, and V. Schurig, *Origins of Life and Evolution of the Biosphere*, **36** (2000), 151.

39. G. Wald, *Ann. NY Acad. Sci.*, **69** (1957), 352.

CHAPTER 5 - CONCLUSIONS

The lag time between experiments lacking a theoretical foundation or theories without supporting experiments has been dramatically diminished in modern times given the exponential rise of the scientific enterprise. The hypotheses of Cairns-Smith (CS) are unusual because they have resisted experiment for decades. The principal researchers and commentators in the origin of life community are clearly enamored with *Genetic Takeover*[1] (GT), and seem poised to embrace it if only they could be provided with a reason for so doing.

Herein, was presented the first experimental test[2] of CS's hypothesis of defect-laden crystals as analogs of pre-biotic genes. The goal was not to solve the problem of the origin of life but was much more modest: to rescue the proposals of CS from the "limbo of uninvestigated hypotheses."[3] Along the way, we came to realize that transferring information encoded in the disposition of screw dislocations, as imagined by CS, is complicated by several factors that lead to 'mutations' in the information stored in the pattern of defects:

Mutation by addition

- The process of cleavage (crystalline mitosis) gives rise to many new growth active hillocks.
- Even crystals with 'perfect' cleavage produce imperfect, complementary halves. The growth dynamics of complementary surfaces will be intrinsically different from identical surfaces that, in any case, are idealizations.

- Macrosteps appear to be abundant sources of new hillocks.
- Stacking disorders at the seed daughter interface of unadulterated seeds also give rise to new dislocations and lattice strain.
- Other strains in the crystal can lead to the heterogeneous nucleation of new dislocations (see below).
- If supersaturation rises above the roughening point, 2D island nucleation also begins to play a factor, leading to growth that is no longer dictated solely by the screw dislocation mechanism.

Mutation by subtraction

- Fluctuations in supersaturation can influence the competition between growth active hillocks for dominance over the growth, leading to overgrowth and loss of information.
- As new hillocks emerge and begin to dominate growth, previous hillocks can become overgrown or pinned such that they are no longer growth active.

Mutation by non-static information content

- The two dimensional, *xy*-spread of a crystal surface that grows by the screw dislocation mechanism provides an ever-changing information template, allowing for defects from other growth sectors to bend into the sector of interest. This possibility is increased when the sector of interest has a slow growing face that comes to dominate the habit in later growth, as is the case with KAP.
- The presence of mixed dislocations (more commonly found in crystals than are pure edge or pure screw types) also lead to an inherently changing pattern of defects as their growth centers move across the surface, by virtue of the lateral component in their Burger's vectors.

Thus, it is clear that the cartoon given in GT (see Figures 1.1 and 1.2) is a considerable oversimplification. These observations forced us to confront the fundamental mechanisms that give rise to screw dislocations. A common presumption is that dislocations in freely grown crystals arise from internal stresses generated by heterogeneous nucleations, including:[4,5]

- *Mechanical stress* – due to bulk inclusions and capture of impurity particles.
- *Stacking error* - probability accidents from the encounter of two nuclei or advancing step fronts.
- *Constitutional stress or heterometry-induced stress*[6]– due to a change in composition resulting in differential contraction and expansion of neighboring regions.
- *Random stress* – due to isolated vibrations from the laboratory environment.

However, such models often fall far short in describing the molecular mechanisms of dislocation generation. In KAP, we observed, via X-ray topography and confocal fluorescence microscopy, new dislocations arising from the mechanical stress introduced by bulk fluid inclusions, but not from overgrown microbeads. Random stresses are certainly possible, though difficult to control. Disorder and stacking errors at the seed-daughter interface were also suggested by the high degree of distortion and new dislocations shown in X-ray topographs of KAP crystals grown from seed.

To further investigate the inter-hillock dynamics, whereby hillocks may be the intrinsic cause of new dislocation nucleation, we performed various quantitative

analyses on the screw dislocation patterns from as-grown crystals. To the best of our knowledge, this is the first time that such macroscopic pattern analysis has been performed on the angular and local density correlations between hillocks resulting from growth-induced screw dislocations. It became clear that such correlations play a significant role in the appearance of new dislocations through growth, and cause the overall pattern of hillocks on a growing crystal surface to be non-random. These non-random elements contained within the hillock distributions validate that a higher level of complexity exists within the information content of crystal defect patterns.

A strong tendency for hillock clustering was observed, with nearest neighbor distributions peaking at < 50 μm. Some, but not all, of these clusters arise from mixed dislocation pairs observed by Halfpenny *et al.*,[7] which presumably also account for some of the <100> correlations. However, there were many more hillock correlations observed along the <100>, <001>, <101>, and <102> directions than what can be accounted for by mixed dislocation pairs. In fact, many of the hillocks in these channels seem to arise from pure screw dislocations (seen by their lack of movement as viewed by confocal microscopy), indicating another correlation mechanism is at work. Stacking errors due to colliding hillock step fronts may be one cause of these angular correlations. A frequent absence of mirror symmetry was also observed in these angular correlations, indicating the involvement of perhaps some form of chiral influence. One possibility proposed was the handedness of the hillock spiral playing a significant role. A second possibility is the presence of unintentional chiral impurities influencing growth dynamics. Furthermore, the mechanism whereby we were able to map out the hillock patterns, i.e. intrasectoral zoning of organic dyes within the hillock fast slopes, could influence their development. While

dislocations certainly are not induced by the entrapment of individual dye molecules, it is conceivable that the angular correlations appearing along the fast-slow boundary lines of the hillocks arise from constitutional stress introduced by the segregation of the dyes into the fast slopes. Thus, investigations into the dye-crystal surface chemistries and interactions with hillock steps ensued.

In the case of 2′,7′-dichlorofluorescein (DCF), it was discovered that selective kink recognition plays an vital role in the process of intrasectoral zoning within KAP hillocks. A wide distribution of orientations and inclusion sites were indicated by single molecule measurements, force-field calculations, and spectroscopic measurements for ensemble average orientations of the dye at different concentrations. DCF is readily incorporated within KAP fast and intermediate steps on the (010) surface, due to its carboxlate for carboxylate (or carboxylic-acid for carboxylic-acid) substitution motif. While DCF can substitute for KAP units in a number of configurations, it is clear that a preference for the *–c* kinks within the fast steps is dominant. This was demonstrated by the modulation of dye uptake and orientations observed upon the addition of specific kink-blocking trivalent cations, Ce^{3+} and Fe^{3+}, as modeled after Hottenhuis *et al.*[8]

Nearly 60 years after Frank[9] first proposed the important role that screw dislocations play in crystal growth, we are still searching for answers to the actual mechanisms whereby growth-induced dislocations appear. In attempting to put a popular theory on the mineral origin of life to the test, we were forced to analyze the nature of hillock nucleation, evolution, and interrelation. Several new scientific contributions emerged from this work, including the local-density and angular correlations of hillock development in crystals, the involvement of

selective kink recognition in the intrasectoral zoning of dyes within KAP, and the mutable nature of crystal defect patterns (even under the absence of externally applied stress).

Like Frank's original work, put forth to the scientific community during the Faraday Discussions of 1949,[9] spurred on a new field of investigation into the role of dislocations in crystal growth, we hope that our work, presented at the Faraday Discussions of 2007,[10] will likewise encourage others.[11] The punched card model of CS is an idealization that does not well represent the hillock dynamics in KAP. There may be another substance, better suited to the idealization. The ultimate model system would require a crystal that cleaves "perfectly", grows in only one dimension through the screw dislocation mechanism, and gives rise to only pure screw-type dislocations. Unfortunately, no such crystals exist. However, the screw dislocation mechanism is only one of many proposed crystal genetic mechanisms laid out in GT. We hope that the demonstrations herein will give more confidence than caution to others so that they might expand upon this work in more biologically relevant crystal systems, while trying to tackle other proposals in GT. In doing so, we may finally break past the fatalism that pervades any discussion of bringing GT within the realm of experimental science.

NOTES AND REFERENCES TO CHAPTER 5

1. a) A. G. Cairns-Smith, *Genetic Takeover and the Mineral Origins of Life*, (Cambridge University Press: Cambridge, 1982). These ideas were first articulated in the following: b) A. G. Cairns-Smith, *J. Theor. Biol*, **10** (1966), 53; c) A. G. Cairns-Smith, in *Towards a Theoretical Biology, I. Prolegomena* ed. C. H. Waddington, (Edinburgh University Press: Edinburgh, 1968); d) A. G. Cairns-Smith, *The Life Puzzle: On Crystals and Organisms and the Possibility of a Crystal as an Ancestor*, (Oliver and Boyd: Edinburgh, 1971); e) A. G. Cairns-Smith, *Proc. Roy. Soc. B*, **189** (1975), 249; f) A. G. Cairns-Smith, *Origins of Life*, **6** (1975), 2657.

2. In 1981 Armin Weiss published a document claiming to have found evidence for replication and evolution in layered silicates (A. Weiss, *Angew. Chem. Int. Ed. Engl.*, **20** (1981), 850.). However, when asked to provide further evidence to the scientific community so that the experiments could be replicated, he did not respond. This led to a public statement published by key origin of life researchers announcing Weiss' claims as inadequate and, until further evidence could be provided, that his claims should be "accepted with caution." (G. Arrhenius, A. G. Cairns-Smith, H. Hartman, S. L. Miller, L. E. Orgel, *Angew. Chem. Int. Ed. Engl.*, **25**(7) (1986), 658.) No further evidence was ever provided.

3. L. E. Orgel, *Trends Biochem. Sci.*, **23** (1998), 491.

4. W. Tiller; in *The Art and Science of Growing Crystals*, p 302. ed. J. J. Gilman (John Wiley and Sons, Inc.: New York, 1963).

5. H. G. Van Bueren, *Imperfections in Crystals*, (North-Holland Publishing Company: Amsterdam, 1960).

6. B. Kahr, A. Shtukenberg, Y. O. Punin, *Optically Anomalous Crystals*, ed. B. Kahr, (Springer Verlag: New York, 2007).

7. G. R. Ester, R. Price, and P. J. Halfpenny, *J. Phys. D: Appl. Phys.* **32** (1999), A128.

8. a) M. H. J. Hottenhuis and C. B. Lucasius, *J. Cryst. Growth*, **78** (1986), 379; b) M. H. J. Hottenhuis, J. G. E. Gardeniers, L. A. M. J. Jeten, and P. Bennema, *J Cryst. Growth*, **92** (1988), 171; c) M. H. J. Hottenhuis and A.

Oudenampsen, *J. Cryst. Growth,* **92** (1988), 513; d) M. H. J. Hottenhuis and C. B. Lucasius, *J. Cryst. Growth,* **94** (1989), 708.

9. F. C. Frank, *Disc. Faraday Soc.,* **5** (1949), 48.

10. T. Bullard, J. Freudenthal, S. Avagyan, and B. Kahr, *Faraday Discussions,* **136** (2007), 231.

11. To see a sampling of science news articles featuring this work, please see Appendix D.

GLOSSARY[1,2,3]

Adatom - ions, atoms, or molecules from the mother liquor that adsorb onto a growing crystal surface and diffuse around until they bond with the crystal lattice or desorb back into solution.

Anisotropic - a state occurring in media wherein the physical properties are direction dependent, in accordance with the atomic structure and symmetry group.

Biaxial crystal - an anisotropic crystal for which there are two directions along which light can travel without any change in its polarization state. All orthorhombic, monoclinic, and triclinic crystals are biaxial.

Birefringence - the splitting of light into two eigenmodes with different velocities and perpendicular polarizations. Also known as double refraction.

Burgers vector - the extra vector that is needed to close a Burgers circuit loop around dislocations in a lattice compared to the equivalent loop around a dislocation-free lattice. The direction of the Burgers vector, in relation to the dislocation line, identifies what type of dislocation it encloses.

Chemical impurities - a molecular-sized point defect within a crystal lattice that disrupts the periodicity of the lattice in its local environment.

Dead zone - When the spacing of impurities that block the attachment of molecules to step edges gets close to the critical step curvature size these impurities can act to stop the growth of the step altogether, effectively decreasing the supersaturation. Depending on impurity concentration, there is a critical supersaturation below which no growth on that surface occurs, known as a "dead zone". Impurities that specifically adsorb into kink-sites do not induce a dead zone.

Diffraction limited - when the resolution of an image is determined by the aperture size.

Edge dislocations - a line defect with a Burger's vector that is perpendicular to the dislocation line.

Fluid inclusions - an entrapment of solvent from the mother liquor into the crystal bulk. This happens during more rapid growth from solutions at higher local supersaturation.

Grain boundaries - a planar defect that separates two regions of different grains or single crystals having different orientations of their lattice with respect to other parts of the crystal. This occurs when multiple crystals growth together. The region of disorder at the boundary is usually very narrow, only one or two building units on either side of the boundary.

Heterogeneous nucleation - miscellaneous, aperiodic nucleation of defects within a crystal due to internal stresses.

Hillocks - topographical features resembling a spiral stepped pyramid that result from the emergence of screw dislocations (mixed or pure type) at a growing crystal surface. Hillocks provide perpetual step edges that dictate crystal growth at low supersaturation.

Intersectoral zoning - when impurities homogeneously deposit within a single growth sector via symmetry-distinct selective interactions with the growing crystal face.

Interstitial atoms - a point defect where an atom or molecule has been introduced into a non-lattice site.

Intrasectoral zoning - when impurities inhomogeneously deposit within a growth sector via selective interactions with polygonized vicinal features on the growing crystal surface.

Lattice vacancies - a point defect where a building unit of the crystal is missing from a lattice site.

Line defect - a one dimensional defect extending through the crystal along some direction. Line defects are dislocations in the crystal lattice, which lead to a misplacement of the lattice along the direction of the dislocation.

Linear dichroism - the differential absorption of plane polarized light that depends on the polarization direction. Also called pleochroism in mineralogy.

Optic axis - direction in a crystal along which light can travel without any changes in polarization or velocity; ie, light traveling along an optic axis behaves as though it were passing through glass or an isotropic medium.

In uniaxial crystals the optic axis coincides with the symmetry axis. In a biaxial crystal there are two optic axes which define the optic plane, and the angle between these axes may vary anywhere from 0 to 90 degrees depending on the crystallographic structure.

Optic normal - direction perpendicular to the optic plane in a biaxial crystal

Optic plane - the plane defined by the two optic axes found in a biaxial crystal. Aslo called the axial plane.

Optical indicatrix - an ellipsoid surface that gives the values of the indicies of refraction for a crystal.

Organic dyes - carbon-based molecular chromophore or luminophore

Perfect dislocation - a dislocation whose Burgers vector is equal to one lattice translation.

Periodic bond chain - algorithm by Hartman and Perdok for predicting crystal morphology and other properties based on the concept that a crystal lattice is composed of continuous chains of bonds with periodicity [*uvw*].[4]

Planar defect - a two dimensional defect in the crystal lattice. It can often be seen as a series of line defects as well.

Point defect - a defect in the crystal lattice that is isolated to a single lattice site or in between lattice sites. These include vacancies, self-interstitials, and impurities.

Polytypism - when sequential layers of a crystal are oriented differently or are of different varieties, common in clays and layered minerals such as mica. A twinning occurs when the original crystal is sheared during growth and the product or "polytype twin" crystal grows in a different orientation off of the original one.

Precipitates - mini crystallites that crash out of solution and get entrapped within the growing crystal.

Screw dislocations - a line defect with a Burger's vector that is parallel to the dislocation line.

Stacking faults - a planar defect in which the regular stacking sequence of the lattice is interrupted.

Steps - a high energy feature of monatomic or polyatomic height, exposed by incomplete layers of a growing crystal surface.

Substitutional atoms - a foreign atom that is similar in size to an atomic building unit of a crystal replaces a proper constituent of the crystal lattice.

Twin boundaries - the planar defect which separates a twin crystal from it the parent crystal; the boundary at which shearing occurs in a crystal.

Voids - a volume defect of empty space within the bulk of the lattice.

Volume defect - a defect in the lattice that extends in three dimensions and usually takes up several units cells worth of space in the bulk of the crystal. Sometimes such defects are even large enough to see by eye or under an optical microscope.

NOTES AND REFERENCES TO GLOSSARY

1. E. A. Wood, *Crystals and Light: An Introduction to Optical Crystallography*, (Dover Publishing, Inc., New York, 1964).

2. A. Shtukenberg and Y. O. Punin, *Optically Anomalous Crystals*, ed. B. Kahr (Springer Verlag: New York, 2007).

3. D. Hull and D. J. Bacon, *Introduction to Dislocations*, (Elsevier Butterworth-Heinemann: Oxford, 2001).

4. P. Hartman and W. G. Perdok, *Acta Cryst.*, **8** (1955) 49-52 (part I), 521-524 (part II), 525-529 (part III).

BIBLIOGRAPHY

Accelrys, *Materials Studio Online Help*, (Accelrys Software, Inc.: San Diego, 2006).

Accelrys, *Materials Studio Getting Started, Release 4.0*, (Accelrys Software, Inc.: San Diego, 2006).

G. Arrhenius, A. G. Cairns-Smith, H. Hartman, S. L. Miller, L. E. Orgel, *Angew. Chem. Int. Ed. Engl.*, **25**(7) (1986), 658.

A. Barbon, M. Bellinazzi, J. Benedict, M. Brustolon, S. Fleming, S.-H. Jang, B. Kahr, and A. Rohl, *Angew. Chem. Int. Ed.*, **43** (2004), 5328.

L.D. Bastin and B. Kahr, *Tetrahedron*, **56**(36) (2000), 6633.

A. D. Becke, *J. Chem. Phys.*, **98** (1993), 5648.

F. Bedarida, *J. Crystal Growth*, **79** (1986), 43.

F. Bedarida, L. Zefiro, P. Boccacci, D. Aquilano, M. Rubbo, G. Vaccari, G. Mantovani, and G. Sgualdino, *J. Crystal Growth*, **89** (1988), 395.

L. M. Belayev, G. S. Belikova, A. B. Gil'varg, M. P. Golovei, I. N. Kalinkina, and G. I. Kosurov, *Opt Spectrosc.* (USSR) **29** (1970), 522.

L. M. Belayev, G. S. Belikova, A. B. Gil'varg, and I. M. Sil'vestrova, *Sov. Phys. Crystallogr.*, **4** (1970), 544.

G. S. Belikova, V. V. Korneev, I. Ya. Nikiforov, *et al.*, *Sov. Tech. Phys. Lett.*, **7** (1981), 308.

M. Bellinazzi, A. Barbon, B. Kahr, J. B. Benedict, and M. Brustolon, *Phys. Chem. Chem. Phys.*, **8**(3) 2006, 379.

J. Benedict, T. Bullard, W. Kaminsky, and B. Kahr, *Acta Cryst. C: Crystal Structure Communications*, **60** (2004), m551.

N. A. Booth, A. A. Chernov, P. G. Vekilov, *J. Mater. Res.* **17** (2002), 2059.

N. A. Booth, B. Stanojev, A. A. Chernov, P. G. Vekilov, *Rev. Sci. Instrum.* **73** (2002), 3540.

J. Borc and K. Sangwal, *Surf. Sci.*, **555** (2004), 1.

T. Bullard, M. Kurimoto, S. Avagyan, S. H. Jang, B. Kahr, *ACA Transactions*, **39** (2004).

T. Bullard, J. Freudenthal, S. Avagyan, and B. Kahr, *Disc. Faraday Soc.*, **136** (2007), 231.

T. V. Bullard, K. L. Wustholz, M. Robertson, J. Freudenthal, P. J. Reid, and B. Kahr, submitted for publication (2008).

W. K. Burton and N. Cabrera, *Disc. Faraday Soc.* **5** (1949), 33.

W. K. Burton, N. Cabrera, and F. C. Frank, *R. Soc. London Philos. Trans. A*, **243** (1951), 299.

N. Cabrera and M. M. Levine, *Philos. Mag.*, **1** (1956), 450.

N. Cabrera and D. A. Vermilyea, in: *Growth and Perfection of Crystals*, eds. R. H. Doremus, B. W. Roberts, and D. Turnbull, (Wiley Publishing: New York, 1958).

A. G. Cairns-Smith, *Genetic Takeover and the Mineral Origins of Life*, (Cambridge University Press: Cambridge, 1982).

A. G. Cairns-Smith, *J. Theor. Biol*, **10** (1966), 53.

A. G. Cairns-Smith, in *Towards a Theoretical Biology, I. Prolegomena* ed. C. H. Waddington, (Edinburgh University Press: Edinburgh, 1968).

A. G. Cairns-Smith, *The Life Puzzle: On Crystals and Organisms and the Possibility of a Crystal as an Ancestor*, (Oliver and Boyd: Edinburgh, 1971)

A. G. Cairns-Smith, *Proc. Roy. Soc. B*, **189** (1975), 249; f) A. G. Cairns-Smith, *Origins of Life*, **6** (1975), 2657.

A. G. Cairns-Smith, *Frontiers of Life, Vol. 1*, eds. D. Batlimore, R. Dulbecco, F. Jacob, and R. Levi-Montalcini, p. 169 (Academic Press: Sand Diego, 2001).

A. G. Cairns-Smith, *Seven Clues to the Origin of Life*, (Cambridge University Press: Cambridge, 1985).

D. J. Carter, A. L. Rohl, J. D. Gale, A. M. Fogg, R. W. Gurney, and B. Kahr, *J. Mol. Struct.* **647** (2003), 65.

D. J. Carter, M. I. Ogden, A. L. Rohl, *J. Phys. Chem. C*, **111** (2007), 9283.

D. Comoretto, L. Rossi, A. Borghesi, *J. Mater. Res.*, **12**(5) (1997), 1262.

Conference proceedings "50 Years of Progress in Crystal Growth," *J. Cryst. Growth*, **264** (2004), xi.

E. R. Davies, *Machine Vision, 3rd Edition,* (Elsevier-Morgan Kaufmann Publishers: San Francisco, 2005).

P. Davies, *The 5th Miracle: The Search of the Origin and Meaning of Life*, (Touchstone: New York, 1999).

D. W. Deamer and G. R. Fleischaker, *Origins of Life: The Central Concepts*, (Jones and Bartlett Publishers: London, 1994).

J. J. De Yoreo, C. A. Orme, and T. A. Land, in: *Advances in Crystal Growth Research*, eds. K. Sato, Y. Furukawa, and K. Nakajima (Elsevier Science B. V.: Amsterdam, 2001).

J. J. De Yoreo and P. G. Vekilov, in *Biomineralization*, eds. P. M. Dove, J. J. De Yoreo, and S. Weiner, (Mineral Soc. Am.: Washington, DC, 2003), p. 57.

J. J. De Yoreo and P. G. Vekilov, in *Reviews in Minerology and Geochemistry: Biomineralization, Vol. 54*, p. 87, eds. P. M. Dove, J. J. De Yoreo, S. Weiner, and J. J. Rosso, (Mineralogical Society of America, 2003).

T. D. Dincer, G. M. Parkinson, A. L. Rohl, and M. I. Ogden, in: *Crystal. Growth Org. Mater. 4th International Workshop, vol. 4*, p. 25, eds. J. Ulrich (Shaker Verlag: Aachen, Germany, 1997).

T. D. Dincer, G. M. Parkinson, A. L. Rohl, and M. I. Ogden, *J. Cryst. Growth*, **205** (1999), 368.

P. M. Dove, K. J. Davis, J. J. De Yoreo, in *Solid-Fluid Interfaces to Nanostructural engineering, Vol. 2*, eds. X. Y. Liu and J. J. De Yoreo, (Kluewer/Plenum Academic Press: New York, 2004).

M. Dudley, *Mat. Res. Soc. Symp. Proc.* **307** (1993), 213.

F. Dyson, *Origins of Life*, (Cambridge University Press: Cambridge, 1999).

M. Elwenspoek and J. P. van der Eerden, *J. Phys. A*, **20** (1987), 669.

E. J. Elzinga and R. J. Reeder, *Geochim. Cosmochim. Acta,* **66** (2002), 3943.

T. A. Eremina, N. G. Furmanova, L. F. Malakhova, T. M. Okhrimenko, and V. A. Kuznetsov, *Kristallografiya* **38** (1993), 236.

G. R. Ester, R. Price, and P. J. Halfpenny, *J. Phys. D: Appl. Phys.* **32** (1999), A128.

G. R. Ester, R. Price, and P. J. Halfpenny, *J. Cryst. Growth,* **182** (1997), 95.

G. R. Ester and P. J. Halfpenny, *Phil. Mag. A*, **79**(3) (1999), 593.

F. C. Frank, *Disc. Faraday Soc.*, **5** (1949), 48.

J. Frenkel, *J. Phys. U.S.S.R.* **9** (1945), 392.

M. J. Frisch, G. W. Trucks, H. B. Schlegel, G. E. Scuseria, M. A. Robb, J. R. Cheeseman, J. A. Montgomery, J. T. Vreven, K. N. Kudin, J. C. Burant, J. M. Millam, S. S. Iyengar, J. Tomasi, V. Barone, B. Mennucci, M. Cossi, G. Scalmani, N. Rega, G. A. Petersson, H. Nakatsuji, M. Hada, M. Ehara, K. Toyota, R. Fukuda, J. Hasegawa, M. Ishida, T. Nakajima, Y. Honda, O. Kitao, H. Nakai, M. Klene, X. Li, J. E. Knox, H. P. Hratchian, J. B. Cross, V. Bakken, C. Adamo, J. Jaramillo, R. Gomperts, R. E. Stratmann, O. Yazyev, A. J. Austin, R. Cammi, C. Pomelli, J. W. Ochterski, P. Y. Ayala, K. Morokuma, G. A. Voth, P. Salvador, J. J. Dannenberg, V. G. Zakrzewski, S. Dapprich, A. D. Daniels, M. C. Strain, O. Farkas, D. K. Malick, A. D. Rabuck, K. Raghavachari, J. B. Foresman, J. V. Ortiz, Q. Cui, A. G. Baboul, S. Clifford, J. Cioslowski, B. B. Stefanov, G. Liu, A. Liashenko, P. Piskorz, I. Komaromi, R. L. Martin, D. J. Fox, T. Keith, M. A. Al-Laham, C. Y. Peng, A. Nanayakkara, M. Challacombe, P. M. W. Gill, B. Johnson, W. Chen, M. W. Wong, C. Gonzalez, J. A. Pople, *Gaussian Development Version, revision D.02*, (Gaussian, Inc.: Wallingford, 2004).

I. Fry, *The Emergence of Life on Earth: A Historical and Scientific Overview*, (Rutgers University Press: Piscataway, 2000).

D. H. Gay and A. L. Rohl, *J. Chem. Soc. Faraday Transactions*, **91** (1995), 925.

M. A. Geday, W. Kaminsky, J. G. Lewis, and M Glazer, *J. Microscopy,* **198** (2000), 1.

J. W. Gibbs, *On the Equilibrium of Heterogeneous Substances, Collected Works*, (Green & Co: Longmans, 1928).

G. H. Gilmer, R. Ghez, and N. Cabrera, *J. Cryst. Growth,* **8** (1971), 79.

A. M. Glazer, J. G. Lewis, and W. Kaminsky, *Proc. R. Soc. Lond. A,* **452** (1996), 2751.

W. S. Graswinckel, F. J. van den Bruele, W. J. P. van Enckevort, and E. Vlieg, *Cryst. Growth and Design,* **7**(2) (2007), 243.

F. J. Green, *The Sigma-Aldrich Handbook of Stains, Dyes and Indicators,* (Aldrich Chemical Company: Milwaukee, 1990).

Groth, P., *Chemische Krsytallographie,* **4** (1917), 724.

R. W. Gurney, *Dyeing Crystals*, Ph.D. Thesis, (Purdue University: West Lafayette, IN, 2000).

R. W. Gurney, M. Kurimoto, J. A. Subramony, L. D. Bastin, and B. Kahr, in: *Anisotropic Organic Materials: Am. Chem. Soc. Symp. Ser.* eds. R. Glaser and P. Kaszynsky (American Chemical Society, Washington, DC, 2001).

R. W. Gurney, C. A. Mitchell, S. Ham, L. D. Bastin, and B. Kahr, *J. Phys. Chem. B,* **104**(5) (2000), 878.

C. Harris and M. Stephens, *Proc. 4th Alvey Vision Conf.*, pp. 147-151 (Plessey Research Roke Manor: United Kingdom, 1988).

D. C. Harris, *Quantitative Chemical Analysis, 5th ed.*, (W. H. Freeman and Company: New York, 1999).

P. Hartman and W. G. Perdok, *Acta Cryst.,* **8** (1955) 49-52 (part I), 521-524 (part II), 525-529 (part III).

R. M. Hazen, *Elements, vol. 1*, **3** (2005) 135.

S. Haussuhl, *Zeitschrift fur Kristallographie,* **196** (1991), 47.

E. Hecht, *Optics, 2nd ed.*, (Addison-Wesley Publishing Company: Massachusetts, 1987).

N. G. Hemming, R. J. Reeder, and S. R. Hart, *Geochim. Cosmochim. Acta* **62** (1998), 2915.

M. H. J. Hottenhuis and C. B. Lucasius, *J. Cryst. Growth,* **78** (1986), 379.

M. H. J. Hottenhuis, J. G. E. Gardeniers, L. A. M. J. Jeten, and P. Bennema, *J. Cryst. Growth*, **92** (1988), 171.

M. H. J. Hottenhuis and A. Oudenampsen, *J. Cryst. Growth*, **92** (1988) 513.

M. H. J. Hottenhuis and C. B. Lucasius, *J. Cryst. Growth*, **94** (1989), 708.

W. Huang, S. Wang, and M. Dudley, *Mater. Res. Soc. Symp. Proc.*, **342** (1995), 67.

Y. Iimura, I. Yoshizaki, H. Nakamura, S. Yoda, H. Komatsu, *Cryst. Growth Des.* **5** (2005), 301.

Y. Iimura, I. Yoshizaki, S. Yoda, H. Komatsu, *Cryst. Growth Des.* **5** (2005), 295.

L. A. M. J. Jetten, *Thesis*, (University of Nijmegen, 1983).

J. L. Jones, K. W. Paschen, and J. B. Nicholson, *J. Appl. Optics*, **2** (1963), 955.

B. Kahr and R. W. Gurney, *Chem. Rev.*, **101** (2001), 893.

B. Kahr and S.-H. Jang, in *Encyclopedia of Supramolecular Chemistry*, vol. *D*, p. 1 (Dekker Encyclopedias by Taylor & Francis Group LLC: New York, 2004).

S. Kauffman, *The Adjacent Possible: A Talk with Stuart Kauffman*, ed. J. Brockman (Content.com, Inc.: New York, 2003).

C. Kittel, *Introduction to Solid State Physics*, (John Wiley & Sons, Inc.: New York, 1953).

H. Klapper, *Mat. Sci. Forum*, **276** (1998), 291.

Kohman; in *The Art and Science of Growing Crystals*, p 152. ed. J. J. Gilman (John Wiley & Sons, Inc.: New York, 1963).

W. Kossel, *Nachr. Ges. Wiss. Gottingen*, (1927), 135.

M. I. Kozlovskii, *Soviet Phys. Cryst.*, **3** (1958), 206.

M. Kurimoto, L. D. Bastin, D. Fredrickson, P. N. Gustafson, S.-H. Jang, W. Kaminsky, S. Lovell, C. A. Mitchell, J. Chmielewski, and B. Kahr, *Mat. Res. Soc. Symp.*, **620** (2000), M9.8.1.

M. Kurimoto, P. Subramony, R. W. Gurney, S. Lovell, J. Chmielewski, and B. Kahr, *J. Am. Chem. Soc.* **121** (1999), 6952.

V. A. Kuznetsov, T. M. Okhrimenko, and M. Rak, *J. Cryst. Growth*, **193** (1998), 164.

M. Lahav, I. Weissbuch, E. Shavit, C. Reiner, G. J. Nicholson, and V. Schurig, *Origins of Life and Evolution of the Biosphere*, **36** (2000), 151.

A.R. Lang, *Acta Cryst.*, **12** (1959), 249.

C. T. Lee, W. T. Yang, and R. G. Parr, *Phys. Rev. B*, **37** (1988), 785.

J. C. M. Li, in *Dislocation Modeling of Physical Systems: Proceedings of the international conference*, ed. M. F. Ashby (Pergamon Press: New York, 1981).

Ch. H. Lin, N. Gabas, J. P. Canselier, and N. Hiquily, *J. Cryst. Growth*, **166** (1996), 104.

X. Ma, M. Dudley, W. Vetter, and T. Sudarshan, *Jpn. J. Appl. Phys*. **42** (2003), 1077.

K. Maiwa, K. Tsukamoto, and I. Sunagawa, *J. Crystal Growth*, **102** (1990), 43.

L. Margulis and D. Sagan, *What Is Life?* (Simon & Schuster, New York, 1995).

I. V. Markov, *Crystal Growth for Beginners*, (World Scientific: Singapore, 1995), see especially Chapter 3.

N. O. Mchedlov-Petrossyan, M. I. Rubtsov, L. L. Lukatskaya, *Dyes Pigm.*, **18** (1992), 179.

N. O. Mchedlov-Petrossyan, N. V. Salamanova, N. A. Vodolazkaya, Y. A. Gurina, and V. I. Borodenko, *J. Phys. Org. Chem.*, **19** (2006), 365.

J. Michl, and E. W. Thulstrup, *Spectroscopy with Polarized Light*, (Wiley-VHC Publishers: New York, 1995).

F. R. N. Nabarro, *Theory of Crystal Dislocations*, (Oxford University Press: Oxford, 1967).

Y. Okaya, *Acta Cryst.* **19** (1965), 879.

T. M. Okhrimenko, G. S. Belikova, L. M. Avdonina, *et al.*, *Growth of Crystals, vol. 15*, p. 102 [in Russian], (Nauka, Moscow, 1986).

K. Onuma, K. Tsukamoto, I. Sunagawa, *J. Crystal Growth*, **98** (1989), 377.

L. E. Orgel, *Trends Biochem. Sci.*, **23** (1998), 491.

S. W. Paddock, *Mol. Biotech.*, **16** (2000), 127.

G. T. R. Palmore, T. J. Luo, T. L. Martin, M. T. McBride-Wieser, N. T. Voong, T. A. Land, and J. J. De Yoreo, *Transactions ACA*, **33** (1998), 45;

J. Paquette and R. J. Reeder, *Geology*, **18** (1990), 1244.

J. Paquette and R. J. Reeder, *Geochim. Cosmochim. Acta*, **59** (1994), 735.

R. A. Pascal, Jr., *Chem. Rev.*, **106** (2006), 4809.

C. S. G. Philips and R. J. P. Williams, in: *Inorganic Chemistry: Principles and Non-Metals*, p. 159 (OUP: Oxford, 1965).

M. Pluta, in: *Advanced Light Microscopy, vol. 2*, p. 146 (Elsevier: New York, 1989).

M. V. Pikunov and A. S. Petukhova, *Kristallografiya*, **22** (1977), 886.

A. Pimpinelli and J. Villain, *Physics of Crystal Growth*, (Cambridge University Press: Cambridge, 1998).

J. Rakovan, R. J. Reeder, *Geochim. Cosmochim Acta*, **60** (1996), 4435 and references therein.

L. N. Rashkovich, E. V. Petrova, O. A. Shustin, and T. G. Chernevich, *Phys. Solid State*, **45** (2003), 400.

L. Reimer, in: *Transmission Electron Microscopy: Physics of Image Formation and Microanalysis*, p. 344, eds. P. W. Hawkes, A. L. Schawlow, A. E. Siegman, K. Shimoda, T. Tamir, and H. K. V. Lotsch (Springer-Verlag: New York, 1993).

R. A. Robinson and R. H. Stokes, *Electrolyte Solutions*, (Butterworths: London, 1959).

A. L. Rohl, D. H. Gay, C. R. A. Catlow, R. J. Davey, and W. C. Mackrodt, *J. Chem. Soc., Faraday Discuss.*, **95** (1993), 273.

A. L. Rohl, D. H. Gay, R. J. Davey, and C. R. A. Catlow, *J. Am. Chem. Soc.*, **118** (1996), 642.

E. K. Sanchez, J. Q. Liu, M. De Graef, M. Skowronski, W. M. Vetter, and M. Dudley, *J. Appl. Phys.*, **91** (2002), 1143.

K. Sangwal, K. Wojcik, and J. Borc, *Cryst. Res. Technol.*, **38**(7-8) (2003), 684.

E. Schrödinger, *What is Life?* (Cambridge University Press: Cambridge, 1944).

H. W. Schutt, *Eilhard Mitscherlich: Prince of Prussian Chemistry*, translated by W. E. Russey (American Chemical Society: Washington, DC, 1997).

A. Shtukenberg, Y. O. Punin, and B. Kahr, *Optically Anomalous Crystals*, ed. B. Kahr, (Springer Verlag: New York, 2007).

Z. Solc, J. Kvapil, J. and Vlcek, *Kristall Tech.*, **8** (1973), 59.

R. Sours, *Uric Acid Crystal Growth*, (dissertation submitted to Georgetown University, 2004) Image adapted from thesis with permission.

I. N. Stranski, *Z. phys. Chem.*, **136** (1928), 259.

W. Tiller; in *The Art and Science of Growing Crystals*, p 302. ed. J. J. Gilman (John Wiley & Sons, Inc.: New York, 1963).

W. N. Unertl, in *Scanning Probe Microscopy and Spectroscopy: Theory, Techniques, and Applications*, p. 113, ed. D. Bonnell (Wiley-VCH: New York, 2001).

H. G. van Bueren, *Imperfections in Crystals*, (North-Holland Publishing Company: Amsterdam, 1960).

J. C. van Dam and F. H. Mischgofsky, *J. Crystal Growth*, **84** (1987), 539.

W. J. P. van Enckevort, *Prog. Cryst. Growth*, **9** (1984), 1.

W. J. P. van Enckevort and L. A. M. J. Jetten, *J. Cryst. Growth*, **60** (1982), 275.

Various authors, *Disc. Faraday Soc.*, **5** (Royal Society of Chemistry: London, 1949).

Various authors, *Disc. Faraday Soc.*, **136** (Royal Society of Chemistry: London, 2007).

A. R. Verma, *Phil. Mag.*, **43** (1952), 441.

W. M. Vetter, H. Totsuka, M. Dudley, and B. Kahr, *J. Cryst. Growth.* **241** (2002), 498.

T. Vicsek, *Fractal Growth Phenomena, 2nd Ed.*, (World Scientific Publishing: New Jersey, 1992).

R. A. Visser, *Neth. Milk Diary J.* **36** (1982), 167.

E. Vlieg, M. Deij, D. Kaminski, H. Meekes, and W. van Enckevort, *Faraday Discuss.*, **136** (2007), 4.

G. Wald, *Ann. NY Acad. Sci.*, **69** (1957), 352.

A. Weiss, *Angew. Chem. Int. Ed. Engl.*, **20** (1981), 850.

S. Wilhelm, B. Gröbler, M. Gluch, and H. Heinz, *Principles of Confocal Laser Scanning Microscopy*, (Carl Zeiss, Inc.: New York).

G. Witzany, *Life: The Communicative Structure*. (Libri Books on Demand, 2000).

E. A. Wood, *Crystals and Light: An Introduction to Optical Crystallography, 2nd ed.*, (Dover Publications, Inc., New York, 1977).

K. L. Wustholz, B. Kahr, and P. J. Reid, *J. Phys. Chem. B.*, **109**(34) (2005), 16357.

K. L. Wustholz, E. D. Bott, C. M. Isborn, X. Li, B. Kahr, and P. J. Reid, *J. Phys. Chem. C*, **111** (2007), 9146.

K. Yamaguchi, Z. Tamura, and M. Maeda, *Acta Crysta. C*, **C53** (1997), 284.

N. Zaitseva, L. Carman, I. Smolsky, R. Torres, and M. J. Yan, *J. Cryst. Growth*, **204** (1999), 512.

Q. L. Zhao and Y. S. Huang, *Acta Phys. Sin.*, 38 (**1989**), 1134.

Q. L. Zhao, *J. Appl. Cryst.*, **27** (1994), 283.

APPENDIX A

CODE FOR FRACTAL ANALYSIS AND MONTE CARLO SIMULATION
Written in Igor Pro Platform[1]
By Theresa Bullard

```
//Use modern global access method.
#pragma rtGlobals=1

//These are Procedure files that give access to certain function packages by WaveMetrics
#include <All IP Procedures>
#include <Concatenate Waves>
#include <TransformAxis>
#include <SaveGraph>


//This macro is used to automatically run through all layers in a stack and call the
//Correlation_Dim macro for each new layer will need to manually change code to reflect
//naming convention of coordinate waves
//New waves are created to store results
Macro RunAllLayers(firstlayer, lastlayer, first_b_coords, b_interval, filterboundary,
unit_conversion)
	variable firstlayer, lastlayer, first_b_coords, b_interval, filterboundary, unit_conversion
	Prompt firstlayer, "Layer number for bottom of stack to start from"
	Prompt lastlayer, "Last layer near surface to analyze"
	Prompt first_b_coords, "What is first layer with b-face coordinates to use?"
	Prompt b_interval, "Interval between layers for b-face coordinates?"
	Prompt filterboundary, "Filter Outliers? (yes = 1, no = 0)"
	Prompt unit_conversion, "What is the voxel size in mm/pixel?"

	PauseUpdate
	Silent 1

	string layername_x, layername_y, b_face_name_x, b_face_name_y, neighborwaves,
		neighborlocwaves, neighborhistwaves
	variable tally, layernum, b_layernum, b_tally
```

```
//Make 2D waves that will store results with column #0 = x projection, column #1 = y
//projection, column #2 = r data
make/o/n=((abs(lastlayer-firstlayer)+1), 3) NormalizedSlope, Uncertainty, FractalDim,
        NumZeroSeparations, TotalDistances
//Make 1D waves that store results for all layers but where values are the same for x, y,
//and r projections
make/o/n= (abs(lastlayer-firstlayer)+1) NumOutliersFiltered, CountingArea,
        b_Area_used, LayerNumber

tally = 0; b_tally=0
layernum = firstlayer
b_layernum = first_b_coords
b_face_name_x = "x_layer"+num2str(b_layernum)+"_b_face"
b_face_name_y = "y_layer"+num2str(b_layernum)+"_b_face"
do
        neighborwaves = "Neighbors"+num2str(layernum)
        neighborlocwaves = "NeighborLoc"+num2str(layernum)
        neighborhistwaves = "NeighborHist"+num2str(layernum)
        layername_x = "x_layer"+num2str(layernum)
        layername_y = "y_layer"+num2str(layernum)

        //only increment b-face name if we are at the next available layer up that has
        //coordinates given otherwise keep using the last one
        if(b_tally == b_interval)
                if(firstlayer < lastlayer)
                        b_layernum += b_interval
                else
                        b_layernum -= b_interval
                endif

                b_face_name_x = "x_layer"+num2str(b_layernum)+"_b_face"
                b_face_name_y = "y_layer"+num2str(b_layernum)+"_b_face"
                b_tally = 0
        endif

        //Run the main macros that analyze the layer's pattern of hillocks
        //Local density correlation function
        Correlation_Dim(layername_x, layername_y, b_face_name_x, b_face_name_y,
                filterboundary, unit_conversion)
        //Angular correlations analysis
        Angle_Correlation_Dim(layername_x, layername_y, b_face_name_x,
                b_face_name_y, filterboundary, unit_conversion, theta_stp)
```

```
            //Store results in various waves
             NormalizedSlope[tally][]=ResultsWave[0][q]
             Uncertainty[tally][]=ResultsWave[1][q]
             FractalDim[tally][]=ResultsWave[2][q]
             TotalDistances[tally][]=ResultsWave[3][q]
             NumOutliersFiltered[tally]= ResultsWave[4][0]
             NumZeroSeparations[tally][]=ResultsWave[5][q]
             CountingArea[tally]=ResultsWave[6][0]
             b_Area_used[tally]=ResultsWave[7][0]
             LayerNumber[tally]=layernum
             Duplicate/o Neighbors, $neighborwaves
             Duplicate/o NeighborLoc, $neighborlocwaves

             Wavestats/q $neighborwaves
             Make/o/n=(ceil(v_npnts/3)) $neighborhistwaves
             Histogram/b={0,3,(ceil(V_npnts/3))} $Neighborwaves, $NeighborHistWaves

            if(firstlayer < lastlayer)
                    layernum += 1
            else
                    layernum -= 1
            endif
            tally += 1; b_tally += 1
        while(tally < (abs(firstlayer-lastlayer)+1))

End


//This macro is to calculate the local density pair correlation function for a 2D distribution of
//(x,y) coordinates. It does both 1D (X or Y) and 2D (R) correlation functions
Macro Correlation_Dim(datawave_x, datawave_y, xtl_outlineX, xtl_outlineY, filterboundary,
        unit_conversion)

        string datawave_x, datawave_y, xtl_outlineX, xtl_outlineY; variable filterboundary,
                unit_conversion
        Prompt datawave_x, "Select X-Data", popup wavelist("*", ";", "")
        Prompt datawave_y, "Select Y-Data", popup wavelist("*", ";", "")
        Prompt xtl_outlineX, "Select X-Coordinates for B-face", popup wavelist("*", ";", "")
        Prompt xtl_outlineY, "Select Y-Coordinates for B-face", popup wavelist("*", ";", "")
        Prompt filterboundary, "Filter Outliers? (yes = 1, no = 0)"
        Prompt unit_conversion, "What is the voxel size in mm/pixel?"

        PauseUpdate
        Silent 1
```

```
//Make 2D matrix for storing results in and label the rows and columns appropriately
make/o/n=(8,3) ResultsWave
SetDimLabel 1, 0, x_1D_results, ResultsWave; SetDimLabel 1, 1, y_1D_results,
        ResultsWave; SetDimLabel 1, 2, r_2D_results, ResultsWave
SetDimLabel 0, 0, Normalized_slope, ResultsWave; SetDimLabel 0, 1,
        slope_uncertainty, ResultsWave; SetDimLabel 0, 2, Fractal_Dim, ResultsWave;
SetDimLabel 0, 3, Total_distances, ResultsWave; SetDimLabel 0, 4,
        Total_outliers_filtered, ResultsWave; SetDimLabel 0, 5, zero_separations,
        ResultsWave;
SetDimLabel 0, 6, Counting_area_mm2, ResultsWave; SetDimLabel 0, 7,
        b_face_area_mm2_used, ResultsWave;


Wavestats/q $datawave_x
variable numpts = V_npnts        //total number of hillocks

string datawave_x_analyzed,  datawave_y_analyzed
datawave_x_analyzed = datawave_x + "_analyzed"
datawave_y_analyzed = datawave_y + "_analyzed"
Duplicate/o $datawave_x, $datawave_x_analyzed
Duplicate/o $datawave_y, $datawave_y_analyzed

//Get actual area of the b-face at this level or the closest data available (mm^2)
variable b_face_area
b_face_area = B_FaceArea($xtl_outlineX, $xtl_outlineY)*unit_conversion^2
ResultsWave[7][]=b_face_area

//Run boundary filters to flag hillocks that lie closer to the border of the b-face. These
//skew the data due to limited area effects.
variable counting_area
counting_area = Filter_Outliers($datawave_x, $datawave_y, $xtl_outlineX,
        $xtl_outlineY)*unit_conversion^2

//This creates a wave called "BoundaryFilter" that now needs to be accessed to look for
//hillocks with a -1 flag indicating they are outside the scanning area. If a hillock is
//outside the scanning area, then this will not be removed from the pattern used for
//counting. It is not possible to include it even when counting from other centers because
//we are looking at the total number of distances without double counting distances.
//Therefore, if I include the distances from each central hillock to the outliers, then I am
//essentially including the outliers as counting centers also. The only thing that would get
//excluded if I were to only cut out the outliers as counting centers but leave them for
//counting from other centers, is the outlier-to-outlier distances.
//Create extra data waves to maintain the original, non-filtered results for comparison
```

```
//with the Filtered results.

ResultsWave[6][]=counting_area

If(filterboundary)
	variable num_outliers
	num_outliers = sum(BoundaryFilter, -inf, inf)*-1
	print "Number of outliers removed = ", num_outliers
	ResultsWave[4][]=num_outliers

	numpts -= num_outliers		//number of hillock centers to include

	//Remove outliers from datawaves and reduce their size, originals have been
	//stored because these are duplicates
	variable j=0, k=0
	do
		if(BoundaryFilter[j] == -1)
			DeletePoints(j-k), 1, $datawave_x_analyzed,
				$datawave_y_analyzed
			k+=1
		endif
		j += 1
	while(j < numpts + num_outliers)
else
	print "No hillocks removed for analysis"
endif



//2D matricies holding all combinations of distances within the accepted region- only will
//want to use values on one side of the diagonal to avoid redundancy
Make/o/n=(numpts, numpts) X_Distances, Y_Distances, R_Distances

variable i=0
do
	//Filtered or Unfiltered Data
	X_Distances[][i] = abs($datawave_x_analyzed[i] - $datawave_x_analyzed[p])
	//1D wave of all distances in x dimension from all other points
	Y_Distances[][i] = abs($datawave_y_analyzed[i] - $datawave_y_analyzed[p])
	//1D wave of all distances in y dimension from all other points

	i += 1
while(i<numpts)
```

```
R_Distances[][]= sqrt(X_Distances[p][q]^2 + Y_Distances[p][q]^2)

//Call the NearestNeighbors function to determine the distribution of nearest neighbors
//Need to do this with the full R_Distances matrix rather than the reduced one so I can
//get true minimum nearest neighbor separations
make/o/n=(numpts) Neighbors, NeighborLoc
Neighbors = FindNearestNeighbors(R_Distances, numpts, p, NeighborLoc)


//only want to use the values on one side of the matrix diagonal so that I am not double
//counting, use -1 as a flag since there are valid zero distances
X_Distances[][] = p<=q ? -1:X_Distances[p][q]
Y_Distances[][] = p<=q ? -1:Y_Distances[p][q]
R_Distances[][] = p<=q ? -1:sqrt(X_Distances[p][q]^2 + Y_Distances[p][q]^2)

variable numdist = numpts*(numpts-1)/2        //Number of total valid distances
variable sumX, sumY, sumR   //used to keep track of how many valid distances have
                            //been scanned

//get max distance info and set initial delta based on this and the relationship
//delta_r = 0.1*r, rounded to the nearest integer if working in pixel units
variable xmax, xstep, ymax, ystep, rmax, rstep
wavestats/q X_Distances
xmax = V_max; xstep = round(xmax*0.1)
wavestats/q Y_Distances
ymax = V_max; ystep = round(ymax*0.1)
wavestats/q R_Distances
rmax = V_max; rstep = round(rmax*0.1)

//Create loop to do counting of distances that fall within desired ranges and load into
//results waves
Make/o/n = (1) X_Radii, Delta_X, Ncount_x, Ncount_x_norm, Y_Radii, Delta_Y,
        Ncount_y, Ncount_y_norm, R_Radii, Delta_R, Ncount_r, Ncount_r_norm
Make/o/n=(numpts) Counter  // size of the number of actual hillocks present
Duplicate/o X_Distances, X_Count, Y_Count, R_Count
X_Count = 0; Y_Count =0; R_Count = 0
Ncount_x = 0; Ncount_y = 0; Ncount_r=0; Ncount_x_norm = 0; Ncount_y_norm = 0;
        Ncount_r_norm=0
X_Radii = xmax; Y_Radii=ymax; R_Radii=rmax
Delta_X = xstep; Delta_Y = ystep; Delta_R = rstep

variable xrange, yrange, rrange, num_r_count, tally
xrange=xmax; yrange=ymax; rrange=rmax; num_r_count=0; tally=0
do
```

```
//*********************************************************************//
NOTE: THESE LINES ARE TO SCAN WITHIN A SHELL OF RADII "rrange" & "rrange -
rstep" RATHER THAN A SPHERE. THE RADIUS SIZES NEED TO BE ROUNDED TO
NEAREST INTEGER ESPECIALLY ONCE DELTA STARTS TO BECOME LESS THAN 1 TO
AVOID ZERO COUNTS. ALSO NEED TO INCLUDE NORMALIZATION BY
#CENTERS/SHELL VOLUMES, THEN NEED TO EXCLUDE OUTER POINTS AS CENTERS
AND LIMIT SCANNING TO XTL B-FACE AREA
//*********************************************************************//


        //These are binary matricies that change for each scan. There is a 1 where the
        //hillock falls within the scanning range or 0 otherwise
        if(xrange >= 1)
        //it is very possible that there are channels of hillocks in 1D (in this case a
        //channel parallel to c-axis) with dist = 0

                X_Count[][] = (-1< X_Distances[p][q] && ((xrange-xstep) <
                        X_Distances[p][q] && X_Distances[p][q] <= xrange)) ? 1:0
        else
                X_Count[][] = 0
        endif
        if(yrange >= 1)
        //it is very possible that there are channels of hillocks in 1D (in this case a
        //channel parallel to a-axis) with dist = 0

                Y_Count[][] = (-1 < Y_Distances[p][q] && ((yrange-ystep) <
                        Y_Distances[p][q] && Y_Distances[p][q] <= yrange)) ? 1:0
        else
                Y_Count[][] = 0
        endif
        if(rrange >= 1)
        //distances are in pixel units, so it is unlikely that any two hillocks will be less
        //than 1 pixel spacing in 2D
                R_Count[][] = (-1 < R_Distances[p][q] && ((rrange-rstep) <
                        R_Distances[p][q] && R_Distances[p][q] <= rrange)) ? 1:0
        else
                R_Count[][] = 0
        endif

        //Now count how many there are for this range and store the results into the
        //Ncount waves for each scanning distance
        tally = 0
        do
```

```
        Counter = X_Count[p][tally]
        Ncount_x[0] += sum(Counter, -inf, inf)
        Counter = Y_Count[p][tally]
        Ncount_y[0] += sum(Counter, -inf, inf)
        Counter = R_Count[p][tally]
        Ncount_r[0] += sum(Counter, -inf, inf)
        tally +=1
while (tally < numpts)

//Keep track of how many centers we've scanned from, before normalizing
sumX += Ncount_X[0]; sumY += Ncount_Y[0]; sumR += Ncount_R[0]

//Add normalizations to Ncount_norm's here before going up to the next radial
//shell size. Normalize by the number of centers / shell volume, area, or length
//depending on # dimensions.This normalizes according to how much space is
//actually physically covered by the points in the whole object versus how much
//space each shell covers

if(xstep == 0)
        Ncount_x_norm[0] = 0                //avoid division by zero
else
        Ncount_x_norm[0] = Ncount_x[0]*numpts/xstep
endif
if(ystep == 0)
        Ncount_y_norm[0] = 0                //avoid division by zero
else
        Ncount_y_norm[0] = Ncount_y[0]*numpts/ystep
endif
if(rstep == 0)
        Ncount_r_norm[0] = 0                //avoid division by zero
else
        Ncount_r_norm[0] = Ncount_r[0]*numpts/(pi*(2*rrange-rstep)*rstep)
endif

//set things up for the next iteration
InsertPoints 0, 1, X_Radii, Ncount_x, Ncount_x_norm, Delta_X, Y_Radii,
        Ncount_y, Ncount_y_norm, Delta_Y, R_Radii, Ncount_r,
        Ncount_r_norm, Delta_R
xrange -= xstep; yrange -= ystep; rrange -= rstep
xstep = 0.1*xrange; ystep =0.1*yrange; rstep =0.1*rrange
if(xstep > 1)
        xstep = round(xstep)
else
        xstep = ceil(xstep)  //i.e., set step size to equal 1 or other nearest non-zero
```

```
                                        //integer since working in pixels
endif
if(ystep > 1)
        ystep = round(ystep)
else
        ystep = ceil(ystep)
endif
if(rstep > 1)
        rstep = round(rstep)
else
        rstep = ceil(rstep)
endif

X_Radii[0] = xrange; Y_Radii[0]=yrange; R_Radii[0]=rrange
Delta_X[0] = xstep; Delta_Y[0] = ystep; Delta_R[0] = rstep

if(sumR == numdist)
                xstep = xrange; ystep = yrange; rstep = rrange
                X_Radii[0] = 0; Y_Radii[0]=0; R_Radii[0]=0
                Delta_X[0] = xstep; Delta_Y[0] = ystep; Delta_R[0] = rstep
        if(sumX < numdist)
        //want to scan the values on one side of the matrix diagonal to see if there
        //are any authentic distances of value 0 not accounted for yet
                duplicate/o X_Distances, countwaveBin
                countwaveBin[][] = X_Distances[p][q] == 0 ? 1:0
                Ncount_X[0] = sum(countwaveBin, -inf, inf)
                sumX += Ncount_X[0]
                if(xstep == 0)
                        Ncount_x_norm[0] = 0          //avoid division by zero
                else
                        Ncount_x_norm[0] *= numpts/xstep
                endif
        endif
        if(sumY < numdist)
                duplicate/o Y_Distances, countwaveBin
                countwaveBin[][] = Y_Distances[p][q] == 0 ? 1:0
                Ncount_Y[0] = sum(countwaveBin, -inf, inf)
                sumY += Ncount_Y[0]
                if(ystep == 0)
                        Ncount_y_norm[0] = 0          //avoid division by zero
                else
                        Ncount_y_norm[0] *= numpts/ystep
                endif
        endif
```

```
        endif

//make sure I get all the valid distances included in the counting without getting into a
//perpetual loop though
while((sumX < numdist) && (R_Radii[0] > 0) )

print "total number of possible distances is ", numdist
print "total counted in X-projection is ", sumX, ". Total counted in Y-projection is ",
        sumY, ". Total counted in R-space is ", sumR

ResultsWave[3][0]=sumX;  ResultsWave[3][1]=sumY; ResultsWave[3][2]=sumR;

//count the number of hillocks locations that have separations of ~0 in x, y, r
//given that my experimenter precision of identifying locations is +/- 2 pixels in x & y,
//and therefore +/- 4 px in r
FindLevel/q/p/r=[0,inf] x_Radii, 2
if(V_flag)
        ResultsWave[5][0] = Ncount_x[0]
else
        ResultsWave[5][0] = sum(Ncount_x, 0, V_levelX)
endif

FindLevel/q/p/r=[0,inf] y_Radii, 2
if(V_flag)
        ResultsWave[5][1] = Ncount_y[0]
else
        ResultsWave[5][1] = sum(Ncount_y, 0, V_levelX)
endif

FindLevel/q/p/r=[0,inf] r_Radii, 4
if(V_flag)
        ResultsWave[5][2] = Ncount_r[0]
else
        ResultsWave[5][2] = sum(Ncount_r, 0, V_levelX)
endif


//Take logorithms - need to do it this way rather than just change scales on graphs to
//allow for fitting a straight line and obtain fractal dimension
Duplicate/o Ncount_x, logNcount_x; Duplicate/o Ncount_y, logNcount_y;
Duplicate/o Ncount_r, logNcount_r
logNcount_x = log(Ncount_x[p]); logNcount_y = log(Ncount_y[p]);
```

```
logNcount_r = log(Ncount_r[p])
Duplicate/o X_Radii, logX_Radii; Duplicate/o Y_Radii, logY_Radii;
Duplicate/o R_Radii, logR_Radii
logX_Radii = log(X_Radii[p]); logY_Radii = log(y_Radii[p]);
logR_Radii = log(R_Radii[p])


DoUpdate      //so that user can see the graphs before choosing lower cutoff
variable min_x = GetLowerCutoff()

//Determine fractal dimension for the Normalized log plots. Use normalized values
//because this accounts for the changing shell size used for counting which will make a
//difference in the density of points counted.

//Determine fractal dimension for X projection of data (d = 1)
wavestats/q Ncount_x
if(V_maxloc <= V_npnts/2)
        wavestats/q/r=[V_maxloc+1] Ncount_x
endif
variable max_x = ceil(X_Radii[V_maxloc])
variable x_slope = FitFractalDim(max_x, min_x, X_Radii, Ncount_x_norm,
        "X_Radii_filtered", "Ncount_X_norm_filterd")
variable x_fractal_dim = x_slope + 1
//note: x_slope should be a negative value  0 < -x_slope < d

ResultsWave[0][0]=x_slope;  ResultsWave[1][0]=W_sigma[1];
ResultsWave[2][0]=x_fractal_dim

//Determine fractal dimension for Y projection of data (d = 1)
wavestats/q Ncount_y
if(V_maxloc <= V_npnts/2)
        wavestats/q/r=[V_maxloc+1] Ncount_y
endif
variable max_y = ceil(Y_Radii[V_maxloc])
variable y_slope = FitFractalDim(max_y, min_x, Y_Radii, Ncount_y_norm,
        "Y_Radii_filtered", "Ncount_Y_norm_filterd")
variable y_fractal_dim = y_slope + 1
//note: y_slope should be a negative value  0 < -y_slope < d

ResultsWave[0][1]=y_slope;  ResultsWave[1][1]=W_sigma[1];
ResultsWave[2][1]=y_fractal_dim

//Determine fractal dimension for 2D "R" data (d = 2)
wavestats/q Ncount_r
```

```
        if(V_maxloc <= V_npnts/2)
                wavestats/q/r=[V_maxloc+1] Ncount_r
        endif
        variable max_r = ceil(R_Radii[V_maxloc])
        variable r_slope = FitFractalDim(max_r, min_x, R_Radii, Ncount_R_norm,
                "R_Radii_filtered", "Ncount_R_norm_filterd")
        variable r_fractal_dim = r_slope + 2
        //note: r_slope should be a negative value  0 < -r_slope < d

        ResultsWave[0][2]=r_slope;  ResultsWave[1][2]=W_sigma[1];
        ResultsWave[2][2]=r_fractal_dim

        print "Fractal Dimensions for X projection = ", x_fractal_dim, ". For Y projection = ",
                y_fractal_dim, ". For 2D pattern = ", r_fractal_dim

        //Run Filter on Lmax to see if there are any outliers we missed - most of these should
        //have been removed by the boundary filter this creates a wave called "OutlierFilter" that
        //can be used to remove these points where, -1 is the flag indicating an outlier, 0 means
        //it's ok for now, just run it to see and check by hand but don't filter any further because
        //this should not be needed
        variable distance_max = LmaxFilter(R_Distances, max_r)

End


//This macro is to calculate the angular pair correlations for a 2D distribution of
//(x,y) coordinates. It does only 2D (R) correlation functions. It is very similar to the local
//density pair correlation function above, except for when we get to the scanning and counting
//method, as well as the actual correlation function. These were actually run in separate
//program files, I just put them here into one file to save on space and avoid repetition of other
//functions.
Macro Angle_Correlation_Dim(datawave_x, datawave_y, xtl_outlineX, xtl_outlineY,
        filterboundary, unit_conversion, theta_step)

        string datawave_x, datawave_y, xtl_outlineX, xtl_outlineY; variable filterboundary,
                unit_conversion, theta_step
        Prompt datawave_x, "Select X-Data", popup wavelist("*", ";", "")
        Prompt datawave_y, "Select Y-Data", popup wavelist("*", ";", "")
        Prompt xtl_outlineX, "Select X-Coordinates for B-face", popup wavelist("*", ";", "")
        Prompt xtl_outlineY, "Select Y-Coordinates for B-face", popup wavelist("*", ";", "")
        Prompt filterboundary, "Filter Outliers? (yes = 1, no = 0)"
        Prompt unit_conversion, "What is the voxel size in pixels/mm?"
        Prompt theta_step, "Angular tolerance or scan size to use"
```

```
PauseUpdate
Silent 1

//Make 1D matrix for storing results in and label the rows and columns appropriately
make/o/n=(8,1) ResultsWave
SetDimLabel 0, 0, Normalized_slope, ResultsWave; SetDimLabel 0, 1,
        slope_uncertainty, ResultsWave; SetDimLabel 0, 2, Fractal_Dim, ResultsWave;
SetDimLabel 0, 3, Total_angles, ResultsWave; SetDimLabel 0, 4, Total_outliers_filtered,
        ResultsWave; SetDimLabel 0, 5, zero_separations, ResultsWave;
SetDimLabel 0, 6, Counting_area_mm2, ResultsWave; SetDimLabel 0, 7,
        b_face_area_mm2_used, ResultsWave;


Wavestats/q $datawave_x
variable numpts = V_npnts       //total number of hillocks

string datawave_x_analyzed,  datawave_y_analyzed
datawave_x_analyzed = datawave_x + "_analyzed"
datawave_y_analyzed = datawave_y + "_analyzed"
Duplicate/o $datawave_x, $datawave_x_analyzed
Duplicate/o $datawave_y, $datawave_y_analyzed

//Get actual area of the b-face at this level or the closest data available
variable b_face_area
b_face_area = B_FaceArea($xtl_outlineX, $xtl_outlineY)*unit_conversion^2
ResultsWave[7]=b_face_area

//Run boundary filters to flag hillocks that lie closer to the border of the b-face.
//These skew the data due to limited area effects.
//Leaving this in so that I can treat only the same data as I did in distance correlations.
//Additionally, if a hillock is near border, then surrounding pair correlations are skewed
//to direction of crystal.
variable counting_area
counting_area = Filter_Outliers($datawave_x, $datawave_y, $xtl_outlineX,
        $xtl_outlineY)*unit_conversion^2

// This creates a wave called "BoundaryFilter" that now needs to be accessed to look for
//hillocks with a -1 flag indicating they are outside the scanning area. If a hillock is
//outside the scanning area, then this will not be removed from the pattern used for
//counting. It is not possible to include it even when counting from other centers because
//we are looking at the total number of distances without double counting distances.
//Therefore, if I include the distances from each central hillock to the outliers, then I am
//essentially including the outliers as counting centers also. The only thing that would get
```

```
//excluded if I were to only cut out the outliers as counting centers but leave them for
//counting from other centers, is the outlier-to-outlier distances. Create extra data waves
//to maintain the original, non-filtered results for comparison with the Filtered results.
ResultsWave[6]=counting_area

If(filterboundary)
	variable num_outliers
	num_outliers = sum(BoundaryFilter, -inf, inf)*-1
	print "Number of outliers removed = ", num_outliers
	ResultsWave[4]=num_outliers

	numpts -= num_outliers		//number of hillock centers to include

	//Remove outliers from datawaves and reduce their size, originals have been
	//stored because these are duplicates
	variable j=0, k=0
	do
		if(BoundaryFilter[j] == -1)
			DeletePoints(j-k), 1, $datawave_x_analyzed,
				$datawave_y_analyzed
			k+=1
		endif
		j += 1
	while(j < numpts + num_outliers)
else
	print "No hillocks removed for analysis"
endif



//2D matricies holding all combinations of pair distances & angles wrt x-axis (which
//should be [-100]) within the accepted region - only will want to use values on one side
//of the diagonal to avoid redundancy
Make/o/n=(numpts, numpts) X_Distances, Y_Distances, Pair_Angles, Temp_Angles

variable i=0
do
	//Filtered or Unfiltered Data
	//2D wave of all distances in x dimension from all other points
	X_Distances[][i] = ($datawave_x_analyzed[i] - $datawave_x_analyzed[p])
	//2D wave of all distances in y dimension from all other points
	Y_Distances[][i] = ($datawave_y_analyzed[i] - $datawave_y_analyzed[p])

	i += 1
```

```
while(i<numpts)

//only want to use the values on one side of the matrix diagonal so that I am not double
//counting, use -1 as a flag since there are valid zero distances
X_Distances[][] = p<=q ? -1:X_Distances[p][q]
Y_Distances[][] = p<=q ? -1:Y_Distances[p][q]

//*****Here is the main equation that is different between the two Correlation Formulas*****//

// the values are converted to degrees and are with respect to the x-axis
Pair_Angles[][] = ((p<=q) && (X_Distances[p][q]!=0)) ? -
        999:(atan(Y_Distances[p][q]/X_Distances[p][q])*180/PI)
Temp_Angles[][]=Pair_Angles[p][q]
Pair_Angles[][] = ((X_Distances[p][q]==0)) ? 90:Temp_Angles[p][q]
Temp_Angles[][]=Pair_Angles[p][q]
Pair_Angles[][] = ((Y_Distances[p][q]==0)) ? 0:Temp_Angles[p][q]

variable numpairs = numpts*(numpts-1)/2  //Number of total valid pairs
variable sumTheta      //used to keep track of how many valid angles have been scanned

//get max angle
variable theta_max
wavestats/q Pair_Angles
theta_max = V_max

//Create loop to do counting of events that fall within desired ranges and load into
//results waves
Make/o/n = (1) Thetas, Delta_theta, Ncount_theta, Ncount_theta_norm
Make/o/n=(numpts) Counter  // size of the number of actual hillocks present
Duplicate/o X_Distances, Theta_Count
Theta_Count = 0
Ncount_theta=0; Ncount_theta_norm=0
Delta_theta = theta_step

variable theta_range, num_count, tally
theta_range=90; num_count=0; tally=0
Thetas = theta_range

do

//*************************************************************************//
NOTE: THESE LINES ARE TO SCAN WITHIN A BOW-TIE SHAPE WITH ANGULAR SPREAD
OF THETA_STEP CENTERED ON THETA. AN ENTIRE 360 DEGREE PIE IS SCANNED AT
THETA_STEP INTERVALS, HOWEVER TAN(40)=TAN(220) SO SCANNING 180 DEG BEAM
```

```
AND ONLY HAVE 180 STEPS. EXCLUDE OUTER POINTS AS CENTERS AND LIMIT
SCANNING TO XTL B-FACE AREA
//*********************************************************************//

        //These are binary matricies that change for each scan. There is a 1 where the
        //hillock falls within the scanning range or 0 otherwise
        Theta_Count[][] = (-999 != Pair_Angles[p][q] && ((theta_range-theta_step/2) <
                Pair_Angles[p][q] && Pair_Angles[p][q] <= (theta_range+theta_step/2)))
                ? 1:0

        //Now count how many there are for this range and store the results into the
        //Ncount waves for each scanning distance
        tally = 0
        do
                Counter = Theta_Count[p][tally]
                Ncount_theta[0] += sum(Counter, -inf, inf)
                tally +=1
        while (tally < numpts)

        //Keep track of how many centers we've scanned from
        sumTheta += Ncount_Theta[0]

        //Not going to normalize here because gets complicated since Area =
        //r^2*theta_range/2 (theta in radians), and have to account for distances between
        //pairs which will vary depending on if the origin is near the edges of the
        //scanning border or towards the middle, and might be different for the two halves
        //of the bow-tie as well. however, theta_range is not a changing parameter here
        //like it was for the radial scanning.
        Ncount_theta_norm[0] = Ncount_theta[0]


        //set things up for the next iteration
        InsertPoints 0, 1, Thetas, Ncount_theta, Ncount_theta_norm, Delta_Theta
        theta_range -= theta_step

        Thetas[0]=theta_range
        Delta_Theta[0] = theta_step


//make sure I get all the valid distances included in the counting without getting into a
//perpetual loop though
while((Thetas[0] >= -90) )  // && (sumTheta < numpairs)
```

```
	print "Total number of possible pairs is ", numpairs
	print "Total counted in Theta-space is ", sumTheta

	ResultsWave[0]=sumTheta

End


//This function is used to eliminate points near the boundaries of the crystal from the counting
//procedure because they skew the data due to boundary effects. The filtering process is based on
//the hexagonal habit of the KAP crystal, and the user must supply the coordinates for the b-face
//of that layer the order of coordinates to enter is 0)+c apex (bottom). 1) lower right corner. 2)
//upper right corner. 3) -c (top) apex. 4) upper left corner. 5) lower left corner, i.e., starting at
//the +c-axis tip and working counter-clockwise around the crystal boundary from there. The
//default filtering is set to come in by 20% of the total width on either side in the a-directions
//(thus only the inner 60% is counted).  And the c-directions limits are set by the y-values of
//either the shortest {110} side, or alternatively the minimum y(upper) value and the maximum
//y(lower) value from the Right & Left side corners. This creates a box around the middle bulk of
//the crystal b-face. All hillocks contained within this box are valid counting centers while all
//hillocks that lie outside it are discarded as centers.  If this filtering is used for changing values
//of the b-face area, then a normalization factor is needed per face
// => (Area of b-face used)/(Area of top surface used)
Function Filter_Outliers(hillock_waveX, hillock_waveY, xtl_outlineX, xtl_outlineY)
	wave hillock_waveX, hillock_waveY, xtl_outlineX, xtl_outlineY

	variable a_FilterPercent = 20 //this is the percentage of the total a-axis width to filter out
	                              //from either side of the crystal in the x directions
//	Prompt a_FilterPercent, "Percentage of a-axis width to set filter boundary at (%)"
//	DoPrompt "Enter a % filter value for the a-axis", a_FilterPercent
//	if(V_Flag)
//		return -1 //User canceled
//	endif

	//Get Minimum x value on right side and maximum x value on left side of crystal b-face
	//border
	variable minX_right, maxX_left
	minX_right = xtl_outlineX[1] < xtl_outlineX[2] ? xtl_outlineX[1]:xtl_outlineX[2]
	maxX_left = xtl_outlineX[4] > xtl_outlineX[5] ? xtl_outlineX[4]:xtl_outlineX[5]

	//Get Minimum y value of upper R/L corners and Maxium y value of lower R/L corners
	variable minY_upper, maxY_lower
	minY_upper = xtl_outlineY[4] < xtl_outlineY[2] ? xtl_outlineY[4]:xtl_outlineY[2]
	maxY_lower = xtl_outlineY[1] > xtl_outlineY[5] ? xtl_outlineY[1]:xtl_outlineY[5]
```

```
	//Come in from right and left sides by a_FilterPercent of total x width
	variable x_width = minX_right - maxX_left
	minX_right -= (a_FilterPercent/100)*(x_width)
	maxX_left += (a_FilterPercent/100)*(x_width)

	//area of the box used that includes the portion of valid centers for determining b-face
	//hillock pattern dimensions
	variable counting_Area = (minX_right - maxX_left)*(minY_upper - maxY_lower)
	Make/o/n=5 ScanningBorderX, ScanningBorderY
	ScanningBorderX[0] = minX_right; ScanningBorderY[0] = minY_upper
	ScanningBorderX[1] = minX_right; ScanningBorderY[1] = maxY_lower
	ScanningBorderX[2] = maxX_left; ScanningBorderY[2] = maxY_lower
	ScanningBorderX[3] = maxX_left; ScanningBorderY[3] = minY_upper
	ScanningBorderX[4] = minX_right; ScanningBorderY[4] = minY_upper


	//create a wave that flags which hillocks need to be filtered from counting for fractal
	//dimension. -1 indicates it needs to be filtered, 0 stays
	duplicate/o hillock_waveX, BoundaryFilter
	BoundaryFilter = ((hillock_waveX[p] > minX_right) || (hillock_waveX[p] < maxX_left)
		|| (hillock_waveY[p] > minY_upper) || (hillock_waveY[p] < maxY_lower)) ? -1:0

	return counting_Area

End


//Calculates the b-face area of the crystal given the coordinates for the outline of the b-face at a
particular layer. Divides the hexagonal shape of KAP into four triangles. The vertices of each
triangle are assigned to coordinates like (xa, ya), (xb, yb), (xc, yc). Then the area of each
triangle becomes 1/2 * ABS[(xb*ya-xa*yb) + (xc*yb-xb*yc) + (xa*yc-xc*ya)] see website for
derivation and more info http://www.btinternet.com/~se16/hgb/triangle.htm  the order of
coordinates to enter is 0)top apex. 1) upper right corner. 2) lower right corner. 3) bottom apex.
4) lower left corner. 5) upper left corner,  i.e., starting at the +c-axis tip and working clockwise
around the crystal boundary from there.
Function B_FaceArea(bFaceX, bFaceY)
	wave bFaceX, bFaceY;

	variable tri_area1, tri_area2, tri_area3, tri_area4, bFace_area
	tri_area1 = 1/2*abs(((bFaceX[1]*bFaceY[0] - bFaceX[0]*bFaceY[1]) +
		(bFaceX[2]*bFaceY[1] - bFaceX[1]*bFaceY[2]) + (bFaceX[0]*bFaceY[2] -
		bFaceX[2]*bFaceY[0])))
```

```
        tri_area2 = 1/2*abs(((bFaceX[2]*bFaceY[0] - bFaceX[0]*bFaceY[2]) +
                (bFaceX[3]*bFaceY[2] - bFaceX[2]*bFaceY[3]) + (bFaceX[0]*bFaceY[3] -
                bFaceX[3]*bFaceY[0])))
        tri_area3 = 1/2*abs(((bFaceX[3]*bFaceY[0] - bFaceX[0]*bFaceY[3]) +
                (bFaceX[4]*bFaceY[3] - bFaceX[3]*bFaceY[4]) + (bFaceX[0]*bFaceY[4] -
                bFaceX[4]*bFaceY[0])))
        tri_area4 = 1/2*abs(((bFaceX[4]*bFaceY[0] - bFaceX[0]*bFaceY[4]) +
                (bFaceX[5]*bFaceY[4] - bFaceX[4]*bFaceY[5]) + (bFaceX[0]*bFaceY[5] -
                bFaceX[5]*bFaceY[0])))

        bFace_area = tri_area1 + tri_area2 + tri_area3 + tri_area4

        return(bFace_area)

End


//This function looks at the number of distances from each center lie outside the max limits for
//the well-behaved portion of the pair-correlation function it requires the user to enter in the
//values from visual inspection of the plots.  Above Lmax, the hillocks are on the outer edges of
//the pattern and therefore are biased towards larger pair distances. Most of these should be
//filtered out by the boundary filter function above, but the ones that are still included within the
//boundary but are on the outer rim will also have high number of distances above Lmax
Function LmaxFilter(R_dist_matrix, maximum_r)
        //this is a 2D wave generated by the main macro containing all inter-hillock distances
        wave R_dist_matrix

        variable maximum_r      //this is the r-position of the max value in Ncount_R

        variable Lmax = maximum_r
        //distances above this value indicate boundary effects from being an outlier on a limited
        //area pattern
//      Prompt Lmax, "radius of outliers limit (pixels)"
//      DoPrompt "Outlier Limit", Lmax
//      if(V_Flag)
//              return -1 //User canceled
//      endif

        //figure out how many outlier distances there are per center
        wavestats/q R_dist_matrix
        variable num_hillocks = sqrt(V_npnts)
        string nameOfBinWave = "R_CountingMatrix"

        Make_Binary(R_dist_matrix, Lmax, nameOfBinWave)
```

```
	wave binWave = $nameOfBinWave

	Make/o/n=(num_hillocks) NumOverThreshColumn, NumOverThreshRow,
		NumOverThreshSum, Tempsum, OutlierFilter

	variable i = 0
	//the following process needs to look at both columns and rows and their sum because
	//R_dist_matrix is only one side of the diagonal. This is for generating a wave that will
	//flag outliers based on secondary criteria of # distances > Lmax
	for(i = 0; i < num_hillocks; i+=1)
		Tempsum = binWave[p][i]
		//sums R_dist_Matrix columns of how many distances are over Lmax
		NumOverThreshColumn[i] = sum(Tempsum, -inf, inf)
		Tempsum = binWave[i][p]
		//sums R_dist_Matrix rows of how many distances are over Lmax
		NumOverThreshRow[i] = sum(Tempsum, -inf, inf)
		NumOverThreshSum[i] = NumOverThreshColumn[i] + NumOverThreshRow[i]

		if(((NumOverThreshColumn[i] > (.36*num_hillocks)) || (NumOverThreshRow[i]
			> (.36*num_hillocks))) && (NumOverThreshSum[i] >
			(.5*num_hillocks)))
			print "Hillock #", i, " qualifies as an outlier"
			OutlierFilter[i] = -1
		else
			OutlierFilter[i]=0
		endif
	endfor


	return (Lmax)

End


//I used a lower_cut =10 for all analyses, based on early analysis
Function GetLowerCutoff()
	variable lower_cut
	Prompt lower_cut, "lower cut-off radius of clustering limit (pixels)"
	DoPrompt "Clustering Limit", lower_cut
	if(V_Flag)
		return -1 //User canceled
	endif
	return (lower_cut)
End
```

```
//Fit pair-correlation function for fractal dimension within appropriate range beween Lmin &
//Lmax. This can be used either on the normalized values or the non-normalized values, prior to
//taking logarithm. Below Lmin hillocks are clustered or in channels and non-random./ Above
//Lmax hillocks are outliers and skew the data, therefore they are not a good sampling due to
//limited pattern area
Function FitFractalDim(upper_cut, lower_cut, radii, Ncount_norm, nameOutputRadii,
        nameOutputNcount)
        variable upper_cut, lower_cut; wave radii, Ncount_norm; string nameOutputRadii,
                nameOutputNcount

        Duplicate/o Ncount_norm, $nameOutputNcount
        wave logN_fit = $nameOutputNcount
        Duplicate/o radii, $nameOutputRadii
        wave logRadii = $nameOutputRadii

        FindLevel/p/q logRadii, lower_cut
        variable lower_range =floor(V_LevelX)
        // get rid of points below the lower cutoff
        DeletePoints 0, (lower_range), logRadii, logN_fit

        FindLevel/p/q logRadii, upper_cut
        variable upper_range = ceil(V_LevelX)
        wavestats/q logRadii
        //get rid of points above the upper cutoff
        DeletePoints (upper_range), (V_npnts-upper_range), logRadii, logN_fit

        //take logarithms so we can now fit the desired range
        logRadii = log(logRadii)
        logN_fit = log(logN_fit)

        string fitname = nameOutputNcount + "_fit"
        Duplicate/D/O logN_fit,$fitname
        CurveFit/q line, logN_fit/x=logRadii /d=$fitname
        wave fit_param = $"W_coef"
        wave fit_sigma = $"W_sigma"
        print "The slope of the fit for ", nameOutputNcount, " is ", fit_param[1], " +/- ",
                fit_sigma[1]

        return (fit_param[1])
End
```

```
// simple function for giving a prompt to the user for input variables mid macro or function
// Here is how it would be called in the macro or other function:
//      variable numdist = numpts*(numpts-1)/2  //Number of total valid distances
//      if(num_r > numdist)
//              print "the number of valid distances is ", numdist
//              num_r = NewNumR_Dialog(numdist)
//              if(num_r == -1)
//                      Abort "Need Valid Number of Distances to Scan With"
//              endif
//      endif
Function NewNumR_Dialog(numdist)
        variable numdist

        variable new_num_r
        Prompt new_num_r, "# of radii exceeds the total valid distances. Please enter a new one"
        DoPrompt "Enter a new number of radii to use", new_num_r
        if(V_Flag)
                return -1       //User canceled
        endif
        return new_num_r
End


//this function generates a binary 2D wave of the 2D image based on a basic threshold value.
//Result is stored in "imagewaveBin"
Function Make_Binary(imagewave, thresh, nameOfBinOutputWave)
        wave imagewave; variable thresh; string nameOfBinOutputWave
        variable numdims

        if(WaveExists(imagewave))
                numdims=WaveDims(imagewave)     //how many dimensions is this wave?
                if(numdims == 2)
                //the following  compare statement will only work for 2D waves, due to indexing
                //needs (can expand later if needed)
                        duplicate/o imagewave, $nameOfBinOutputWave
                        wave binWave = $nameOfBinOutputWave
                        binWave[][] = imagewave[p][q] >=  thresh ? 1:0
                else
```

```
                print "Must use 2D wave"
                return 0
        endif

    else
        print "Invalid Wave"
        return 0
    endif

End


Macro CreatGrid(spacing, size, num)
    variable spacing=0, size, num
    Prompt spacing, "Grid Spacing (enter 0 if auto calculate)"
    Prompt size, "Total number of grid points per side"
    Prompt num, "Number of grid points (enter 0 if auto - only if spacing given)"

    PauseUpdate
    Silent 1

    if(spacing == 0)
        if(num != 0)
            spacing = size/(trunc(sqrt(num)))
            num = (ceil(sqrt(num)))^2
            print spacing
        else
            print "must enter non-zero value for either spacing or number of grid
                points (or both)"

        endif
    else
        num = trunc((size/spacing + 1)^2)
    endif

    Make/o/n=((num), 2) Grid_coords
    Make/o/n = (num) gridx, gridy
    Grid_coords = 0
    variable i = 0, j = 0, k = 0
    do
        do
            print k, j
            Grid_coords[i][0] = k
```

```
                Grid_coords[i][1] = j
                j += spacing
                i += 1
            while (j <= size)
            j=0
            k += spacing

        while (i < num)

        gridx = Grid_coords[p][0]
        gridy = Grid_coords[p][1]

End


//Generate a random pattern for a single layer or area
//num = number of points to generate; min and max X, Y parameters define the rectangular area
//to enclose the pattern
Function GenerateRandom(num, min_x_R, max_x_L, min_y_Up, max_y_Low)
        variable num, min_x_R, max_x_L, min_y_Up, max_y_Low

        if(num >0)
            Make/o/n = (num) Rand_X, Rand_Y

            Rand_X = (enoise(abs(min_x_R-max_x_L)/2) + abs(min_x_R+max_x_L)/2)
            Rand_Y = (enoise(abs(min_y_Up-max_y_Low)/2) +
                abs(min_y_Up+max_y_Low)/2)
        endif
End


//Kill random selection of events based on the number of hillocks that died in corresponding
crystal layer
Function KillEvents(num_to_kill, wave_x_rand, wave_y_rand)
        variable num_to_kill; wave wave_x_rand, wave_y_rand

        if(num_to_kill>0)
            variable i=1
            do
                wavestats/q wave_x_rand
                DeletePoints (round(enoise(V_npnts/2) + V_npnts/2)), 1, wave_x_rand,
                    wave_y_rand
                i+=1
            while(i<=num_to_kill)
```

```
        endif
End

//Monte Carlo a Random distribution that mimics the progression of crystal growth from a
//particular crystal set. i.e., use the same areas and number of hillocks per layer as a crystal that
//I want to compare values to. This macro requires that the waves used for corresponding hillock
//layers have the -1's in them where there are dead hillocks
//When I did the angular correlation analysis, I ran the Monte Carlo as it is given here, and then
//ran the waves generated here through the RunAllLayers macro to do the Angular Correlation
//function.
Macro MonteCarloGrowth(firstlayer, lastlayer, first_b_coords, b_interval, filterboundary,
        unit_conversion, scale_binwidth)

        variable firstlayer, lastlayer, first_b_coords, b_interval, filterboundary, unit_conversion,
                scale_binwidth
        Prompt firstlayer, "Layer number for bottom of stack to start from"
        Prompt lastlayer, "Last layer near surface to analyze"
        Prompt first_b_coords, "What is first layer with b-face coordinates to use?"
        Prompt b_interval, "Interval between layers for b-face coordinates?"
        Prompt filterboundary, "Filter Outliers? (yes = 1, no = 0)"
        Prompt unit_conversion, "What is the voxel size in mm/pixel?"
        Prompt scale_binwidth, "What bin width to do based on scaling? (pixels ~ 3, mm ~
                0.045)"

        PauseUpdate
        Silent 1

        string layer_basename, layername_x_rand, layername_y_rand, b_face_name_x,
                b_face_name_y, neighborwaves, neighborlocwaves, neighborhistwaves
        string prev_layer, prev_x_rand, prev_y_rand
        variable tally, layernum, b_layernum, b_tally, total_events
        variable minX_right, maxX_left, minY_upper, maxY_lower
        variable prev_dead, prev_wavesize, total_dead, num_to_kill, num_to_create

        //Make 2D waves that will store results with column #0 = x projection, column #1 = y
        //projection, column #2 = r data
        make/o/n=((abs(lastlayer-firstlayer)+1), 3) RandNormalizedSlope, RandUncertainty,
                RandFractalDim, RandNumZeroSeparations, RandTotalDistances
        //Make 1D waves that store results for all layers but where values are the same for x, y,
        //and r projections
        make/o/n= (abs(lastlayer-firstlayer)+1) RandNumOutliersFiltered, RandCountingArea,
                Rand_b_Area_used, RandLayerNumber

        tally = 0; b_tally=0
```

```
layernum = firstlayer
b_layernum = first_b_coords
b_face_name_x = "x_layer"+num2str(b_layernum)+"_b_face"
b_face_name_y = "y_layer"+num2str(b_layernum)+"_b_face"
prev_layer = "none"

do
	//only increment b-face name if we are at the next available layer up that has
	//coordinates given otherwise keep using the last one
	if(b_tally == b_interval)
		if(firstlayer < lastlayer)
			b_layernum += b_interval
		else
			b_layernum -= b_interval
		endif

		b_face_name_x = "x_layer"+num2str(b_layernum)+"_b_face"
		b_face_name_y = "y_layer"+num2str(b_layernum)+"_b_face"
		b_tally = 0
	endif

	//Get Minimum x value on right side and maximum x value on left side of crystal
	//b-face border
	minX_right =$b_face_name_x[1] < $b_face_name_x[2] ?
		$b_face_name_x[1]:$b_face_name_x[2]
	maxX_left = $b_face_name_x[4] > $b_face_name_x[5] ?
		$b_face_name_x[4]:$b_face_name_x[5]

	//Get Minimum y value of upper R/L corners and Maxium y value of lower R/L
	//corners
	minY_upper = $b_face_name_y[4] < $b_face_name_y[2] ?
		$b_face_name_y[4]:$b_face_name_y[2]
	maxY_lower = $b_face_name_y[1] > $b_face_name_y[5] ?
		$b_face_name_y[1]:$b_face_name_y[5]


	//wavenames for this layer
	neighborwaves = "RandNeighbors"+num2str(layernum)
	neighborlocwaves = "RandNeighborLoc"+num2str(layernum)
	neighborhistwaves = "RandNeighborHist"+num2str(layernum)
	layer_basename = "x_layer"+num2str(layernum)
	layername_x_rand = "x_rand_layer" +num2str(layernum)
	layername_y_rand = "y_rand_layer" +num2str(layernum)
	wavestats/q $layer_basename
```

```
total_events = V_npnts

//Simulate random events based on what happened in corresponding layer of
//hillocks
if(stringmatch(prev_layer, "none"))
        make/o/n=(total_events) $layername_x_rand, $layername_y_rand
        GenerateRandom(total_events, minX_right, maxX_left, minY_upper,
                maxY_lower)
        $layername_x_rand = Rand_X
        $layername_y_rand = Rand_Y

else    //i.e., not the first layer in the sequence
        //Kill points of corresponding # of dead hillocks for this layer compared to
        //previous layer
        duplicate/o $prev_x_rand, $layername_x_rand
        duplicate/o $prev_y_rand, $layername_y_rand
        wavestats/q $prev_layer
        prev_wavesize = V_npnts
        FindLevels/q $prev_layer, -1
        prev_dead = V_LevelsFound
        FindLevels/q $layer_basename, -1
        total_dead = V_LevelsFound
        num_to_kill = total_dead - prev_dead
        KillEvents(num_to_kill, $layername_x_rand, $layername_y_rand)

        //Generate points of corresponding # of new hillocks for this layer
        //compared to previous layer
        num_to_create = total_events - prev_wavesize
        wavestats/q $prev_x_rand
        if(num_to_create > 0)
                InsertPoints (V_npnts-num_to_kill+1), num_to_create,
                        $layername_x_rand, $layername_y_rand
                GenerateRandom(num_to_create, minX_right, maxX_left,
                        minY_upper, maxY_lower)
                $layername_x_rand[V_npnts-num_to_kill, (V_npnts - num_to_kill
                        + num_to_create)] = Rand_x[p-(V_npnts-num_to_kill)]
                 $layername_y_rand[V_npnts-num_to_kill, (V_npnts -
                        num_to_kill + num_to_create)] = Rand_y[p-(V_npnts-
                        num_to_kill)]
        endif
endif

//Run the main macros that analyze the layer's pattern of hillocks
```

```
        Correlation_Dim(layername_x_rand, layername_y_rand, b_face_name_x,
                b_face_name_y, filterboundary, unit_conversion)
        Angle_Correlation_Dim(layername_x_rand, layername_y_rand, b_face_name_x,
                b_face_name_y, filterboundary, unit_conversion,  theta_stp)


        //Store results in various waves
         RandNormalizedSlope[tally][]=ResultsWave[0][q]
         RandUncertainty[tally][]=ResultsWave[1][q]
         RandFractalDim[tally][]=ResultsWave[2][q]
         RandTotalDistances[tally][]=ResultsWave[3][q]
         RandNumOutliersFiltered[tally]= ResultsWave[4][0]
         RandNumZeroSeparations[tally][]=ResultsWave[5][q]
         RandCountingArea[tally]=ResultsWave[6][0]
         Rand_b_Area_used[tally]=ResultsWave[7][0]
         RandLayerNumber[tally]=layernum
         Duplicate/o Neighbors, $neighborwaves
         Duplicate/o NeighborLoc, $neighborlocwaves

         Wavestats/q $neighborwaves
         Make/o/n=(ceil(v_npnts/3)) $neighborhistwaves
         Histogram/b={0,(scale_binwidth),(ceil(V_npnts/3))} $Neighborwaves,
                $NeighborHistWaves

        if(firstlayer < lastlayer)
                layernum += 1
        else
                layernum -= 1
        endif
        //flag name for next round
        prev_layer = layer_basename
        prev_x_rand = layername_x_rand
        prev_y_rand = layername_y_rand

        tally += 1; b_tally += 1
    while(tally < (abs(firstlayer-lastlayer)+1))

End


//This is created specifically to find the minimum nearest neighbor distances in the R_Distances
//matrix,  which gives the relative distances between all hillocks
```

```
Function FindNearestNeighbors(Rdist_matrix, num_hillocks, which_hillock, loc_outputwave)
	wave Rdist_matrix, loc_outputwave; variable num_hillocks, which_hillock

	make/o/n=(num_hillocks) temp_distances
	temp_distances = Rdist_matrix[p][which_hillock]

	temp_distances = temp_Distances[p]<=0 ? 100000:temp_Distances[p]

	wavestats/q temp_distances

	loc_outputwave[which_hillock] = V_minLoc

	return (V_min)
End


Macro KillGraphs()
	String GraphList,GraphName
	Variable i1,i2,len

	Silent 1
	GraphList=WinList("*", ";", "WIN:1")
	i1=0
	i2=0
	len=strlen(GraphList)
	do
		if (i2>=len)
			break
		endif
		if (cmpstr(GraphList[i2], ";")==0)
			GraphName=GraphList[i1,i2-1]
			DoWindow/K	$GraphName
			i1=i2+1
			i2=i1
		endif
		i2+=1
	while (1)
End
```

```
//should probably only run this macro after you feel good about the data analysis and are just
//trying to create plots for publication. This actually changes the values of the waves that are
//used in the analysis, so unless you want to change the scaling of all coordinate waves don't run
//this until end.
Macro RescalePlot(scalefactor, plotname)
	variable scalefactor; string plotname
	Prompt plotname, "Select Graph for Rescaling", popup winlist("Graph*", ";", "")
	Prompt scalefactor, "What is the conversion factor in mm/pixel?"

	PauseUpdate
	Silent 1

	variable wavesinplot, i=0
	string tempstringname
	GetWindow $plotname wavelist		//this stores names of all wavenames in the plot into
						//a 3 column textwave called W_WaveList, where
						//column 0 is wavenames
	wavesinplot = numpnts(W_WaveList)/3

	do
		tempstringname = W_WaveList[i][0]
		$tempstringname *= scalefactor
		i+=1
	while(i < wavesinplot)

End


//Use this macro if the coordinate frame of the crystal is slightly rotated from the x-y coordinate
//frame. This is needed because my scanning border and zero-separations counting are all
//dependent on the a and c axes being aligned with x and y.
Macro RotateCoords(x_wave, y_wave, rot_angle)
	string x_wave, y_wave; variable rot_angle
	Prompt x_wave, "Select x-coordinates", popup wavelist("*x*", ";", "")
	Prompt y_wave, "Select y-coordinates", popup wavelist("*y*", ";", "")
	Prompt rot_angle, "By what angle do you wish to rotate (degrees)?"

	PauseUpdate
	Silent 1

	wavestats/q $x_wave
	variable numpts = V_npnts
	Make/o/n=(2, numpts) CoordMatrix
	CoordMatrix[0][] = $x_wave[q]
```

```
    CoordMatrix[1][] = $y_wave[q]

    rot_angle *= Pi/180

    Make/o/n=(2, 2) RotationMatrix
    RotationMatrix[0][0] = cos(rot_angle)
    RotationMatrix[0][1] = -sin(rot_angle)
    RotationMatrix[1][0] = sin(rot_angle)
    RotationMatrix[1][1] = cos(rot_angle)


    MatrixMultiply RotationMatrix, CoordMatrix
    $x_wave = M_product[0][p]
    $y_wave = M_product[1][p]

End
```

NOTES AND REFERENCES FOR APPENDIX A

1. *Igor Pro 4.01A*, (WaveMetrics, Inc.: 2000). Igor Pro is an all-inclusive data processing application based on the use of "waves" or matrix algebra to bypass the use of do-loops for many functions. It includes spreadsheets, plotting, image process, pre-defined functions, and user-defined macros and functions all in one application. The version of this software that I own is old and operates on Mac OS 9 (Classic Environment).

APPENDIX B

COMPUTER VISION HILLOCK DETECTION

While qualitative visual inspection of luminescent hillock images is straightforward, manually transferring this information into analyzable, quantitative data can become very laborious (see Chapter 4, Section 4.2.1). Computer vision algorithms offer one avenue for automated feature detection, allowing for more efficient analysis of larger volumes of data.[1] Tasks that the human eye and brain can perform so easily, however, involve a number of complex processes that must be accounted for in automated image analysis. It requires several steps of processing, reduction, and interpretation based on objective, programmable criteria. With the guidance and assistance of Dr. Gerald Seidler[2] from the University of Washington Department of Physics, I worked intensively for several months applying such routines to our confocal images. The methods we attempted and the recommended future directions are included herein, as a supplement to the work reported in Chapter 4.

The key features of the hillock image profile that can be exploited for feature detection are:

- A sharp corner at the apex of each hillock.
- Well-defined straight lines extending from the apex (along the fast-slow boundary of the hillock), where the angular spread between these two

lines, and the orientations of the lines are the same for every hillock on a crystal.

- If one were to draw a straight line across the image that intersects one of the edges marking a hillock fast-slow boundary, the intensity profile would go from background intensity, to suddenly bright, to gradually less bright (see Figure B.1).

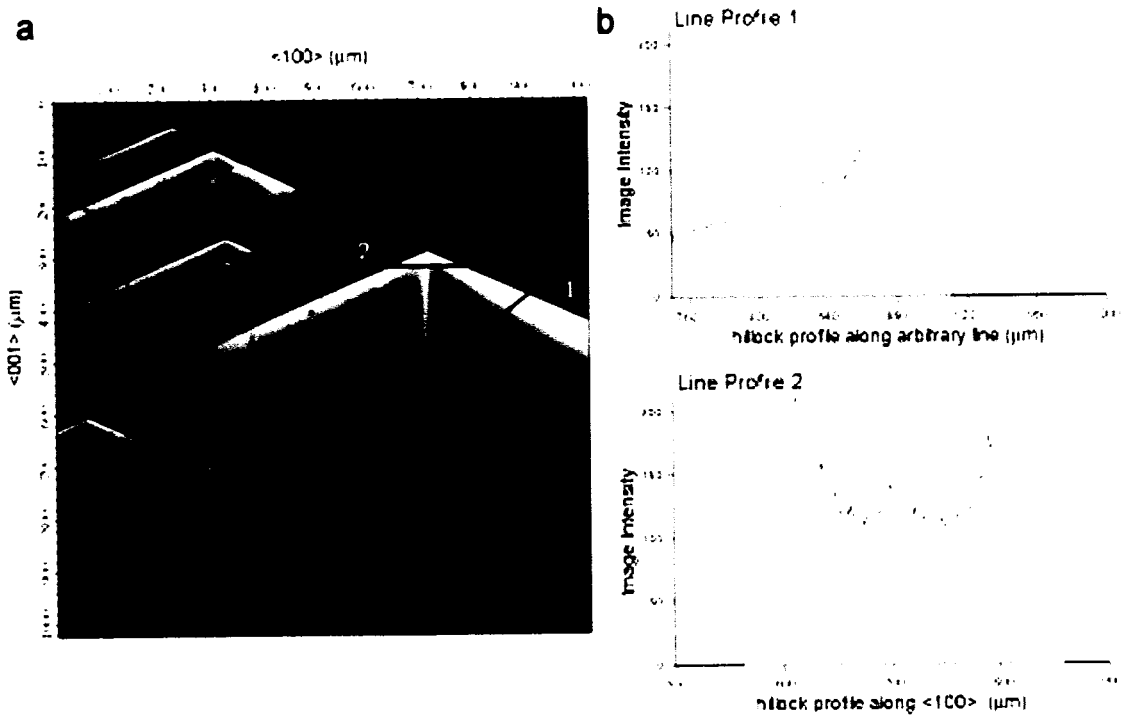

Figure B.1. *Intensity line profiles of dyed hillock.* a) Sample confocal image of KAP hillocks dyed with 10^{-5} M DCF. b) Intensity profiles of the gray-scale image along lines 1 and 2 shown in (a). Profiles show sharp intensity gradients at the 'chevrons' demarcating the fast from the slow slopes of the hillocks.

Given the sharp intensity gradients that occur at the hillock fast-slow boundary lines, we decided to start with a simple gradient analysis, involving the Laplacian operator ($\nabla^2 I(x,y)$) and a threshold setting, to identify where the

greatest discrete shifts in intensity were. The use of a threshold serves to reduce the data to a simple black and white image, as well as eliminate noise. Figure B.2 gives an example of this process for a section (b) of the crystal shown in (a) to which the Laplacian has been applied (c), and then anything below a threshold intensity of 120 was removed from the image in (d).

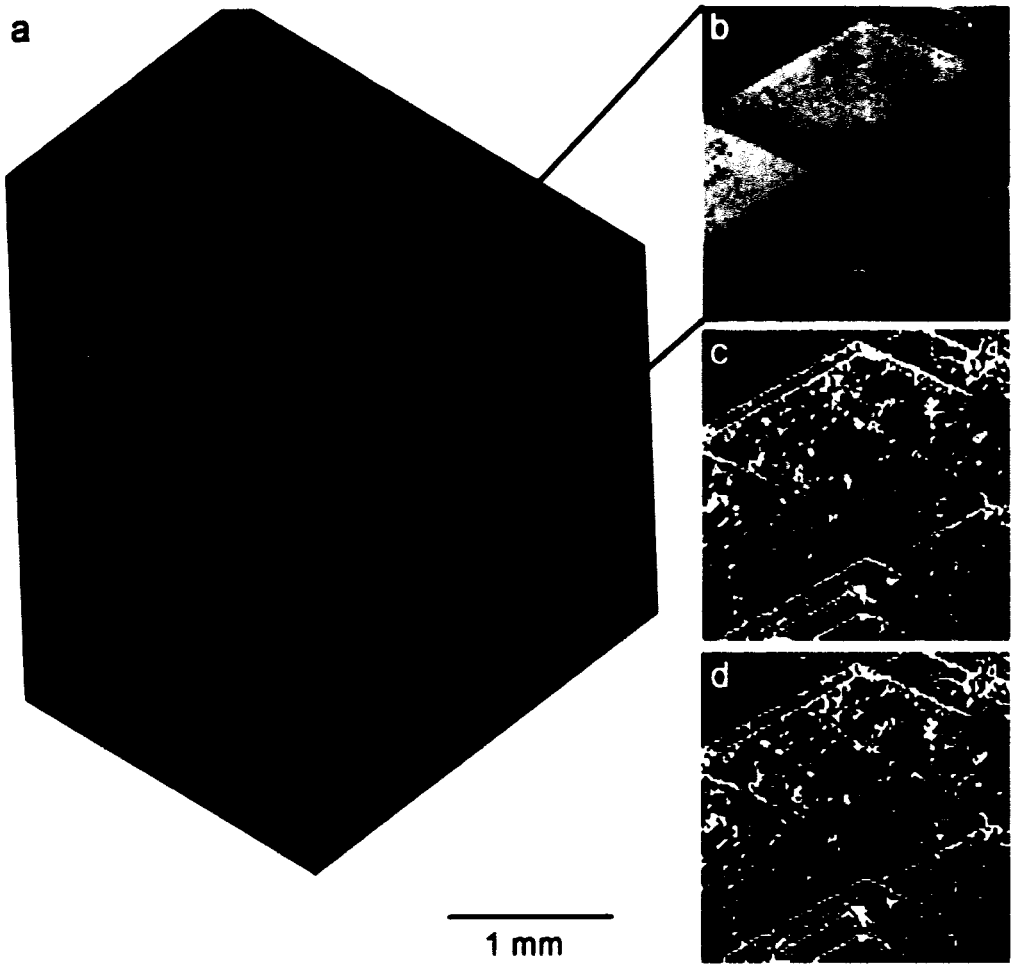

Figure B.2. *Laplacian and threshold operators applied to hillock image.* a) A confocal image of the surface layer for a KAP/LGSFY (10^{-5} M) crystal. b) a slightly magnified segment of the crystal shown in (a) that was selected for analysis. c) The result of applying the Laplacian operator to the image in (b). d) The resulting binary image from setting a threshold of 120 to the image shown in (c).

As can be seen in Figure B.2d, this simple set of operations was not robust enough to efficiently distinguish the hillocks from the noise created by "splotches" on the surface of the crystal. We next used a more involved gradient technique involving a circular gradient mask to smooth out some of the noise features, in addition to the use of a threshold. The circular mask consisted of a 5×5 matrix with effective radius of 2.1 pixels, an example of which is given in Figure B.3.

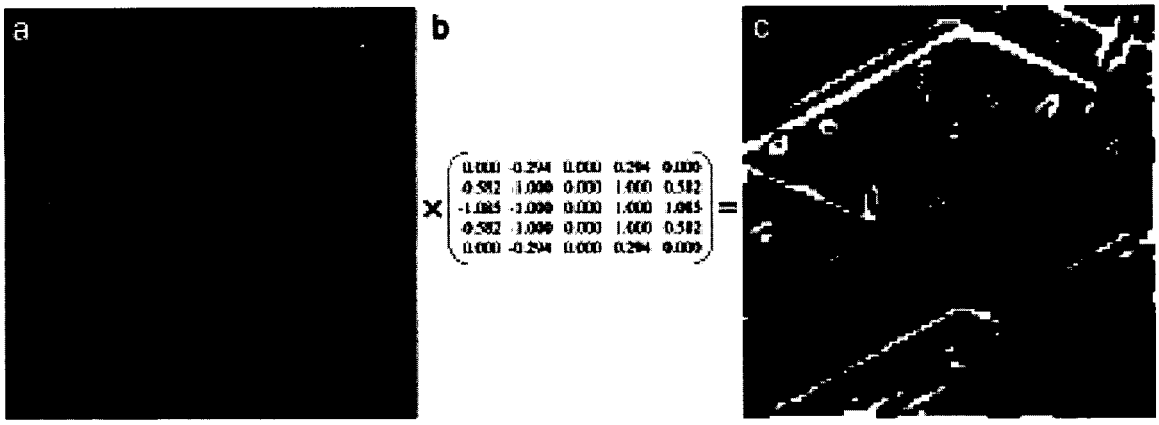

Figure B.3. *Circular gradient and threshold operations applied to hillock image.* a) Sample of confocal image showing in Figure B.2. b) Circular mask applied across the image. c) Resulting binary image after applying a threshold of > 55 to the circular gradient operated image. This method improved signal to noise, however several hillocks were eliminated from the final image due to contrast differences.

The circular gradient and threshold method resulted in much better signal to noise, however it also eliminated many valid hillocks, due to their varying contrast. Thus, we decided to give template matching techniques a try instead of relying upon intensity gradients alone. Template matching is a simple process of using a matrix that mimics the expected intensity profile of the feature of interest. We first applied an edge template that mimicked the intensity profile in Figure B.1b (scaled to a maximum value of 1), and where the slope of the edge could be

varied. Two templates were created, one for each edge direction of a hillock. Figure B.4 shows examples for each step of this process, with (a) and (b) showing the intensity profiles convolved with the templates indicated below each image, and (c) shows the final binary image obtained from adding the template-scanned images and then passing the result through a threshold of 20.

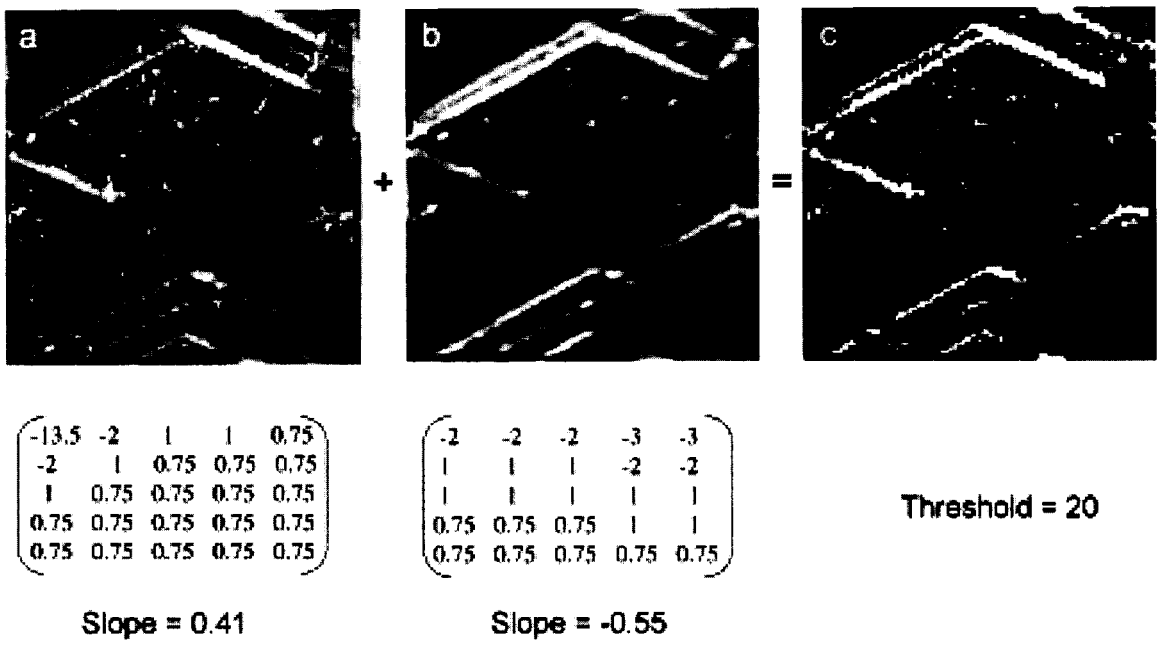

Figure B.4. *Edge template matching operations applied to hillocks.* a) An edge template for the [100] side of the hillocks, with slope = 0.41 was applied to the sample image shown in Figure B.2b. b) An edge template for the [$\bar{1}$00] side of the hillocks, with slope = -0.55 was applied to the same sample image. These two images were then added together and passed through a threshold (≥ 20) to give the binary image shown in (c).

In comparing Figure B.3c and Figure B.4c it can be seen that the edge template matching helped to draw out more of the hillock lines than the circular gradient, however extraneous data from surface splotches are still getting through. Thus, we took the template matching a step further by creating a single corner template

to match the entire hillock profile at its apex, rather than two edge templates summed separately. Since the hillock edges extend for many pixels, whereas the surface splotches are more isolated, we decided to use a larger (11 × 11) template to create greater reliability in hillock recognition and noise elimination (Figure B.5)

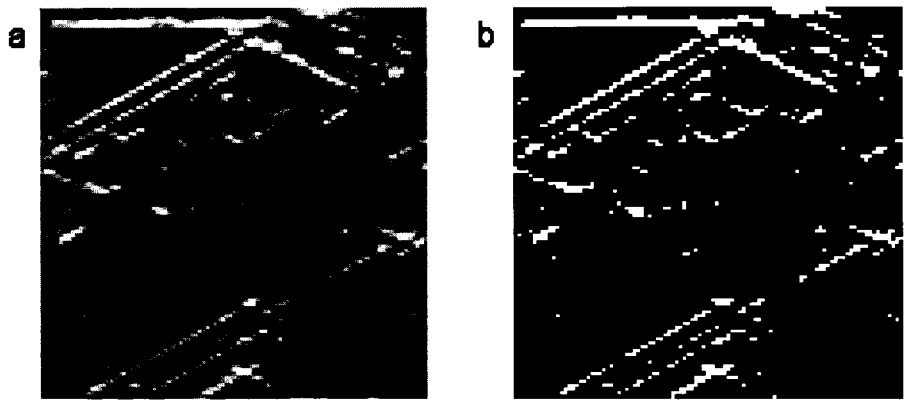

Corner Mask
Slope = ± 0.4

$$\begin{pmatrix} 0.95 & 0.95 & 0.95 & 0.95 & 0.95 & 0.95 & 0.95 & 0.95 & 0.95 & 0.95 & 0.95 \\ 0.95 & 0.95 & 0.95 & 0.95 & -2 & -2 & -2 & 0.95 & 0.95 & 0.95 & 0.95 \\ 0.95 & 0.95 & -2 & -2 & -2 & -2 & -2 & -2 & -2 & 0.95 & 0.95 \\ -2 & -2 & -2 & -2 & 1 & 1 & 1 & -2 & -2 & -2 & -2 \\ -2 & -2 & 1 & 1 & 1 & 1 & 1 & 1 & 1 & -2 & -2 \\ 1 & 1 & 1 & 1 & 0 & 0 & 0 & 1 & 1 & 1 & 1 \\ 1 & 1 & 0 & 0 & 0 & 0 & 0 & 0 & 0 & 1 & 1 \\ 0 & 0 & 0 & 0 & 0 & 0 & 0 & 0 & 0 & 0 & 0 \\ 0 & 0 & 0 & 0 & 0 & 0 & 0 & 0 & 0 & 0 & 0 \\ 0 & 0 & 0 & 0 & 0 & 0 & 0 & 0 & 0 & 0 & 0 \\ 0 & 0 & 0 & 0 & 0 & 0 & 0 & 0 & 0 & 0 & 0 \end{pmatrix}$$

Threshold = 2

Figure B.5. *Corner template matching operation applied to hillocks.* a) Image resulting from applying the 11 × 11 corner template (inset) to the raw sample image shown in Figure B.2b. b) Resulting binary image after passing the data through a threshold of 2.

Yet again, the operations do not appear to be robust enough to eliminate the noise while still pulling out the hillock features that occur at varying contrast. Furthermore, template matching is only good to the degree that it matches the exact pattern of the corner in width, slopes, angular spread, and intensity

gradients. In all the above mentioned operations, the use of thresholds consistently posed a challenge due to varying contrast between hillocks. Thus, we began searching for a more robust, threshold-independent corner detector.

Hough transform methods, which search for intersections in parameter space and isolate corners by interpolation, are often cited as being robust feature detectors.[1] However, these methods are more computationally intensive and are therefore usually reserved for detecting non-ideal corners or more rounded shapes. Thus, we did not attempt the Hough transform methods with this data, and were instead directed to the Harris detector algorithm as a robust, combined corner-edge detector.[3] The Harris detector uses a matrix of the following form:

(B.1)
$$G(x) = \begin{pmatrix} \frac{dI_x}{dx}^2 & \frac{dI_x}{dx}\frac{dI_y}{dy} \\ \frac{dI_x}{dx}\frac{dI_y}{dy} & \frac{dI_y}{dy}^2 \end{pmatrix} = \begin{pmatrix} \lambda_1 & 0 \\ 0 & \lambda_2 \end{pmatrix}$$

where $I(x,y)$ is the intensity map of the image. When this matrix is diagonalized, the eigenvectors (λ_1 and λ_2) become the key identifiers of the feature profile, with the vector giving the edge direction and the value giving the edge magnitude. If $\lambda_1 = \lambda_2 = 0$, the image region is flat or of constant brightness. If $\lambda_1 > 0$ and $\lambda_2 = 0$, then the it describes an ideal edge (discrete step function in intensity), with λ_1 indicating the direction orthogonal to the edge. If $\lambda_1 \geq \lambda_2 > 0$, the feature is a corner, where the eigenvalues indicate the level of contrast at that corner. The uniqueness of the Harris detector algorithm, is to quickly calculate the corner response by finding features where both eigenvalues are large using the following formula:

(B.2)
$$C(x,y) = \det(G) - k \times \mathrm{trace}^2(G) = \lambda_1\lambda_2 - k(\lambda_1 + \lambda_2)^2$$

where k is a tunable user-defined scalar (Harris suggests 0.04 for good corner detection). This results in an intensity map of feature response, from which corners can be extracted by various means. One method for corner extraction is to apply a threshold to small tiles of the image at a time, and sort the features for each tile according to their corner response value, and select out the desired features. Another method is to search for local maxima on the corner response map $C(x,y)$. While a threshold-independent approach is to vary the detection sensitivity parameter, k: large k leads to less sensitivity and fewer corners, small k leads to more sensitivity and more corners. With this approach, one can then use a contour plot in eigenvalue space as shown in Figure B.6 to identify edge regions ($C < 0$), flat regions ($C \sim 0$), and corner regions ($C > 0$).[3]

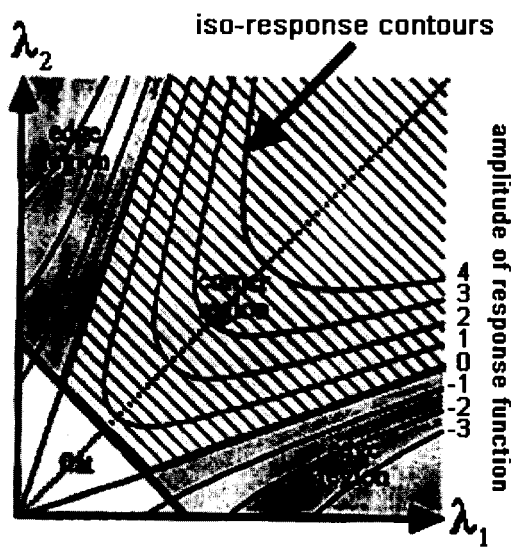

Figure B.6. *Harris detector eigenvalue contour map for feature selection.* When the corner response function curves fall at values of $C < 0$, the features are of edge profiles. If $C \sim 0$, the intensity profile is constant or flat. When $C > 0$, there is a large gradient in two orthogonal directions, indicating a corner. (Image reproduced from Harris and Stephens in Ref. 3).

The Harris detector holds promise for identifying hillock apices under varying rotation and illumination. Unfortunately, this is as far as I got with this work. However, I do feel that this would be a profitable undertaking for future students who are drawn in this direction.

NOTES AND REFERENCES TO APPENDIX B

1. E. R. Davies, *Machine Vision, 3rd Edition,* (Elsevier-Morgan Kaufmann Publishers: San Francisco, 2005).

2. Dr. Gerald Seidler is an Associate Professor and the principle researcher with the Microstructural Kinetics Laboratory at the University of Washington Department of Physics, Box 351560, Seattle, WA 98195-1560. (206)-616-8746, seidler@phys.washington.edu.

3. C. Harris and M. Stephens, *Proc. 4th Alvey Vision Conf.*, pp. 147-151 (Plessey Research Roke Manor: United Kingdom, 1988).

APPENDIX C

SAMPLE REFERENCE LIST

Figure 2.2

- Lab book #1
- Image file location (pics:KAP_images: KAP_DCF_FluorDIC_AFM_new_flat.tif)
- KAP/DCF (10^{-5} M) grown by spontaneous nucleation at 30 °C by slow evaporation. DIC, fluorescence, AFM photos

Figures 2.10 - 2.14

- Lab book #1
- Image file location (Dissertation:Thesis_Chapters:Chapter2:Dyes: KAP_LG_*)
- Data files located in (TVB_hillocks:our_research:KAP_LG:*)
- KAP/LGSFY (10^{-5} M) grown by spontaneous nucleation at 30 °C by slow evaporation, DIC, fluorescence, LD, absorbance spectra

Figures 2.15 - 2.19

- Lab book #3
- Image file location (Dissertation:Thesis_Chapters:Chapter2:Dyes: KAP_Erio_*)
- Data files located in (TVB_hillocks:our_research:KAP_ERIO:*)
- KAP/Erio (10^{-5} M) grown by spontaneous nucleation at 30 °C by slow evaporation, DIC, fluorescence, LD, absorbance spectra

Figures 2.20 - 2.24, 2.27, 3.1-3.4 and Tables 3.1, 3.2

- Lab book #2 and #3
- Image file location (Dissertation:Thesis_Chapters:Chapter2:Dyes: KAP_DCF_*) also see (papers&reports:TVB&KLW_KAP_DFC_paper:*)
- Data files located in (Dissertation:key research info:DCF:*)
- KAP/DCF (various concentrations) grown by spontaneous nucleation at 30 °C by slow evaporation, DIC, fluorescence, LD, absorbance spectra

Table 2.3

- Calculations in lab book #3, page 132.

Figure 2.26

- Lab book #3
- Image file location (Dissertation:Thesis_Chapters:Chapter2:Dyes: KAP_DCF_*)
- Data files located in (Dissertation:key_research_info:DCF:Absorption Spectra:solution spectra:pH_DCF_studies:*)
- KAP/DCF (5×10^{-5} M) grown by spontaneous nucleation at 30 °C by slow evaporation, DIC, fluorescence, LD, absorbance spectra

Table 2.4

- Calculations in lab book #3, page 118.

Figures 2.28 - 2.29, 3.10 - 3.15, and Tables 2.5, 3.3 - 3.6

- Lab book #3
- Image file location (Dissertation:Thesis_Chapters:Chapter2:Dyes: KAP_DCF_*) also see (papers&reports:TVB&KLW_KAP_DFC_paper:*)
- Data files located in (Dissertation:key_research_info:MS Modeling:*)
- Modeling results for DCF species into KAP (010) steps

Table 2.6

- See lab book #3 for confocal specs.

Figure 2.33, 4.13-4.15

- Confocal notes dispersed throughout lab books 1-3.
- Image file location (Dissertation:Thesis_Chapters:Chapter2:Confocal:*)
- Data files located in (TVB_hillocks:our research:confocal_KECK:* and …:confocal_NTUF:*)
- Confocal images, movies, and mosaics

Figure 2.34 - 2.36, 4.16 - 4.34, Table 4.1, and Appendix A

- File locations (Fractal Analysis:CorrDim_Analysis:*)
- Fractal analysis results from various samples, final images used, plus the Igor Pro programs.

Figure 2.37

- Lab books #2 and #3
- All designs and testing of the crystal growth flow system

Figures 3.5 - 3.9

- Lab book #3 and Miranda Robertson's lab book
- Data files located in (Dissertation:key research info:DCF:cations:*) also see (papers&reports:TVB&KLW_KAP_DFC_paper:*)
- KAP/DCF studies with trivalent cations

Figures 4.1 - 4.6

- Lab book #2
- Image files located in (pics:OriginOfLife:*) and (papers&reports:FaradayDiscussions06:Figures:*)
- Information transfer from seed studies with KAP growth.

Figure 4.7

- Lab book #2
- Image files located in (Dissertation:key research info:ParticulateInclusion:*)
- Particulate inclusion studies with qdots and polystyrene beads in KAP

Figures 4.8 - 4.12

- Lab book #3
- Image files located in (Dissertation:key research info:x-ray_topography&KAP:*)
- X-ray topography results from Alexey Voloshin and samples specs we sent him.

Appendix B figures

- Image and Data files located in (Dissertation:key research info:Machine Vision:*)
- Computer vision detection of luminescent hillocks and confocal image processing.

VITA

Theresa V. Bullard

SUMMARY OF QUALIFICATIONS

- Ph.D. in physics with emphasis on interdisciplinary experimental research
- Experienced at quantitative data analysis
- Efficient at learning new subjects and material
- Notable breadth and adaptability
- Effective communication and team leadership

EDUCATION

Ph.D. in Physics. University of Washington, Seattle, WA. 2008.

M.S. in Physics. University of Washington, Seattle, WA, 2001.

B. S. in Physics, Minor in Computer Science, Minor in Mathematics, University of Denver, 1998.
GPA: 3.88/4.0, *Magna Cum Laude*. Awarded 4-year Academic Honors Scholarship, and senior year Physics Merit Scholarship.

EXPERIENCE

Ph.D. Dissertation Research, University of Washington.
(Kahr Research Group - Chemistry and Crystallography). 2005-2008.

- Performed first experimental tests for a popular theory on the mineral origin of life using dyed crystals, confocal laser scanning microscopy, and fractal analysis.

Research Assistant, University of Washington, UW Royal Research Fund.
(Kahr Research Group - Chemistry and Crystallography). 2004-2005.

- Researched crystal defect-impurity interactions of dyed crystals using Confocal Laser Scanning Microscopy and fractal analysis methods.
- Implemented machine vision algorithms for automated feature identification and image processing.

NSF funded IGERT Fellow, University of Washington, Center for Nanotechnology.
(Kahr Research Group - Chemistry and Crystallography). 2003-2004.

- Researched nanoscale crystal-impurity interactions of mixed crystals using atomic force microscopy and confocal laser scanning microscopy.

Graduate Student Fellow, Battelle, Pacific Northwest National Laboratory. (National Security Directorate). Summer 2002

- Designed, assembled, and experimented on model gamma ray detectors consisting of scintillating materials and fibers, wavelength shifting optics, and photomultiplier tubes. Implemented a new design, based on these experiments, into the "Highly Portable Neutron Detector" to be used for homeland security detection of weapons-grade radioactive material.

Research Assistant, University of Washington, Center for Experimental Nuclear Physics and Astrophysics. (Sudbury Neutrino Observatory). 1998 - 2002

- Operated the Sudbury Neutrino Observatory (SNO) detector both remotely and in the underground control room
- Played a key role in the preparation and assembly of He3 proportional counters (Neutral Current Detectors, NCDs), under class 1000 clean room conditions, for SNO.
- Developed algorithms for the analysis of NCD data using techniques such as Fourier transform analysis, pulse-shape characterization, least-squares fitting routines, pulse topology categorization, Monte Carlo simulation, and other diagnostics.
- Programmed software processors for event-by-event, modular analysis of digitized data.

Teaching Assistant, University of Washington, Physics Department. Autumn 1998 & Winter 2003

- Taught physics tutorial and laboratory sessions with about 30 undergraduate students per class.
- Facilitated in Study Center to assist students with homework and answer questions.

DOE funded Intern/Research Assistant, University of Denver, Physics Department.
(Atomic and Molecular Physics Group). 1997 - 1998

- Designed and built a stand-alone vacuum experiment for the study of neutral-to-ion conversion surfaces used in the Low Energy Neutral Atom (LENA) Imager, flown on the IMAGE Satellite. Interfaced this experiment's hardware with a computer via LabVIEW.

DOE funded Intern/Research Assistant, University of California, Santa Cruz. (Santa Cruz Institute of Particle Physics). Summer 1997

- Researched and developed front-end electronic read-out systems and microchips, for use in conjunction with silicon microstrips in high energy particle detectors.

Research Assistant, University of Denver, Physics Department. (Atmospheric Physics Group). 1996 - 1997

- Assembled and aligned optics for an atmospheric spectrometer.
- Maintained Database.

OTHER SKILLS AND ACCOMPLISHMENTS

Communication:

- Taught physics tutorial and laboratory sessions with about 30 undergraduate students per class.
- Delivered research results and various proposals in both oral and poster presentations.
- Created visual display for presentation of SNO operations and results.
- Designed marketing materials, posters, and fliers for various events.
- Composed and edited technical documents.
- Wrote and edited event proposals, newsletters, and contact letters for the physics Career Development Organization.
- Participated in science news writing training for communicating science to the general public.
- Actively presented to general audiences on a variety of topics ranging from wellness, to youth, to philosophy.

Leadership:

- Supervised research projects conducted by junior graduate and undergraduate students.
- President of a registered student organization, CDO, that organized career-related seminars, workshops, and networking events for physics and astronomy students.
- Managed 10 graduate students for CDO and established an operational budget.
- Initiated and organized first annual UW physics-industry "Networking Day".
- Mentored incoming graduate students.
- Served on the Executive Board as the House Manager of the University of Denver Delta Zeta Sorority, and was an integral part of the decision making for the chapter.

Computer Skills:

- Extensive knowledge in: IGOR Pro, PowerPoint, Microsoft Office, Netscape Communicator™.
- Working knowledge in: C/C++, Unix, PERL, HTML, Basic, LabVIEW, Metrowerks CodeWarrior, Windows/DOS™, Mac OS™, Microsoft Outlook Express™, ImageJ & NIH Image, Adobe Photoshop™, Accelrys MS Modeling Suite, Mathematica™
- Familiarity with: VX-REXX, Mathcad, SolidWorks.

RELEVANT COURSES

Electronic Theory of Materials	Bonding & Structure
Crystal Dislocations	Science Writing
Quantum Mechanics	Electromagnetism
High Energy Physics	Thermodynamics
Statistical Mechanics	Experimental Nuclear Physics
Classical Mechanics	Contemporary Physics
Intro to Quantum Field Theory	Numerical Methods
Nuclear Astrophysics	Electronic Theory of Materials

PUBLICATIONS

Publications Related to Thesis

- "Role of Kinks in Dyeing Crystals: Confocal Luminescence Microscopy from Single Molecules to Squared Centimeters"
  T. V. Bullard, K. L. Wustholz, M. Robertson, J. Freudenthal, P. J. Reid, and B. Kahr
  To be published (2008)

- "Test of Cairns-Smith's 'crystals-as-genes' hypothesis"
  T. Bullard, J. Freudenthal, S. Avagyan, and B. Kahr
  Disc. Faraday Soc., **136** (2007), 231.

- "Luminescence Imaging of Growth Hillocks in Potassium Hydrogen Phthalate"
  T. Bullard, M. Kurimoto, S. Avagyan, S. H. Jang, B. Kahr
  ACA Transactions, **39** (2004).

- "Potassium salt of phthalaic acid hydrate dimmer, monobasic: New structure and correction to the literature"
  J. Benedict, T. Bullard, W. Kaminsky, and B. Kahr
  Acta Cryst. C: Crystal Structure Communications, **60** (2004), m551.

Sudbury Neutrino Observatory Collaboration Publications

- "Array of low-background He-3 proportional counters for the Sudbury Neutrino Observatory"
  The SNO Collaboration (Amsbaugh, JF; Anaya, JM; Banar, J; *et al.*)
  Nuclear Instruments & Methods in Physics Research Section A – Accelerators, Spectrometers, Detectors, and Associated Equipment, **579**(3) (2007), 1054.

- "Determination of the nu(e) and total B-8 solar neutrino fluxes using the Sudbury Neutrino Observatory Phase I data set"
  The SNO Collaboration (Aharmim, B; Ahmad, QR; Ahmed, SN; *et al.*)
  Phys. Rev. C, **75**(4) (2007), 045502.

- "Electron energy spectra, fluxes, and day-night asymmetries of B-8 solar neutrinos from measurements with NaCl dissolved in the heavy-water detector at the Sudbury Neutrino Observatory"
  The SNO Collaboration (Aharmim, B; Ahmed, SN; Anthony, AE; *et al.*)
  Phys. Rev. C, **72**(5) (2005), 055502.

- "Electron antineutrino search at the Sudbury Neutrino Observatory"
  The SNO Collaboration (Aharmim, B; Ahmed, SN; Beier, EW; *et al.*)
  Phys. Rev. D, **70**(9) (2004), 093014.

- "Measurement of the total active B-8 solar neutrino flux at the sudbury neutrino observatory with enhanced neutral current sensitivity"
  The SNO Collaboration (Ahmed, SN; Anthony, AE; Beier, EW; *et al.*)
  Phys. Rev. Lett., **92**(18) (2004), 181301.

- "Constraints on nucleon decay via invisible modes from the Sudbury Neutrino Observatory"
  The SNO Collaboration (Ahmed, SN; Anthony, AE; Beier, EW; *et al.*)
  Phys. Rev. Lett., **92**(10) (2004), 102004.

- "Neutral current and day night measurements from the pure D2O phase of SNO"
  The SNO Collaboration (Hallin, AL; Beier, EW; Biller, SD; *et al.*)
  Nucl. Phys. B: Proc. Supp., **118** (2003), 3.

- "Direct evidence for neutrino flavor transformation from neutral-current interactions in the Sudbury Neutrino Observatory"
  The SNO Collaboration (Ahmad, QR; Allen, RC; Andersen, TC; *et al.*)
  Phys. Rev. Lett., **89**(1) (2002), 011301.

- "Measurement of day and night neutrino energy spectra at SNO and constraints on neutrino mixing parameters"
  The SNO Collaboration (Ahmad, QR; Allen, RC; Andersen, TC; *et al.*)
  Phys. Rev. Lett., **89**(1) (2002), 011302.

- "Measurement of the rate of nu(e)+d -> p+p+e(-) interactions produced by B-8 solar neutrinos at the sudbury neutrino observatory"
  The SNO Collaboration (Ahmad, QR; Allen, RC; Andersen, TC; *et al.*)
  Phys. Rev. Lett., **87**(7) (2001), 071301.

INTERESTS, ACTIVITIES, AND AWARDS

- *Officer* of the Career Development Organization for Physicists and Astronomers at the University of Washington.
  - *Vice President*, September 2003 - present.
  - *President*, July 2001 - June 2002.
  - *Chair of Guest Speaker Relations*, July 2000 - June 2001.
- *Committee Member for Educational Outreach and for Industry Connections.* Nanotech Student Association at the University of Washington. July 2003 - present.
- *IGERT Fellow.* Awarded for Integrative Graduate Education and Research Training in Nanotechnology at the University of Washington. 2003-2004.
- *Physics Scholar.* Awarded senior year scholarship base on merit at the University of Denver. 1998.
- *Honors Student.* Awarded 1/2-tuition academic honors scholarship at the University of Denver.
  September 1994 - July 1998.
- *NCAA Athlete*, Women's Volleyball. Awarded athletic scholarship at the University of Denver. August 1994 - November 1997.
- *Participant* on the Substance Abuse Prevention Task Force, May 1996.
- *Dean's Honor Roll*, multiple times throughout college for taking at least 15 quarter hours and achieving the G.P.A. of at least 3.75. University of Denver.
- *Hornbeck Scholar.* This award is for outstanding service and scholarship, and having completed 12+ quarter hours and earning a G.P.A of 4.0. University of Denver, 1995-1996
- *Achievement in Undergraduate Research*, 1995-1996.
- *All American Scholar*, 1996-1998.
- *Colorado Athletic Conference All Academic*, 1995-1997.
- *Creative Writer*, with writings in both prose and poetry

NATIONAL AFFILIATIONS

American Physical Society, American Institute of Physics, Society of Physics Students, Alpha Lambda Delta, Golden Key Society, Order of Omega, Delta Zeta Sorority.